Relation entre auto-organisation et création/résorption de défauts microstructuraux sous irradiation laser ultrabrèves

Anthony Abou Saleh

N° d'ordre NNT :
2019LYSES001

THESE de DOCTORAT DE L'UNIVERSITE DE LYON
opérée au sein de
Laboratoire Hubert-Curien

Ecole Doctorale N° 488
Sciences Ingénierie Santé SIS

Spécialité de doctorat : Physique
Discipline : Interaction laser-matière

Soutenue publiquement le 08/01/2019, par :
Anthony Abou Saleh

Relation entre auto-organisation et création/résorption de défauts microstructuraux sous irradiation laser ultrabrèves

---

Devant le jury composé de :

GERARD O'CONNOR	Rapporteur	National University of Ireland
PHILIPPE DELAPORTE	Rapporteur	Université d'Aix-Marseille
LEONID V. ZHIGILEI	Examinateur	University of Virginia
LUDOVIC DOUILLARD	Examinateur	Iramis CEA Saclay
ANNE TANGUY	Examinatrice	INSA Lyon
FLORENT PIGEON	Examinateur	Université Jean-Monnet
JEAN-PHILIPPE COLOMBIER	Co-directeur de thèse	Université Jean-Monnet
FLORENCE GARRELIE	Directrice de thèse	Université Jean-Monnet

Résumé

L’irradiation des matériaux par des impulsions laser ultrabrèves déclenche un agencement anisotrope de la matière à l’échelle nanométrique: des structures de surface périodiques induites par laser (LIPSS). L'énergie laser déposée et distribuée de manière inhomogène dans le matériau induit des contraintes thermiques locales et des changements de phase transitoires entraînant ainsi des modifications microstructurales.

Cette thèse porte sur le rôle de l'altération de la surface irradiée ainsi que les modifications microstructurales en profondeur dans la contribution à la formation des LIPSS, en établissant une corrélation entre l'auto-organisation de la matière et la génération de défauts en tenant en compte de l'orientation cristalline. Comme les LIPSS sont générés au seuil de transition de phase, l’étude de la corrélation avec les défauts induits est alors pertinente.

Une étude expérimentale couplée à des simulations de dynamique moléculaire effectuées à l’Université de Virginie suggère que l'altération de surface générée par une irradiation d'échantillons monocristallins de Chrome dans le régime de spallation est susceptible de jouer un rôle majeur dans le déclenchement de génération de LIPSS de haute fréquence spatiale. La microscopie à force atomique ainsi que les résultats de simulations attestent que les caractéristiques de rugosité de surface à l'échelle nanométrique dépendent de l'orientation cristalline. La forte rugosité de surface générée par la première impulsion laser active la diffusion de la lumière laser et l’exaltation du champ local lors des irradiations ultérieures, ce qui génère des structures LIPSS de haute fréquence plus prononcés du côté (100) que celle du (110). Une étude expérimentale approfondie, utilisant la microscopie électronique rétrodiffusés et transmission, a révélé que le Cr (110) est plus susceptible d'être endommagé que les autres orientations cristallines de surface. On constate que les défauts induits par le laser peuvent altérer la topographie de surface et la région sous-jacente, ce qui peut avoir un impact sur les caractéristiques des centres de rugosité favorisant la formation de structures de fréquence spatiale élevée.

Afin d’accéder à la transition de phase subie dans la région de formation des LIPSS, une approche d'analyse microstructurale à haute résolution couplée à des calculs hydrodynamiques est utilisée, comprenant la croissance épitaxiale et la nanocavitation. La formation de structures de fréquence spatiale élevée est le résultat de nanocavités périodiques piégés sous la surface, ainsi que des nanocavités apparues à la surface des matériaux cubiques faces centrées.

De plus, étant donné que le feedback dans la formation des LIPSS est souvent évoquée, le comportement dynamique des surfaces a été sondé par microscopie électronique à photoémission et étayé par des calculs électromagnétiques. Un caractère périodique des photoélectrons émis par les creux des LIPSS a été mis en évidence, ce qui a permis de vérifier la modulation du dépôt d'énergie.

Le travail effectué contribue non seulement à progresser vers l'objectif général d’élucider le phénomène complexe multi-échelles de la formation des LIPSS, mais ouvre une nouvelle voie expérimentale pour générer des structures non conventionnelles avec des périodicités extrêmes (~60nm), offrant ainsi de nouvelles opportunités pour le traitement laser ultrarapide des métaux.

Abstract

Irradiation of materials by ultrashort laser pulses triggers anisotropically structured arrangement of matter on the nanoscale, the so-called laser-induced periodic surface structures (LIPSS), or 'ripples'. Ultrashort laser energy deposited and distributed inhomogeneously in the material launches local thermal stresses and transient phase changes yielding microstructural modifications.

This thesis focuses on the role of irradiated surface alteration as well as in-depth microstructural modifications in promoting LIPSS formation, by establishing a correlation between self-organization of matter and defect generation taking into account crystalline orientation. Since LIPSS are generated at the threshold of phase transition, then the correlation with defects formation is relevant.

An experimental study coupled with molecular dynamic MD simulations performed in the University of Virginia suggest that surface alteration generated by a single pulse irradiation of monocrystalline Cr samples in the spallation regime is likely to play a main role in triggering high-spatial frequency LIPSS generation upon irradiation by multiple laser pulses. Atomic force microscopy as well as computational results suggested that the nanoscale surface features are crystalline orientation dependent. The higher surface roughness generated by the first laser pulse activates scattering of the laser light and the local field enhancement upon irradiation by the second laser pulse, leading to the formation of much more pronounced high-spatial frequency structures on the (100) surface as compared to (110) one. An extended in-depth experimental study, using electron backscattered and transmission microscopy, combined with large-scale two-temperature model TTM-MD simulations revealed that Cr (110) is more likely to get damaged. It is found that laser-induced defects can alter the surface topography and the region beneath it which can impact in turn the roughness center features promoting high-spatial frequency structures formation.

In order to infer the phase transition undergone in the LIPSS region, a high resolution microstructural analysis approach coupled with hydrodynamic calculations is employed, including epitaxial regrowth and nanocavitation. High-spatial frequency structures formation is found to be the result of periodic nanovoids trapped beneath the surface as well as nanocavities emerged at the surface on fcc materials.

Furthermore, since optical feedback in LIPSS is often evoked, the behavior of dynamical surfaces was probed by photoemission electron microscopy and supported by electromagnetic calculations. A periodic character of photoelectrons emitted from nanoholes was unveiled, which in turn verified a modulated energy deposition.

The performed work not only contributes to the progress towards the general goal of untangling the complex multiscale phenomenon of the LIPSS formation, but unlocks a new experimental setup to generate unconventional structures with extreme periodicities (~60 nm), which offers new opportunities in ultrafast laser processing of metals.

Contents

Acronyms

LIPSS	Laser-Induced Periodic Surface Structures
LSFL	Low-Spatial Frequency LIPSS
HSFL	High-Spatial Frequency LIPSS
nf	Near-Field
ff	Far-Field
TTM	Two-Temperature Model
MD	Molecular Dynamic
AFM	Atomic Force Microscopy
SKU	Kurtosis
EBSD	Electron Back-Scattered Diffraction
HR-EBSD	High-Resolution EBSD
EBSP	Electron Back-Scattered Pattern
BC	Band Contrast
LM	Local Misorientation
MAD	Mean Angular Deviation
GND	Geometrically Necessary Dislocations
SEM	Scanning Electron Microscope
SE	Secondary Electrons
FEG	Field-Emission Gun
TEM	Transmission Electron Microscope
STEM	Scanning TEM
ADF	Annular Dark Field
HAADF	High-Angular Annular Dark Field
SAED	Selected Area Electron Diffraction
BF	Bright Field
DF	Dark Field
FIB	Focused Ion Beam
PEEM	Photoemission Electron Microscope
1PPE-PEEM	1-Photon PhotoEmission PEEM
3PPE-PEEM	3-Photons PhotoEmission PEEM
CC	Cross Correlation
FOV	Field Of View
STED	STimulated Emission Depletion
STORM	Stochastic Optical Reconstruction Microscopy
PALM	Photoactivated Localized Microscopy
SNOM	Nearfield Scanning Optical Microscope
EAM	Embedded Atom Model
WDM	Warm Dense Matter
SEW	Surface-scattered Electromagnetic Wave
FDTD	Finite-Difference Time-Domain
FFT	Fast-Fourier Transform
SPP	Surface Plasmon Polaritons
RAA	Radially Average Autocorrelation

Chapter 1

Introduction

In this chapter, laser-induced periodic surface structures and microstructural defects generation are introduced. The first part establishes a background on ripples, where different types of periodic nanostructures can be generated respecting irradiation parameters. The second part defines the problematic regarding a lack of comprehension in LIPSS origin, where it is often evoked. The interrelation between the formation of a privileged order of matter and defects is also unraveled. The third part summarizes the structure of this thesis, discussing the goal and the outline of each chapter.

1.1 Background

Femtosecond laser interaction with material surfaces has become ubiquitous, entailed by both inquisitiveness and a tremendous variety of applications in fields scaling from nanotechnology to material science among others. The output of interaction between energetic laser radiation and materials provokes local energy deposition driving permanent alteration of the processed surface, which paves the way towards bulk (3D processing) and surface structuring. The high localization of energy untangles a strong potential for laser structuring and fabrication in view of ultrashort timescales where the interaction is spatio-temporal confined, strongly dependent on irradiation parameters.

Near the energy threshold modification of most materials, it is possible to generate a periodic alignment of surface ripples, referred to laser-induced periodic surface structures (LIPSS). These (quasi-) periodic lines are a universal phenomenon gaining an increasing attraction since the advent of ultrashort lasers where ripples can be generated in a simple single-step process, which leads to surface functionalizing tailoring mechanical, electrical, chemical, tribological, wetting and optical properties upon ultrashort laser irradiation. LIPSS periodicities lower than the laser wavelength can be reached, ranging from a few tens of nanometers to a few microns, on almost any material (metals, semiconductors and dielectrics)[1], even those having a bandgap greater than the laser wavelength[2], and are formed in a broad range of pulse durations, starting from continuous[3] to femtosecond pulsed wave irradiation[4].

Regardless of the weak comprehension dealing with LIPSS formation mechanism, the beginning of the 21th century was crowned with significantly growing number of publications related to the search term ‘laser-induced periodic surface structures’, aroused by the observation of uncommon LIPSS structures with periods quite lower than the laser wavelength. These non-classical periodic arrangement of matter were referred to high-spatial frequency LIPSS (HSFL), or nanoripples, distinguished from the classical slightly sub-wavelength sized ripples, termed low-spatial frequency LIPSS (LSFL).

For irradiation with an angle of incidence normal to the surface, LSFL typically shows periods close to or slightly smaller than the laser wavelength ($\lambda/2 \leq \Lambda_{LSFL} \leq \lambda$), while HSFL exhibit periods considerably smaller than the irradiation wavelength ($\Lambda_{LSFL} < \lambda/2$). HSFL are mainly formed for laser pulse durations ranging from fs to ps. Therefore, the growth availability of systems producing ultrafast laser pulses strongly amplifies the actual research on LIPSS. HSFL can be divided into three sub-categories, regarding ripples orientation and periodicities: far-field parallel ff$_{//}$, near-field parallel nf$_{//}$ and near-field perpendicular nf$_{\perp}$, as indicated in fig 1.1b in the Fourier space. The ff and nf structures are formed via the coherent superposition between the refracted field and the scattered far/near-field, respectively[5]. Finally, LIPSS with periodicities larger than the laser wavelength, generally called ‘grooves’, can be generated when increasing the incident pulse energy. Grooves can be orientated parallel or perpendicular to the electric field polarization.

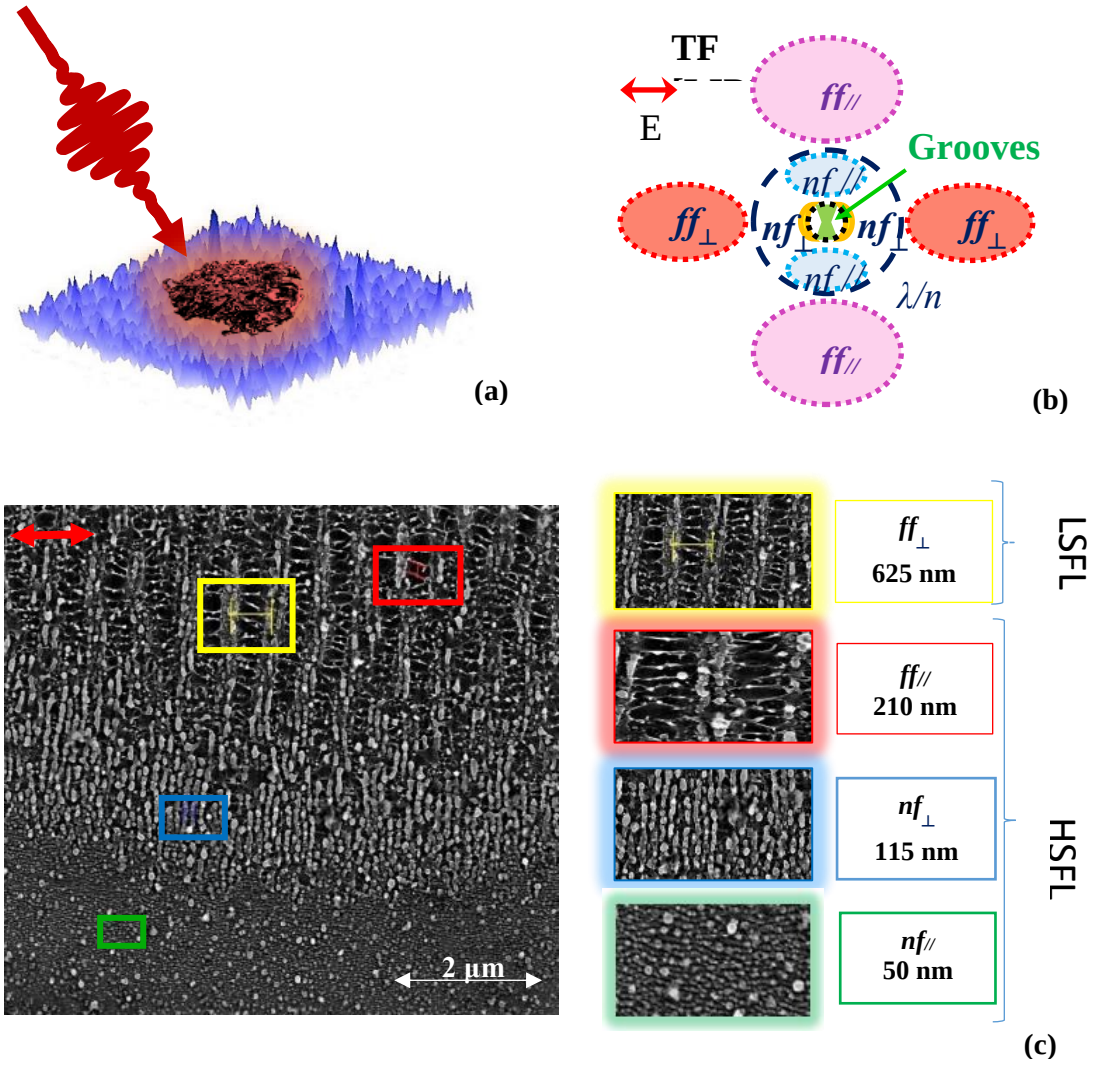

Fig 1.1 (a) Interaction scheme of incident laser beam with a random rough surface. (b) Different types of LIPSS formed under normal incidence, represented in the Fourier space. The far-field ff structures result from the superposition between the scattered far-field and the refracted field, while the near-field nf structures are triggered by the coherent superposition between the scattered near-field and the refracted field[5]. The perpendicular and parallel indexes signify that the structures are perpendicular/parallel to the electric field polarization. (c) illustrates a scanning electron microscope micrograph of a site irradiated with 30 laser shots in the sub-single shot ablation fluence regime on a Cr (100)[6]. Different types of periodic nanostructures can be observed in the same laser modified area, highlighted by different colors according to their orientations and periodicities. The electric field polarization is represented by the double red arrow.

1.2 Problem definition

Actually, several theories have emerged to interpret privilege order formation following laser surface irradiation[5–12]. However, phenomenon complexity lies on the fact that some aspects remain unclear despite the major advances made in this area, and are still under debate. In fact, from a basic point of view, the intricate role of inter and intra-pulse physical processes involved in periodic arrangement of matter underlines the challenging character of LIPSS. Following

laser energy absorption by the electronic system, the energy is delivered to the lattice system, involving a multitude of driven thermal, hydrodynamical and chemical effects. The final morphology of LIPSS, i.e. amplitude, periodicity, can be impacted by those events in most cases via spatial modulation of material removal (ablation), relying on the interplay between a variety of mechanisms beside 'feedback phenomena' as a result of repetitive surface irradiation. Thus a unified LIPSS theory is currently lacking along with various aspects disputed in the literature. Notably, the origin of HSFL is controversially discussed. Apart from the mechanisms of self-organization[13], oxidation[12] and twinning[14], a second harmonic generation[2,15] as well as evanescent fields at nanocorrugated dielectric surfaces[16] and the implication of different plasmonic effects[17–19] were also suggested.

Respecting the complications that can be implemented by the tremendous amount of physical processes involved in the feedback mechanism, revert to the first pulse impinging the surface triggering the onset of LIPSS formation is necessary. However, as a single pulse in the sub-ablation regime can alter surface topography and the region beneath it on the atomic scale, an attention to defects generation should be traced, whether these microstructural modifications on the surface or in-depth can assist self-organization of matter, or hinder material structuring. Furthermore, preceding the formation of periodic surface structures, it was established that laser energy is deposited and distributed in a modulated and inhomogeneous way in the material, initiating local thermal stresses and/or transient phase changes that can lead to microstructural modifications[20], strongly dependent on crystalline orientation. LIPSS are generated at the threshold of phase transition, then the competition with defects is relevant.

Since different oriented planes possess different atoms density, surface energies, potential bonding-sites[21,22], plane spacing and surface tension, thermal and mechanical response of metal surfaces after energy absorption may be affected. Thus one can suppose that crystal orientation may play a significant role in the course of laser-matter interaction[23–25]. As a consequence, following irradiation, material relaxation and henceforward LIPSS formation may also vary regarding crystal orientation.

Up to now, the competition between microstructural defects generation and a privileged order of matter formation has not been investigated previously on the atomic scale. However, it was revealed by a mesoscopic study that the onset of LIPSS formation and laser-induced lattice distortion is crystalline orientation dependent[20,26]. As a function of the crystal orientation, the crystal exhibiting a highest storage of lattice defects evince a weak tendency to form LIPSS[20,26]. Since their dimension is well below the diffraction limit along with intriguing physical processes debated in the literature concerning their formation, HSFL must be put on the forefront of ripples formation investigation. Irradiated surface alteration as well as microstructural modifications in-depth contribution on HSFL formation, taking into account crystalline orientation, has not been elucidated previously and constitutes the core of this thesis. In addition, to enrich our comprehension on the feedback mechanism leading to LIPSS formation, the behavior of dynamical surfaces are probed.

1.3 Outline

This thesis was performed in Hubert-Curien laboratory, Saint-Etienne, France, in the frame of SelfOrDef project, labeled by LABEX MANUTECH SISE (sciences et ingénierie de surface et des interfaces) of Lyon University, a group of academic labs and industries. The experimental work for laser irradiation was supported by the laser-matter interaction group in Hubert-Curien lab. This work enabled access to different characterization microscopies: Atomic force microscopy which allows topographical investigation of laser induced-roughness and LIPSS morphology was performed by Stéphanie Reynaud at the Hubert-Curien laboratory. Electron back-scattered diffraction characterization of LIPSS and defects was performed at Ecole nationale supérieure des mines de Saint-Etienne EMSE, by Claire Maurice. Thin lamellas extraction as well as in-depth characterization of defects was carried out at Mateis INSA Lyon by Thierry Douillard employing focused ion beam and the transmission electron microscopy. In order to probe the dynamic of LIPSS formation, a collaboration was established with the radiation-matter institute of CEA-Saclay, using the photoemission electron microscopy technique by Ludovic Douillard.
For theoretical analysis, a collaboration was made with the University of Virginia, where Leonid Zhigilei and his coworkers performed molecular dynamic simulations on laser-induced defects. Finally, electromagnetic calculations and hydrodynamic simulations were performed at the Hubert-Curien laboratory by Anton Rudenko.

The main objective of this thesis relies on the establishment of an interrelation between laser-induced periodic arrangement of matter and defects, taking into account irradiation parameters as well as sample features, more precisely, crystalline orientation and material type. Aiming for this objective required work splitting into three connected parts: The first part consists of elucidating the influence of crystalline orientation on the formation of high-spatial frequency nanostructures and defects, accounting for a surface and in-depth analysis. Since LIPSS are generated at the threshold of phase transition with relevant competition with defects, the second part infers the phase transition undergone in the nanostructures region, including epitaxial regrowth and nanocavitation. The third part entails dynamical investigation of low-spatial frequency nanostructures, since the intriguing role of feedback mechanism in defining the final morphology of these nanostructures is often evoked. Furthermore, the control of the transient roughness centers, contributes to the progress towards the general goal of untangling the intriguing multiscale phenomenon of nanostructures formation.

This thesis is organized as follows:
In chapter 2, we review an up-to-date state of the art linked to the fundamental processes between ultrashort laser and matter, the case of metals being specifically considered. Starting with chronological events occurring after laser energy absorption driving the system to ablation, the resulting output, ranging from defects generation to material structuring, is largely discussed. It exposes different scenarios leading to the formation of laser-induced periodic surface structures (LIPSS). LIPSS formation dependence on crystalline orientation and material properties beside defects generation is questionable and brought to the forefront of the following chapters.

Chapter 3 starts with describing techniques for sample preparation as well as laser experimental setups for single and double-pulse sequence generation. In order to investigate microstructural defects generated beneath the surface, electron backscatter diffraction EBSD along with transmission electron microscope TEM are employed and several corresponding characterization tools are applied. For LIPSS features analysis, atomic force microscope AFM and scanning electron microscope SEM are also used. Finally, local near-field distribution mapping using photoemission electron microscope PEEM is also reported for probing the dynamic of LIPSS formation.

Chapter 4 evokes the contribution of surface roughness on enhancing the local near-field. The induced surface topography generated by a single pulse irradiation of body-centered-cubic (bcc) monocrystalline Cr samples is investigated experimentally and computationally for laser fluences that produce high spatial frequency nanostructures HSFL in the multi-pulse irradiation regime. We show that the spallation-induced roughness is likely to play a prominent role in triggering the generation of high frequency LIPSS upon irradiation by multiple laser pulses, strongly dependent on crystalline orientation.

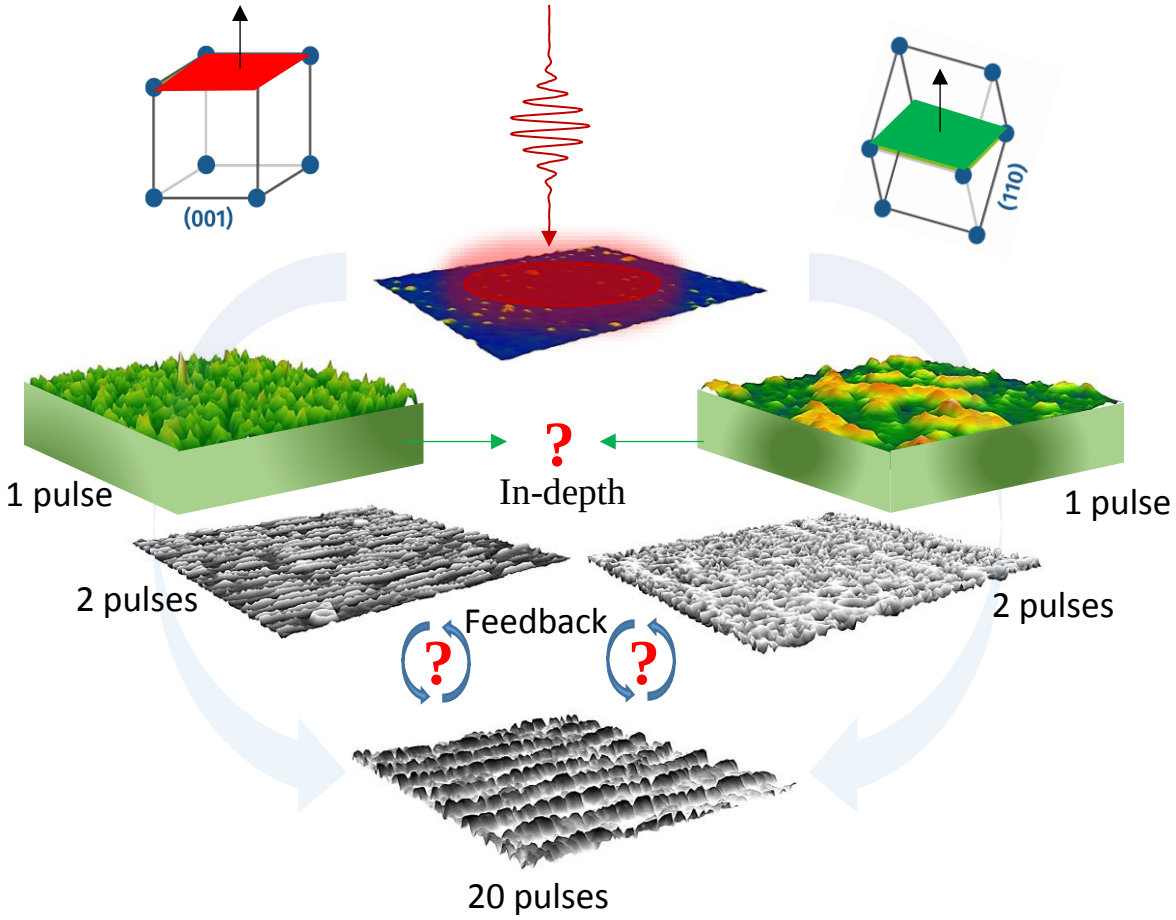

Fig. 1.2 A sketch that summarizes the outlook of this work starting from surface contribution to HSFL formation, passing by the role on microstructural modifications in-depth in promoting HSFL formation for a low dose irradiation. This process is strongly dependent on crystalline orientation and ends by the problem of feedback mechanism regarding LSFL formation for a high dose of laser irradiation where the crystalline orientation exhibits similar behavior.

Chapter 5 supplies our understanding regarding the singular response of different crystalline orientation to laser irradiation in the single irradiation regime. Experimental surface and in-depth characterization of single Cr crystals irradiated close to the onset of phase explosion regime reveals crystal defects introduced by the short pulse laser irradiation. (110) orientation provides a strong tendency to generate defects. Molecular Dynamic simulations performed under the same experimental conditions reproduce the generation of dislocations and vacancies on the (110) orientation. It is found that laser-induced defects can alter the surface topography and the region beneath-it, which can impact in turn the roughness centers features promoting HSFL formation.

Chapter 6 extends the triggering events concerning the formation of nanostructures far below the diffraction limit to face-cubic-centered (fcc) materials as Nickel. Since the role of periodic thermomechanical dynamics in this swift and strongly confined regime has not been elucidated, a high resolution microstructural analysis approach is employed to infer the phase transition undergone in the LIPSS region, including epitaxial regrowth and nanocavitation. HSFL formation is found to be the result of periodic nanovoids trapped beneath the surface as well as nanocavities emerged at the surface. The kinetics are probed and evaluated by an original strategy combining double-pulse irradiation and a hydrodynamic modeling approach.

Chapter 7 supplements our comprehension on the dynamics of LIPSS formation in the multi-pulse regime. Photoemission electron microscopy is employed to experimentally investigate the pulse-to-pulse evolution of the local near-field distribution on a set of periodic surface arrangements of matter that consist of different periodicities induced earlier by ultrashort laser pulses with different laser shots on Titanium. The experimental data are interpreted by comparison with electromagnetic simulations and calculations. We unveil the periodic character of electrons photoemitted from nanoholes in the LIPSS region, where a periodic behavior of the laser energy deposition is undoubtly verified, following the same modulation of LIPSS periodicity. By correlating LIPSS periodicity with that of photoelectrons, and by revealing nanoholes location and concentration owing to the local-field enhancement, we demonstrate that the scattering on the high nanoholes concentration reduce LIPSS periodicity.

Chapter 8 offers a new experimental setup for the generation of odd nanostructures with ultimate periodicities around 60 nm and dimensions of 20 nm by controlling the transient surface roughness. Owing to non-altered surface, scattering process is reduced conserving the isotropy features of the surface. With extreme irradiation conditions, some period agencement of ‘nanowells’ are reported on fcc (Nickel) material.

Finally, the main results and conclusions are summarized in chapter 9, paving the way towards future research suggestions.

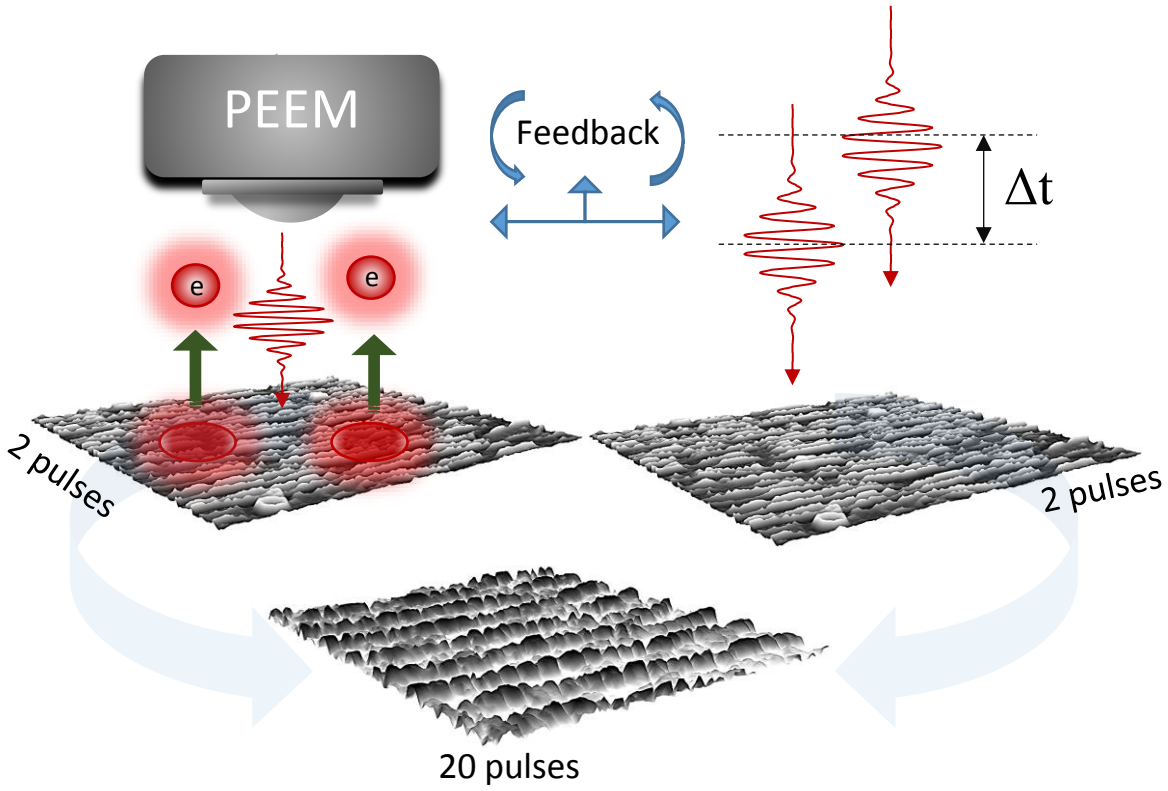

Fig. 1.3 Different experimental setups employed to probe the dynamic of LIPSS formation: Photoemission electron microscope PEEM as well as double-pulse sequence irradiation offer an innovative approach to investigate feedback mechanism following LSFL formation.

Chapter 2

Laser-matter interaction in the femtosecond regime -State of the art-

This chapter provides an up-to-date bibliographical overview on laser-matter interaction in the femtosecond regime, the case of metals being specially scrutinized. Starting with describing the sequential events following laser energy deposition triggering system ablation, the resulting yield, ranging from defects generation to anisotropic arrangement of matter, is widely discussed. First, we investigate laser-induced defects in crystalline targets, by pinpointing the role of shear stresses on emitting dislocations, where slip planes are activated. Then, regarding materials structuring, several scenarios leading to the formation of laser-induced periodic surface structures (LIPSS) are exposed. LIPSS formation dependence on crystalline orientation and material features is also introduced.

2.1 Femtosecond laser sources and applications

Femtosecond laser sources, developed over the last three decades, allows to explore the behavior of materials under extreme thermodynamic conditions on one hand, and to resolve temporally the dynamics of the local structure, electronic properties and phase transitions. They are also useful in studying interactions occurring in the field of femtochemistery, where the motion of atoms in a molecule is investigated during a chemical reaction. These fundamental processes are established on timescales similar to the natural oscillation periods of atoms and molecules, ranging from femtosecond to hundreds of picoseconds, i.e. vibrational modes of a molecule, electron transfer in a photosynthesis and period of phonon vibrations in a solid occur on the picosecond timescale. In fact, dynamic properties visualization of the irradiated target can be achieved owing to the temporal resolution of the incident laser pulses on the femtosecond timescale. By examining the atomic and electronic structure on this ultrashort scale, it is possible to decipher the primary response of matter, after laser irradiation. If we want to investigate, for example, structural changes that can occur in the crystal's lattice, these modifications must be in the same state. Otherwise, an average blur effect can occur. Another important feature of ultrashort laser sources lies on their ability in delivering extremely high powers. Recently, Gérard Mourou and Donna Strickland, 2018's Nobel Prize recipients, have developed a technique called chirped pulse amplification (CPA) which modifies an initial ultrashort pulse emitted by a conventional laser using an optical system. This pulse on the order of the nanosecond is stretched then amplified and recompressed. As a result, a femtosecond laser pulse is emitted from the output of the optical device which power can reach the pettawatt (10^{15}W). This technique can therefore amplify the initial power of a laser by a factor of 1000 to 100000 and accelerate particles up to energies of the order of GeV, over extremely short distances. As a consequence of high powers, nonlinear phenomena, i.e. multiphoton absorption, can occur. A 50 fs pulse duration and an energy of 1 mJ which provides a power of 20 GW will produce a considerable intensity on the 10^{15} Wcm^{-2} order, after being focused on a focal spot of about 100 μm^2. This intensity corresponds to an electric field of about 10^{11} Vm^{-1} which is greater than the electric field spotted by the electron in the hydrogen atom[27]. As a result of ultrashort timescales and high intensities provided by femtosecond laser pulses, where nonlinear and ultrafast phenomena can occur, the confinement of energy hence raises the probability for each charge carrier to interact with a photon.

2.2 Mechanism of laser interaction with metals

2.2.1 Absorption and relaxation of ultrafast laser energy

The optical response to the incident laser wavelength is obviously band structure dependent in the case of solid state materials. In a metal, unlike band-gap materials, high energetic electrons occupy partially fully filled bands, and the transition from an occupied to an empty state does not involve an excitation threshold. Nevertheless, incident laser energy absorption reaches only a few percent since a large part of the radiation is reflected. In fact, the electric field is

effectively screened on account of the high electronic conductivity. Considering the process of optical absorption by free electrons, the absorption mechanism is associated with a collision process referred to inverse Bremsstrahlung process. For materials possessing free electrons in their conduction bands, incident photons absorption is traditionally decomposed into intraband and interband contribution. Intraband absorption is a quantum mechanical process which involves a collision partner during the interaction and requires either a phonon or another electron, in the particular case of the so-called 'Umklapp' phenomena[28]. A global modification of the electronic wave vector is necessary for this type of transition. Interband absorption is often perceived as an absorption mechanism of one electron, since it does not necessary implies another partner (direct process). An electron changes band during this transition involving optical selection rules. However, there may be so-called 'indirect' transitions involving other particles such as phonons, modifying the wave vector during the transition.

A common model applied to describe energy evolution within the irradiated system takes into account electrons on one hand and crystal lattice on the other, as two thermodynamic systems at internal equilibrium. It is known as the *two-temperature model*, describing both systems relaxation after electronic temperature's sharp rise (Te) of conduction band electrons, compared to that of the crystal lattice (Ti)[29]. This model will be discussed in the following section.

Electrons occupying states below Fermi edge can absorb incident photons energy and thus move to higher energy states above Fermi edge. The process of ultrashort laser interaction with metals take place over three time intervals[30]. Firstly, immediately after laser excitation, the electron system is in a non-equilibrium state[31], favored by two competing processes: the first process is the ballistic motion of the excited electrons deeply in the material, with velocities close to Fermi velocity, i.e. about 10^6 m/s[32]. Recent study shows that a transient orbital-dependent thermalization can take place[33]. The second process is more general: it concerns the evolution of electron temperature following collisions between excited electrons and electrons which are around Fermi level[34]. Once the thermal equilibrium between hot electrons is reached, a second time interval begins, characterized by a Fermi distribution and temperature difference between electrons and lattice. This hot electron bath is initially located inside the optical absorption depth, and electrons are scattered deeply in the material with a speed considerably slower than that of the ballistic motion. This diffusion is governed by the electron-phonon coupling cooling the electron bath, and can be described by the TTM, discussed in the following section. Finally comes the third interval in which the electrons and crystal lattice reach thermal equilibrium by a heat exchange between the two systems, due to their different thermal capacities.

2.2.2 Electron and ion temperatures: Two-temperature TTM model

During the absorption of the laser energy by the conduction band electrons, their thermal energy is transferred to the lattice via electron-phonon scattering within the energy deposition zone yielding an increase in the temperature and reorganization of matter. In the frame of electron-phonon interaction, electrons do not directly interact with lattice ions. Hence the interaction is not collisional but Coulombian. The vibration of ions lattice implies deviation of equilibrium positions, and thus a modification of the interaction with electrons. The interaction continues until reaching thermal

equilibrium between two different systems: a hot electron system and a cold ion system (corresponding to the lattice). The thermal equilibrium takes place after a few picoseconds and is material dependent. The *two temperature model*, developed by Anisimov in 1974, is composed of a system of heat diffusion equations, coupled by an energy transfer term described by the temperature difference between the two systems, multiplied by the electron-phonon coupling force $\gamma_{e\text{-}ph}$ (or electron-ion in plasma phase):

$$\begin{cases} \dfrac{\partial \varepsilon_e}{\partial t} = \dfrac{C_e \partial T_e}{\partial t} = -\nabla(K_e \nabla T_e) - \gamma_{e\text{-}ph}(T_e - T_i) + S(\vec{r},t) \\ \dfrac{\partial \varepsilon_i}{\partial t} = \dfrac{C_i \partial T_i}{\partial t} = -\nabla(K_i \nabla T_i) + \gamma_{e\text{-}ph}(T_e - T_i) \end{cases} \quad (2.1)$$

The heat capacities per unit volume of the electrons and ion/lattice subsystems are C_e and C_i respectively. K_e and K_i are the electronic thermal conductivities and S(t) the laser heating source term, corresponding to the energy laser deposition on the surface. This system allows thus energy redistribution, owing to thermal diffusion due to thermal non-equilibrium increase. The coupling strength defines both the ion heating rate and the electron-ion thermalization timescale, acting on the speed of phase changes and the mechanical pulse causing ejection on the surface and ceasing more or less early electronic thermal diffusion. We note that in Nickel, for example, the energy transfer from electron to the lattice is faster than in Chromium, since the electron-phonon coupling constant in Nickel ($2x10^{17}$ $Wm^{-1}K^{-1}$) is greater than that for chromium ($1.3x10^{17}$ $Wm^{-1}K^{-1}$)[35–37].

In the femtosecond irradiation regime, electron and lattice coupling during the pulse is non-significant. After the laser pulse and energy delivery to the lattice and heat conduction, electrons are cooled. In the case of picosecond and nanosecond pulse duration regimes, the electron temperature during the pulse becomes quasi-stationary ($T_e \backsimeq T_i$). During the laser pulse, the lattice heating occurs and losses are compensate by laser absorption.

The TTM enables theoretical predictions on heating rates or melting thresholds for example, and has been broadly applied in experimental observations explanation on laser-irradiated metals[38–41]. If the model is easily implementable in a low excitation approach (below the melting threshold), the difficulties increase when it is inserted into molecular dynamics[42] or hydrodynamic codes[43]. Lattice material parameters may be modified during calculation time in the frame of phase transitions. Indeed, each parameter (capacitance, conductivity and coupling) depends on the electronic and ionic temperatures, free electron density and matter density of the materiel, requiring behavioral models out of equilibrium. A set of laws and models used in the hydrodynamic code Esther, used in chap 6, describing this phase of two temperatures, from the solid phase to plasma, can be found in reference[44]. Such hydrodynamic approaches require a material state equation for each of the considered materials. In classical molecular dynamic approaches, an electronic temperature-dependent potential EAM (Embedded Atom Model) adjusted from ab initio calculations is used to describe the interactions between atoms. The question of energy deposition S(r,t) can be treated in a more or less complex form, ranging from a simple Beer-Lambert energy deposition $I=I_0 e^{-\alpha t}$ where α is the absorption coefficient, to a non-trivial modeling based on an approximation of the Maxwell equations in a non-homogenous medium, employed in chap 6 and 7.

2.2.3 Mechanisms driving laser ablation

Ultrashort laser ablation[45] , the mechanism consisting of material removal from solid surfaces or bulk irradiated with an ultrafast laser pulse, is of high fundamental and practical importance attracting experimental as well as theoretical research[27,46–48]. Laser-induced ablation investigation is a complicated task accounting for a wide variety of timescales demanding different multiscale approaches. In the frame of our work, in order to describe ultrafast laser ablation, we focus on excitation with visible light ($\lambda \approx$ 800 nm) at a fluence close to the ablation threshold. For a better approximation, we account for one-dimensional descriptions when spatial scales are involved. In this case, the waist of the Gaussian laser beam is much larger than the depth of the absorbed energy, which is usual for melting and ablation experiments involving ultrashort laser pulses. Material response to initial excitation is affected by material type and characteristics along with laser parameters. Concerning different materials, we can differentiate in general between absorbing materials with free conduction band electrons, i.e. metals, and band-gap transparent materials, i.e. dielectrics and semiconductors. We restrict ourselves in describing short pulse laser ablation of metals. Material response to the laser excitation is complex, and can include different mechanisms strongly depending on the laser fluence: transient modification of material properties induced by a strong electronic excitation, photomechanical effects provoked by the relaxation of laser-induced stresses, rapid transient phase transitions taking place under fast laser energy absorption and material expansion conditions, electrons ejection and plasma formation, along with complex phenomena occurring in the ejected ablation plume. Fig 2.1 shows an overview of the typical mechanisms ranging from energy absorption to ablation, accounting on the appropriate timescales and fluence. Regarding the low calorific capacity of electrons, electronic temperature rises sharply. The excited electrons then deliver their energy deeper into the irradiated target, thermalize with ion lattice via electron-phonon coupling on the picosecond time scale, described in the TTM section. This extremely fast rise in ionic temperature, taking place in a constant volume, which can be considered as an isochoric process, leads to a sharp rise in pressure that reach several gigapascals. This difference between local pressure and surrounding pressure is manifested by the radial emission of a compressive wave. This mechanic wave is divided into two parts: a part which propagates deeper into the core of the target, and a part towards the surface, which provokes its reflection and transforming it into a tensile wave with opposite propagation direction.

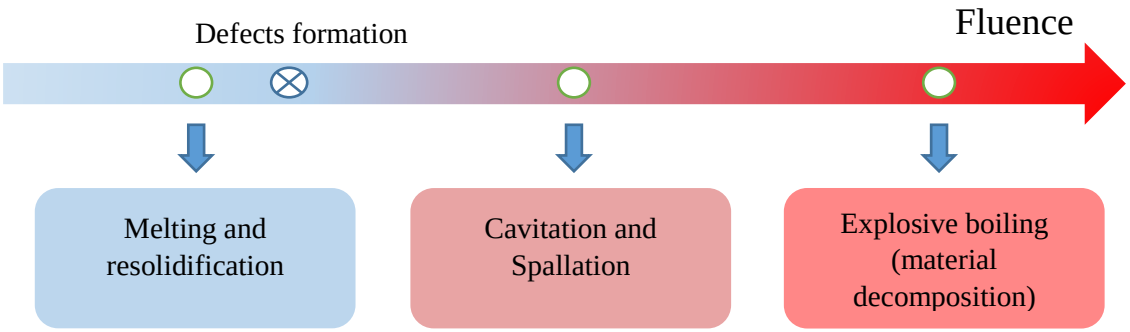

Fig. 2.1 Mechanisms driving laser ablation as a function of the fluence. For sub-spallation fluences, the system experiences melting and resolidicitaion. In the case of sub-phase explosion regime, cavitation of the melting region leads to ejection of a liquid layer from the surface of the target. Increasing the fluence above the phase explosion will eject multiple liquid layers and lead to ablation of the material. Defects are generated in the melting and resolidification regime.

In the case of incident laser fluence between surface melting and cavitation/spallation threshold, confinement of the initial ions system fast heating takes place within the first tens of nanometers from the surface, i.e. 20 nm and 50 nm for Ni targets[49] and Cr targets[50] respectively, for an absorbed laser fluence higher than the melting threshold for each material.

Turning to temperature evolution analysis, melting process can be homogenous (classical melting) or heterogeneous (known as two-stage melting process), strongly dependent on fluence, while remaining below the spallation threshold. For heterogeneous melting process, it can be divided into two parts: a component of a fast melting process characterized by homogenous nucleation and development of several liquid layers within the crystal overheated area. The second component of the melting process, which follows the first component, is much slower, corresponding to the propagation of a well-defined melting front deeper into the target. The scene of the two-phase melting process has been reported in various publications for different types of materials irradiated with femtosecond laser pulses in the melting regime. MD simulations revealed the two-stage melting process for the following targets Ni, Au, Cr and Al[49–53].

The transition between homogeneous (low fluence) to heterogeneous (high fluence) melting process can be described as follows: in the low fluence regime, the fast homogeneous melting forms liquid/crystal interface within the top tens of nanometers layers of the target, corresponding to the heated region during initial electron-phonon equilibrium. Resolidification thus takes place after interface cooling between the melted region and the crystal by heat conduction to the bulk. In the case of higher fluences, the liquid-crystal interface formed by fast homogenous melting is located deeper than in the case of low fluence. Heat conduction thus surpasses the interface, rising its temperature, and moves the melting front deeper in the bulk. Resolidification takes place as soon as the temperature of the melting region reaches a sub-melting threshold value. In this case, a modification of the propagation direction of the melting front occurs, and the liquid region starts to shrink.

Further increase in the laser fluence above the melting threshold, while remaining below phase explosion threshold, results in voids coalescence, a process known as cavitation, and material separation consisting of a melted layer from the bulk of the material, known as spallation. In fact, the buildup of unloading tensile wave from the reflection of the compressive wave by the surface of the irradiated target coincides with voids appearance due to tensile wave propagation in the melted region. Relaxation of tensile stresses lead to nucleation, growth and coalescence of multiple voids in the liquid zone. Thus the mechanical stability of the region subjected to cavitation becomes weak, which provokes ejection of a liquid layer from the bulk of the target. The stability of the liquid layer can be disrupted due to the local fluence variation in the case of a Gaussian beam laser, and dynamics of the spallation process. As a consequence, the ejected melted layer can be decomposed into liquid droplets[43]. It should be noted here that photomechanical spallation is a general process that can be induced on various types of materials.

Fluence increase above the spallation threshold provokes ejection of multiple liquid layers or droplets from the surface of the target. The surface layer of the target is significantly overheated. Here we remain in the spallation regime and the surface temperature does not reach the temperature required for the onset of the explosive boiling.

For laser fluences that drive the irradiated surface region to temperature that exceeds the phase explosion threshold[54] , material ejection that was dominated by photomechanical spallation brought by the relaxation of laser-induced stresses is controlled by explosive boiling driven by a fast decomposition of the overheated material into liquid droplets and vapors mixed in an ablation plume. In this phase diagram, it corresponds to material expansion at higher temperature. In this work, the used fluences presented in this thesis are in the sub-phase explosion regime in order to generate LIPSS.

2.2.4 Transient state of the material

The power of ultrashort lasers generates and modifies the free electron population in the conduction band of the material. High speed material excitation prevents it from relaxing by thermal expansion and thus allows isochoric heating of free electrons remaining degenerate at high density. Indeed, the surface-heated layer has a typical thickness of the order of magnitude of the optical skin thickness, which is about 10 nm for most metals. The displacement of this surface layer during 100 fs is given from the speed of expansion, close to the sound's speed (~5000 ms^{-1}) in the solid. For an electronic temperature typically of the order of 5 eV, the displacement is approximately 1 nm, which means increasing the distance between each atomic layer by 10%, typically ~ 0.3Å. The isochoric heating appears to be a legitimate approximation. In the regime of solid-density electron heating, the kinetic energy of the electrons is of the same order of magnitude as the electronically potential energy, which corresponds neither to the conventional matter nor the plasma physics regime (weakly coupled). Recently, the term Warm Dense Matter (WDM)[55–57] has emerged to describe this boundary state between the two domains. The density of the matter goes from an order of magnitude below that of the solid ($\rho_0/10$) to a dozen times its value (10 ρ_0). The temperature varies between 0.1 and a few tens of eV. In this regime, matter is often degenerate, strongly coupled and non-ideal.

Fig 2.2 illustrates the features of the thermodynamic regime achieved in the applications of interest. It is obvious that we are in the WDM regime, at least during the solid-phase electron-phonon non-equilibrium phase, or plasma-electron phase.

Most specifically, with the fluences involved in our experiments (< 2 J/cm^2), we do not exceed a T_e temperature of 3 eV and a plasma temperature T_i of 0.5 eV. The majority of processes that interest us are controllable by modifying the pulses temporal duration up to a few tens of picoseconds. On this time scale, the surface relaxes and reaches densities close to the critical density ρ_{cr}. The zone corresponding to the formation of laser-induced periodic surface structures (LIPSS) is located at the solid-liquid transition and, in the current state of our knowledge, is not supposed to go beyond the liquid-gas binodal line.

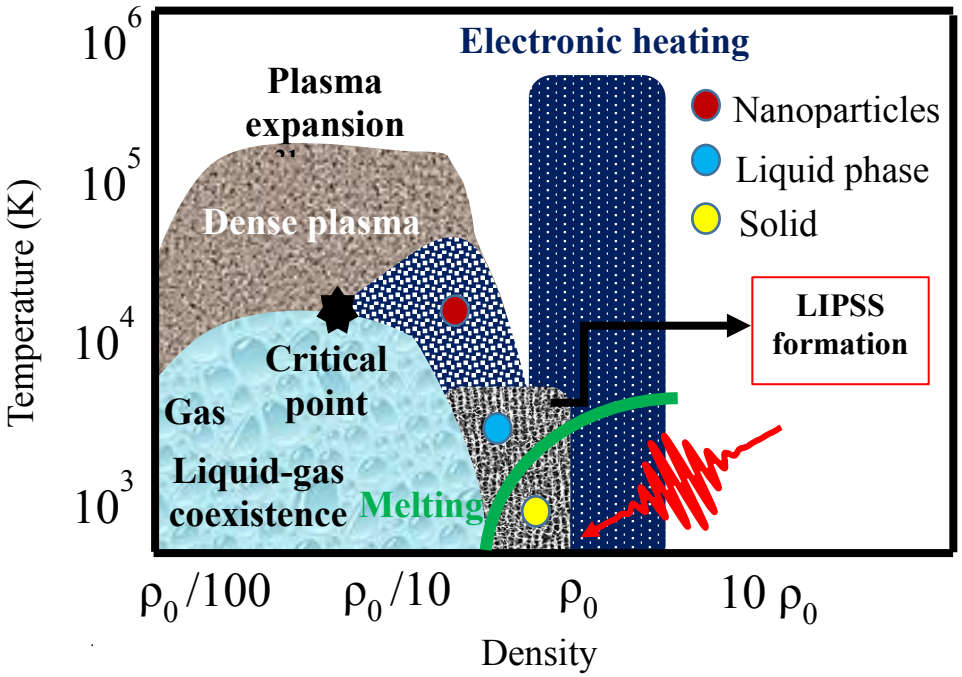

Fig.2.2 Thermodynamic diagram representing the transient phases reached by the material, as a result of an ultrashort laser irradiation. The zone of interest in this work is highlighted by the blue and yellow circles, where LIPSS formation occurs after solid-liquid transition.

2.3 Generation of crystal defects irradiated by short laser pulses

Laser-induced surface modification is in the center of many novel processes and fabrication methods, including for example laser surface annealing, hardening and alloying[58–61]. Surface properties enhancement is brought out by changing the structure and composition of a surface layer done by the generation of metastable phases, creation/annealing of crystal defects, grain refinement and redistribution of the elements mixture. We have seen in section 2.2 that the interaction between ultrashort laser pulses and a metal surface starts when free conduction band electrons transiently absorb energetic incident photons, leading to a sharp rise in the electronic temperature. Energy is then conducted deeper into the irradiated material by the excited electrons, bringing the electron-lattice system into thermalization through electron-phonon coupling on the picosecond timescale[29]. Thus a rapid melting and resolidification involving crystal defects generation are produced by lattice heating, occurring on the timescale ranging from hundreds of picoseconds to nanoseconds. For multiple laser pulses, accumulated damage exhibits through slip bands formation, surface roughening growth and corresponding surface reflectivity modification[62,63].

2.3.1 Brief history

In 1982, a study lead by C.D. Marss and al.[64] revealed slipping on metal surfaces (Mo, Al, and Cu) irradiated by femtosecond laser pulses at 492 nm. They showed that the slip threshold is related to the intensity of the mechanical

stresses and the absorption coefficient of the metals[64]. The thermodynamic model of Sparks and Loh[65] was applied in order to study single-pulse laser induced defects. One year later, Koumvakalis, Lee and al.[62] have explained that localized surface defects and impurities on diamond-turned copper and silver are responsible for the single-pulse damage threshold, whereas the accumulation of mechanical strain induced deformations is responsible for the damage threshold for multiple pulses. Following that year, in 1984, Cullis and al.[66] studied the influence of crystalline orientation on Si growth in the melting regime. They found that defects as twins and amorphous phases can occur on the (111) orientation. If the resolidification rate is driven beyond the maximum velocity growth, defects are formed on all orientations. In 1988, Jee and his coworkers[67] investigated single-pulse defects on monocrystalline metals, such as copper and aluminum. They revealed that the damage fluence depended strongly on the crystalline orientation. For Cu and Al, the threshold damage of the (111) orientation is lower than that of the (110) and (100) orientations. (111) oriented planes in fcc materials are more subject to form crystal defects[26,67], and are less resistant to plastic deformation. Furthermore, they showed that the damage threshold decreases by increasing the number of laser pulses impinging the surface of the metals. It was also found that in the 'submelting' regime, below melting fluence threshold, material damage can be caused by laser irradiation through thermal stresses[67]. Later that year, Yater et al.[68] have found that (111) orientation promotes the formation amorphous layers on Si. The amorphisation behavior of the (110) and (100) orientations is similar, in contrast to the (111) orientation which exhibits a different resolidification mechanism with inherent instability in the solid-liquid interface.

At higher laser fluences, above the melting regime, a rapid melting followed by epitaxial resolidification of a thin surface layer can take place. As a consequence, high density of crystal defects is generated, i.e. stacking faults, vacancies, interstitials, voids, dislocations and twin boundaries[14,69–71]. For further increase in fluence, surface morphology can undergo considerable structural modifications. We can cite the generation of nanocrystalline surface layer, surface nanospikes characterized by pentagonal twinned structural elements[72,73] as well as subsurface voids generation captured by a fast advancing solidification front[73]. In this regime, microstructural modifications can be prolonged down to a significant depth below the irradiated surface, where dislocations and deformation twins can be produced by laser-induced shear stresses, in regions far below laser melting front and ablation. Twinning was revealed on a work carried out on Ni materials[14], in which a relationship between melting/resolidification process and HSFL formation was established. Melting process was highlighted by nanometric lamellar structures generation (twins, epilayers) on the Ni surface irradiated region. In the multiple irradiation regime, the appearance and growth of HSFL parallel to electric field laser polarization is observed in the thick twin domains in the center of the impact, which support the connection between melting, high degree of supercooling and HSFL generation.

2.3.2 Types of defects

Imperfections and defects in crystalline materials are normally classified corresponding to their dimensions as follows: zero dimensional defects known as point imperfections, i.e. vacancies and self-interstitials, one dimensional defects known as line imperfections, i.e. edge and screw dislocations, two dimensional defects know as plane/surface

imperfections, i.e. stacking faults and twinning and three dimensional defects known as volume imperfections, i.e. inclusions and voids.

Regarding point defects, they consist of a missing atom or an atom present in an irregular place in the crystal structure. For self-interstitial for example, as shown by the red circle in fig 2.3a, it is an extra atom that has crowded its way into an interstitial void in the crystalline structure. These types of defects only take place in metals exhibiting low concentrations as they distort and significantly stress the tightly packed lattice structure. Vacancies are unoccupied positions.

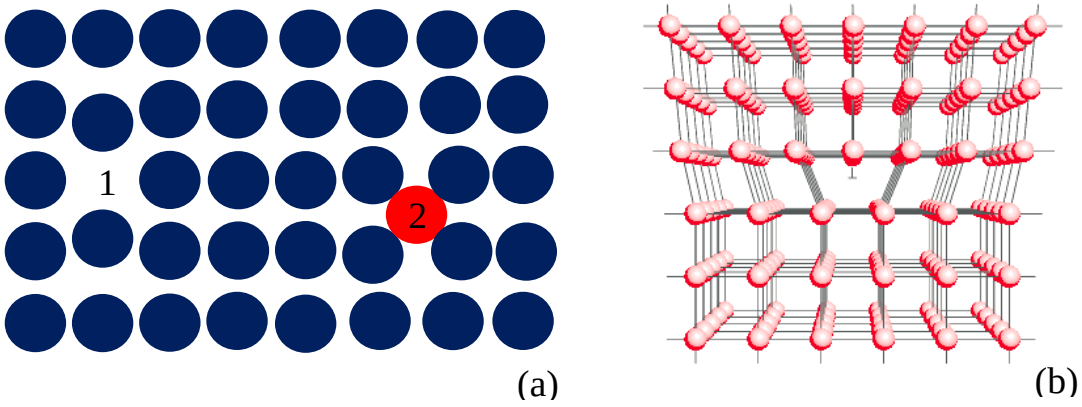

Fig 2.3 Schematic representation of (a) different point defects in a crystal, where number 1 designates a vacancy and number 2 represents a self-interstitial, circle marked by the red color and (b) dislocations[74] .

They are usual, especially at high temperature conditions where atoms randomly diffuse leaving behind empty lattice sites. A disturbance of the long-range stacking sequence can promote two other usual types of crystal defects, as stacking faults and twin domains. A stacking sequence modification over a few atomic spacings can generate stacking faults, while a modification over many atomic spacings forms a twin domain.

2.3.3 Dislocations and plastic deformation

A random deformation of a material can be always understood as the sum of a modification in volume and shape at constant shear. If we suppose that the crystal structure is constant, volume modification is recovered when the load is suppressed. In fact, the atoms can merely relax back to their equilibrium sizes. Conversely, shape modification, may or may not be restored, since relaxation of the atoms drive them into new displaced positions configurationally similar to their original sites. Plastic deformation is a continuous modification in shape as a result of a shear[75].

There are three common ways describing a crystal shape modification under a constant volume. First, single atoms can be displaced by diffusion process, known as diffusional creep[76,77]. As a result, the crystal can become more or less longer

according to the directional flow of atomic diffusion. Second, all the atoms in the crystal can move at the same time in order to accomplish the shear. For example, in mechanical twinning[78,79], one part of the crystal, which is homogenously sheared, stays atomically linked to the residue along a mutual twin plane. Third, and most frequently, atomic planes can slip over one another like cards in a deck, causing the growth of an overall localized shear within definite planes[80].

In the frame of a perfect crystal, displacing an atom initially at a position r by a distance of about *R(r)* from its site means that the crystal is subject to a strain *ε*. If the crystal is then strained, it is likely to be exposed to a stress *σ*. Hence, a crystal deformed under a tensile stress yields plastic deformation occurring by slip on well-defined set of parallel crystallographic planes, referred to slip planes, which modifies the geometry of the sample. Slip always occurs along a regular set of directions within these planes, known as slip directions, which must lie in the slip plane[81,82]. Thus a slip system consists of slip planes and slip directions combination. When the shear stress, proceeding along the slip direction on the slip plane, reaches a critical value, slip takes place. This critical shear stress is linked to the stress required to put dislocations in motion across the slip plane.

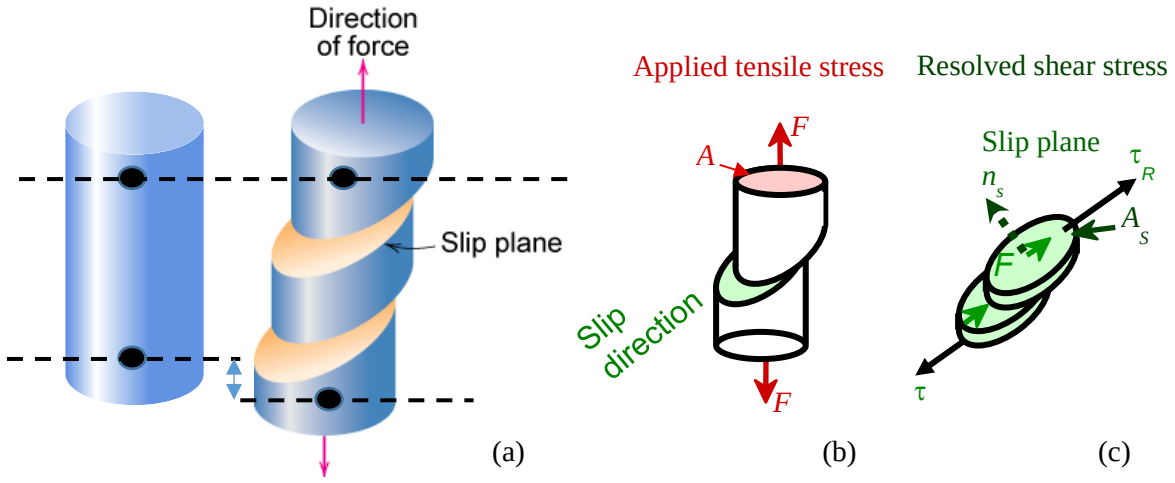

Fig 2.4 Applied shear stress induced plastic deformation (a) Unslipped single crystal fixed at top end and single crystal after plastic deformation by tensile stress in the direction of the pink arrow. Slip occurs on distant parallel planes (b) Slip plane and slip direction (c)

The necessary applied stress to launch plastic deformation of a material under a tensile load is called the tensile yield stress. Equation 2.2 states the relation between the tensile yield stress T_R and the shear stress σ acting along a slip direction.

$$T_R = \frac{\text{resolved force acting on slip plane}}{\text{slip plane's area}}$$

$$T_R = \frac{\mathrm{F}}{\mathrm{A}} \cos\lambda \cos\varphi \; = \; \sigma \cos\lambda \cos\varphi \tag{2.2}$$

Where F corresponds to the resolved force acting on slip plane, A the slip plane's area, λ the angle between F and the slip direction, and φ the angle between F and the vector normal to the slip plane. For a material with a fixed dislocation density and purity, the value of T_R at which slip occurs is found to be constant, known as the critical resolved shear stress T_C. This is Schmid's Law[83–85].

$$T_C = \sigma_Y \cos\lambda \cos\varphi \quad (2.3)$$

The $\cos\lambda \cos\varphi$ product is known as Schmid factor *M*.

In a given crystal, many available slip systems can be active[86]. As the tensile load's magnitude increases, the resolved shear stress increases on each system until eventually T_C is reached on one system. Thus the crystal begins to plastically deform by slip on this system, referred to *primary slip system*. The stress required to cause slip on the primary slip system is the yield stress of the single crystal. As the load is increased further, T_C may be reached on other slip systems, which begin then to operate. From Schmid's Law, it is apparent that the primary slip system will be the system with the greatest Schmid factor.

Slip is a plastic deformation mode. A second deformation mode, known as twinning[14,78–80], is observed for certain metals, especially hcp[80] and fcc[14] crystal structures. During slip process, a considerable displacement is observed on planes quite apart from each other. During twinning, a partial displacement successively occurs on a high number of contiguous planes. In addition, in the context of our work, a detailed analysis of the structural modification on a bcc target irradiated by femtosecond laser pulse was performed in collaboration with Zhigilei group[71] based on large-scale-atomic level simulations. It was found that laser energy deposition which produces a combined effect between fast temperature variation and significant thermoelastic stresses yielded both transient structural modification, i.e. high density of stacking faults along the {110} oriented planes and the generation of permanent crystal impurities in the sub-surface region of the irradiated crystal, i.e. high density of vacancies, interstitials and dislocations[71].

2.4 LIPSS formation approaches

2.4.1 Brief History

Considering LIPSS discovery by Birnbaum in 1965[87], their examination has developed into a scientific evergreen[88]. After irradiation by a focused ruby laser beam, Birnbaum announced LIPSS formation on monocrystalline polished germanium surfaces. He addressed their generation to a diffraction effect and considered that the surface regularity of straight lines is triggered by material removal at the maxima of the electric field intensity[87]. In 1973, a few years later following Birnbaum's discovery, Emmony and al. stated that the interference between incident laser beam with scattered wave at surface defects centers and scratches is behind LIPSS formation[89]. For systems generating trains of laser pulses, it becomes apparent very quickly that laser fluence and scanning velocity/number of pulses impacting the surface play a key role by controlling LIPSS occurrence experimentally, apart from laser wavelength and electric field polarization direction. In the early 1980s, experimental results obtained by Keilmann and Bai led to a new explanation regarding ripple formation process. They established the central role of propagating electromagnetic surface waves, polaritons, interfering with the incident laser beam[90]. Nearly in the meantime, two research groups around Sipe

and Siegman reported separately extended theories, discussed in the following section, concerning LIPSS formation[91,92], where this terminology has been launched to the literature in 1982 by Sipe and his group[93].

2.4.2 Analytical and dynamical approaches

Based on a sequence of three pioneering publications[91,94,95], Sipe and his co-workers investigated the interaction of an incident electromagnetic wave with a microscopically rough surface theoretically and experimentally, by launching the so-called *efficacy factor* η. This model proposes to separate the solid into two parts: a thin layer consisting of surface irregularities and a bulky material. It suggests that the size of the thin layer is small with respect to the laser wavelength. This hypothesis is consistent with polished materials and a laser wavelength of about 800 nm. Sipe theory assumes transverse variation of an initial random surface, which can be decomposed analytically into a sum of individual spatial frequencies. It is possible to calculate the amount of light diffracted by each of these frequencies below the surface. Thus the total intensity on the material results from the superposition of the primary laser radiation and the scattered waves by surface roughness centers. This model consists of spatial frequency determination of the initial surface variation which will undergo a more or less high growth rate. The efficacy factor is thus calculated for each of the frequencies and is generally represented in reciprocal space (k_x,k_y). The latter serves as a scalar function proportional to the inhomogeneous energy deposition into the irradiated target[91], and describes the efficacy of the surface roughness in triggering inhomogeneous absorption of radiation. The classical model strengths lies in its remarkable ability to predict possible ripples wave vectors $\boldsymbol{k}$ of the surface, with $\boldsymbol{k}$ equals $2\pi/\Lambda$ and Λ equals λ/n where n is the index of the material and Λ LIPSS periodicity. The orientation and angle of incidence θ dependence is also correctly described. The efficacy factor theory is actually the most universally accepted theory of LIPSS which clearly involves *surface-scattered electromagnetic waves* (SEW), and does not include any feedback mechanism. Nevertheless, if LSFL are rather well described, HSFL and grooves are not rendered properly[96–98]. Hence transient modification of the material and optical properties must be taken into account. Bonse and his co-workers proposed a dynamical approach by combining the classical Sipe model and the Drude model importing the optical properties of solid excitation by laser radiation. On one hand the Sipe-Drude model[15] states that a strong absorption due to the interference between the incident and scattered electromagnetic waves on the surface triggers LSFL formation, and on the other, it provides an explanation of the periods lower than the laser wavelength by a transient change in the optical properties of the material[4,99–104]. Thus this model takes into account the extremely intense nature of the interaction with ultrashort laser pulse, where Sipe model is applied to a material whose dielectric constant has been modified in order to involve the effect of the excited electronic gas[105]. This approach suggests that intense femtosecond pulses can induce a change in the refractive index due to the transient generation of quasi free electrons in the solid conduction band. Nevertheless this model has some limitations because some results are hard to explain. This is the case of the capillary wave, structures parallel to the laser polarization with periods ranging from 1.1 to 2 µm, observed during a higher fluence irradiation. These structures certainly result from the interaction between two surface waves propagating with certain angle. However, the question remains open as to

the phenomena leading to the creation of these two waves. Furthermore, the near-field is not well reproduced as the selvedge is not well described.

2.4.3 Self-organization approach

The classical approach considers that a modulated energy deposition due to some optical interference, is imprinted into an induced ablation pattern leading to a modulated surface morphology, where the ripples formation process is lithography-like. This model supposes a passive contribution of the irradiated material. Another approach, known as *self-organization model*, developed by Reif and his co-workers, considers the dynamics of the interaction between ultrashort laser pulses and the irradiated material, inspired from an adopted surface erosion model, in particular energetic ions induced surface sputtering. In this case, the irradiated target plays an active role: the physical mechanisms of ultrashort laser ablation implies the generation of a significant instability in the laser-affected spot. It should be noted that femtosecond laser ablation is a pulsed process, in contrast to surface bombardment with an energetic ion beam, where surface instability is reached continuously after direct ions kinetic energy transfer to the lattice. Thus laser energy deposition and desorption/rearrangement of massive components are temporally separated. After being focused onto the target, energetic photons promptly excites electrons in case of multiphoton excitation, where their emission is considerable observed during the pulse, which yields to crystal binding perturbation and softening[106] through redistribution of the absorbed energy. As a result, crystal lattice is destabilized and perturbed on a time scale of about 100 fs[107]. Furthermore, individual elements, e.g. ions, atoms and clusters, are emitted (coulomb explosion) driving the surface equilibrium order into distortion. The system is then sorely unstable and far away from thermodynamic equilibrium. The relaxation of the nonequilibrated system pushed by an abrupt gradient in lattice order takes place on a short timescale via macroscopic material ejection and surface reorganization. A competition between surface erosion and atomic diffusion result in a surface instability associated with reorganization of the irradiated target, thus triggering surface pattern formation. In this approach, the laser electric field polarization, which is considered as a control parameter, breaks the distribution symmetry of the initial electron kinetic energy and modifies the excitation flow probability, aligning ripples according to the principal direction of the energy transfer. In other terms, laser polarization controls ripples orientation by an anisotropic energy deposition. In addition, contrary to the classical theory where LIPSS periodicity are influenced by the angle of incidence and laser wavelength, *Self-organization model* considers that ripple periodicity depends only on the laser fluence coupled into the material and the corresponding surface self-diffusion factor.

2.4.4 Electromagnetic approach

While the *self-organization model* suggests that an unstable surface region, reached by crystal binding perturbation and softening, induces a high degree surface instability which relaxes via self-organization and triggers the spontaneous formation of self-organized surface pattern in the laser-affected region with a periodicity defined by the instability Eigen modes, the electromagnetic model states that LIPSS are fingerprints of light localization. Finite

Difference Time Domain (FDTD) approaches[5,10,108,109] have been deployed over the past few years to evaluate the spatial distribution of the electromagnetic field at the surface of the irradiated target, and thus highlight the effects of polarization and surface roughness on LIPSS formation. Early studies[10,108] proved to be very promising to overcome Sipe's calculations for LIPSS generation, extending the zoology of possibly formed structures of electromagnetic origin. In fact, the efficacy-factor theory has various drawbacks: the transient modification of the material's properties during laser pulse irradiation, the interpulse feedback mechanisms and the dependence on the pulse duration itself, remain unsolved and are not considered in the theory. While this issue was partially solved by Dufft[15], Bonse and their co-workers[4] by introducing the Sipe-Drude model, the FDTD is employed for further investigation. In the FDTD method, in order to account for interpulse feedback processes, each incident laser pulse is considered to modify the surface roughness by ablation (referred to holographic ablation model, developed by Skolski and his group), according to the profile of the absorbed energy. The results quoted as FDTD-feedback simulations, state that LIPSS formation can be well understood in the frame of electromagnetic theory, where LSFL, HSFL (in particularly HSFL orthogonal to laser polarization which is a striking result) and grooves develop in the simulation domain. Another study aims to complement skolski's approach by integrating a change in the optical and topological properties of the material. Optical indexes modified by the change of the electronic structure via Ab-initio in a 3D-FDTD calculations were inserted[110] . In the case where a variation of the optical index is neglected, it was shown that HSFL parallel to laser polarization are almost as marked as the LSFL. Conversely, in the calculations made from the indices strongly modified, LSFL are exalted by surface plasmon excitation and HSFL are not very visible. It was demonstrated that the formation of LIPSS is intrinsically related to the coherence of the laser by randomizing spatial phase in generating finite domains of ripples[5,111]. It was revealed that LSFL are generated via the interference between the incident wave and the far-field scattered wave, whereas HSFL are triggered via the interference between the incident wave and the near-field scattered wave[5,111]. Thus an electromagnetic modeling appears to be sufficient to predict accurately the periods created. Many investigations are possible regarding the effects of energy deposition dynamics. A transient change in the electronic temperature and the optical index can be taken into account during calculation, via an electronic temperature in the first surface cells. A gradient of thermal and optical properties would be taken also into account. From a surface modulation following that of the energy deposit, the feedback effects could be much more widely studied.

2.4.5 Surface plasmons as initiators of inhomogeneous laser energy deposition

A surface plasmon is an electromagnetic wave resulting from a collective oscillation of free electrons located at the interface between two different mediums, such as the interface between a metal and a dielectric (air for example). This results in a drop in the reflectivity of the metal due to an incident beam energy transfer to the free electrons near the metal/dielectric interface when the coupling conditions are satisfied. These modes have the property of concentrating the electromagnetic energy in regions far below the diffraction limit. This open possibilities in nanophotonics[112,113]. The resonance of plasmons depends on various parameters such as the nature of materials: noble metals (gold, silver, nickel) are often used in practice for their interesting optical behavior (low plasma frequency) and the possibility of plasmonic excitation in the visible wavelength range. Plasmon excitation leads to a strong absorption and local electromagnetic

field exaltation. Plasmonic modes began to attract interest from the beginning of the 20th century (Zenneck 1907, Mie 1908, Sommerfeld 1909). Then in 1968 Otto[114] shows that the total attenuated reflection can provoke excitation of these surface waves. Kretschmann and Raether[115] obtained the same result from a different configuration of the attenuated total reflection method. These studies made it possible to progress in the area of surface plasmon, particularly in the context of the characterization of thin films and the study of processes occurring on metal interfaces. Recent advances in the various fields of application such as structuring, manipulation and observation at the nanoscale help to revitalize this area.

For materials exhibiting strong absorption, i.e. semiconductors and metals, LSFL are usually formed with an orientation perpendicular to laser polarization, with periods close to the laser wavelength, deviating slightly of about 10% ($\Lambda_{LSFL} \backsimeq \lambda$). It is widely accepted that these types of structures are triggered by interaction between incident laser pulses and an electromagnetic scattered wave by the roughness centers, which may involve the excitation of surface plasmon polaritons (SPP)[91,116–120]. This excitation channel is of high interest since non-active materials (dielectrics and semiconductors) with initial plasmonic behavior can be transformed transiently into metallic state, which satisfies SPP excitation conditions [Re(ε) < -1], once the density of the conduction band electrons exceeds a critical value[116,118,121,122]. For clarity, the LSFL periodicity is often directly related to the SPP wavelength ($\Lambda_{LSFL} \backsimeq \Lambda_{SPP}$) in the LIPSS literature[120]. In the well accepted SPP model of a plane metal-dielectric (air) interface under normal incident laser irradiation, the SPP period Λ_{SPP} is connected to the bulk dielectric permittivity ε via $\Lambda_{LSFL} = \Lambda_{SPP} = \lambda$ x Re $\{[(\varepsilon+1)/\varepsilon]^{1/2}\}$[120,123,124]. For low number of laser pulses, the LSFL and SPP periods can be concurrent as the surface corrugations are still quite small (depth $d << \lambda$). Nevertheless, it should be highlighted that the simple expression of Λ_{SPP} is not satisfied once an adequate deep surface relief is generated[113]. In addition, the positive feedback multipulse regime notably affects the LSFL formation. Therefore the validity of the SPP model has to be taken carefully into consideration.

2.4.6 Capillary scenario and triggering of surface instability

In order to complete our comprehension regarding periodic surface structures phenomena on laser irradiated surface of metals, taking into account that a purely electromagnetic vision of the energy deposit is not enough to explain the observed growth, a subsequent step involving a movement of matter in liquid form is part of studies in progress.

A theoretical analysis of coupled phenomena was undertaken, first by evaluating the characteristic times of the different effects, and more precisely by a linear stability analysis of the free surface, and finally by a one-dimensional model integrating plasmonic, thermal and hydrodynamic effects[125,126]. It was shown that the characteristic times of certain effects that can destabilize the transient fluid layer are less than the resolidification time. The plasmonic effects lead to a spatial structuring of the temperature field at the very first moments after laser pulse, as well as a pressure global pulse that can give rise to a strong transverse acceleration of the interface[43].

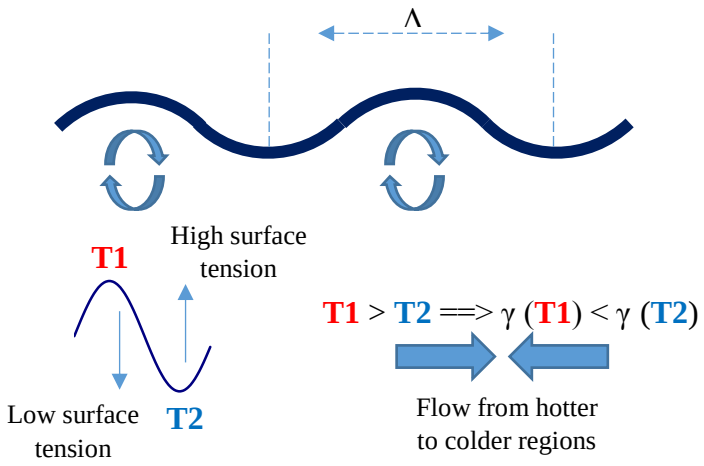

Fig. 2.5 Illustration of fluid flow by Marangoni effect from hot zones to cold zones, initiated by a modulated laser energy deposition[125].

The hydrodynamic effects are mainly related to the dynamics of the free surface of a thin liquid layer treated in the slow slop approximation (lubrication). The dependence of the surface tension with the temperature is supposed to lead to material flows of Marangoni type with a characteristic time T_m which can be written as follows:

$$T_m \cong \frac{1}{4}\left|\frac{\partial\sigma}{\partial T}\right|^{-1}\frac{\eta\Lambda^2}{h_m\Delta T} \tag{2.4}$$

where h_m is the liquid Nickel thickness, σ its surface tension, η the dynamic viscosity, Λ the period of the dynamic viscosity and ΔT the superheating within this modulation. It was estimated that T_m equals 18 ns[127,128] and that the accumulation of 20 pulses was necessary to modify the topography of a metal accordingly, given the short life of the liquid layer, estimated at less than 1 ns[125].

2.5 Feedback regarding LIPSS formation

In spite of the fact that a single pulse can optically interfere with a scattered wave triggering LIPSS formation[116,129], noticeable and well-aligned LIPSS are usually generated in the multipulse regime. The first pulse impinging the surface yields roughening of the surface for the following laser pulses, where the new distribution of the roughness centers gains particular spatial frequencies for better radiation absorption. During exposure to multiple laser pulses, via positive feedback, LIPSS pattern is formed by certain suitable spatial periods. Fig 2.6 assembles feedback processes regarding LIPSS generation, which can take place during a single pulse duration time (intrapulse effects), or which may take place during consecutive pulses (interpulse effects).

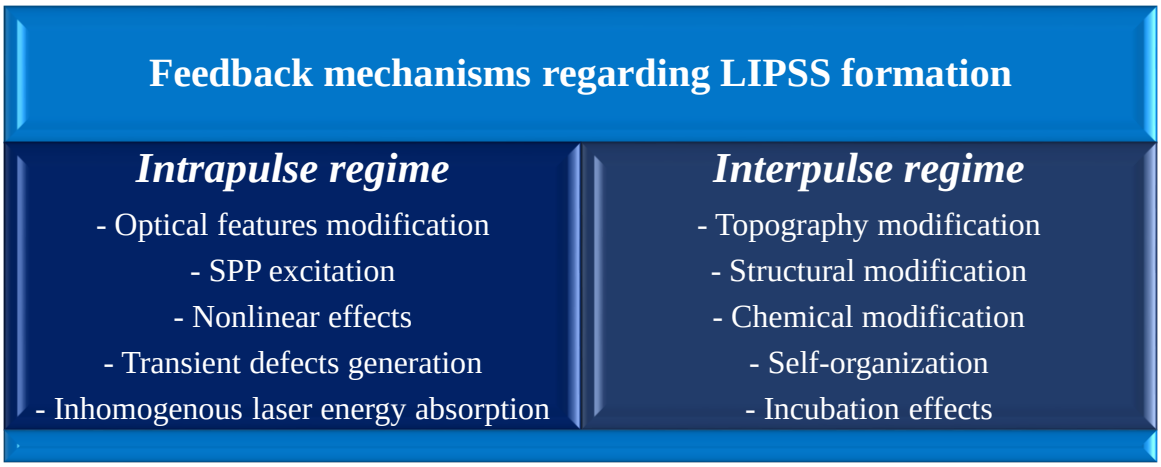

Fig. 2.6 A summary that assembles feedback mechanisms that can occur in the course of LIPSS formation, which can take place during a single pulse duration time (intrapulse effects), or which may take place during consecutive pulses (interpulse effects).

Intrapulse regime can involve transient modification of the optical properties of the irradiated material[92,130,131], surface scattered electromagnetic waves SEW excitation[91,132,133], stimulation of transient defects states i.e. stacking faults and self-trapped excitons in dielectrics[134], non-linear effects i.e. second harmonic generation[2,15], and spatially inhomogeneous absorption[135]. LIPSS control is influenced by the directional scattering and field enhancement features[136] following SEW stimulation during the laser pulse irradiation. In 1982, Fauchet and Siegman observed that LIPSS can be 'coherently connected' when the laser spots overlap spatially[137], upon line scanning across a germanium wafer surface by focusing ps laser pulses. Lately, Ruiz de la Cruz and his colleagues revealed that the regularity of LSFL on Cr films can be remarkably mended if the laser beam scanning direction is perpendicular to its polarization[138].

Interpulse regime impacts morphologies of the irradiated surfaces via ablation[108] or hydrodynamical melt flows[95,139,140], structure distortion of the material at the surface between amorphous and crystalline states[96,141,142], altering thus optical constants. In addition, incubation effects promoting stable defects states[143], decreasing the damage thresholds as investigated by Yee and his colleagues[67], chemical reaction with the ambient environment, i.e. oxidation[9,144,145] and self-organization involving a competition between surface erosion and atoms scattering are also practicable[7]. Huang and his coworkers proposed an interpulse feedback process suitable to LSFL control, by analyzing the resonant coupling of the laser-induced pattern period to SPP[118]. It was shown that an increase in the scanning velocity/incident number of laser pulses lead to LSFL period decrease. In fact, the deepener of LSFL relief following irradiation by few laser pulses leads to a shift of the SPP's resonant wavelength, reducing thus LSFL periods.

2.5.1 LIPSS morphology dependent on irradiation parameters

As discussed in the previous sections, the fastest and direct method for experimentally LIPSS processing and control is feasible by multiple single-pulse irradiation sequences. LIPSS growth can be manipulated via laser wavelength

λ, the angle of incidence θ, the electric field polarization state and peak fluence φ_0, the scanning velocity or the number of laser shots N impinging the surface, and the ambient medium's refractive index n_0.

Local fluence of the laser Gaussian beam has a significant influence on LIPSS, as shown in fig. 2.7.

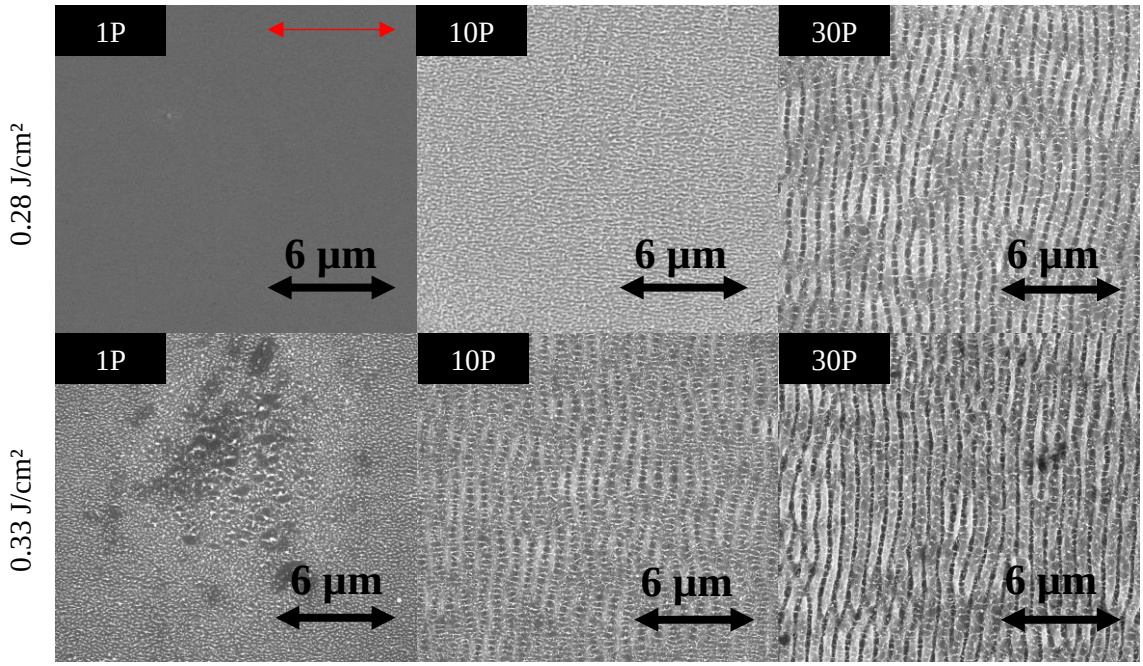

Fig 2.7 SEM images of different sites irradiated by different number of laser pulses and different fluences in order to show the evolution of LIPSS topology on Cr (100) orientation. The red arrow bar shows the incident electric field polarization. 0.28 J/cm² corresponds to a fluence below the single-shot ablation threshold, while 0.33 J/cm² represents a fluence above the single-pulse ablation threshold, which is 0.3 J/cm².

It is widely accepted that LSFL period is linearly proportional to the laser wavelength $\Lambda_{LSFL} = C.\lambda$, despite the fact that the slope C is related to the given material properties and laser irradiation conditions, as indicated in ref.[11,146]. LIPSS periodicity dependence on the angle of incidence has already been reported in ref. [91,92,132,133,147,148]. Taking into account the state of incident laser polarization (s or p) and the angle of incidence, LIPSS periods was found to follow the relation $\Lambda_{LSFL,p} \backsimeq \lambda/[\xi \pm \sin\theta]$, and $\Lambda_{LSFL,s} \backsimeq \lambda/[\xi^2 - \sin^2\theta]^{1/2}$,where ξ equals $|Re(\varepsilon)|/[|Re(\varepsilon)|-1]$[133]. In the frame of strong absorbing and materials exhibiting plasmonic behavior, these equations are reduced to $\Lambda_{LSFL,p} \backsimeq \lambda/[1 \pm \sin\theta]$ and $\Lambda_{LSFL,s} \backsimeq \lambda/\cos\theta$, as investigated theoretically by Sipe and his coworkers in the efficacy factor model[91].

Considering laser fluence, different types of LIPSS can be generated on the same solid. In ref. [97,122,149,150] several authors has studied the influence of local fluence on LIPSS periodicity. It was revealed for most materials that LIPSS period increases moderately with fluence. In addition, the number of laser shots N is another parameter which has a tremendous impacts on LIPSS periodicity. Increasing N leads to a decrease in Λ_{LSFL} by several 10% on metals and semiconductors[97,118,151]. This effect can be explained by the high positive feedback of interpulse and intrapulse number, as discussed in the previous section. It should also be noted that the various articles dealing with the subject mention

that the formation of LIPSS is reached only after several sets of incident pulses[106]. Nevertheless, colleagues at the Hubert-Curien laboratory demonstrated the observation of LIPSS with a single laser pulse[101].

Beside laser parameters and material properties, the ambient medium can affect the LIPSS period. For example, it was shown that Λ_{LSFL} decreases by a factor ranging from 0.1 to 0.4 for irradiation in liquid, with an invariable LIPSS orientation[152–154].

2.5.2 Irradiation by a train of double pulses

In the frame of continuous wave and pulsed lasers with pulse duration ranging to nanoseconds, there's a temporal overlap between laser energy absorption and material removal. Femtosecond and picosecond laser processing define in timescales a debatable question whether mechanisms yielding LIPSS formation starts in the early stage (assumption I) of laser energy deposition to the solid or at an ulterior time where self-organized reorganization of material begins (assumption II). In order to answer this question, two harmonious approaches had been addressed: the first approach sheds light on temporally beam shaping in order to tailor the deposition of optical energy (i.e. double-pulse experiments in the femtosecond regime, where the 2 pulses of a sequence having equal energies), while the second approach carries time-resolved experiments (pump-probe experiments, where the energy of the pump pulse is higher than that of the probe pulse) to study the ultrafast dynamics of LIPSS generation.

Assumption I is evidenced by the first approach, by installing a Mach-Zehnder interferometric, in order to produce double-fs-pulses[155]. Kim et al. have demonstrated that LIPSS formation is due to the collective oscillations of hot electrons on the surface of the material[156]. Sending a subsequent pulse disturbs these oscillations for a time less than that of hot electrons energy transfer to the cold ions. Mindaugas et al. have evidenced the existence of three fluence and time delay regimes between the two crossed polarized pulses, for which LIPSS period evolves linearly[157]. In addition, they revealed that the characteristic modification of LIPSS periodicity and orientation is second pulse dependent [157]. Hashida and her coworkers testify that LIPSS orientation follows the sum vector of the electric field of the two laser pulses impinging a titanium surface, where the fluence of each pulse was set below the multipulse damage threshold, i.e. only the joint action of both pulses yields LIPSS structuring[158]. LIPSS orientation characterization was described by a multi-photon process on the surface of the metal. Bonse et al. have extended the single color studies into a two-color scheme using parallel or crossed polarized ultrafast double-pulse sequences[124,159]. The evolution of LIPSS (LSFL) morphology as a function of time delay has been investigated on three types of materials: dielectrics (Fused silica), a semiconductor (silicon) and a metal (titanium). For LIPSS formation, different behavior was observed depending on the material. LIPSS morphology dependence on the time delay for silicon and titanium can be explained by a plasmonic mechanism. In contrast to semiconductors and metals, a different non-plasmonic mechanism is at the origin of LIPSS on dielectrics, where the first pulse generates a spatial modulation of the conduction band electrons, while the second pulse amplifies this distribution. It was also shown that for plasmonic materials, LIPSS morphology is determined by the second pulse of the sequence[159]. Besides the double-pulse features (state of polarization, time-delay, energy ratio) influence on the

final direction of LIPSS, ripples covered-spot area was studied[155]. In the context of sub-threshold irradiation conditions, the ripples-covered surface area exhibits a monotonous decrease with the time delay.

2.6 Mesoscopic aspects: Influence of crystalline orientation on LIPSS and defects

In the context of periodic surface structuring, irradiated material characterization has not been relatively studied a lot on a mesoscopic scale by LIPSS community. Few studies had been initiated on metals, whereas such characterization can provide rich information on the local thermodynamic history undergone on the first nanometers beneath the surface, affected by nanostructures formation. An electron backscatter diffraction (EBSD) is an efficient tool enabling visualization of deformations induced in crystals that had undergone strong constraints.

The effect of the crystalline orientation of the irradiated material on the formation LIPSS for polycrystalline nickel samples has been published[26]. This original work explains the inhomogeneity of the formation of structures on the surface of a metal irradiated by a small number of pulses. This locally non-uniform formation is attributable to the singular responses of the different crystalline orientations present on the surface. Figure 2.8 summarizes some results obtained in this work where the comparison of SEM images (a) and EBSD (b) taken on the same sample of irradiated nickel clearly shows a disparity of the structure dependent on the grain considered. The lower part of the laser impact corresponds to an oriented crystal (111) while the other two grains have oriented planes (213) and (215). Three particular areas were magnified to observe the presence or absence of LIPSS, in the grains or in the vicinity of a grain boundary. This result indicates a high dependency in the crystalline orientation, the oriented plane (111) appearing less favorable than the others for the formation of LIPSS on its surface. Figure 2.8c shows results reinforcing this observation on another impact with crystalline planes of directions orthogonal to (111), that is (100) and (110). This impact was analyzed by HR-EBSD (figure 2.8d), revealing a more pronounced disorientation for (111) than for the other plans. This means that the defects formed are more important for this plane than for the other planes. In other words, a competition seems to be played between the absorbed laser energy converted into crystalline defects or in the form of periodic surface structuring, potentially possible when a solid-liquid phase change occurs. The higher density of defects observed for the crystalline plane (111) has recently been attributed to the formation of twins[14].

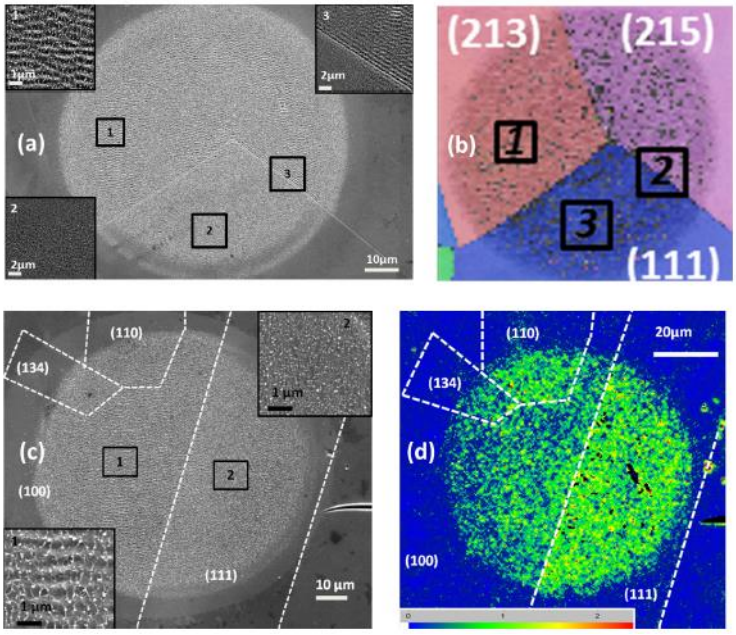

Fig 2.8 (a) SEM image of a site irradiated with 20 laser pulses at 0.3 J/cm². b) EBSD mapping where the color depends on the crystalline orientation with respect to the normal to the surface[26]. The indices corresponding to the crystalline planes are indicated. Each numbered region is visible in the insets of the figure on the left. (c) SEM image of a site irradiated with 18 laser pulses at 0.38 J/cm². (d) Local disorientation mapping by EBSD indicating greater distortion of the crystal planes (111)[26] . (c,d) clearly illustrate the competition between the formation of LIPSS and the accumulation of defects[26] .

A first in-depth study of crystalline lattice rotation levels[20] was first undertaken for different zones in the formed structured and the associated sub-layer after cross-section focused ion beam (FIB) cutting. The local disorientation of crystalline planes is shown in figure 2.9, where the false color mapping shows an inhomogeneous disorientation of about 2.5° (in green) ranging punctually up to 3°.

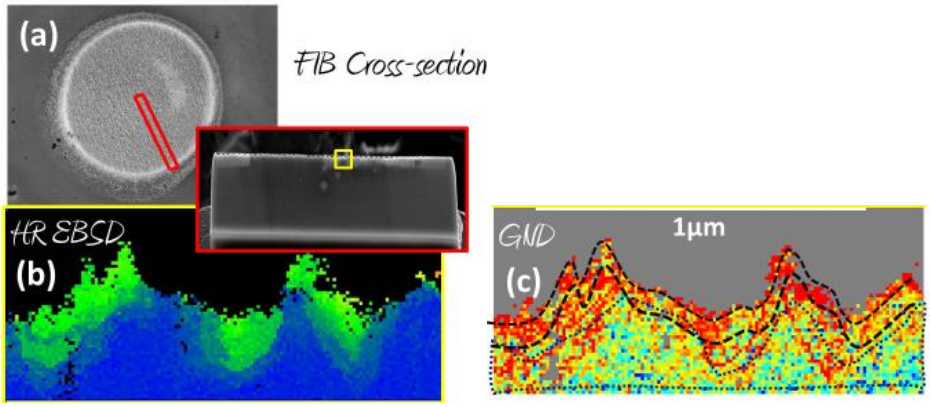

Fig. 2.9 (a) Performing focused ion-beam (FIB) cut to access LIPSS cross-section characterized by high resolution electron backscatter diffraction HR-EBSD. (b) Strong disorientation is observed in both ridges and holes. (c) Dislocation density mapping evaluated by the GND method. In the extreme surface region, the dislocation density is evaluated at 10^{16} m^{-2}, which can correspond to the liquid-solid transition zone estimated by a hydrodynamic density calculation[20] .

A dislocation density mapping carried out by the geometrically necessary dislocations (GND) method enables association of the observed disorientations with a high local density of dislocations. The density decreases with depth. Dislocations level estimation makes it possible to correlate the measured defects with the observed topology, without, however, specifying the origin of these defects, and several other tracks can be taken, apart from those discussed.

2.7 Conclusion

In this chapter, we have recalled the general principles of material laser interaction. In this thesis, we are specifically interested in metals. We also discussed the mechanisms of femtosecond-metal laser interaction and laser absorption processes in this case. A presentation of the physical mechanisms leading to laser ablation of metals as a function of fluence were also discussed. Generation of crystal defects irradiated by short pulsed laser on metals was also reviewed. Then, we present the main parameters influencing the formation of LIPSS and presented some hypothesis explaining the mechanisms of the formation of these structures. Finally, we briefly discussed the influence of crystalline orientation on LIPSS and defects generation, this approach being extended in the following chapters. In the next chapter, we will begin with a description of the experimental setup used in this study as well as a presentation of the different instruments employed to analyze our results.

Chapter 3

Experimental methods

The purpose of this chapter is to describe the different experimental and characterization tools used during the various experiences performed. The first part is dedicated to sample preparation techniques, i.e. mechanical and electrolytical polishing, and pointing out the type of targets irradiated in this work. The second part presents employed laser setups for surface irradiation. This involves generating femtosecond pulses of energy close to the millijoule via the laser system used in the laboratory, where double-pulse train generation employing a Mach-Zehnder interferometer as well as single pulse train generation are presented. Laser fluence determination based on Liu method is also discussed. In order to characterize microstructural defects generated beneath the surface, electron backscattered diffraction EBSD performed at Ecole Nationale Supérieure Des Mines de Saint-Etienne along with transmission electron microscope TEM carried out at CLYM (Mateis, INSA Lyon) are employed and several corresponding characterization tools are applied and described. For LIPSS features analysis, atomic force microscope AFM and scanning electron microscope SEM are also used. Finally, local near-field distribution mapping using photoemission electron microscope PEEM at CEA Saclay is reported for probing the dynamic of LIPSS formation.

3.1 Sample preparation

To perform quality and accurate laser irradiation of metal surfaces, it is often not possible to use the sample as it is. A preliminary phase of preparation is necessary, constituting of surface preparation to reduce the material's dimension and to prepare it for irradiation, followed by microscopy studies. The primary objective is to reduce the micro-roughness and thus drastically limit the risk of adherence of dirt or other deposits, which has the effect of improving the cleanability of the surfaces and reducing in turn the local absorption. Thus sample preparation is an essential activity that precedes surface laser irradiation.

3.1.1 Samples

In this thesis, different metals were prepared for laser irradiation in order to study LIPSS formation as well as defects generation. For laser induced defects dependence on crystalline orientation, 3 chromium monocrystalline samples having different orientations, (100), (111) and (110), and a chromium polycrystalline were employed. The choice of body-cubic-center (bcc) Cr samples lies on the fact that these type of materials do not engender twin domains, as in the case of fcc materials, i.e. Nickel. Thus investigation of laser-induced surface defects and in-depth on bcc materials reveals other types of defects. For LIPSS formation, bcc (Cr), fcc (Ni) as well as hexagonal (Ti) materials were used. In order to study crystalline orientation dependence on LIPSS formation, Cr(100) and Cr(110) were irradiated.

We perform a two-stage polishing for our samples, consisting of a mechanical and electrolytical polishing, described in the following sections.

3.1.2 Mechanical polishing

For mechanical polishing, the paper we used comes with abrasive particles with fine and controlled particles of silicon carbide (SiC). If the surface of the sample is not flat, we start with a "coarse" paper, P800, then move successively to finer grain paper, P1000 and P2500 (Pxxx denotes the European P-grade). Between two polishing papers, we clean the sample thoroughly to remove any particles from the previous paper that may have become embedded. In general, we use an ultrasonic bath, then cross the polishing direction: for a given paper, we always polish in the same direction, and we cross the directions from one paper to another, which allows to highlight the residual stripes of the previous step. After mechanical polishing, we proceed to electrolytical polishing, described in the following section.

3.1.3 Electrolytical polishing

Electropolishing consists of removing metal from a piece immersed in an electrolyte of a given composition, into which passes an electric current. Samples are connected to the anode while the cathode is connected to a suitable conductor. The electric circuit is completed by an electrolyte in which the two poles are immersed. The applied current is a direct current. The metal part immersed in the electrolytic bath is positively charged (anode). When applying the current, electrolyte acts as a "tool" that removes metal ions from the sample. The ions are attracted to the cathode but most of the dissolved metals remains in solution. Some ions settle in the form of mud on cathodes, which requires regular cleaning to maintain the performance of installation. Oxygen release on the surface of the metal further enhances the electrolytic action. It should be noted that electropolishing is a process that does not induce distortion: electropolished samples are not subject to mechanical stress or thermal stress, as they would be with abrasives. Electrolytical polishing was performed at Ecole National Supérieure des Mines de Saint-Etienne EMSE. The equipment is a microprocessor-controlled LectroPol-5 polishing machine, delivered by Struers company.

Before proceeding with electrolytic preparation, the correct method must be selected. Struers equipment offers 10 standard methods for different materials. If none of these methods can be applied to the material, it is possible to select the correct electrolyte from the Electrolyte Selection list. Once the electrolyte has been selected, the polishing voltage must be determined. To do this, we will use the scanning function integrated in the electrolytic preparation equipment. Once the sample is installed on the polishing table, a preset voltage range is scanned to determine the current density curve. This curve is used to determine the polishing voltage for the polishing or thinning process. The other parameters to be defined are the polishing time and the flow rate. Once all the application parameters have been set, they can be saved to the database and reused for further polishing tasks. The polishing of some materials can be done by means of several electrolytes. The right choice depends on the composition of the material and the desired analysis.

Table 3.1 provides the electrolytical parameters used for polishing Cr and Ni samples.

Sample	Time (s)	Voltage (V)
Ni	60	25
Cr	40	30

Tab 3.1 Electrolytical parameters used for polishing Cr and Ni samples.

3.2 Femtosecond laser pulses

3.2.1 Laser chain

The femtosecond laser system used in this work is made up of the following elements: A femtosecond oscillator that generates ultrashort pulses of relatively low energy (~ nJ) at high frequency (~ MHz) and at a wavelength of 800 nm., a pump laser generating nanosecond pulses at a wavelength of 532 nm and a repetition rate of 1 kHz and an amplification stage for amplifying the pulses produced by the oscillator at mean of the pump laser.

The properties of the different elements of the laser chain are summarized in Table 3.2. Figure 3.1 describes the organization of the different elements constituting the amplified laser used in this work.

The active medium of the femtosecond oscillator consists of a Ti: Sapphire crystal. Its optical pumping is carried out using a Nd: YVO4 Verdi diode whose emission, centered around 1064 nm, is reduced to 532 nm by a doubling crystal (LBO) which is the optimal wavelength for pumping the Ti: Sapphire crystals. The generation of ultrashort pulses is based on the compensation between two optical phenomena: the wavelength dispersion and the Kerr effect.

Laser	Element	Output pulse duration	Frequency	Energy/pulse	Wavelength
Coherent LEGEND Elite	Mantis oscillator Evolution Amplificator	30 fs 8 ns 35 fs	80 MHz 1 kHz 1 kHz	6.25 nJ 20 mJ 4 mJ	800 nm 527 nm 800 nm

Table 3.2 Characteristics of the laser chain.

On one hand, the dispersion comes from the dependence of the medium index on the used wavelength. Thus, the value of the refractive index can vary with the wavelength. In the case of a so-called normal dispersion, the index decreases with laser wavelength, and the low wavelengths are the slowest during their passage in the crystal. On the contrary, in the case of an anomalous dispersion, the index increases with the wavelength, and it is the long wavelengths which are slowed down. In the case of a short pulse moving in an anomalous dispersion medium such as Ti: Sapphire, the edge of the pulse is shifted to high frequencies while its tail is shifted to low frequencies.

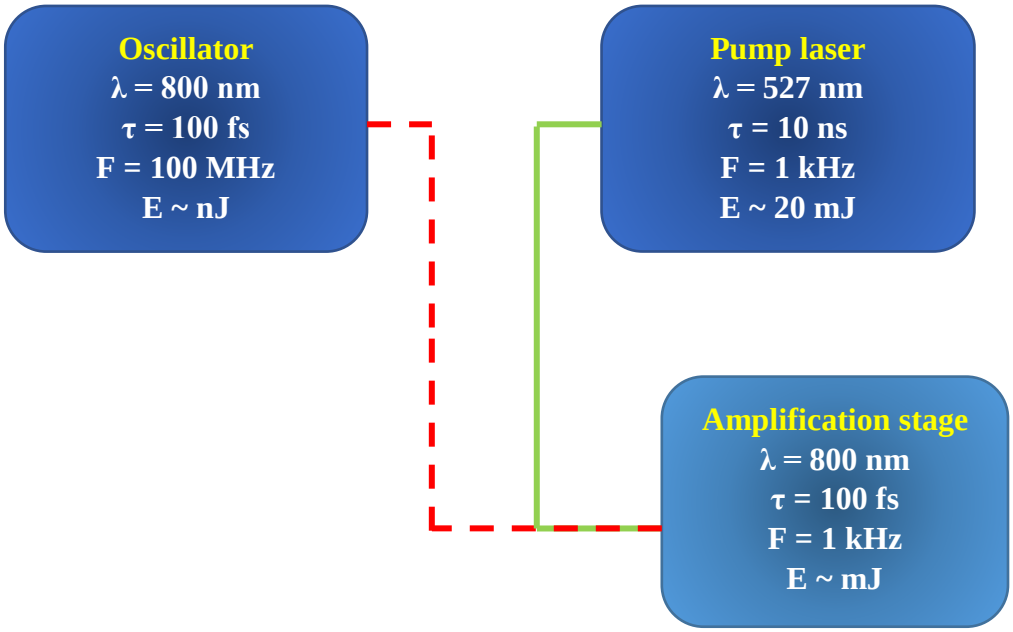

Fig. 3.1 Schematic diagram of the femtosecond amplification system

On the other hand, the Kerr effect characterizes the index variation of a medium subjected to a strong electric field. We will describe here the optical Kerr effect as it is the intense electric field that is responsible for this index variation. This is then proportional to the irradiance, itself proportional to the square of the electric field. In the case of propagation of a Gaussian laser pulse, this phenomenon has two main consequences. First, it induces a self-focusing of the beam. Indeed, the optical index increases more in the center of the beam than on its edges. This index gradient plays the same role as a lens and concentrates the energy at the center of the crystal. Then the Kerr effect causes the auto-phase modulation. When passing a pulse in a Kerr effect medium, the edge of the pulse is shifted to low frequencies while the tail of the pulse is shifted to the high frequencies.

For sufficient laser energy, the compensation of the anomalous dispersion by phase auto-modulation thus makes it possible to keep pulses of short duration in the amplifying medium. It is then a question of favoring the pulse modes of strong energies during the creation of the laser signal. This is possible owing to the self-focusing phenomenon, which modifies the optical path of the high energy pulses in the laser cavity. It is then a question of optimizing the laser cavity so that the optical path of the pulse modes is preferred.

The objective is to exploit three properties of Ti: Sapphire: an anomalous dispersion, the optical Kerr effect, and a LASER potential effect at 800 nm pumped at 532 nm. The signal from the oscillator is sent to the amplification stage where it is joined by the pump laser. For the pump laser used in this work, the medium consists of Nd: YLF with laser transition wavelength of 1053 nm. A Q-switch system produces pulses of a few ns duration, clocked at 1 kHz and twenty mJ of energy for each pulse. The output wavelength, 527 nm, is obtained by frequency doubling. This is optimal for pumping Ti: Sapphire crystals intended to amplify the femtosecond laser pulses centered at 800 nm. However, the oscillator signal cannot be directly amplified by the pump signal

Indeed, the peak power of femtosecond pulses of a few mJ of energy as we want to obtain them is of the order of 10^9 to 10^{10} W, exceeding the threshold of damage of the amplifying media used. The system is based on the principle of frequency drift amplification[160], revealed by the 2018 Nobel Prizes recipients Gérard Mourou and Donna Strickland. Diffraction gratings at the input of the amplifier disperse the femtosecond frequency signal, in order to temporally stretch the pulses and reduce their peak power. A compressor composed of gratings whose alignment is electrically controllable makes it possible to reach the shortest possible pulse duration, at the end of the laser pulse.

The misalignment of this last compression stage also makes it possible to greatly increase the pulse duration of the laser after amplification. In particular this method will be used to obtain longer pulses, up to ten picoseconds, on the LEGEND laser. The ejection of the pulse amplified by the laser is performed by means of computer controlled Pockels cells. Programs provided by the manufacturers allow you to select the number of shots to be made and their rate (maximum 1 kHz, or a fraction of this frequency).

3.2.2 Generation of double pulses train by a Mach-Zehnder configuration

In our work, we generate sequences of one-color double-pulses by using a Mach-Zehnder interferometer. Fig 3.2 represents a scheme of the one-color fs-double pulse experimental setup used in our work. A commercial Ti: Sapphire regenerative laser amplifier (Coherent) highlighted by the number 1 in the figure provides linearly polarized pulses with a pulse duration equals to τ = 150 fs. The laser operates at a central wavelength of 800 nm with a repetition rate of 1 KHz.

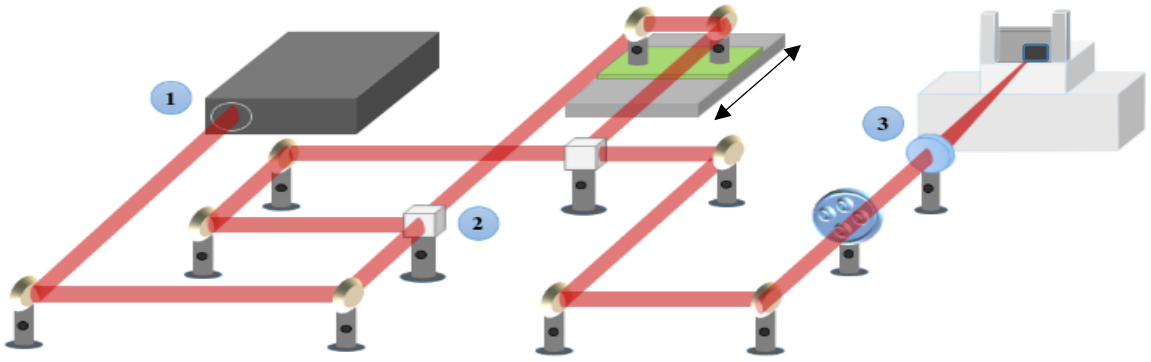

Fig. 3.2 Experimental setup describing one-color fs-double pulse generation using a Mach-Zehnder interferometer. Number 1 represents the femtosecond laser system, number 2 the cube beam-splitter and number 3 the focusing lens.

An electromechanical shutter, integrated in the fs-laser system, allows the selection of a desired number of laser pulses. A standard Mach-Zehnder interferometer was used to process these single fs-pulses into double fs-pulses sequences, where N_{DPS} represents the number of double pulse sequences. A cube, marked by the number 2, was used to separate the beam into two parts. In the mobile arm, the beam passes through a computer-controlled linear-translation stage

(physik instrumente) which allows the control of the time delay between the two pulses. It is an M404.8PD plate allowing a displacement of 200 mm, which gives the possibility to reach delays between the pulses higher than the nanosecond. The minimum possible displacement of 0.25 µm makes it possible to easily create precise delays of a few hundred femtoseconds. For polarization and energy control, a half-wave plate with a polarizer inserted in one of the arms optionally rotates the state of polarization direction and thus generates parallel or cross-polarized one-color double fs-pulses. Negative delays implies the arrival of s-polarized pulse prior to p/s-polarized pulse. Each pulse of the double pulse sequence is kept below the LIPSS formation threshold of the corresponding material. Thus the joint action of the double pulses lead to LIPSS formation. In other terms, 'sub-damage threshold conditions' were realized in all cases. This is schematically shown in fig 3.3.

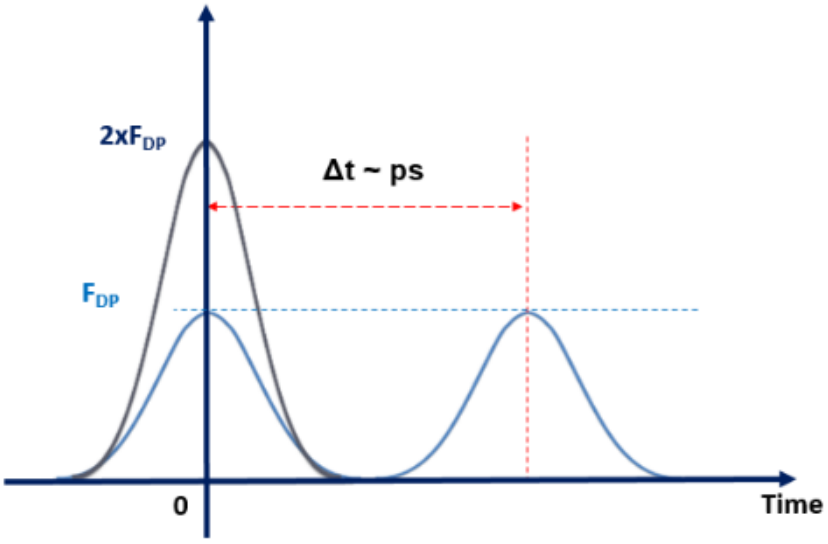

Fig. 3.3 A schematic representation of a sequence of double pulses with a time delay Δt. Each pulse of the double pulse sequence is kept below the LIPSS formation threshold of the corresponding material. Thus the joint action of the double pulses lead to LIPSS formation.

The collinear double-pulse sequences are focused normally onto the surface of the sample by a lens of 250 mm focal length, marked by the number 3. The waist radius w_0 and the ablation threshold for one pulse are quantified in single pulse experiments using Liu method, described in the following section. All experimental irradiations were done in ambient air. Careful attention has been paid to the spatial alignment of the two arms, where the two focused spots on the target's surface are superimposed.

For single pulse use of the femtosecond laser system without double pulses, it is necessary to hide an arm of the interferometer or to go through a different optical path. Indeed, when the optical path between the two arms becomes weak, for delays between pulses less than 300 fs, interference fringes appear. This optimizes the alignment of the device by making them fully disappear. However, the slightest displacement of the movable arm and its return to the origin can generate new ones, induced by the roll and the swing of the micrometer plate. The inaccuracy of the return to the origin of the platinum can also generate fringes of interference to infinity. It therefore seems easier to use only one arm of the interferometer when one wants to have a single pulse rather than to make long and tedious adjustments each time. Due

to the temporal separation of the pulses when the arms are not equidistant from the separator, these fringes no longer appear during the realization of double pulses.

3.2.3 Laser fluence determination: Liu or D² method

When irradiating a material under conditions that can lead to ablation, the fluence is a paramount parameter. We define the fluence F, expressed in J/cm², as follows: the energy per pulse E (the number of photons hf) per unit area Σ of the laser beam: $F = E/\Sigma$. For lasers with uniform spatial distribution of energy (excimer laser for example), this measurement is easy since it is sufficient to measure the surface of a laser impact and the power of the laser.

In this work, the femtosecond lasers used do not have a uniform but Gaussian spatial distribution of energy. It is no longer possible to simply measure the surface of an impact, which varies according to the total energy of the laser pulse. The energy ratio of the pulse/ablated surface then no longer makes sense. To rectify this problem, the method proposed by Liu[161] is used to simply measure the spot size of Gaussian beams.

We consider a Gaussian radial distribution of the beam energy on the target. F_c is defined as the fluence at the center of the spot (peak fluence) and r the distance at the center of the spot. For a Gaussian beam, the beam width, ω, is the distance to the center of the spot for which the intensity is divided by e², where e represents the Euler constant. Finally, we define the ablation threshold fluence of the material F_{th}, and r_{th} the radius beyond which the ablation no longer takes place. These different parameters are illustrated in Figure 3.4.

The spatial distribution F(r) of the laser fluence is therefore given here by:

$$F(r)=F_c\, e^{-2\frac{r^2}{w^2}} = F_c\, e^{-2\frac{\pi r^2}{\pi w^2}} \tag{3.1}$$

Where πr² and πω² being respectively the surfaces of the studied zone and the laser spot Σ. We can define the ablated surface threshold Σ_{th} (corresponding to threshold):

$$\frac{F_{th}}{F_c} = e^{-\frac{2\Sigma_{th}}{\Sigma}} \tag{3.2}$$

Or

$$\Sigma_{th} = \frac{\Sigma}{2}\,[\ln F_c - \ln F_{th}] \tag{3.3}$$

However, in the case of a Gaussian distribution, the peak value is twice the average value of the distribution. So we have an average fluence of $F_c = 2 \times F$. For a single pulse with energy E:

$$F_c = 2\,x\,\frac{E}{\Sigma} \tag{3.4}$$

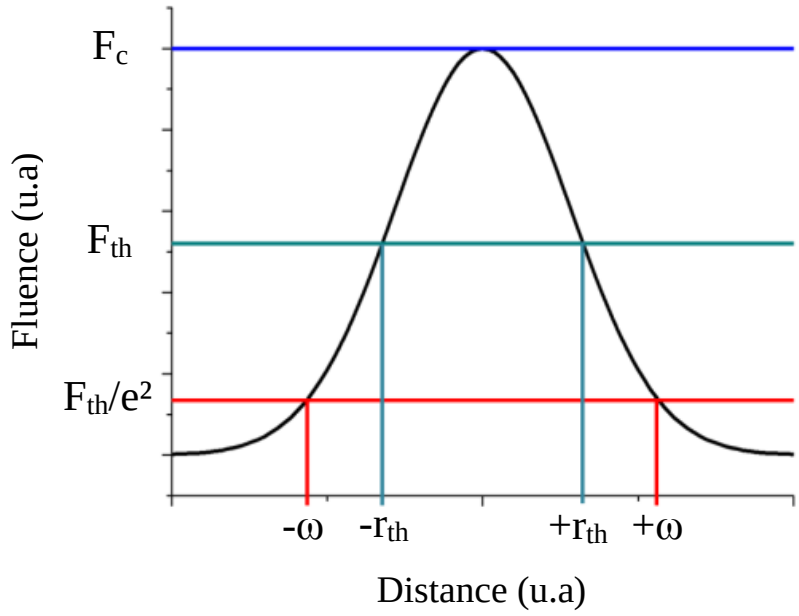

Fig. 3.4: Radial distribution of the laser fluence. Fc represents the peak fluence, while Fth represents the ablation threshold fluence.

In the same way, one can consider the laser pulse of minimum energy allowing to damage the material E_{th}, whose peak value of the fluence distribution will be solved:

$$F_c = 2 \text{ x } \frac{E_{th}}{\Sigma} \tag{3.5}$$

Thus we obtain:

$$\Sigma_{th} = \frac{\Sigma}{2}[\ln E_c - \ln E_{th}] \tag{3.6}$$

The measurement of the laser energy is done using a calorimeter and measuring the average power delivered at a given frequency. It is then sufficient to achieve the same type of impact as to find the focal point, this time changing the laser energy without affecting the position of the focusing lens. By performing a series of impacts on the material at different fluences, it is possible to represent the ablated surface Σ_{th} according to the logarithm of the energy ln (E). It is then possible to exploit the affine relation between these two values (equation 3.6) to go up, by a linear fit, to the surface Σ of the laser spot

We therefore have a linear relationship between the ablated surface and the logarithm of the energy. From 3.6, the slope of the line represents the half of the beam area. We can also determine the energy and the threshold fluence with ln E = ln F = 0.

Fig 3.5 shows the plot of laser fluence threshold for 1 pulse on Cr sample with (100) oriented planes using the D^2 method.

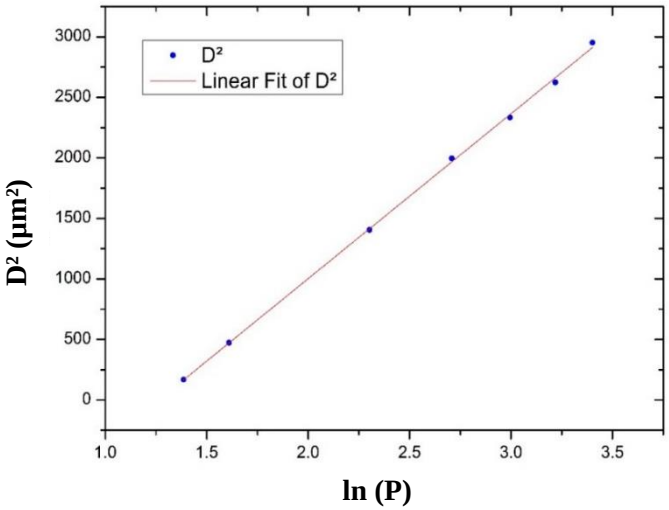

Fig. 3.5 Linear regression performed on laser-induced ablation craters on a Cr sample at the focal plane in order to determine the single pulse ablation threshold using Liu method.

For example, the slope of the curve is equal to $\Sigma/2 = 7.93 \times 10^{-6}$. This leads to a laser spot area of 1.6×10^{5} cm^2 and therefore a single pulse laser fluence ablation threshold of 0.33 J/cm^2.

3.3 Microscopy for laser-induced modification characterization

3.3.1 Optical microscopy

The use of the optical microscope is a preliminary method of characterization, performed after each femtosecond laser materials irradiation experiment. Optical microscopy gives quick and immediate access to the various impacts, and thus allows the selection of interesting results, to be analyzed using scanning electron microscopy with a high resolution. The instrument used is a Zeiss optical microscope, incorporating a DFC 32O digital color camera, which is equipped with "AxiovisionLE" software developed in a ZVI Carl Zeiss image format. The microscope used allows a magnification ranging from 50 up to 1000 and has several methods of characterization according to the different samples to be studied. For high-resolution analyzes, such as LIPSS, we will use the scanning electron microscope (SEM) to obtain a higher magnification.

3.3.2 Atomic Force Microscopy

AFM is a microscope with a local probe allowing to visualize the surface topography of a sample with a resolution of about 1 nm. Its operating principle is based on the interactions between the specimen and a nanometric tip mounted on a micro-lever, moving in 3 directions of space via a piezoelectric. The interaction forces between the probed surface and the tip are deduced directly from the bending measurement of the micro-lever. Practically, we measure the reflection of a laser on the tip, to determine the flexion of the lever.

Scanning is established commonly according to the following modes:

The contact mode: The sweeping is done by a physical contact between the tip and the surface of the sample, until the creation of a repulsive force between the tip's atoms and surface atoms. This force creates a deflection of the lever and is measured by the laser. The variations of the repulsive forces due to the reliefs are recorded to give rise to a topographic image.

Non-contact mode: The tip vibrates vertically (around its proper frequency), at a distance ranging from 5 to 15 nm from the surface of the sample. The attractive force, which represents a disturbance for the oscillations, modifies the amplitude, the phase and the frequency of the vibration according to the average height of the tip. The electronic excitation makes it possible to detect this modification by supplying the electrical signal used for regulation. The absence of contact between the tip and the surface remains a main advantage of this mode, because it preserves the quality of the tip. On the other hand, the attractive force (generally sensitive to the height of the tip) is much weaker than that of deflection used in the contact mode, the quality of the image is therefore not as good as that obtained in the first mode. In addition, the presence of a vapor layer at the surface under ambient conditions can trap the tip if the vibration is performed at an amplitude that is not sufficiently large. This mode is therefore often used.

Tapping mode: The tip vibrates at a very short distance from the surface to the point where it touches the surface, when it is in its lowest position, the contact is therefore intermittent. The force linking the tip and the surface, varies from attraction to repulsion. In the non-contact mode, it is taken into account to keep the average height constant, this is guaranteed by providing a good vibration amplitude. As for the quality of the given image, the intermittent contact mode is comparable to the contact mode, moreover, it avoids better damage problems, adhesion or low sensitivities regarding contact or non-contact mode.

The AFM used is of type Agilent 5500. The topographic images obtained in the context of our study are made in contact mode, by S. Reynaud. Among the limitation of this technique, the rapid wear of the tip is probably the most troublesome.

3.3.3 Electron microscopies

3.3.3.1 Why use electrons?

In 1925, Louis De Broglie first speculated that the electron had wave-like features, with a wavelength considerably less than visible light. Two years after, two independent research groups around Davisson and Thomson performed experiments on classic electron-diffraction, which investigated the wave nature of the electrons. After then, the idea of an electron microscope was proposed, and the term was first used by Knoll and Ruska in a research paper in 1932 [162,163]. This publication contributed in surpassing the light microscope's resolution limit. For scientists conducting experiments on materials, Hirsh and co-workers in Cambridge developed a theory concerning electron-diffraction contrast with which we can now characterize, different types of crystal defects, i.e. line and planar defects, often in a quantitative form.

A significant feature of electrons is that they are one type of ionization radiation. In fact, by ceding a part of its energy to individual atoms in the sample, they are efficient in ejecting inner-shell electrons that are tightly bound due to the attractive electric field of the nucleus. The benefit of using an ionization radiation, i.e. electrons, lies on the fact that it produces a broad range of secondary signals from the sample and are summarized in fig. 3.6, which shows the interaction between an incident electron beam with a sample.

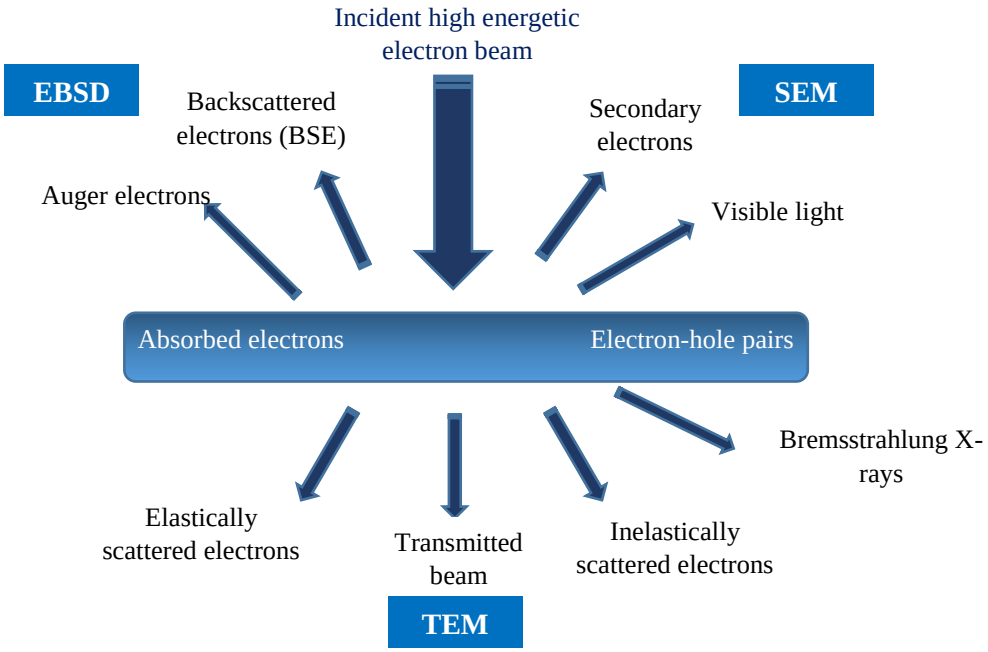

Fig. 3.6 Different processes that result through interaction of electrons with matter.

The electron-sample interaction lead to dissipation of this energy as a variety of signals, when the incident electrons are decelerated in the specimen due to interactions. The signals can include secondary electrons producing SEM images, backscattered electrons, diffracted backscattered electrons, photons, visible light and heat.

3.3.3.2 Scanning electron microscope SEM

The scanning electron microscope (SEM) used in our work is of type 'Nova NanoSEM' equipped with a FEG, marketed by the company FEI. It has two types of resolutions: The first allows to work in high resolution, and the second, called 'immersion mode', enables a maximum resolution of 1 nm, for a magnification of 300000. SEM uses electrons rather than light, to form an image that represents the morphology of the surface. The operation principle of the SEM lies on the emission of an electron beam of high energy, focused by condenser lenses and sweeping the surface of the sample. Accelerated electrons produced by the field emission gun (FEG) carry important amounts of kinetic energy. Secondary electrons and backscattered electrons are generally used for imaging samples:

On one hand, secondary electrons are most precious for representing morphology and topography of the samples. When the acceleration voltage is constant, electrons density depends on the angle between the surface and the beam. The smaller this angle, the higher the number of secondary electrons emitted. On the other, backscattered electrons are most valuable for studying contrasts in composition in multiphase samples.

The SEM is equipped with an evacuation system that produces a stable vacuum in the order of 10^{-9} bar. This vacuum is necessary to maintain a good quality of the beam, and to avoid contamination of the sample. The analyzed samples in our work are of conductive types. This implies working in high vacuum mode. The quality of the images and the analytical precision that can be achieved with a SEM require a fine, intense and stable electronic spot on the sample.

3.3.3.3 Electron backscattered diffraction

Electron backscattered diffraction (EBSD) is equipped with SEM technique attached to an accessory system. EBSD is used to provide the crystallographic nature of metals, semiconductors, ceramics and minerals quantitatively. It also reveals information about grain features, i.e. grain sizes, grain boundaries characteristics and grain orientation. In addition, texture and sample's phase can be identified. The EBSD's spatial resolution is limited to the SEM, but in the case of high performance modern field emission SEM (FE-SEM), grains with 20 nm size can be reasonably measured. The angular resolution limit is approximately 0.5°. Concerning the sample's size, it is dependent on the capability of the SEM chamber and stage to orient the specimen at an angle of 70° which is the universal proper tilt used to extract maximum signal. The appropriate working distance ranges from 5 to 30 mm.

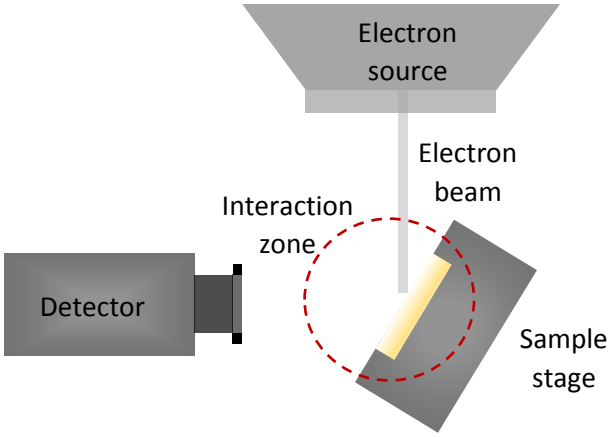

Fig. 3.7: Schematic representation of the EBSD equipment, where we show the beam emitted from the source and interacting with the yellow sample, tilted at 70° which provides maximum yield. The EBSD detector collects retrodiffused electrons

EBSD operates by tilting the plane of a flat and polished specimen to a value of stage typically 70° with regards to the shallow angle of about 20°. The use of a 10-30 kV accelerating voltage with incident beam currents ranging from 1 to 50 nA produces electron diffraction on the surface of the specimen from the stationary incident beam point, from which an electron backscatter diffraction pattern (EBSDP) originates spherically from this point, known as Kikushi bands[164–169]. A picture representing Kikushi bands is given by fig. 3.8.

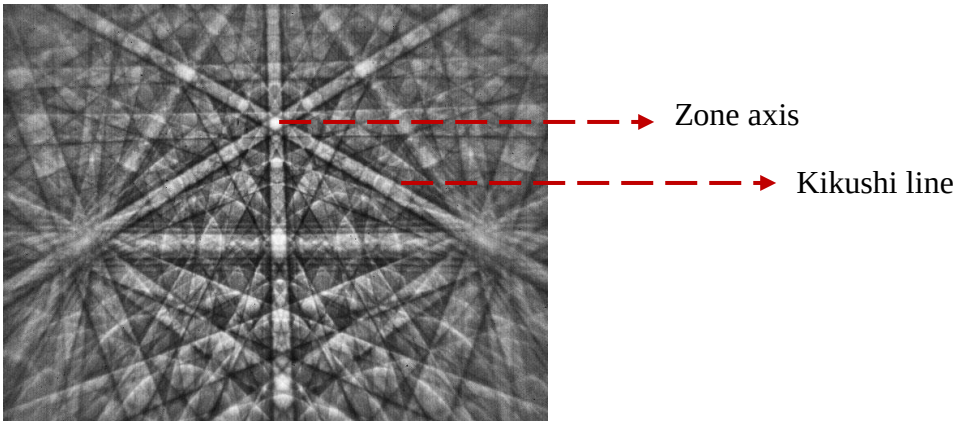

Fig. 3.8 Each band represents a diffraction of a family of planes. Intersection of bands accounts for the interaction of planes (zone axis), and the angle between bands represent the angle between planes. Band widths is proportional to the interspace between crystalline planes

The interaction between the FEG emitted electron beam and the crystal lattice yields low energetic backscattered electrons which are canalized and subjected to different paths leading constructive and destructive interferences. A diffraction pattern can be obtained on a phosphoric screen placed at a short distance from the tilted specimen in the path

of the diffracted electrons. In fact, the detector is composed of a digital camera which the phosphor screen illuminates its CCD chip intersecting the spherical diffraction pattern.

Lattice parameters, spatial crystal's orientation, incident electron beam wavelength as well as the distance detector-sample define the electron backscattered pattern EBSP. A computer integrated software analyses the diffracted pattern by detecting a number of Kikushi bands employing an optimized Hough transform. When the orientation and phase are known, the EBSP is considered to be indexed.

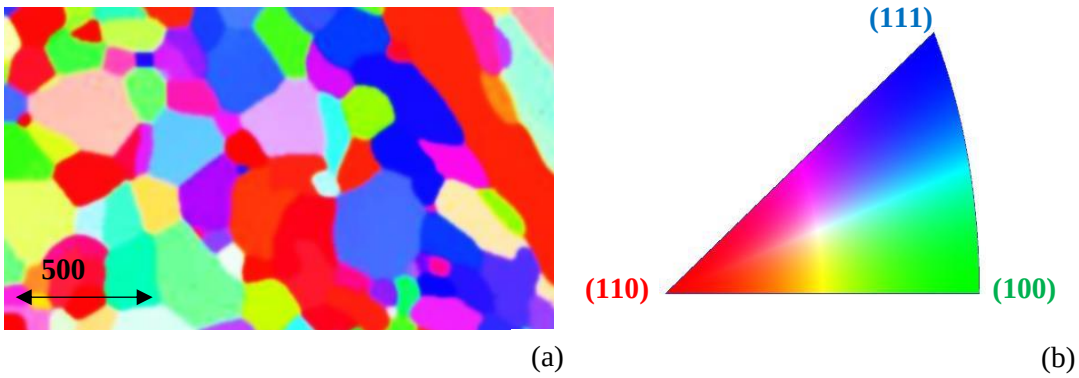

Fig. 3.9 (a) EBSD mapping of the crystalline orientation of a Cr polycrystalline sample, before irradiation. (b) Key orientation color map.

In the frame of our work, different EBSD's tools were used to characterize ultrashort laser induced crystal defects, i.e. band contrast, mean angular deviation and local misorientation.

The *band contrast (BC)* is defined as a quality factor of the diffracted pattern/Kikushi bands emanating from the Hough transform. It gives a description of the Kikushi bands average intensity with regard to the overall intensity within the EBSP. The BC image consists of byte scaled values ranging from 0 (low contrast) to 255 (high contrast). BC maps show the microstructure in a qualitative form. The Kikushi bands originating from undeformed regions are of good quality. Thus the EBSP's appear light on the image. On the contrary, if the Kikushi bands are of poor quality, the EBSP's appear dark.

Mean angular deviation (MAD) is a number that describes the correlation between the actual EBSP and the simulated EBSP. It specifies the average angular misfit between detected and simulated kikushi bands.

Local misorientation (LM) calculates the local misorientation between a pixel and its surrounding eight pixels. This tool is useful for studying plastic deformation.

3.3.3.4 Transmission electron microscope (TEM)

TEM exists conceptually in two forms: the TEM's, for which the incident beam on the sample is a plane wave, as in the case of a benchtop microscope, and the STEM (scanning transmission electron microscope), which is similar to the confocal optical microscope. Modern microscopes work in both modes. An electron gun produces a beam which passes through a series of condenser lenses to adjust the size and angle of incidence of the beam. The beam then reaches the sample, a first image produced by the objective lens. It should be noted that the objective lens is the most important element, because the resolution of the image will depend on its quality. In addition, the objective lens hardly grows (≈ × 10), this role being devolved to the projection lenses. After crossing the objective lens, the intermediate lens will either form a second image, if its object plane coincides with the image plane of the objective lens, or form an image of the diffraction pattern, if its object plane coincides with the focal plane of the objective lens. Thus one of the obvious advantages of transmission electron microscopy can be seen: by modifying the value of the focal length of the intermediate lens (in practice, a simple push button modifying the current in the intermediate coils), the image is easily obtained or the diffraction pattern of the same area. Finally, the projection lenses will enlarge the image or the diffraction pattern formed and project it on the detector, which may be a fluorescent screen, a photo plate or more commonly a scintillator coupled to a CCD camera

In the case of TEM, the sample is illuminated by a wide beam, and it is the detector that is resolved spatially. In the case of STEM, it is the opposite, since we will scan a beam focused on the sample, and measure the signals of interest at each point of this scan. These signals are usually measured on a spatially unresolved detector, as is the case for the darkfield signal. The image is then formed sequentially, assigning each scanned point the intensity of the measured signal. The STEM mode is particularly well suited to chemical analysis, because one of the signals detected at each point with the black background signal may be a spectroscopic signal.

The spatial resolution of a TEM is about 0.2 nm. This is the typical distance between two atoms in a solid. This resolution is 1000 times greater than an optical microscope.

In a TEM/STEM, the principle signal of electrons that one can detect are the transmitted (forward) scattered electrons, backscattered electrons (BSE) and secondary electrons (SE). Fig 3.10 summarizes various type of electrons detectors in a TEM/STEM. The primary detector, called the bright-field BF detector, collects the forward-scattered electrons on axis. A second detector, known as the annular dark-field detector ADF, picks up forward-scattered electrons through small angles < ~ 4°, and finally, the high angular annular dark field detector HAADF, used in our work, collects electrons scattered out to high angles.

Thin lamellas were prepared by focused ion beam technique FIB at Mateis lab in Villeurbanne by T. Douillard. In order to protect the surface of the laser impact, a layer of a few 100 nm thick tungsten was deposited. A focused ion-beam with an accelerative voltage of 30 keV consisting of Gallium atoms milled the sample and lift-out technique was used for lamellas extraction from the surrounding milled zone.

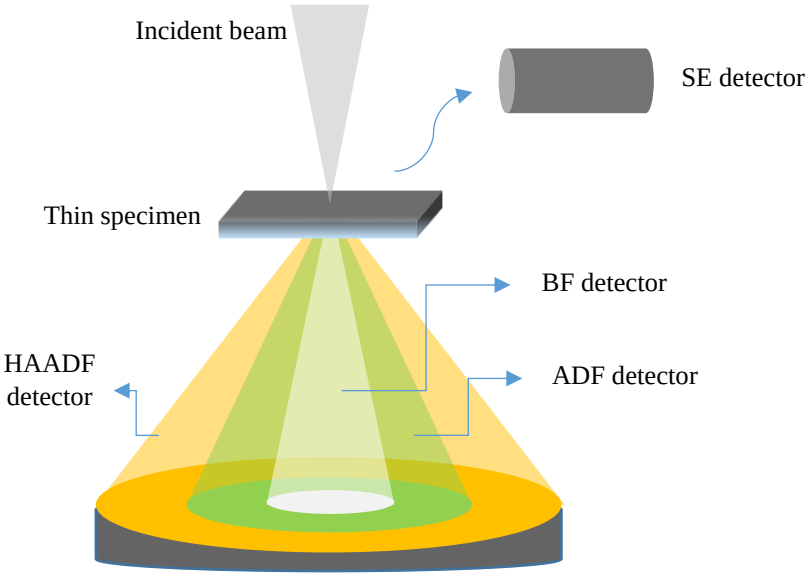

Fig. 3.10 Schematic of the HAADF, conventional annular dark-field (ADF) and BF detectors in a TEM.

3.3.4 Local-field probing

3.3.4.1 Brief history

Recently, tremendous efforts have been undertaken in order to localize the regions with intense electromagnetic enhancement within the structures of interest, often referred to as 'hot spots'. Prediction of the hot spots localization has been tackled by numerical solutions. Schatz et al. carried out discrete dipole approximation DDA calculations on triangle dimers separated by a gap of 2 nm[170], where the hot spots were located at the tips of the triangles. For a matrix consisting of nanoholes, simulations predicted that the hot spots were located around the rim of the nanohole[171]. Basically, all simulations were undertaken on nanohole arrays with diameters half their periodicity. No complete series of simulation has shown the evolution of the hot spots localization. Experimentally, numerous techniques have emerged maintaining non-contact examination, i.e. Stimulated Emission Depletion STED microscopy[172], Stochastic Optical Reconstruction Microscopy STORM[173,174], Photoactivated Localized Microscopy PALM[175] near-field scanning optical microscope SNOM[176] and Photoemission Electron Microscope PEEM. Since the mid-1980s, it was attested that PEEM is an effective tool in surface science[177–180]. Considering exceptional application areas where PEEM has succeeded, one can mention the study of chemical surface reaction, a process occurring in real time[181], growth mechanism[182,183], surface diffusion[184] and magnetism[185–187]. Recently, with the advent of reliable femtosecond laser sources, PEEM with multiphoton absorption has been widely employed in plasmonics for surface plasmon polaritons investigation[188–192], attracting significant attention regarding their potential in confining light beyond the diffraction limit. Multiphoton photoemission experiments enabling access to the spatial distribution of nonlinear effects date back to 2001[193] providing

preliminary observations. Nevertheless, it took a few years later for physical measurements to establish a comprehensible relationship between the nonlinear photoemission and optical near field distribution related to a plasmon resonance. In 2005, it was clearly revealed that PEEM is a powerful tool in mapping the optical near field with the resolution of the emission electron microscope (25 nm)[194]. Soon after, the spatiotemporal propagation of surface plasmon resonance mapped by pump probe PEEM experiments was investigated precisely[189,195,196]. Currently, the active research groups engaging a determined use of the n-photon photoemission (nPPE)-PEEM microscopy in the field of plasmonic are still few[192,195,197–202], but new involvement often appear with the growth of the technique's interest[203–207], where three types of plasmonic investigations can be worth (nPPE)-PEEM employment: mapping of the objects of interest with dimensions below the incident wavelength, SPP's dynamics and propagation, and near field manipulation.

3.3.4.2 Photoemission electron microscope

The photoemission electron microscopy technique (PEEM) is well suited to complete LIPSS dynamics study, since it allows to directly probe the electric field on the surface of a metallic lattice. This technique allows to optically excite modes and to detect photo-emitted electrons, which forms a mapping of the surface with a lateral resolution of 25 nm (this resolution has recently reached a few nanometers owing to a recent method of correcting aberrations), much higher than the resolution obtained with an optical detection, since it is the aberrations of the electronic imagery and, lastly, the wavelength of the electrons, which limit the resolution. PEEM characterization was performed at radiation-matter institute IRAMIS of CEA Saclay by Ludovic Douillard.

PEEM is a full-field microscopy method, which relies on the collection of electrons photo-emitted by the excited surface. The schematic diagram of the assembly is shown in figure 3.11. Unlike scanning electron microscopy (SEM), there is no electron beam that scans the surface of the sample. The surface is illuminated homogeneously by a Titanium: Sapphire laser, at an angle of incidence of 0°, similar to incident angle of femtosecond laser beam used to form LIPSS in our work. The laser is tunable between 690 nm and 1100 nm. We fix the PEEM laser wavelength to 800 nm which is identical to the irradiating laser in LIPSS formation experiment. A half-wave plate is placed in the laser beam in order to be able to change the excitation polarization. It is therefore possible to vary the wavelength and the excitation polarization of the laser, according to the exact laser irradiation parameters used to generate LIPSS. The pulse duration of the laser is 140 fs and the spot has a diameter of 300 µm. The excitation by a pulsed laser is imposed by the fact that the process of photoemission is strongly non-linear. Indeed, the energy of three photons is necessary to extract an electron in the case of an oxide titanium. An electrostatic lens, which produces a rotationally symmetrical electric field makes it possible to focus the photoemitted electron beam. A static electric field of 20000 V is applied between the sample, mounted on a piezoelectric stage, and the objective (distant at 4 mm). This field accelerates the emitted electron beam and thus increases the lateral resolution (the chromatic aberrations of the objective lens generate a wide distribution of the kinetic energy of the electrons).

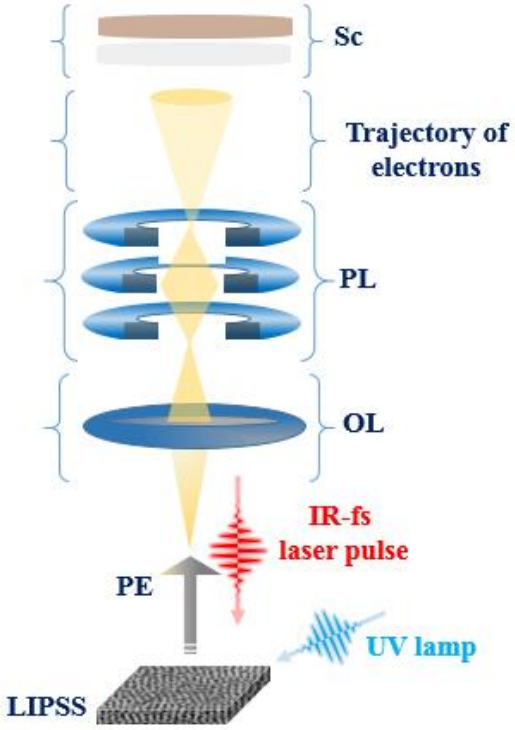

Fig. 3.11 PEEM channel employed in our work to probe LIPSS pre-structured on a Ti sample. PE represents photoelectrons emitted from the surface, OL objective lens, PL projective lens and SC screen.

The hot spots originating from high roughness centers which emits high energetic photoelectrons may mask those of lower energy. To overcome this problem, the cross-correlation between a 3PPE-PEEM image, with a hot spot carefully chosen is required, which gives a fingerprint of all the emitting sites. The cross-correlation technique is an effective analysis tool, notably when noise is present in the image. This technique accounts for the determination of the normalized cross-correlation between a reference image (3PPE-PEEM in our case) and a mask (a hot spot). The purpose of this step is to identify the occurrences of the mask on the reference image. A visualization of an image treated with this technique is displayed in figure 3.12. The topography in fig 3.12a corresponds to a site pre-irradiated with 20 laser shots at 0.24 J/cm², where LSFL are formed. Photoelectrons with different intensities can be seen emitted from different locations, where hot spots originating from high energetic photoelectrons can mask those of lower energy. In order to reveal all the emitting centers, a cross-correlation of the 3PPE-PEEM image with a mask is performed, which imprints all the emitting centers, as shown in fig 3.12b.

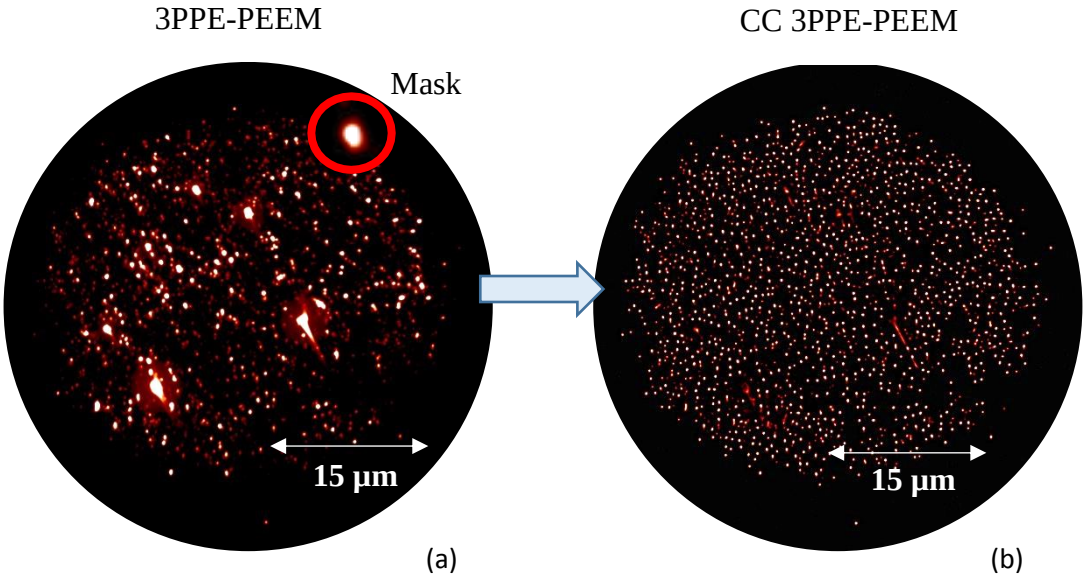

Fig 3.12 Cross-correlation CC technique employed in order to reveal all the emitting centers of a site pre-structured with LSFL at 20 laser shots and 0.24 J/cm². (a) 3PPE-PEEM image where hot spots of high intensity mask those of lower intensity. (b) CC 3PPE-PEEM image imprinting all the emitting centers.

3.4 Conclusion

In this chapter, we have described the different experimental tools employed in this work that allow to investigate the competition between laser-induced privileged order of matter and microstrucutal defects. The first part was dedicated to sample polishing (mechanical and electrolytical polishing) and surface preparation for laser irradiation. The second part accounted for the laser chain components description, followed by the illustration of the laser setup that enables one-color fs-double pulse generation using a Mach-Zehnder interferometer, and a single pulse use of the laser setup. We have also shown laser fluence determination using Liu method. Laser-induced surface modification were analyzed using a scanning electron microscope and an atomic force microscope for topographical examination. Surface characterization of defects was assisted by electron backscattered diffraction, while in-depth characterization was carried out using a transmission electron microscope, after thin lamellas extraction by focused ion beam technique. Finally, the study of dynamical topographies was performed by a photoemission electron microscope, which enable to investigate the dynamics of LIPSS formation. These devices will be used in the next chapters, presenting all the obtained results.

Chapter 4

Laser-induced surface roughness contribution on HSFL formation

In this Chapter, the surface structures generated by a single pulse irradiation are investigated experimentally and computationally for laser fluences that produce high spatial frequency nanostructures in the multi-pulse irradiation regime for bcc materials. We combine experimental characterization of HSFL generated on monocrystalline Cr targets with surface orientation of (100) and (110) with a thorough computational analysis of the laser-induced spallation process based on a MD simulation of a (100) Cr target performed by Eaman Abdul-Karim in Leonid Zhigilei group at the university of Virginia. The results of this joint study support the notion of a strong connection between the frozen surface morphology predicted in the simulation and the pulse-to-pulse evolution of surface roughness observed in the experiments. The spallation-induced roughness provides favorable conditions for positive feedback promoting the HSFL formation. The dependence of the HSFL formation on the crystal orientation is likely to be related to differences in the characteristics of surface morphology generated by the first laser pulse. These results have been published in Applied Physics A by A. Abou-Saleh et al. (2018)[6].

4.1 Objectives and experimental methods

In the spallation regime, the roughening of the surface generated by the first laser pulse may increase surface absorption and activate a feedback mechanism driving the evolution of the initial random surface roughness towards the periodic ripples that maximize the laser energy absorption. The initial roughness generated by the first pulse, therefore, may play an important role in defining the LIPSS formation by subsequent repetitive laser irradiation. The characteristics of the nanoscale surface morphology generated by laser spallation are defined by a complex interplay of the laser-induced melting, nucleation and percolation of subsurface voids in the molten part of the target, formation of a transient foamy structure of liquid regions connecting the spalled layer with the bulk of the target, followed by breakup and rapid freezing of the transient liquid structures

In the first part, two monocrystalline samples having different surface orientations defined by Miller indexes (100) and (110) were irradiated. The two samples were first mechanically then electrolytically polished, which yields a surface roughness of about ~5 nm before irradiation. A Titanium-Sapphire femtosecond laser system (Legend Coherent, Inc.) operated at a central wavelength of 800 nm with a pulse duration of about 50 fs was used to irradiate Cr samples at a repetition rate of 1 kHz under air pressure. Laser pulses were linearly polarized and attenuated through a pair of neutral density filters before being focused onto the sample surfaces through normal angle of incidence. Laser induced surface modification was analyzed using scanning electron microscope and an atomic force microscope, presented in chapter 3.

4.2 LIPSS formation on Cr

4.2.1 High-dose irradiation regime and different types of periodic surface structures

Since low spatial frequency LIPSS require a relatively high number of laser pulses to promote positive feedback, a Cr sample with (100) surface orientation has been irradiated with 30 pulses and incident fluence of 0.3 J/cm², below the single pulse phase explosion threshold. A complex arrangement of surface topography generated by the laser pulses can be seen in the SEM images shown in Fig. 4.1. As already presented in chapter 1, four types of LIPSS that differ by their orientation and periodicity can be distinguished in the images, namely, the Far Field perpendicular (ff$_{\perp}$), Far Field parallel (ff$_{//}$), Near Field perpendicular (nf$_{\perp}$) and Near Field parallel (nf$_{//}$), where the parallel and perpendicular refer to the ripple orientation with respect to the laser beam polarization.

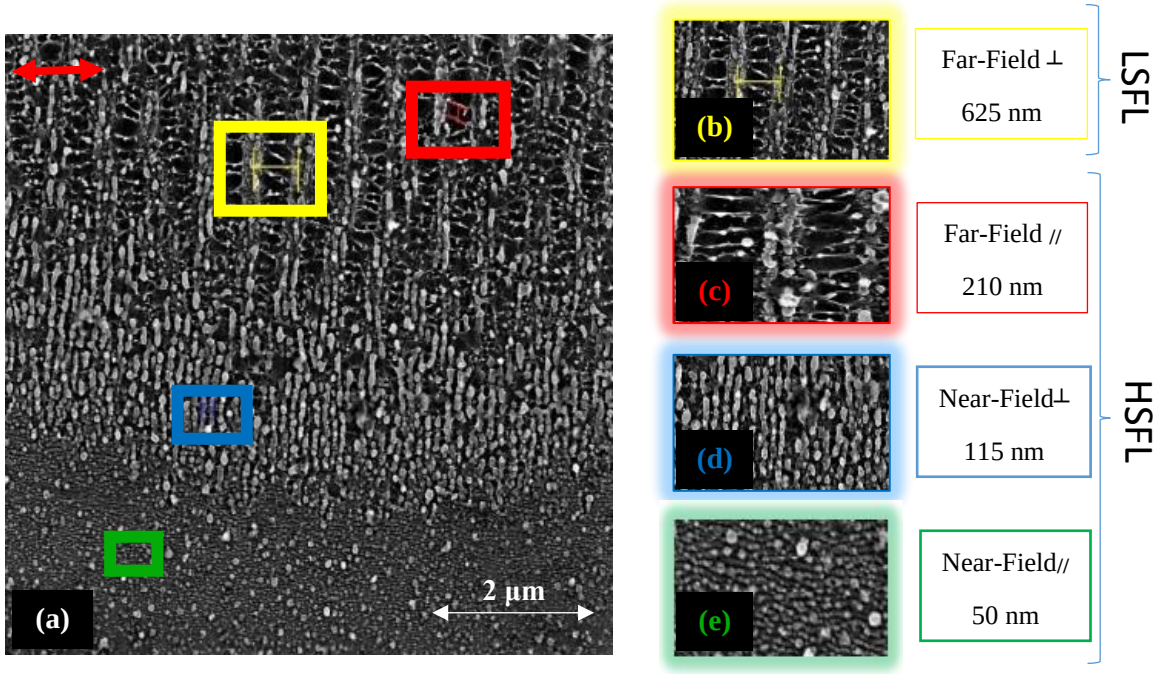

Fig. 4.1 SEM micrographs representing different types of LIPSS generated on (100) Cr target irradiated by 30 pulses at an incident laser fluence of 0.3 J/cm², about 10% below the single pulse phase explosion threshold, F_{th}. (a) A large part of the laser spot where all types of LIPSS are present. (b) LSFL (FF⊥) structures with period of ~625 nm, close to laser wavelength. (c) HSFL (ff$_{//}$) structures formed between LSFL structures. (d) HSFL (nf ⊥**)** structures formed on the periphery of LSFL. (e) HSFL (nf$_{//}$) structures formed on the periphery of the spot, with periods much smaller than the laser wavelength. The direction of linear laser beam polarization is indicated by the red double arrow in the top left corner of (a). This image is identical to fig 1.1c.

The origin of these structures and physical mechanisms leading to their formation can be ascribed to coherent interference between scattered waves and refracted near and far fields as evidenced by recent electromagnetic calculations[5]. In other words, different scattering conditions (near field enhancement, scattered far-field superposition, coherent superposition with incident beam, *etc*.) resulting from different local roughness can provoke different nanoscale rearrangements of material. However, one can mention that several alternative approaches have been proposed in literature to explain the formation of such structures, including surface oxidation and high harmonic generation[12], laser-induced surface plasma waves[208], and surface self-organization[7,104,209]. In this work, we focus our attention on the nf$_{//}$ structures, since they appear upon exposure to a low energy dose and more generally for a low number of laser pulses. In fact, for a high number of laser pulses, the concept of scattered wave becomes questionable. The analysis of the experimental observations for one or two laser pulses is addressing the onset of the LIPSS formation and allows for a more direct comparison with the results of modeling reported in section 4.4.

4.2.2 Low-dose irradiation regime: HSFL formation on Cr (100) and Cr (110)

The formation of $nf_{//}$ LIPSS is observed for a narrow range of laser fluences below the phase explosion threshold for single pulse irradiation. The structures discussed in this work are generated at an incident fluence of 0.3 J/cm², which is defined as the "peak fluence" of the Gaussian laser pulse obtained by dividing the total optical energy by $\pi\omega^2/2$, where ω is the Gaussian beam waist[161]. The values of single pulse ablation threshold fluence, F_{th}, determined for two monocrystalline samples with different surface orientations are very similar to each other, 0.33 J/cm² for (100) and 0.32 J/cm² for (110) surfaces. Recent results of ab initio calculations reveal that the optical properties of Cr are not sensitive to the surface crystal orientation and do not exhibit large variation in the range of electron temperatures realized under irradiation conditions considered in this study[210]. The absorbed fluence, therefore, can be estimated using a constant value of reflectivity of Cr at 800 nm, R = 0.55[211], which yields ~0.13 J/cm² for the incident fluence of 0.3 J/cm² used in the experiments. This value of the absorbed fluence is in the range between the spallation and phase explosion thresholds predicted in atomistic simulations performed for Cr targets[50], 0.10 J/cm² and 0.28 J/cm², respectively.

Laser induced surface modification generated on two targets with (100) and (110) surface orientation by irradiation with two laser pulses at an incident fluence of 0.3 J/cm² is analyzed in Scanning Electron Microscope (SEM), with representative images shown in Fig. 4.2.

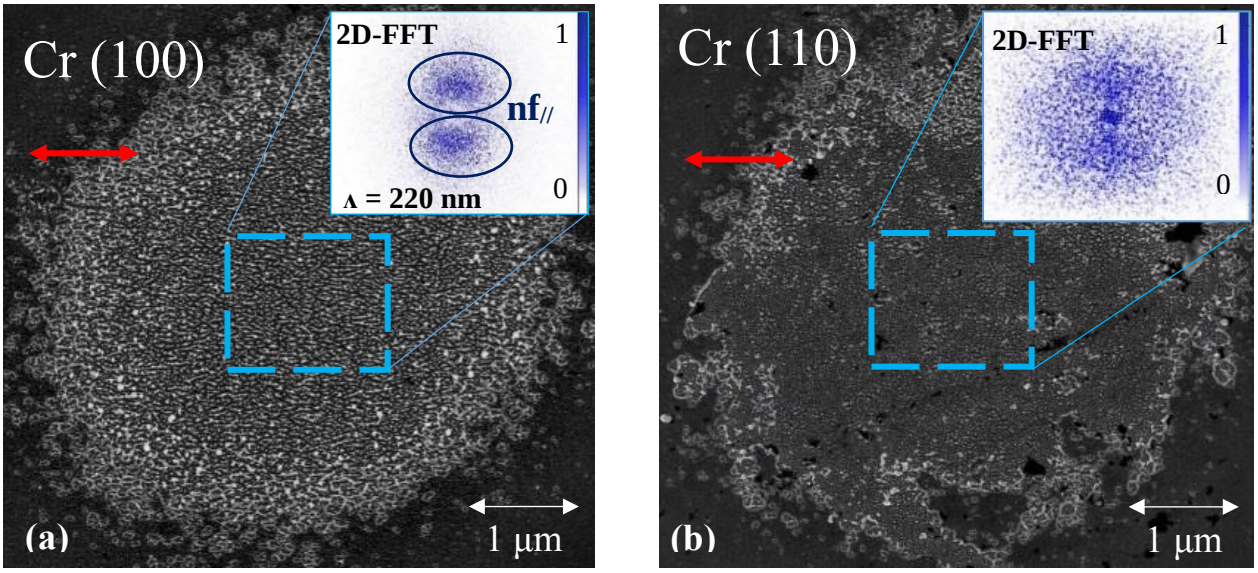

Fig. 4.2 SEM micrograph of Cr targets with (a) (100) surface orientation and (b) (110) surface orientation irradiated by 2 laser pulses at an incident fluence of 0.3 J/cm² , *i.e.*, about 10% below the single pulse phase explosion threshold, F_{th}. The direction of linear laser beam polarization is indicated by the red double arrows. Insets in both images show FFT of the surface topography for regions outlined by the green dashed squares.

The mere visual analysis of the SEM images suggests that elongated surface structures parallel to the direction of the laser beam parallelization are formed in the center of the laser spot on (100) surface, but are absent on (110) surface. In order to highlight this difference, the two-dimensional (2D) fast Fourier transform (FFT) amplitude was calculated for regions within the laser spots outlined by blue dashed squares in Fig. 4.2. Two similar symmetric zones can be identified

on the FFT plot shown as an inset in Fig. 4.2a for the laser-processed (100) surface, indicating the presence of $nf_{//}$ structures parallel to laser polarization with periodicity of about 220 nm. It is worth noting that for small number of pulses, i.e. under conditions of minimal feedback, the transient surface topography favors $nf_{//}$ structures exhibiting periodicities larger than those generated by multi-pulse feedback irradiation. For (110) surface, the FFT image shown in the inset of Fig. 4.2b exhibits a larger dispersion of the FTT peaks and reflects a much weaker tendency towards the HSFL formation, as compared to (100) surface.

The strong dependence of the generation of $nf_{//}$ structures on the crystallographic surface orientation can be related to the hypothesis that the HSFL result from superposition of waves scattered by roughness centers and implying local field enhancement[5,111]. Most studies agree that surface roughness is necessary to initiate the LIPSS formation. Furthermore, a sufficiently rough surface is needed to support the excitement of a surface wave and to cause instability which gives rise to the structuring. In order to investigate the origin of the distinct propensities of targets with (100) and (110) surface orientations to the formation of $nf_{//}$ by two pulse laser irradiation, the information on surface roughening induced by the first laser pulse is needed and is discussed in the following section.

4.3 Spallation-induced roughness generation

As discussed above, the formation of HSFL is likely to be strongly affected by the shapes and size distribution of surface features generated by the first laser pulse. Thus, the surface roughness produced by a single laser pulse irradiation of (100) and (110) Cr targets is analyzed here for the same laser fluence (between the thresholds for spallation and phase explosion) that is used in the 30- and 2-pulse surface modification discussed in the previous sections. The surface topography in the centers of the laser-modified regions is characterized by the Atom Force Microscope (AFM), and representative AFM micrographs are shown for the two samples in Fig. 4.3. A statistical parameter that can be used to characterize the randomness of laser-generated surface roughness and sharpness of surface spikes is kurtosis (sku). This parameter is larger than 3 for "spiky" surfaces, lower than 3 for "bumpy" surfaces, and equal to 3 for completely random surface roughness. The more peaks a laser modified surface has, and the sharper the peaks are, the higher is the sku value of the surface. The sku values evaluated for (100) and (110) surface orientations are 5.59 and 1.97 respectively. These values are consistent with qualitative observations one can make from the visual analysis of Fig. 4.3, where the fine nanoscale roughness observed for (100) surface is in a sharp contrast with a much coarser roughness of the (110) surface dominated by large bumps and flat-top mesas. Morphological features induced by the first pulse on the (100) orientation are connected by nanorims with length ranging from 10 to 16 nm, as shown in Fig. 4.3d. This important observation provides a strong support to the hypothesis that the spiky character of roughness generated by the first laser pulse irradiation of (100) surface plays a key role in the activation of the scattering mechanism leading to the formation of $nf_{//}$ structures, whereas a much smoother (110) surface emerging from the first pulse irradiation is less amenable to the HSFL formation.

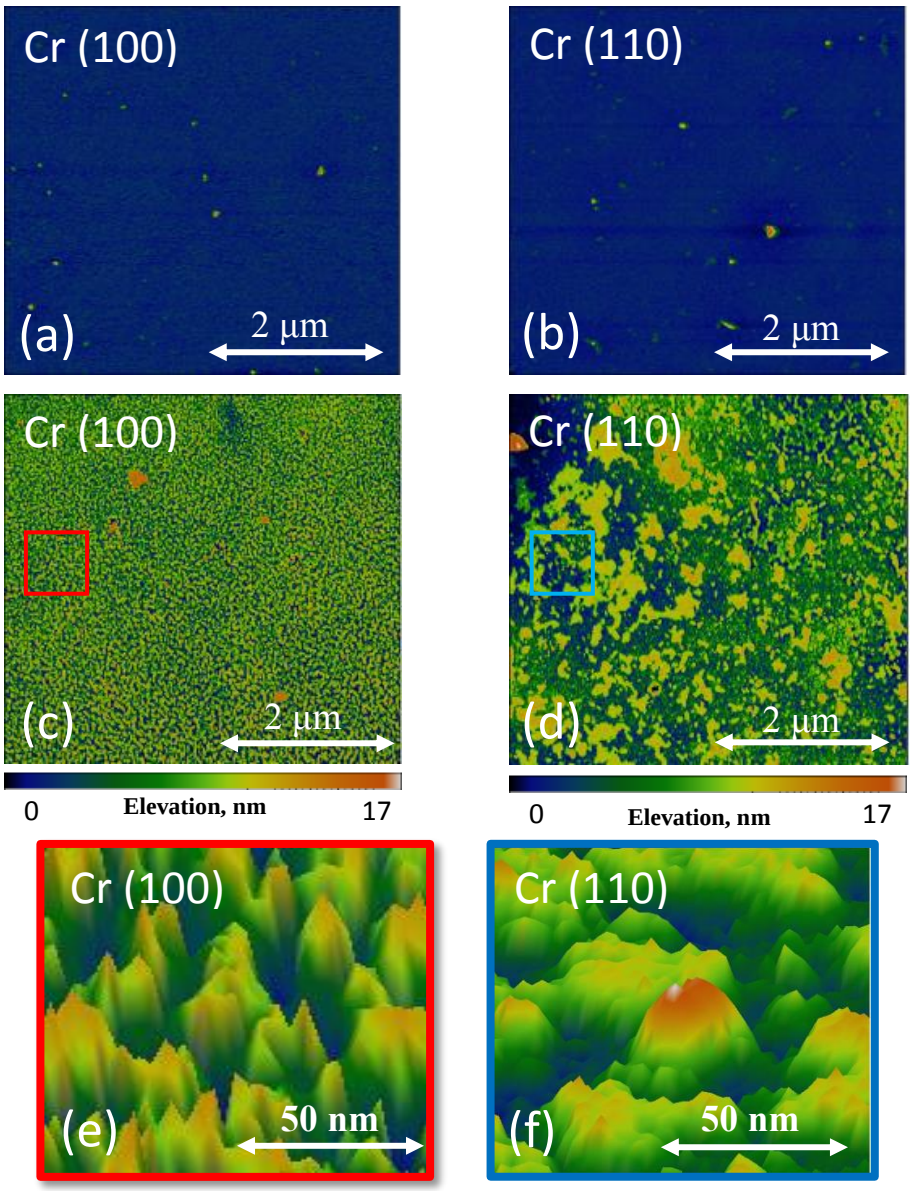

Fig. 4.3 AFM micrographs of Cr targets before and after single pulse laser irradiation. (a,b) Targets with (100) and (110) surface orientations before laser irradiation. (c,d) Targets with (100) and (110) surface orientation irradiated at an incident fluence of 0.3 J/cm², i.e., about 10% below the single pulse phase explosion threshold, F_{th}. (e,f) 3D view of surface topography shown for regions outlined by the red and blue squares in (c,d) respectively.

In order to elucidate the physical mechanism responsible for the creation of the initial surface morphology by a single pulse laser irradiation, a large-scale atomistic simulation of laser interaction with a (100) Cr target is performed for irradiation conditions similar to those used in the experiments.

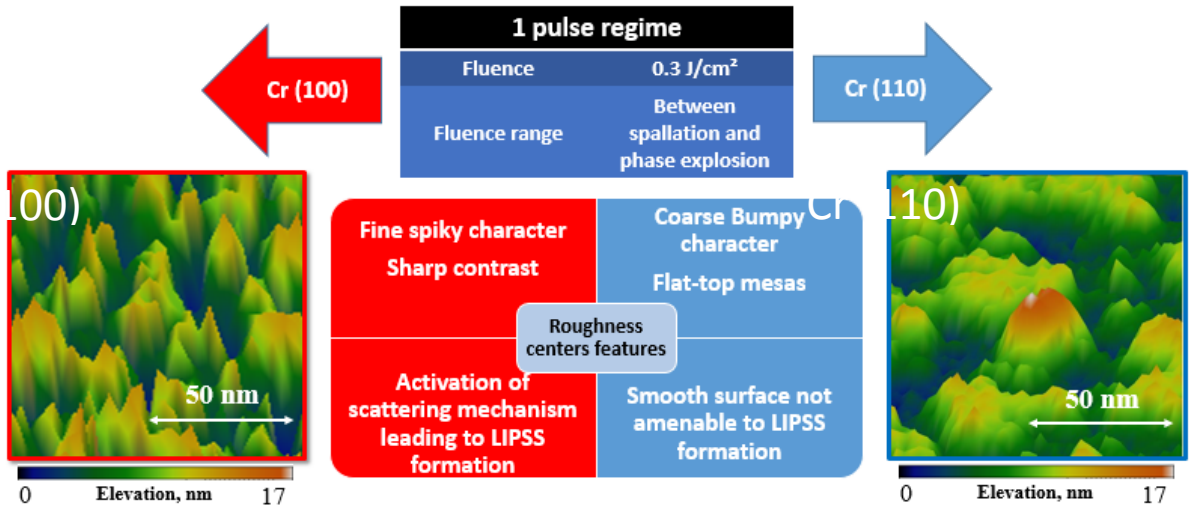

Fig. 4.4 A summary about spallation-induced roughness generation on Cr(100) and Cr(110).

4.4 Large-scale atomistic simulation of laser spallation

The large-scale atomistic simulation and calculations were performed by the group of Leonid Zhigilei at the University of Virginia.

4.4.1 Numerical methods

The large-scale atomistic simulation aimed at revealing the processes responsible for the formation of surface roughness in the spallation irradiation regime are performed for a Cr target with (100) surface orientation irradiated by a 50 fs laser pulse at an absorbed fluence of 0.11 J/cm^2, which is only ~10% above the spallation threshold. The simulation is performed with a hybrid atomistic–continuum model, which combines the atomistic MD representation of laser-induced structural and phase transformations with a continuum-level description of the electron sub-system based on the two-temperature model (TTM). A complete description of the combined TTM-MD model is provided in Refs.[49,72,212], whereas the parameterization of the model for Cr is described in Refs.[50,71]. Below, we only provide a brief description of the computational setup used in the simulation results reported here.

The interatomic interactions are described by the embedded atom method (EAM) potential parametrized for Cr[71]. The potential provides a relatively accurate and computationally inexpensive description of Cr experimental properties, including lattice parameter, cohesive energy, elastic constants and their temperature dependence, melting temperature, and vacancy formation energy. To ensure a realistic representation of the spallation process and generation of nanoscale surface morphology, the simulation is performed for a large system (~126 million atoms) with lateral (parallel to

irradiated surface) dimensions of 100 × 100 nm^2 and the depth of the surface region of the target represented with atomic resolution equal to 150 nm. Periodic boundary conditions are applied along the lateral directions, a free boundary is used at the top surface of the target, and a pressure-transmitting boundary condition[71,213–215] is imposed at the bottom of the atomistic part of the system. The TTM part of the model extends down to 1 μm to ensure the absence of any significant increase in the electron or lattice temperatures at the bottom of the computational domain by the end of the simulation. The thermophysical properties of Cr entering the TTM equations (electron-phonon coupling, electron heat capacity, and thermal conductivity) are described in Ref.[71]. Irradiation by a 50 fs laser pulse is represented through a source term added to the TTM equation for the electron temperature [212], with an optical penetration depth of 15 nm at a laser wavelength of 800 nm[211] assumed in the simulation.

4.4.2 Surface roughness generated in the spallation regime

The general mechanisms responsible for the material ejection in regime of photomechanical spallation has been studied in a number of earlier computational studies, *e.g.*[49,50,72,214–220], although the analysis of surface morphology produced by the spallation process has been hampered by the short length- and time-scales of most of the atomistic simulations reported so far. Here, we first briefly review the mechanisms of the laser spallation and then focus on the analysis of the surface morphology enabled by the relatively large scale of the simulation reported in this work.

The thermodynamic conditions leading to laser spallation are illustrated by the contour plots of the spatial and temporal evolution of density, temperature, and pressure in the surface region of the irradiated target shown in Fig. 4.5. The black lines in the contour plots separate the transiently melted surface region from the crystalline part of the target. The laser excitation of the conduction band electrons is followed by fast electron-phonon equilibration and leads to a rapid increase of the lattice temperature in the surface region of the target from 300 K to ~3700 K during the first 5 ps after the laser pulse, Fig. 4.5b. The rapid heating causes prompt homogeneous melting of a 36-nm-deep surface region of the target superheated above the limit of crystal stability[53,212,221]. The laser energy deposition and equilibration occur under conditions of so-called inertial stress confinement, *i.e.*, on a timescale that is shorter than the time required for the mechanical relaxation (expansion) of the heated surface region[216,222]. The almost constant-volume heating results in the generation of compressive stresses, while the interaction of the laser-induced compressive stresses with the free surface of the irradiated target produces a tensile component of the stress wave propagating into the bulk of the target, as can be seen from the pressure contour plot in Fig. 4.5c. At a certain depth under the surface, the tensile stress exceeds the dynamic strength of the molten material and leads to the nucleation and growth of subsurface voids in a process that is commonly called the laser induced cavitation or spallation[8,216,223]. The appearance of voids is reflected in the density contour plot shown in Fig. 4.5a, where the reduction of density is first observed at about 30 ps after the laser pulse. The low-density region expands with time, as the voids grow, coalesce, percolate, and eventually produce an array of elongated liquid bridges that connect the bulk of the target to a top molten layer accelerated in the direction away from the target by the initial relaxation of laser-induced stresses.

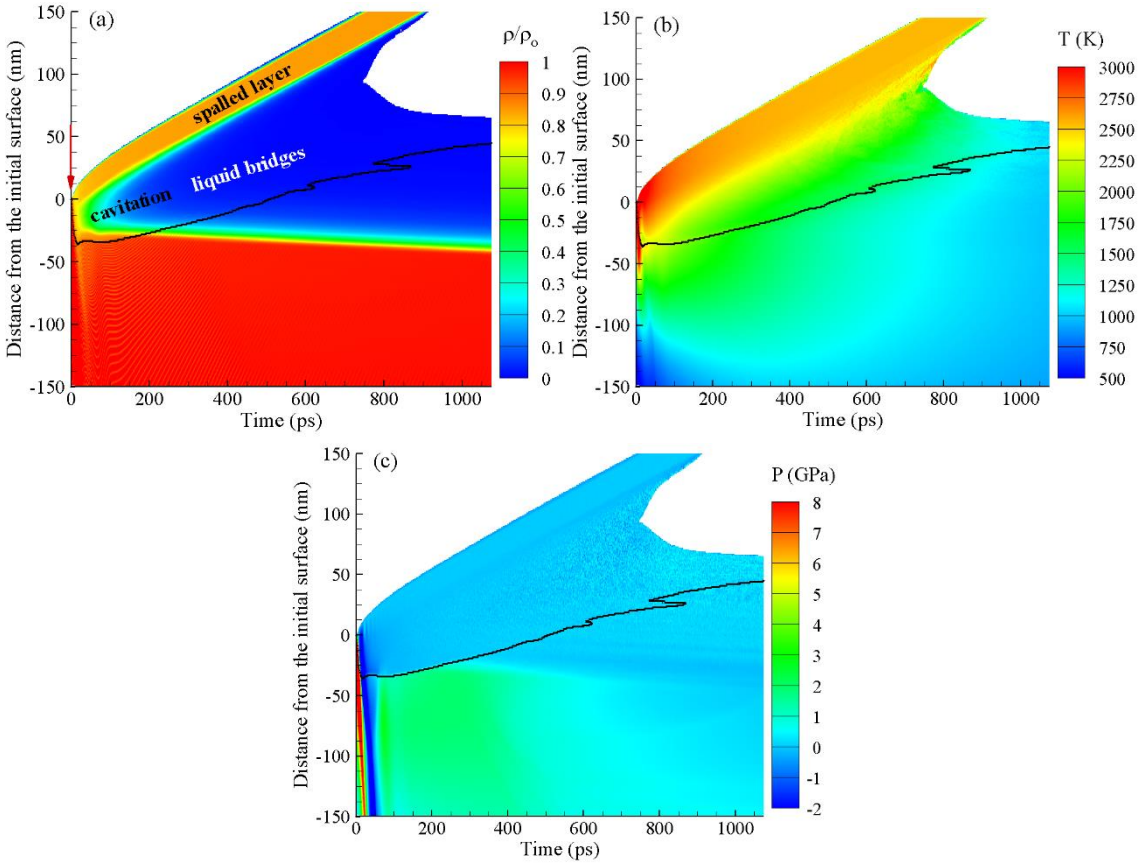

Fig. 4.5 Contour plots of the spatial and temporal evolution of (a) density, (b) temperature, and (c) pressure, in a large-scale TTM-MD simulation of a bulk (001) Cr target irradiated by a 50 fs laser pulse at an absorbed laser fluence of 0.11 J/cm^2, ~10% above the spallation threshold. The laser pulse is directed along the Y-axis as shown by the red arrow in (a). The black line separates the melted region from the crystalline part of the Cr target. The visual picture of the sub-surface "cavitation" region evolving into an array of "liquid bridges" connecting the "spalled layer" with the rest of the target can be seen in Fig. 4.6.

The extension of the liquid bridges hardly decelerates the top layer that continues to move away from the target at an almost constant velocity of ~180 m/s. The elongation of the liquid bridges proceeds simultaneously with solidification of lower parts of the bridges adjacent to the target, as evidenced by the extension of the black line marking the location of the solidification front in Fig. 4.5 into the low-density region that corresponds to the liquid bridges. The upward motion of the molten layer leads to eventual breakup of the liquid bridges and complete separation of the layer from the target by ~750 ps.

The visual picture of the processes described above is provided by a series of snapshots of atomic configurations taken at different times in the course of the simulation and shown in Fig. 4.6. The snapshots illustrate the appearance of a large number of voids in the molten part of the target by 50 ps, the evolution of the cavitation region into a "forest" of liquid bridges by 200 ps, and the breakup of the bridges upon further upward motion of the top molten layer. Only a small number of gas phase atoms can be seen inside the growing sub-surface voids, thus providing further evidence for the photomechanical nature of the cavitation/spallation process, *i.e.*, the driving force for the nucleation and growth of the voids is the relaxation of the laser-induced stresses rather than the vapor pressure in the boiling process.

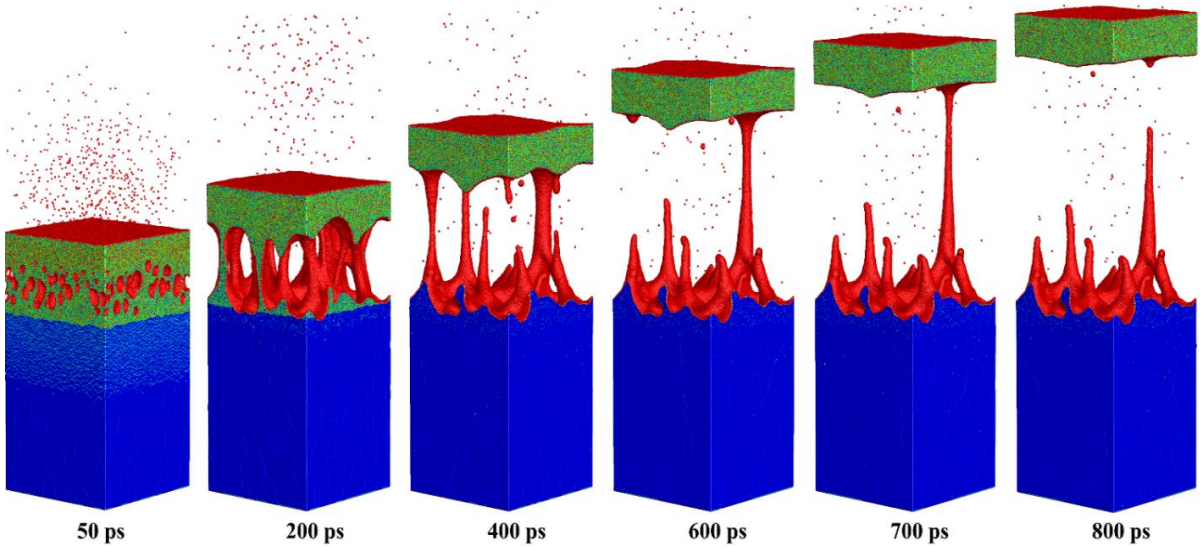

Fig. 4.6 Snapshots of atomic configurations obtained in a TTM-MD simulation of laser spallation of a bulk (001) Cr target irradiated with a 50 fs laser pulse at an absorbed laser fluence of 0.11 J/cm^2. The laser pulse is directed from the top of the images. The atoms are colored according to their potential energies: the dark blue regions represent the bcc Cr structure, green regions correspond to the molten Cr, and the atoms at the top surface of the target and at the internal surfaces appearing in the spallation process are colored red. The light blue stripes that can be seen in the crystalline part of Cr target at 50 ps and disappear at later time represent the unstable stacking faults[71] transiently appearing in the system in response to the uniaxial expansion caused by the dynamic relaxation of the laser-induced stresses.

In contrast to the smaller-scale simulations, where the voids quickly "outgrow" the lateral size of the computational cell and self-interact to promote a prompt separation of the top liquid layer shortly after the void nucleation, *e.g.*,[212,216,218,219], the evolution of voids illustrated in Fig. 4.6 takes longer time and proceeds through the formation of a transient foamy structure of interconnected liquid bridges connecting the upper 27-nm-thick liquid layer with the rest of the target. The size of the largest elongated void and the distances between the liquid bridges are substantially smaller than the lateral size of the computational cell, suggesting that the size effects and the periodic boundary conditions are not introducing any major artifacts into the dynamics of the spallation process. This enables us to continue the simulation until the time of complete resolidification of the surface region and to perform analysis of the final surface morphology generated in the spallation process, which is reported in the next section.

4.4.3 Surface roughness generated in the spallation process

The nanoscale surface morphology generated in the spallation process is illustrated in Fig. 4.7 where a side and a top views of the surface structure are shown for a time of 1056 ps, when eight out of nine surface spikes produced via the spallation and breakup of the liquid bridges are already completely crystallized.

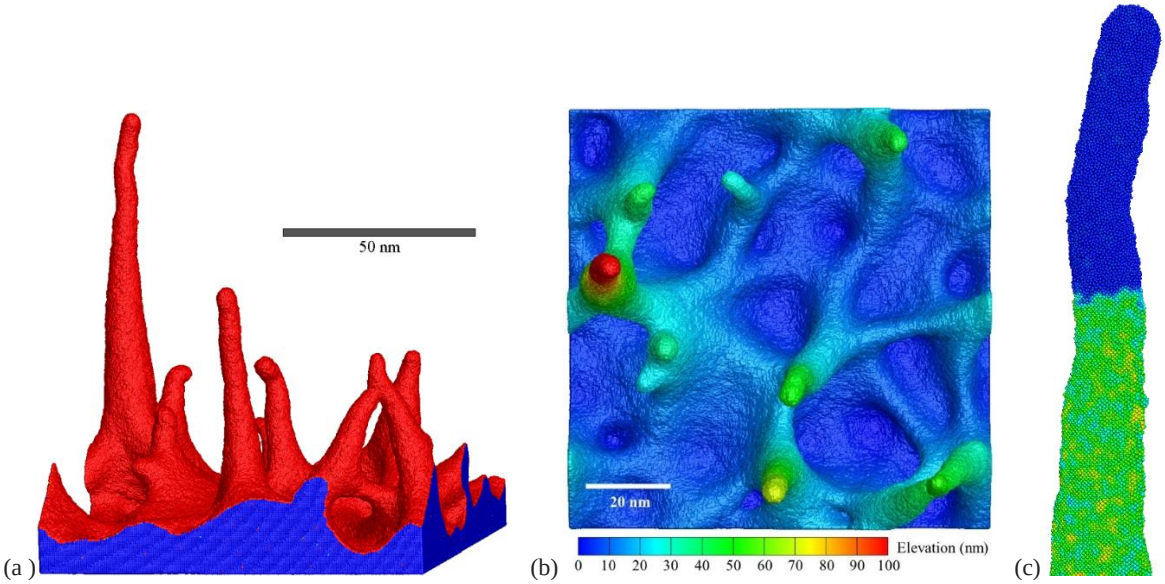

Fig. 4.7 Side (a) and top (b) views of the frozen surface morphology generated in a TTM-MD simulation of laser-induced photomechanical spallation of a bulk (001) Cr target irradiated with a 50 fs laser pulse at an absorbed laser fluence of 0.11 J/cm^2. The 100×100 nm^2 surface region features nine solidified spikes with length ranging from 12 to 110 nm. An enlarged view of a top 40 nm part of the tallest spike is shown in (c). The atoms in (a) are colored according to their potential energies with the same coloring scale as in Fig. 4.5. In (b), the atoms are colored according to their elevation with respect to the initial level of the surface. In (c), the atoms are colored by the local order parameter, so that the lower crystalline part (green) could be clearly distinguished from the top part that remains amorphous (blue).

The characteristic morphological features present on the surface include nine spikes with the length ranging between 12 and 110 nm, nanocavities, nanoprotrusions, and nanorims connecting the spikes and outlining the nanocavities. Several small subsurface voids are also present at the base of some of the frozen spikes (not visible in Fig. 4.7 but revealed in the detailed analysis of the resolidified targets). Eight out of the nine spikes are fully crystallized through the rapid propagation of the crystal-liquid interface from the bulk of the single crystal target.

The crystallization front accelerates with increasing undercooling, reaches its maximum velocity of ~150 m/s at a temperature of about $0.75T_m$, and then slows down as the temperature continues to drop further after the separation of the spalled layer from the liquid bridges. By the time of 1056 ps, for which the images are shown in Fig. 4.7, only the top 20 nm part of the tallest spike remains disordered, as can be seen from the enlarged view of the tip of the spike in Fig. 4.7c. The atoms in Fig. 4.7c are colored by the local order parameter[212], so that the front of the epitaxial crystallization could be clearly identified. The crystallization front is still moving upwards, and one can expect complete crystallization of the spike within the next nanosecond. Note that despite the disordered structure of the tip of the tallest spike, its shape does not undergo any significant changes following the formation of the spike through the breakup of the liquid bridge (compare snapshot for 800 ps in Fig. 4.6 with Fig. 4.7a). This observation can be related to the rapid drop of the temperature of the spike (and corresponding increase in viscosity), which is already as low as $0.45T_m$ at the end of the simulation.

The surface morphology predicted by the TTM-MD simulation of laser spallation of Cr target is consistent with the results of experimental imaging of nanoscale surface roughness produced in femtosecond laser processing of different

metals, *e.g.*, Cu[224,225], Au[226], Ag[227], and W[228]. The surface structures observed in the experiments feature elongated frozen nanospikes, nanorims and nanocavities, which are very similar to the simulated surface morphology shown in Fig. 4.7. The characteristic sizes of the surface features, however, are sensitive to the properties of target material and irradiation conditions (number of laser pulses and relative magnitude of the laser fluence with respect to the spallation threshold), thus hindering the establishment of direct quantitative links between the computational predictions and the experimental data. The coordinated computational – experimental study of Cr targets irradiated in the same spallation regime, reported in this work, provides an opportunity to bring the connection between the modeling predictions and experimental observations to the quantitative level. In particular, the inspection of the AFM image shown for Cr (100) surface in Fig. 4.3c,d indicates that several frozen spikes with heights exceeding 10 nm are present on an area with dimensions of 100 × 100 nm^2, which is in a good agreement with the surface morphology shown for the same surface area in Fig. 4.7b

A number of possible explanations have been suggested in literature for the formation of surface nanostructures on metal surfaces irradiated by femtosecond laser pulses. A possible spatial variation of the absorbed laser energy (due to the inhomogeneity of the incident laser beam, the enhanced absorption by surface defects, or the interference of the incident laser light with surface scattered waves), leading to the formation of localized nanoscale melted regions and redistribution/expulsion of the molten material driven by the temperature gradients is suggested as the origin of nanoscale surface morphology in Ref.[224]. The possible role of heterogeneous melting of the irradiated surface is discussed in Ref.[228], while the relaxation of laser-induced stresses and spallation are highlighted in the analysis reported in Refs.[225,227].

The results of the simulation presented in this work provide a convincing evidence in favor of the scenario where the nanoscale surface roughness appears as a result of spallation proceeding simultaneously with rapid resolidification of the transiently melted surface region of the target. The generation, coarsening, and percolation of subsurface voids in the molten part of the target lead to the formation of liquid bridges and vertical walls separating the voids, see, *e.g.*, a snapshot for 200 ps in Fig. 4.6. As the top molten layer moves away from the target, the liquid walls and bridges break up and retract due to the action of the surface tension. The breakup of the liquid bridges, however, proceeds simultaneously with the advancement of solidification front from the bulk of the target, which captures and freezes the transient liquid structures generated in the dynamic spallation process. Actually, the solidification front reaches the base of the liquid bridges as early as ~200 ps, as manifested by the black line entering the low-density region in Fig. 4.4a and the blue (crystalline) region extending into the bridges by 400 ps in Fig. 4.6. By the time the liquid bridges break up and the spalled layer separates from the target (~750 ps), some of the smaller nanospikes are already completely solidified and only the longest ones remain partially melted. The competition of the evolution of the shapes of the liquid parts of the spikes driven by the minimization of the surface energy with the rapid solidification is defining the final shapes of the nanospikes. In particular, the bent shapes of the nanospikes clearly visible in Fig. 4.7a, as well as spherical "heads" that would form if the solidification would be slightly slower, are commonly observed in the experimental images[224–226,228]. Note that in addition to the advancement of the solidification front from the bulk of the target observed as the only solidification mechanism in the simulation reported in this paper, an additional contribution from the

homogeneous nucleation of new crystallites is possible if a sufficiently strong undercooling is reached in the liquid parts of the nanospikes, as has been demonstrated for Ag in Ref.[72].

The mechanistic insights into the formation of frozen surface features obtained in the simulation of laser spallation of a (100) Cr target also provide a hint to the possible explanation of the strong dependence of the surface topography on the crystallographic orientation of the irradiated surface. The velocity of crystallization front propagation is faster for (100) crystal-liquid interface as compared to more densely packed (111) or (110) interfaces[229], while the optical absorption, melting depth, and magnitude of the laser-induced pressure wave are not expected to exhibit a strong orientational dependence. The slower solidification front propagation for the densely packed interfaces leaves more time for the surface tension to smooth out the molten surface features generated by the breakup of the liquid bridges to the spalled layer.

4.5 Conclusion

The physical mechanisms responsible for the formation of HSFL in femtosecond laser interactions with metal surfaces are investigated in a joint experimental and computational study that combines a detailed analysis of surface morphology produced by 30, 2, and 1 pulse irradiation of monocrystalline Cr samples with a large-scale molecular dynamics simulation of laser interaction with a Cr target performed in the same irradiation regime. The electron and atomic force microscopy analysis of the irradiated surfaces reveals that the material response to the first laser pulse is strongly dependent on crystallographic surface orientation, with (100) Cr surface exhibiting the formation of higher and more refined nanoscale surface roughness as compared to (110) surface. The higher surface roughness generated by the first laser pulse activates scattering of the laser light and the local field enhancement upon irradiation by the second laser pulse, leading to the formation of much more pronounced high spatial frequency structures on the (100) surface as compared to (110) one. When applying additional laser pulses, different types of periodic surface structures start to emerge due to the interference between the incident laser light and waves scattered by roughness centers strengthening specific periodicities by positive feedback. The appearance of the periodic surface structures, therefore, can be traced back to the initial surface roughness generated by the first laser pulse.

To reveal the processes responsible for the formation of the surface roughness by single pulse laser irradiation, a large-scale atomistic simulation is performed by L. V. Zhigilei group at the university of Virginia for a (100) Cr target irradiated in the spallation regime. The simulation provides a detailed picture of the spallation process driven by the relaxation of the laser-induced stresses and leading to the formation of complex nanoscale surface roughness featuring elongated frozen nanospikes, nanorims and nanocavities with dimensions similar to those observed experimentally. The results of the simulation suggest that the characteristics of nanoscale surface morphology are defined by the competition between the evolution of transient liquid structures generated in the spallation process and the rapid resolidification of the surface region of the target. The strong dependence of the surface topography produced in single pulse irradiation experiments on the crystallographic orientation of target surface may be related to the anisotropy of the crystallization

front propagation, which provides more time for the relaxation of molten surfaces when the solidification process is slower. The connection between the initial nanoscale roughness generated by the first laser pulse and the subsequent formation of periodic surface structures, established in the present study, contributes to the progress towards the general goal of untangling the complex multiscale phenomenon of the LIPSS formation. A summary about HSFL formation dependence on crystalline orientation is presented in fig 4.8.

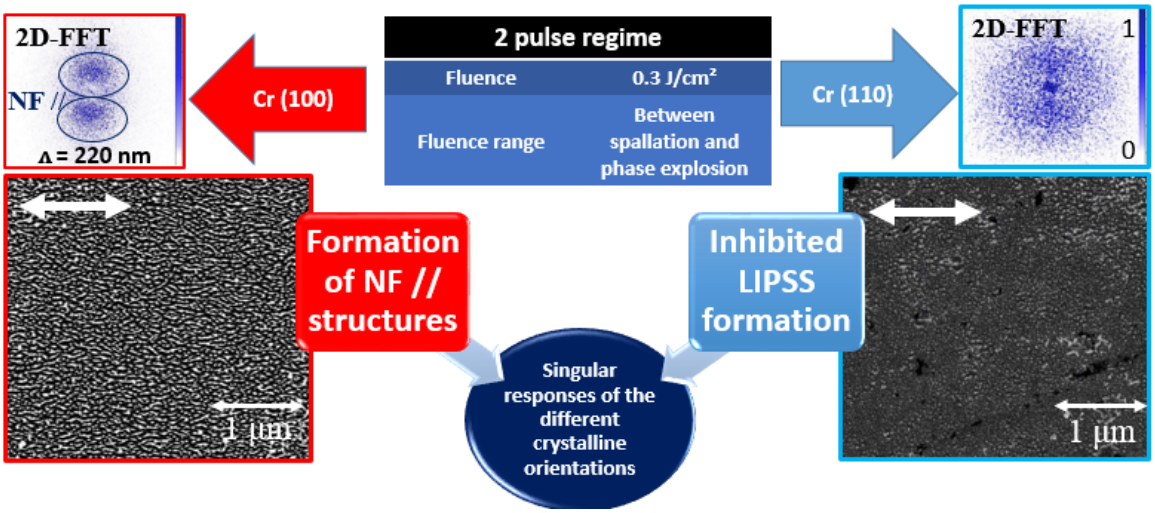

Fig. 4.8 A summary about HSFL formation dependence on crystalline orientation.

Since HSFL formation is strongly crystalline orientation dependent, an attention must be addressed to the microstrucutiral modifications on the surface and beneath it, which constitutes the objective of the following chapter.

Chapter 5

Laser-induced defects dependence on bcc crystalline orientation: a connection to HSFL formation

In this chapter, an experimental characterization and microstructural analysis using electron backscattered diffraction (EBSD) and transmission electron microscope (TEM) of monocrystalline chromium samples having different orientation growth and a polycrystalline Cr irradiated under conditions where defects are produced, is combined with molecular dynamics (MD) simulations of short pulse laser interaction with a bcc metal, having the same orientations as that of the experimental study. MD simulations were performed by the group of Leonid Zhigilei at the University of Virginia. The generation of crystal defects is found to be strongly dependent on crystal orientation, where (110) orientation on bcc materials is more favorable to lattice damage.

"Crystals are like people: It is the defects in them which tend to make them interesting!"- Colin Humpphreys

5.1 Introduction

In ultrashort pulse interaction with metals, the rapid deposition of laser energy may not only provokes fast melting and resolidification of irradiated material's surface, but can trigger also the emission of strong compressive stresses, as discussed in the previous chapter in the case of short pulse laser interaction with a Cr(100) target in the spallation regime. The relaxation of the laser-induced stresses occurring simultaneously with the surface melting and resolidification of the processed target, can promote the onset of high density of crystal defects generation (stacking faults, vacancies, dislocations) along with physical and mechanical properties modification of the surface layer.

An experimental and computational surface investigation of laser-induced roughness in the previous chapter unveiled the singular response of crystalline orientation respecting HSFL generation, connected to the contrast in roughness centers features, where Cr (100) target was more amenable to HSFL formation. The surface analysis performed in the previous chapter is completed in this chapter with an experimental and computational in-depth investigation of laser-induced microstructural modifications on Cr with three different orientations, (100), (110) and (111) in the sub-spallation regime.

The mechanism responsible for the generation of point defects (vacancies), unstable stacking faults as well as dislocations is revealed. The first part of this chapter accounts for an experimental characterization of laser-induced defects employing EBSD and TEM, followed by TTM-MD simulations performed by the group of Leonid Zhigilei at the University of Virginia on similar conditions. The joint study suggests that the generation of crystal defects on the surface and in-depth can influence the surface topography, triggering or not HSFL formation.

5.2 Experimental conditions

In this work, a Cr polycrystalline sample and three Cr monocrystals having different orientation growth, (100), (111) and (110) were irradiated. All samples were polished mechanically firstly, which yields an abundance of scratches, then polished electrolytically, a final pre-irradiation process which gives a surface roughness of about 5 nm for all samples. The one-pulse generation system described in chapter 3 was employed to irradiate Cr samples. The laser operated at a central wavelength of 800 nm, with a pulse duration of 50 fs and a repetition rate of 1 kHz. Ablation threshold was calculated using Liu method[161] described in chapter 3. Ablation thresholds fluence F_{th} of monocrystalline samples are very close for each crystal orientation (0.33 J/cm² for (100) and (111) oriented planes, 0.32 J/cm² for (110) oriented planes). The irradiation fluence was fixed at 0.3 J/cm² for monocrystalline samples, and 0.27 J/cm² for polycristal sample. Laser induced defects were characterized using EBSD system, with operation conditions leading to a probed depth of about 20 nm. In order to investigate laser induced damage beneath the surface, two lamellas were extracted from the center area of the laser spot on (100) and (110) orientations, by the standard focused ion beam (FIB) lift-out technique, and then analyzed in CLYM facility by Thierry Douillard using transmission electron microscope, equipped with a High Angular Annular Diffraction Field (HAADF) detector. The scattering that is collected by the

HAADF detector is proportional to the Rutherford scattering cross-section that has a Z^2 dependence on the atomic number Z of the scattering bulk.

5.3 Laser-induced defects on polycrystalline chromium sample

In order to investigate the response of different crystal orientation to ultrashort laser pulse regarding laser induced defects on a single sample, different regions of a polycristal chromium sample having different orientation growth, (100), (110) and (111) were irradiated with a simple pulse at a peak fluence of 0.27 J/cm², under 10% of the single pulse ablation threshold F_{th} for Cr. Same experimental conditions were applied for all laser impacts. Fig 5.1a shows the zone of interest of the polycristal irradiated with 1-pulse impacts. Color-coded EBSD orientation map, where the color depends on crystal orientation with respect to the surface normal, shows (100) orientation in red, (111) orientation in blue and (110) orientation in green. The standard EBSD color-coding triangle is shown as inset. Band Contrast EBSD tool (BC), which is a measure of the average Kikushi bands intensity with respect to the overall intensity of the Electron Back-Scatter Pattern (EBSP) quality factor, is shown in fig 5.1b for the grain boundary between (111) and (100) orientations, and in fig 5.1c for the grain boundary between (100) and (110) orientations. Each pattern is assigned to a band contrast value, and these values are then plotted as gray levels of pixels making up a map of the scanned area. This is useful in getting a visual estimation of features that cause poor band contrast. BC is scaled from 0 to 255, which represents minimum to maximum contrast difference. 1-pulse impacts on the (110) orientation shows higher marked contrast than (111) orientation. (100) orientation shows no contrast difference. Laser shots impacting the grain boundary between (110) and (100) oriented planes, are cut in band contrast map. In fact, if Kikushi bands have a high intensity with respect to the EBSP overall intensity, the EBSP is of high quality and the BC is assigned a low value which represents a low contrast. If not, EBSP would be of poor quality and results in a high BC value.

This result strongly suggests that defects induced in (110) orientation impacts are deeper and high in density, because Kikushi bands diffraction pattern presents a low quality for 20 keV electron acceleration, which corresponds to a depth of about 20 nm under the surface. This visual observation on a polycrystalline sample needs further confirmation and investigation on monocrystalline samples.

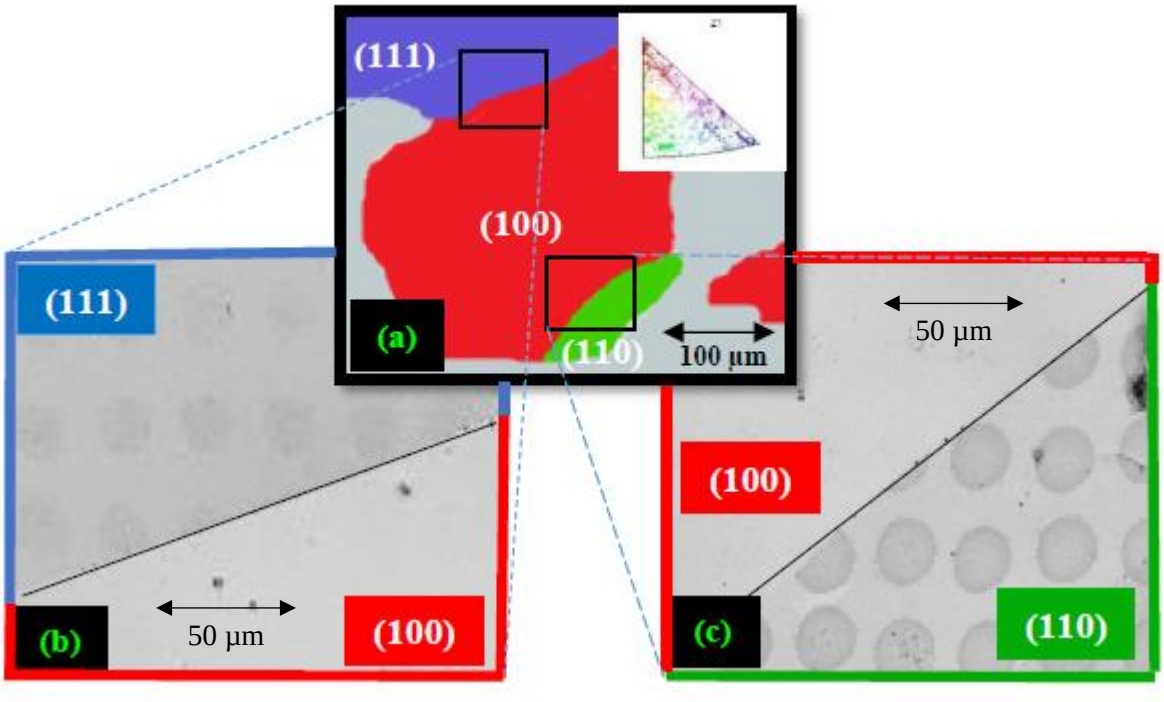

Fig. 5.1 EBSD characterization of a chromium polycrystalline surface irradiated with 1 pulse of femtosecond laser, at 0.27 J/cm² under laser ablation threshold for 1-pulse. (a) Color-coded EBSD orientation map at 10° for the zone before irradiation, showing (111), (100) and (110) orientations. The standard EBSD color-coding triangle is shown as inset in (a). (b) Band contrast map of grain boundary between (111) and (100) orientations. (c) Band contrast map of grain boundary between (100) and (110) orientations. The black lines indicate the grain boundaries between different orientations.

5.4 Laser-induced defects on monocrystalline chromium samples

5.4.1 Surface analysis

The visual results obtained for a polycrystalline Cr sample need further investigation and confirmation on Cr monocrystalline samples. Fig. 5.2 presents monocrystalline samples having different orientation growth, (100), (110) and (111) irradiated by 1 and 2 laser pulses at an incident fluence of 0.3 J/cm², under approximately 10% of F_{th}. Same Cr polycristal experimental conditions were applied for Cr monocrystals.

Band contrast (BC) is shown in fig 5.2b for the 3 orientations. As the darker the area, the higher degree of lattice defects, it is clear that orientation (110) shows higher degree of lattice damage than orientation (111) and (100), since the band contrast is darker on orientation (110). Orientation (100) shows no marked contrast, indicating good Kikushi bands quality. In the interest of gaining access to lattice strain and defect density, the mean angular deviation tool (MAD), which is a measure of how well positions of the bands in the simulated EBSP match those in the actual EBSP, was used. In other terms, it indicates the misfit between the measured and the calculated angles between bands. Thus the larger the MAD value, the higher the misfit and the lower the indexing confidence.

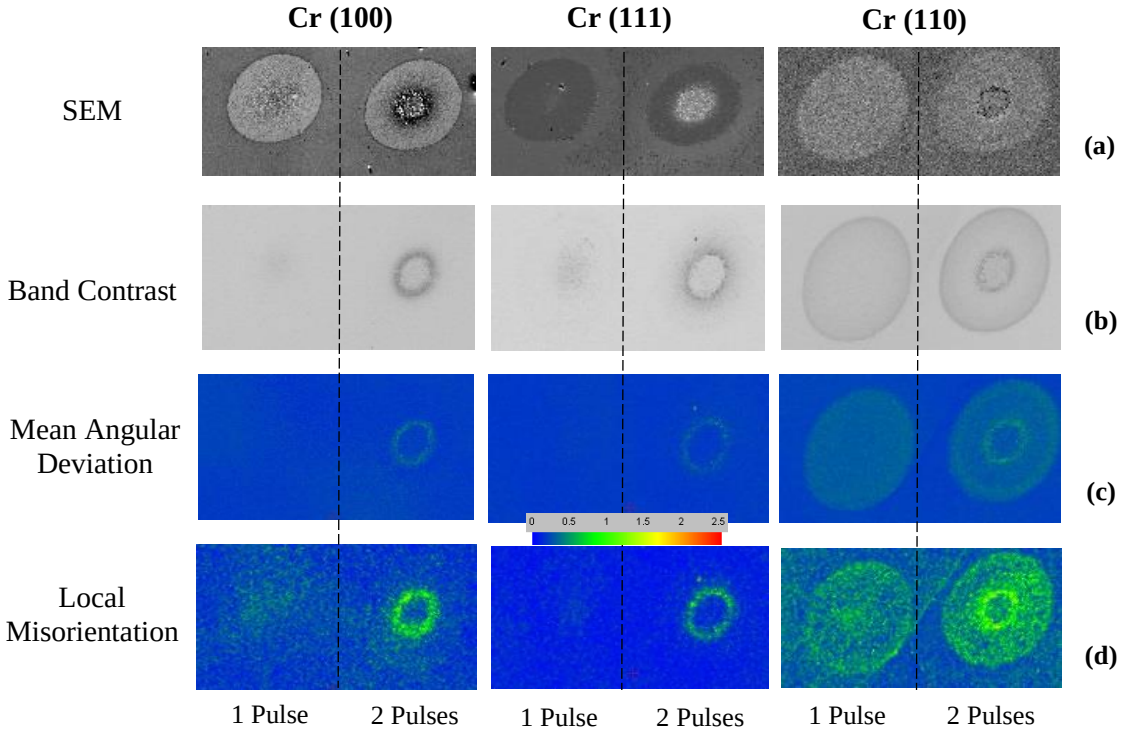

Fig.5.2 (a) SEM micrograph, (b) Band Contrast, (c) Mean Angular Deviation, (d) Local Misorientation, of monocrystalline Cr surface having different orientation growth, irradiated by 1 and 2 pulses for a fluence F< Fth, with a fluence fixed at 0.3 J/cm. Color gradient is shown as inset for mean angular deviation and local Misorientation. A black line is drawn in order to distinguish 1 pulse and 2 pulses impacts.

Fig 5.2c shows the MAD calculated for the 3 orientations (100), (111) and (110). Since misorientation mapping is useful for studying plastic deformation, Local Misorientation (LM) tool was used, which calculates the misorientation between a pixel and its eight surrounding pixels. LM for crystalline orientations is visible on fig. 5.2d, where false-color mapping shows an inhomogeneous Misorientation (in green) on (110) orientation higher than that on (111) and (100) orientations. LM can be associated to the generation of high local dislocations density, thus high plastic deformation on the (110) orientation.

EBSD characterization of laser induced defects shows that (110) crystal orientation is more likely to get damaged. This result is reproducible on monocrystalline samples. In fact, when a crystal is deformed, its atomic planes are distorted. As a consequence, a greater angle distribution originating from crystal diffraction planes is obtained by the lattice non-uniformity. Indeed, Kossel cones emanating from the sample present a greater variation. On the diffraction pattern, this is manifested by blurring Kikushi bands edges[230,231]. Furthermore, from the Bloch wave's theory, this distortion inhibits the propagation of the Bloch waves resulting in a decrease in contrast of the Kikushi bands. The higher dislocation density deteriorates the quality of the diffraction pattern due to the higher lattice distortion[232]. The observed defects can be due to phase changes as well as to higher stresses at greater depth.

5.4.2 In-depth analysis

After laser induced damage characterization on 1 pulse impacts by EBSD tools, an investigation of defects generated beneath the first layers from the surface has been carried out on the (100) and (110) orientations, extreme cases which showed different behaviors regarding EBSD results. Thus TEM-HAADF has been used in order to reveal microstructural changes in depth. Two 10 µm long thin lamellas were extracted from the center of the same one-pulse impacts characterized by EBSD tools, as shown in fig. 5.3a and b. HAADF imaging, referred also to Z-contrast imaging, which uses the high-angle Rutherford-scattered electrons, is illustrated in fig 5.3c and d, for orientations (100) and (110) respectively.

We notice the formation of a particular layer having a depth of 50 nm under the surface in the center of the 1-pulse impact on the (110) orientation, with a darker contrast than that of the bulk. No marked contrast has been identified under the surface of the 1-pulse impact on (100) orientation.
Electron diffusion factor is a function of the scattered electron angle Θ and can be approximated by the following formula[233–235]:

$$f_{e(q)} = \frac{1}{2\pi^2 a_0 q^2} Z \tag{5.1}$$

Where fe(q) is the electron diffusion factor, $q = (2 \sin \Theta)/\lambda$ is a parameter, function of the scattered electron angle Θ and the de Broglie electron wavelength λ, $a_0 = \varepsilon_0 \hbar^2/\pi m_0 e^2$ represents the Bohr's radius, m_e is the electron rest mass, ħ is the reduced plank constant, e the elementary charge, and Z the atomic number, Thus the square of the electron diffusion factor is proportional to Z^2. As a consequence, electron scattered intensity is proportional to the square of the atomic number. Scattered intensity I at an angle Θ is then given by

$$I = 1.7 \sum_i (Z_i V \rho_i) \tag{5.2}$$

where Z represents the atomic number, V the probed volume and ρ goes for atom density. Fig 5.3 shows scattered intensity profile among the (110) lamella's depth, in HAADF mode. An intensity drop of about 18% is obtained in the 50 nm-particular zone which presents darker contrast. This reveals generation of high density vacancies. Their condensation and gathering can contribute to dislocations. The experiments performed on monocrystalline samples as well as polycrystalline chromium sample give clear evidence that ultrafast laser induced defects generation is crystal orientation dependent, and matches with predictions of TTM-MD simulations performed for Cr targets having different orientation growth, (100), (111) and (110), presented in the following section. Here, we are dealing only with dislocations and point defects (vacancies and interstitials), since no twins were observed, either by EBSD surface analysis or FIB induced lamellas cross section TEM examination. We have shown that (110) orientation is more likely to get damaged. In fact, the speed of lattice temperature rise process after energy transfer via electron-phonon coupling determines the magnitude of the compressive wave generated. The faster the temperature rise, the greater the amplitude.

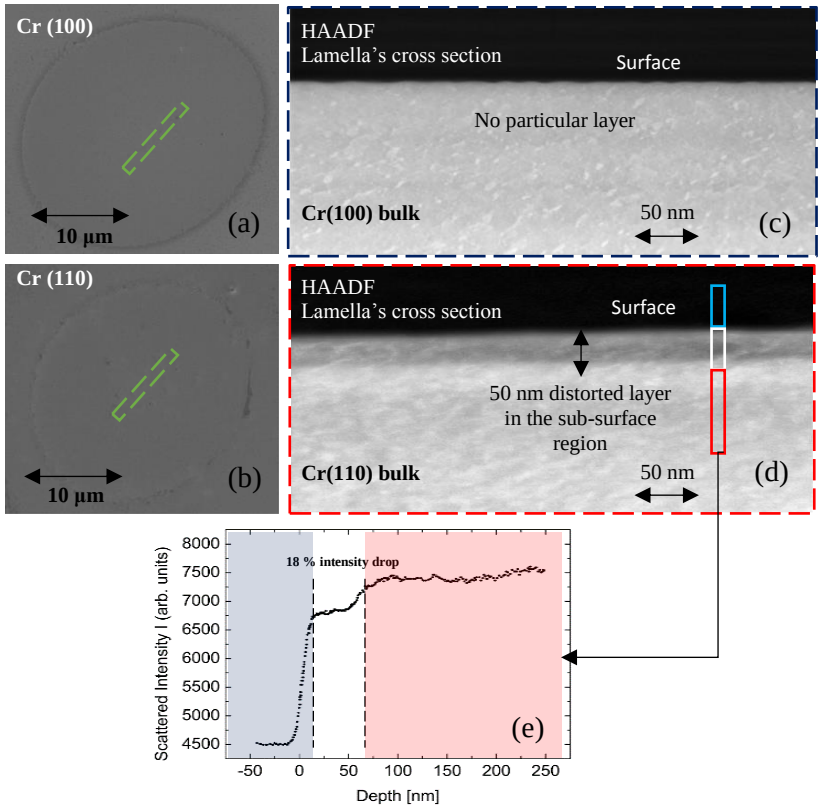

Fig. 5.3 (a) and (b) Lamella's extraction zone by FIB lift-out technique from the center of the 1 pulse impacts for (100) and (110) orientations respectively. (c) and (d) High Angular Annular Dark Field (HAADF) lamella's cross section analysis for (100) and (110) orientations respectively. A particular layer of 50 nm depth is visible under the surface of the (110) orientation. Marked contrast was never observed on (100) orientation. (e) Scattered intensity versus depth profile. Blue, white and red rectangles among depth show graph analysis region. An intensity drop of 18% was found in the 50 nm particular region.

Thereby, tensile wave's amplitude, which can be a function of electron-phonon coupling efficiency, is crystal orientation dependent. The reason behind the stopping of tensile wave increasing lies on the fast emergence of spallation, which can affect liquid temperature. This can explain the early formation of HSFL on (100) orientation in the spalled zone, and their absence on (110) orientation, where liquid resistance to tensile wave is weak. While crystal orientation response to ultrashort laser interaction with bcc metals has not been studied in the literature regarding types of laser induced defects, computational and theoretical analysis presented in the following section on chromium samples having the same orientations used in our experiments provides strong correlation between types of defects generated and crystal orientation growth, which follows our experimental results.

5.5 Structural modifications revealed by molecular dynamics simulations

In this section, the conditions causing transient and permanent structural modifications in the surface region of a Cr target irradiated by a femtosecond laser pulse are investigated accounting on the results of a large-scale TTM-MD

simulations performed by the university of Virginia. The generation of point defects as well as dislocations in bcc Cr targets are investigated below.

Density functional theory (DFT) calculations on optical properties for excited Cr was performed. We observe a very weak modification (few percent < 5%) of the reflectivity in the range of fluence considered. This can be explained by a stable d-band of Cr metals which spread out on a large energy domain. Consequently Fermi smearing has nearly no effect on the optical properties. This result explains why the experimental fluence and the following simulation parameters are in good agreement. Furthermore, we have also tried some calculations on slab geometries with different crystal orientation, and we do not observe any significate optical properties modifications.

5.5.1 Generation of crystal defects in Cr (001), (110) and (111)

In order to study laser-induced dislocations dependence on the crystalline orientation of the irradiated material, three-large scale TTM-MD simulations were carried on (001), (110) and (111) Cr targets which are irradiated by a 50 fs laser pulse at an absorbed fluence of 800 J/cm², following the same experimental parameters used to irradiate the Cr monocrystalline targets. The snapshots shown in fig. 5.6 concerning the atomic configurations obtained in the large-scale TTM-MD simulation of a (001), (110) and (111) Cr targets are quenched employing the velocity damping technique. The atoms in these snapshots are colored according to their potential energies. It should be noted here that atoms possessing energies lower than -3.99 eV which belong to the original bcc crystal structures are blanked in order to ensure a better view of the laser-induced defects. Using this representation, atoms that belong to either the free surfaces (atoms colored in red), the liquid/melted regions (atoms colored in green) and laser-induced crystal defects (atoms colored in blue) are only showed. After the absorption of the laser pulse energy, simulations reveal the emission of dislocations from the melting fronts which propagate then deeper into the targets simultaneously with the expansion of the melted region depth. A persisted emission of new dislocations and their multiplication leads to an increase of the dislocations density. The snapshots in fig 5.6 unveil the rapid propagation of the dislocations in (110) Cr sample down to the bottom of the computational system, where they are driven back by the non-reflecting boundary. In contrast to the rapid motion of dislocations in (110) target, a slower propagation of dislocations is observed in (111) target, where they reach a depth of 115 nm in the sub-surface region by the end of the simulation. Furthermore, the formation of high density of vacancies is also revealed during the resolidification process, and the generation of vacancies deeper inside the bulk of the targets respecting the non-conservative propagation of the dislocations, as can be seen in fig 5.6 for the (110) and (111) Cr targets. While the dynamic relaxation of laser-induced stresses produces transient unstable stacking faults in Cr(001) target, a high density of point defects, i.e. vacancies and interstitials, are generated. It should be noted here that the emission of dislocations is absent in the Cr target with (100) orientation, which is consistent with the experimental results.

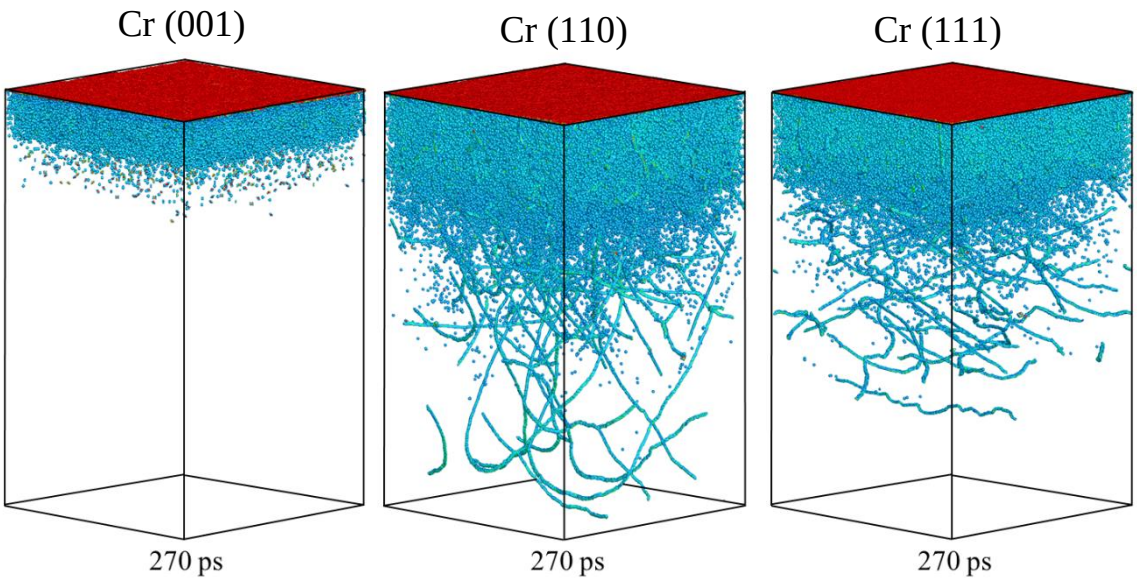

Fig. 5.6 Snapshots of atomic configurations obtained in a large-scale TTM-MD simulation of (001), (110) and (111) Cr targets irradiated with a 50 fs laser pulse at an absorbed laser fluence of 800 J/m^2, which is 66% above the threshold for surface melting. The snapshots are quenched to 0 K in order to reduce thermal noise in atomic positions and energies. Atoms are colored according to their potential energy and all the atoms that have energies below -3.99 eV and belong to the original bcc crystal structure are blanked to display the crystal defects. The red atoms in the top layer of the snapshots belong to the free surface of the target while the atoms in the green region (30, 70, and 180 ps) represent a melted region. Ref: Dissertation of E.T. Karim under the supervision of L.V. Zhigilei[263].

These snapshots support the notion of a correlation between dislocations emission and residual compressive stresses relaxation.

In order to furnish a clear comprehension on the dislocations emission in (110) and (111) Cr targets, the resolved shear stress, described in chapter 3, is calculated for the 48 slip systems for atomic configurations generated in the simulations. The results are discussed in the following section. Obviously, in both (110) and (111) targets, the increase of the resolved shear stress just below the melting front to more than 3 GPa at the onset of the simulation including the high compressive stresses scaled between 2.5 and 3 GPa can be the main reason to the comprehension of the generation of dislocations in the samples. Concurrently, the inhibition of transient stacking faults respecting the uniaxial expansion of the two targets can be elucidated by the calculation of the Schmid factor for the appearance of unstable stacking faults respecting the {011} planes for the three orientations (001), (110) and (111). Calculation results point out that the Schmid factor achieves its maximum value of 0.5 in four out of six {011} planes for (011) target and lessens to 0.25 and 0 for (110) and (111) targets, respectively. These results show that the weak value of the Schmid factor hinders the generation of the stacking faults in the (110) and (111) targets.

Therefore, we can infer that the formation of dislocations with Burgers vectors a<100> is due to the reactions between dislocations with Burgers vectors (a/2)<111>. Several dislocation loops with Burgers vectors (a/2)<111> are also observed in the two simulations at locations with a high density of vacancies, With the existence of a high density of

vacancies along with the rapid undercooling process, the dislocation loops are believed to form initially with Burgers vectors on {110} planes and then shear to become perfect dislocations.

5.5.2 Resolved shear stress investigation on Cr (001), (110) and (111) targets

The discrepancy between dislocations emission in the (110) and (111) Cr samples and their absence in (001) Cr sample in the melting regime, underlines an explicit understanding on the onset conditions of dislocations emission in the irradiated targets, which are crystallographic orientation dependent. Therefore, resolved shear stresses calculation in the 48 slip systems is performed for the three large-scale simulations discussed in the previous sections.

The calculation includes the general form of the Schmid's law represented by:

$$\tau_{nd} = \sum_{k=1}^{3} \sum_{m=1}^{3} l_{mn} l_{dk} \sigma_{mk} \tag{5.3}$$

Where τ_{nd} represents the resolved shear stress, n and d represent the normal to the slip plane and the direction of the slip, respectively, l_{mn} is the cosine of the angle between n and the uniaxial force, l_{dk} is the cosine of the angle between d and the uniaxial force and σ_{mk} the magnitude of the tensile stress.
The results unveils the maximum value of the resolved shear stress for the three systems, which is 2.93, 3.68 and 4.00 GPa for (001), (110) and (111) respectively, which is spotted in multiple slip systems of {112} <111> type. Whereas the resolved shear stress maximum value in the (001) orientation is somewhat lower than the ones in (110) and (111) orientations, the atomic configurations snapshots show only the transient generation of unstable stacking faults in the simulation. In order to shed more light on the contrast between the three systems, the resolved shear stress temporal and spatial evolution is plotted for the slip planes in fig 5.7, along with the pressure plots including the denoted maximum tensile and compressive values.

The interesting point here is that it is not just the magnitude of the resolved shear stress that is important, but where and when the maximum level of stress is achieved. Starting with the (001) orientation and considering the slip system (112)[111], where the maximum resolved shear stress of 2.93 GPa is noticed, we examine the resolved shear stress spatial and temporal evolution as well as pressure in this orientation. A remarkable observation from the contour plot of the resolved shear stress in fig 5.7a is that the shear stress values remain in the sub-melting front at its vicinity, and do not surpass ~130MPa during the first 20ps from the laser pulse, which is even below the yield strength of Cr.

This can be explained by an alternative relaxation of the shear stresses through internal slip along {011} planes leading to the transient appearance of the large number of stacking faults. The retraction of the stacking faults leads to an increase in the shear stress below the liquid-crystal interface up to ~1.2 GPa in twelve slip systems, but it is not high enough to cause the emission of the dislocations. The maximum resolved shear stress reaches its maximum value, ~2.93 GPa, at a

depth of 120 nm below the surface at about 40 ps after the laser pulse. At this time and place, this is already too cold for the homogeneous nucleation of dislocation loops. On the contrary, a different picture of the pressure evolution and shear stress resolved for the slip system (112)[111] is noticed in fig 5.7b for the (110) target. The maximum value of the resolved shear stress in this orientation is scaled between 3.5 and 4 GPa, with the shear stress approaching this value in several slip systems at about 20ps from the laser pulse at a depth of about 30 nm in the sub-surface region. The conditions of the tremendous dislocations emission from the melting front are promoted by the generation of strong shear stresses in the prompt vicinity of the melting front, besides the high lattice temperature exceeding the melting temperature of Cr. Simultaneously, the propagation of the dislocations deeper into the target is facilitated by the pressure oscillations, the high lattice temperature and the quasi-static uniaxial lattice expansion that preserves relatively elevated level of resolved shear stress, ~ 1 GPa, in the zone that is not accessed by the dislocations. Dislocations propagation deeper into the target lessens the shear stresses and causes the relaxation of the residual compressive pressure from 1.7 GPa to less than 1 GPa by the end of the simulation.

Concerning the (111) orientation, the results of the resolved shear stress is somewhat similar to the ones discussed previously for the (110) orientation, which is evidenced from the contour plots in fig 5.7c of the temporal and spatial evolution of the resolved shear stress for the (211)[111] slip system, where the shear stress reaches its maximum value of 3.7 GPa. In the (111) target case, dislocations are emitted from the melting front where the maximum resolved shear stress is reached after 20ps from the laser pulse. The lattice temperature is near the melting temperature and the compressive pressure is around 3GPa at the time and depth of the dislocations emission. Regardless the pressure increase to 3.2 GPa at depth of 32 nm in the sub-surface region by the time 50 ps, the resolved shear stress promptly decreases to less than 1 GPa in most of the slip systems excluding six slip systems where the resolved shear stress is close to 1.3 GPa. The residual compressive stresses are partially relaxed only down to the depth of 115 nm from the surface, which is the maximum depth reached by the dislocations at the end of the simulation, owing to the slow propagation of dislocations.

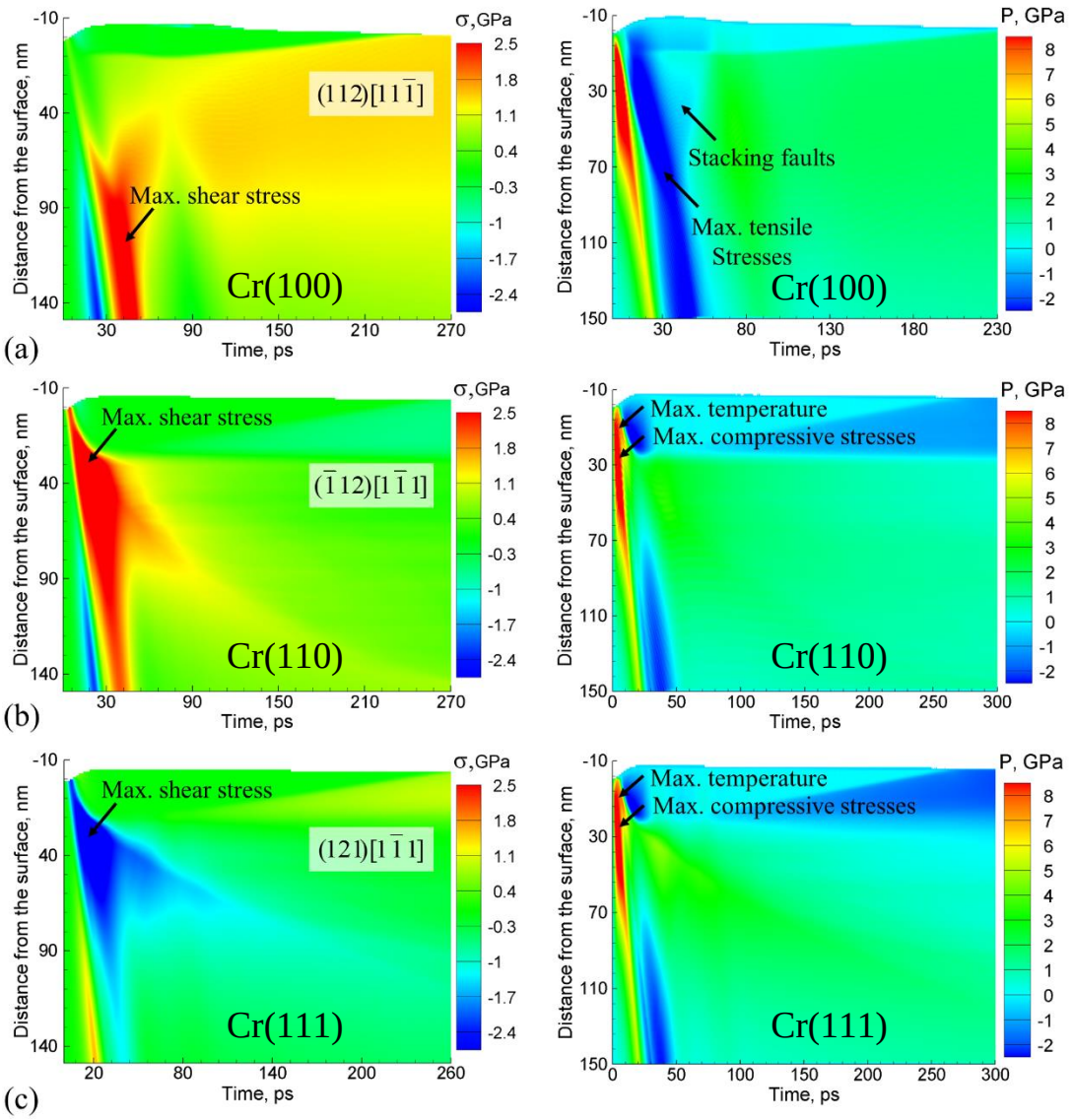

Fig. 5.7 Contour plots of the spatial and temporal evolution of the resolved shear stress (left) and pressure (right) obtained in TTM-MD simulations of (001), (110), and (111) Cr targets irradiated with a 50 fs laser pulse at an absorbed laser fluence of 800 J/m^2, which is 66% above the threshold for melting and solidification. The contour plots of the shear stresses are shown for the slip systems where the highest resolved shear stress is detected. Ref: Dissertation of E.T. Karim under the supervision of L.V. Zhigilei[263].

5.6 Discussion

There is a semi-quantitative agreement between the simulations and experiments. First, we indeed see that dislocations are generated much more readily in (110) and (111) targets as compared to (100) ones. The difference between (110) and (111) is less pronounced, but, indeed, the dislocations propagate deeper in the case of (110). The values of the absorbed fluences are also in a reasonable agreement, particularly given the uncertainty with the reflectivity that, in principle, may change during the pulse due to the electronic excitation.

In the previous chapter, it was shown that the preferential HSFL formation on (100) orientation was related to the spiky character of the roughness centers featuring elongated frozen nanospikes which enhances thus the local near-field. Furthermore, the strong dependence of the surface roughness on the crystallographic orientation of the irradiated target was found to be influenced by the velocity of the crystallization front. One can speculate that the generation of dislocations in (110) and (111) changes the way laser melting proceeds when the surface is exposed to subsequent pulses. Indeed, the time to resolidification is longer and this allows for the surface to relax.

5.7 Summary

In this chapter, it was revealed that generation of crystal defects is crystalline orientation dependent upon irradiation with a single pulse in the melting regime. Experimentally, a qualitative EBSD study showed that Kikushi bands are of poor quality in the case of (110) as compared to (111) and (100) orientations. An in-depth study conducted by HAADF revealed a distorted layer in the case of (110) orientation, where the inelastic electron scattered intensity is dropped by 18%. This can be explained by the generation of a high density of point defects and dislocations. The experimental results were validated by TTM-MD simulations performed on bcc targets in the same conditions. It was revealed that the emission of dislocations is related to the resolved shear stresses and the availability of the slip systems that can be activated by the uniaxial expansion of the surface region. According to the simulations, the dislocation emission is observed during the melting process (~100 ps), but additional dislocations do, indeed, form during solidification. Moreover, almost all vacancies are generated by resolidification. In principle, the high density of vacancies may lead to the formation of small dislocation loops. But, according to the simulations, this process is making a negligible contribution as compared to the resolved shear stress mechanism of the dislocation formations revealed in the simulations.

The investigation of crystal defects in bcc Cr target with (001) orientation indicate the formation of high density of stacking faults inside the bulk target. The formation of these unstable stacking faults coincides with the propagation of the tensile component of the stress wave, which results in uniaxial expansion of the lattice in the [001] direction. This uniaxial expansion activates multiple shifts in the {110} crystallographic planes that are oriented at 45^{o} with respect to the [001] axis of expansion. The relaxation of the tensile component brings about gradual removal of the stacking faults from the system due to the relaxation of the lattice deformation.

The investigation of the crystal defects in these simulations illustrates the formation of dislocations inside the bcc Cr target during the resolidification process, in addition to the formation of high density of point defects, vacancies on (110) and (111) orientations. Resolved shear stress calculation elucidate that the high resolved shear stress value in (110) and (111) orientations in the sub-melting front, along with the high lattice temperature, underlines the emission of the dislocations.

Chapter 6

Self-arranged periodic nanovoids triggering HSFL formation on fcc material

In this chapter we employ a high resolution microstructural analysis approach to infer the phase transition undergone in the LIPSS region, including epitaxial regrowth and nanocavitation. We unveil the periodic nature of the subsurface nanocavitation and demonstrate this is due to light self-arrangement. While the inhomogeneous periodic absorption is investigated by electromagnetic simulations, the dynamics interlinking transient melting, nanocavitation and LIPSS formation are asserted by a pump-probe like experiment and two-temperature (2T-)hydrodynamics modeling. This work was published in ACS Photonics by X. Sedao, A. Abou-Saleh et al. (2018).

6.1 Introduction

In this work, a better understanding of LIPSS formation is pursued, by pinpointing the function of near-field enhancement and periodic nanocavitation. We demonstrate, with proper controlling laser parameters, that a feedback effect can be introduced in, and aforementioned merits can be combined elegantly and be used for patterning 10-150 nm sized features on the surface as well as at sub-surface region. During ultrashort laser material interaction, depending on laser dose and surface crystal orientation, lattice heating may entail rapid melting, cavitation, spallation and ablation, within a space of nanometer scale and within a few picoseconds time window. Regular nanocavitation has already been experimentally reported on aluminum surface layer but the microstructural and periodicity features in relation with LIPSS generation and grow was not established. Initial surface inhomogeneity could trigger highly periodic redistribution of the electromagnetic field when a laser pulse impinges upon the surface. The physical nature of the subwavelength energy modulation relies on a coherent superposition of scattered waves with incident/refracted light assisted by surface plasmonic excitation and near field effects contributing to sub-100 nm re-ordering of the field. Thereafter, the thermo-mechanical response of the material, involving defect formation and/or transient melting with ultra-rapid resolidification, plays an important role in LIPSS formation.

6.2 Nanostructures induced by field scattering on rough surface

The irradiated target was a single crystal nickel with a surface orientation (100) and an initial surface roughness R_a = 1 nm before laser irradiation. In multi-shot experiments, a first laser pulse randomly modifies the topography of the surface by creating roughness centers that are to be seen by the next pulses. All the successive laser pulses impinge on a surface being constantly altered by the previous pulses and being roughened constantly, from an initially quasi-flat surface to a significant roughness at later stage. The light coupling involves polarization effects on the newly formed roughness centers, at the origin of LIPSS generation with two different periodic scales on the irradiated surface. The smallest structures (50 nm to 200 nm) are parallel to the laser polarization and result from local field enhancement on roughness[5,111]. Consequently, we will refer to them as $nf_{//}$ in light of their near-field nature. Corresponding to roughness-dependent radiation remnants[91], they are often called high spatial frequency LIPSS (HSFL) of type r in literature[10]. On the other hand, the structures formed from superposition of far field scattered fields on roughness centers with incident/refracted fields will be referred to as ff[5,111]. These oriented structures can be parallel ($ff_{//}$) and they are coined HSFL of type-d for dissident structures, or be perpendicular ($ff_{\perp}$, also known as LIPSS of type s and corresponding to low spatial frequency LIPSS (LSFL)).

In order to elucidate the nature and role of near/far field scattering processes, and the effects of surface roughness features in the formation of these structures with different orientation and periodicity, we performed 3D electromagnetic simulations solving linear Maxwell equations[111]. The intensity distributions established upon coherent scattering from a set of randomly distributed nanovoids on the metal-air interface was calculated by Anton Rudenko. With a 800 nm

wavelength incident light, fig. 6.1 depicts typical transverse intensity patterns obtained 20 nm below the metal surface resulted from the scattering by nanovoids of R=30 nm with a concentration C = 2% (average inter-void distance d_{hh}=120 nm) and by larger nanovoids of R=50 nm with a lower concentration C = 0.2% (d_{hh}=550 nm).

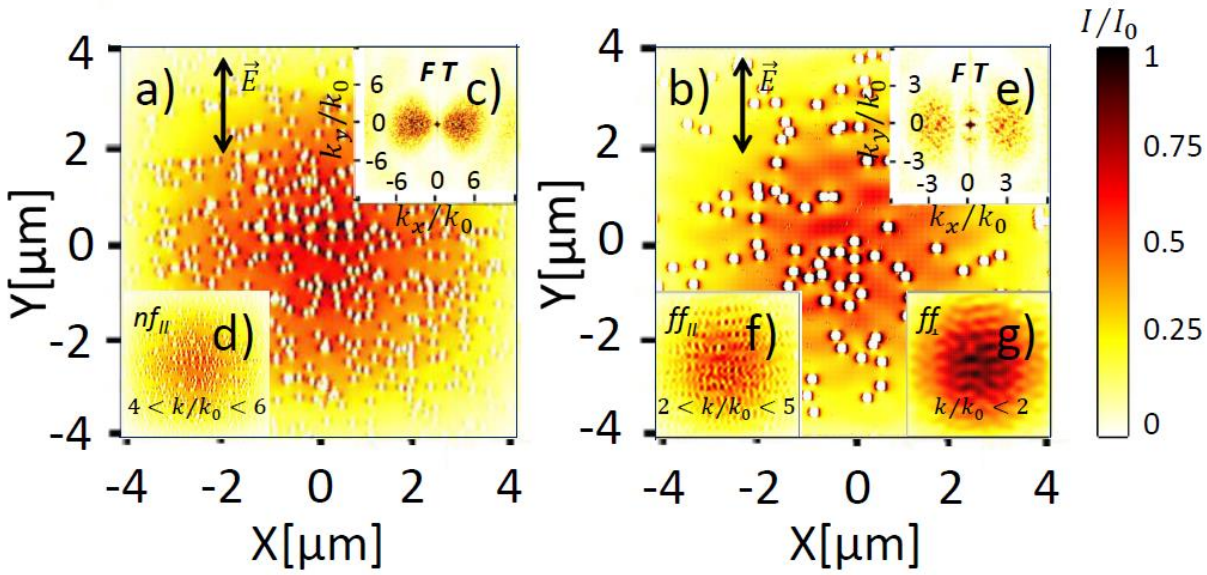

Fig. 6.1 (a,b) intensity distributions calculated by 3D-FDTD simulations 20 nm below Ni rough surface in the transverse plane perpendicular to laser propagation and (c, e) their Fourier transforms (FT). The distributions with the frequencies of interest, corresponding to $nf_{//}$, $ff_{//}$ and $ff_{\perp}$ features, are filtered for (d) $4 < k=k_0 < 6$, (f) $2 < k=k_0 < 5$, and (g) $k=k_0 < 2$, where $k_0 = 2 =$ is the wave-vector normalized to laser wavelength = 800 nm. Rough surface consists of (a) nanovoids of R = 30 nm with a high concentration C = 2% or (b) larger nanovoids of R = 50 nm with a lower concentration C = 0:2%.

The size and concentration were chosen to model the surface roughness developing in the course of laser irradiation, and corresponding to experimental conditions that will be discussed in the following sections. In the case of nearly touching nanovoids, local non-radiative near-field effects dominate over far-field effects, resulting in intercoupling between nanovoids and quasi-periodic polarization dependent pattern formation with deeply subwavelength periodicity <λ/3 close to metal-air interface. Fourier Transform (FT) of the spatial distribution shown in fig. 6.1c reveals a large spectrum of subwavelength frequencies indicating a high periodicity dispersion, whereas filtering of the spatial distribution from random noise allows us to identify continuous periodic lines of nf// structures with [λ/6-λ/4] spacing. The vicinity of the nanovoids is crucial to enhance high frequency response of the nanovoids, whereas the concentration is likely to affect the dominant periodicity. At higher separation distances, however, the nanovoids cannot interact via near field intercoupling since the near-field scattered fields decrease rapidly with the distance from the nanovoids centers r (as $\backsimeq 1/r^3$)[236].The interference effects between the incident and the far-field scattered waves as well as coherent superposition of the scattered far-fields are dominant as a feedback to the surface ripples development (far-fields decay slower as 1/r). To emphasize the importance of the far-field effects, the larger nanovoids with lower concentration are considered in fig. 6.1b, as the scattered field increases with the size of the scattering centers. Thus, the scattered electric fields are proportional to the electric dipole moments in the far-field approximation [236], consequently to R^3.

The far-field intensity enhancement is expected to increase ≃ 25 times growing the nanovoids size from R = 30 nm to R = 50 nm. Two discrete frequency regions are of interest on the Fourier Transform in fig. 6.1e. The structures of the periodicity close to laser wavelength are oriented perpendicular to laser polarization (ff⊥), whereas the structures of lower periodicity with parallel orientation are also detected (ff$_{//}$). To underline the presence of well-ordered ff$_{//}$, we apply Fourier transformation, filter the dominant frequencies in the range of 2-5 times lower than laser wavelength (with periodicity lower than ff⊥ and higher than nf$_{//}$ features) and reconstruct the spatial distribution by applying inverse Fourier transform in fig. 1(f). The rigorous analysis of the revealed spatial distribution allows us to assert that the patterns of enhanced intensity, oriented parallel to laser polarization, are related not to discrete positions where the nanovoids are located beneath the transverse plane, but to nonlocal coherent superposition of the scattered far-fields from the nanovoids. That is the reason why, thereafter, we refer to these structures as ff$_{//}$. By applying low frequency filtering, we identify clearly ff⊥ features on the spatial intensity distribution in fig. 6.1g. Their origin is directly related to the interference of the incident wave with the scattered cylindrical surface waves from the nanovoids, decaying fast on the distance of a few laser wavelengths along the metal surface[237].

In our experiments, far-field and near-field features were obtained either simultaneously or not, depending upon different laser conditions, and were subjected to subsequent high resolution microstructural analysis. Since the growth of nf$_{//}$ requires the presence of roughness centers but may be undermined by a strong feedback, 2 laser pulses were applied, to form solely nf$_{//}$ on the surface of the target, at a near ablation threshold fluence Fth. The formation of ff⊥ requires a higher feedback, therefore the laser fluence was set to a lower value near melting threshold[14], and a high number of laser pulses (46 pulses) was used.

6.3 Nanocavitation induced by near-field enhancement

The surface modifications in the laser impact area were visualized using a scanning electron microscope (SEM). Microstructural examination in the direction normal to the surface (i.e. from the surface to sub-surface to bulk) was carried out using a field emission high-resolution transmission electron microscope (HR-TEM) system on cross-section thin foils extracted from laser irradiated sites using a focused ion beam (FIB) system, performed at CLYM facility by Thierry Douillard. Classical work as bright field (BF) or dark field (DF) imaging and selected area electron diffraction (SAED) were performed, but also scanning transmission (STEM) imaging was used in association with a high angle annular dark-field (HAADF) electron collection. This last method offers the advantage to produce images without any diffraction contrast but with an atomic number contrast. It was decided to conform the thin foil to lie 45 degree angle with respect to the laser polarization, to ensure that the both ff$_{//}$ and ff⊥ could be potentially visualized at one time, where it was applicable.

Figure 6.2 represents nf$_{//}$ features produced with 2 laser pulses at near ablation threshold fluence. The matter from a tiny central area of the laser spot is removed by spallation and nf$_{//}$ formation takes place. The top-view of the central area is shown in the SEM image (fig. 6.2a). The boxes highlight the nf$_{//}$ structures in the center, and the rim of the spallation

crater. Spallation, where liquid layers are ejected from the surface, is due to relaxation of laser induced stresses generated beneath the surface, which coincides with the nucleation, growth and coalescence of multiple voids[50]. The insets illustrate these sites in greater details. In the rim region, small patches of surface bursts are observed. There are also some surface reliefs present in this region without marked material removal. The red bar across the image diagonal indicates the extraction location of the TEM thin foil. According to the radial distance from the center towards peripheral of the laser impact (hence gradually decreased local laser fluence following a Gaussian energy distribution), a few typical sites, representing spallation, $nf_{//}$ and nanovoids formation, are chosen and their cross-sectional HAADF images are given in fig. 6.2b. In the central 3 μm radius region the $nf_{//}$ nanostructures are thin ridges formed seamlessly on the surface (two bottom images in fig. 6.2b). These thin ridges rarely appear to be upright. Instead, they more than often bend alternatively towards one side or another, a strong indication of past-existence of some nanocavities. Further away from the spot center, a 3-5 μm radius ring region is the transition area where the rim is located. The $nf_{//}$ from both inside of the rim and the detaching surface, related to spallation process[14,73], are evident. Outside the rim, in a region with radius reaching beyond 5 μm, burst cavities are merely visible (fig. 6.2a). The HAADF images (two top images in fig. 6.2b), however, reveal unbroken detaching surface layers and nanovoids trapped underneath the surface. The above observation could be fully interpreted using the near-field theory if one assumed the energy coupling was strongly localized at the nanocavitation sites, causing spallation of the material between the $nf_{//}$ ridges in the center area and nanovoids formation in the off-center areas. This assumption is affirmed by the microstructures underlain. Coupled BF and DF images were taken from aforementioned three distinct regions (fig. 6.2c). Fig. 6.2d shows the SAED pattern generated from the surface region of the TEM thin foil. Zone axis [011] was used to obtain the BF images, and the DF images were acquired with diffraction spot (200). The three regions exhibit, predominantly, epitaxial regrowth. For instance, the $nf_{//}$ in the central 3 μm radius circular region (fig. 6.2c top), and the material surrounding the subsurface nanovoids in the outer region with radius greater than 5 μm (fig. 6.2c bottom), are entirely epitaxially regrown.

The only exception appears at the 3-5 μm radius rim region (fig. 6.2c middle): the surface layer covering the cavity is visible in the BF image but not so in the counterpart DF image, suggesting a different local crystallographic orientation. This layer might have been disrupted due to the mechanical stress from spallation and surface detaching. Overall, these observations imply that under the local field enhancement, the nanovoids are the sites experiencing strong energy coupling, while the surroundings, i.e. the ridges of $nf_{//}$ are the sites with weak energy coupling hence melting and epitaxial regrowth. The central periodicity of $nf_{//}$, $\Lambda = 145$ nm, is determined from the SEM image, and further affirmed by FT analysis (fig. 6.2e). This accords well with the electromagnetic investigation discussed in the previous section, where roughness conditions foster near-field regime as seen in fig. 6.1a.

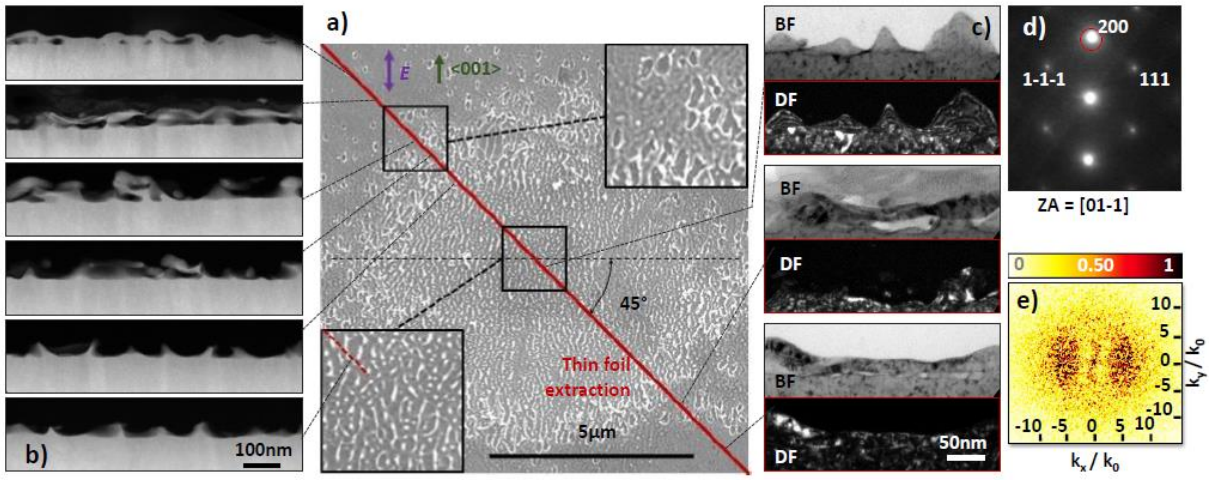

Fig 6.2 Figure 2: nf// nanostructures produced on Ni (100) surface after fs-laser irradiation at near threshold fluence, peak fluence 0.38 J/cm², 2 pulses. (a) SEM image of the central area, with notations of laser polarization (E), crystal direction h001i, TEM thin foil extraction, and 2 insets revealing nf// and the rim area in greater details. (b) HAADF images at distinct regions of the impact. Voids are seen beyond 5 µm distance from the center. The central 3 µm radius area is occupied by nf//. Between 3 µm and 5 µm radius defined circular band region, an intermediate ring with mixed voids and nf// features is found. These three locations are further examined, and presented in (c): couples of BF/DF showing epitaxial growth of nf// and of outer region (the defects present in the crystal were probably introduced during the sample preparation by FIB). The intermediate ring region exhibits material de-bonding, probably a layer that has not epitaxied. (d) SAED pattern with zone axis [01_1] used to obtain the BF and DF images with diffraction spot (200). (e) FT spectrum of the SEM image showing nf// frequency distribution.

6.4 Nanocavitation in feedback regime

Following the assumption raised, further experiment was carried out at high number of pulses and a lowered incident laser fluence, near melting threshold, as positive feedback conditions of irradiation are the most used regime of LIPSS formation. Figure 6.3 presents the surface and cross-section examinations of a laser impact with ff// and ff⊥ co-existence, made at 0.19 J/cm² with 46 pulses. More laser pulses are needed here for the LIPSS to appear, a sign of accumulation and feedback functions at play. It is reasoned that near-field enhancement was needed at first to localize the laser energy (the nominated laser fluence is too moderate to initiate material removal), and at a later stage the interference effect led to ff⊥ formation. Similar to the representation of fig. 6.2, a small central area of the laser impact was examined and the results are illustrated in fig. 6.3. The SEM image (fig. 6.3a) depicts the spot center, where both of the ff// and ff⊥ structures are clearly seen in a 5 µm radius area. The FT inset sums up the spatial alignment and periodic features of these ff structures. They are remarkably comparable to the FDTD simulations pointing out coherent superposition of far-field scattered fields (fig. 6.1b). The TEM thin foil extraction is marked by the red bar and an overview of the foil (before being thinned for TEM investigation) is shown in fig. 6.3b.

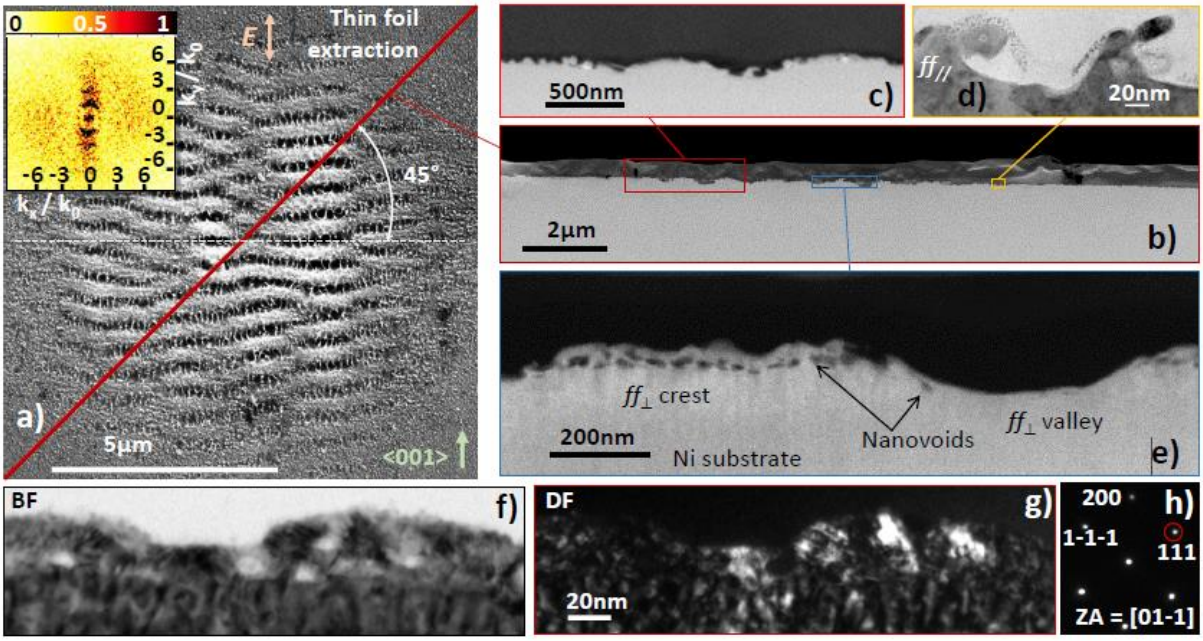

Fig 6.3 ff⊥ and ff// produced on Ni (100) after 46 pulses at a fluence of 0.19J/cm2. (a) SEM image illustrating co-existence of ff⊥ and ff// in the center, with notations of laser polarization (E), crystal direction h001i, and TEM thin foil extraction. FT analysis is displayed as inset, highlighting the crossed ff features. (b) SEM image of the foil, after FIB milling. The red-box highlighted area, where both ff⊥ and ff// are visible, is shown at a higher magnification in (c). The blue and yellow boxes indicated areas feature ff⊥ and ff//, respectively. These areas are further examined and shown in (d) and (e). (d) BF image of 2 ff// structures, the tips of which appear to curl up. (e) HAADF image of thinned TEM foil. Nanovoids are observed predominantly under ff⊥ crests but also a few beneath the valleys. (f-g) Typical coupled BF/DF images showing epitaxy growth of the surface layer (the present defects may be due to FIB sample preparation). (h) SAED pattern with zone axis [011] used to obtain the BF and DF images with diffraction spot (111).

The red box highlights an area featuring ff// and ff⊥, and the details of this localized area is presented in fig. 6.3c, where the ff// in the valley of the ff⊥ are visibly contorted, much alike a frozen burst of a nanovoid underneath the surface. Then the foil was thinned down to the order of 100 nm for TEM analysis. Two smaller areas with only ff// and only ff⊥ are highlighted by blue and yellow boxes in fig. 6.3b and their BF and HAADF images are given in fig. 6.3d and 6.3e, respectively. The high resolution BF image (fig. 6.3d) unveils the bending tips of the ff// ridges, which is thought to be frozen shell of a nanovoid burst. Many nanovoids of about 5-10 nm in size are disclosed, after FIB thinning, arranged themselves in a quasi-periodic manner, some 10-20 nm underneath the surface of ff⊥ crests (fig. 6.3e).

A few nanovoids are also identified in the ff⊥ valley area, but they are scarce compared to those located in the crest. The valleys echo the interference constructive parts, locally enhanced absorption caused the nanocavitation and collapse, whereas the crests are weak absorption counterparts so the nanovoids are formed and frozen. This is strengthened by the microstructural analysis: coupled BF and DF images given in figs. 6.3f and 6.3g substantiate epitaxy re-growth of the ff⊥ crest. Figure 6.3h is the concerning SAED pattern. Zone axis [011] was used to obtain the BF image and the DF image was procured using diffraction spot (111).

6.5 Probing transient surface dynamics

In a second set of experiments, single-color femtosecond double-pulse train was used to irradiate monocrystalline Ni sample having (100) orientation growth under conditions forming HSFL nanostructures. A Michelson interferometer transformed single pulses into double-fs-pulse sequences. The number of double-pulse-sequences N_{DPS} was set to 2. Time delay Δt between the two linearly polarized pulses of a sequence was varied between 0.2 and 20 ps. The peak fluence F of each pulse of the double-pulse-sequence are equal, and always kept below the half of the ablation threshold F_{th} for 1 pulse. Hence, only the joint action of both pulses results in a permanent surface modification. Fig. 6.4a displays laser induced surface modification as a function of the double-pulse time delay Δt. The ratio of the spallation surface and the HSFL covered surface to the total laser modified surface for which $F>F_{max}/e^2$ is given by the blue and red curve respectively.

The two curves exhibit an extended pronounced peak within 2-5 ps delays, and diminish fast for delays larger than 5 ps. HSFL nanostructures in the direction parallel to laser polarization are formed for delays between 0.6-14 ps, as indicated by the blue graph. HSFL covered surface area significantly decreases at 6 ps and vanishes completely for delays larger than 14 ps. The same behavior can be seen for the spallation surface area. When the first pulse arrives to the sample, a significant part of its energy is absorbed and relaxed via electron-phonon coupling and electron thermal diffusion thus initiating a rapid and localized heating producing in turn a temporal and spatial discontinuity of density, followed by surface melting. Whereas the first pulse can alter electronic band structures and drive the system into a non-equilibrium thermal state, a second delayed pulse with the same fluence and same polarization is sufficient to force the surface to undergo spallation and HSFL formation, strongly depending on the double-pulse delay. Spallation, where liquid layers are ejected from the surface, is due to relaxation of laser induced stresses generated beneath the surface, which coincides with the nucleation, growth and coalescence of multiple voids. For small delays < 0.4 ps, hot electron at the surface of the material generated by the first pulse can be disturbed by the second delayed pulse before energy transfer from the electrons to the lattice. Thus no spallation nor HSFL nanostructures are formed as energy is not sufficient to cause cavitation in the melted subsurface region. For delays between 0.6 ps and 2 ps, a strong modification of thermodynamic and optical properties of the material is generated. Therefore, absorption of the second delayed pulse laser energy increases due to a decrease in Ni reflectivity, which favors conditions leading to voids formation in the liquid region. In this case, energy exceeds spallation threshold, where it is sufficient to cause cavitation, followed by spallation of the melted layer. In fact, the first pulse energy has sufficient time to be delivered from the excited electrons to the atomic vibrations, which leads to a rapid heating and forms a liquid region of depth depending on the first pulse fluence. A second delayed pulse will encounter a melted zone which can influence laser induced processes in the surface region of the irradiated target. Interaction between second delayed pulse and the liquid region induced by the first pulse provides the driving force for a buildup of high compressive stresses in the surface region of the irradiated target. An unloading tensile component of the stress wave is generated following the relaxation of the compressive stress in the presence of free surface.

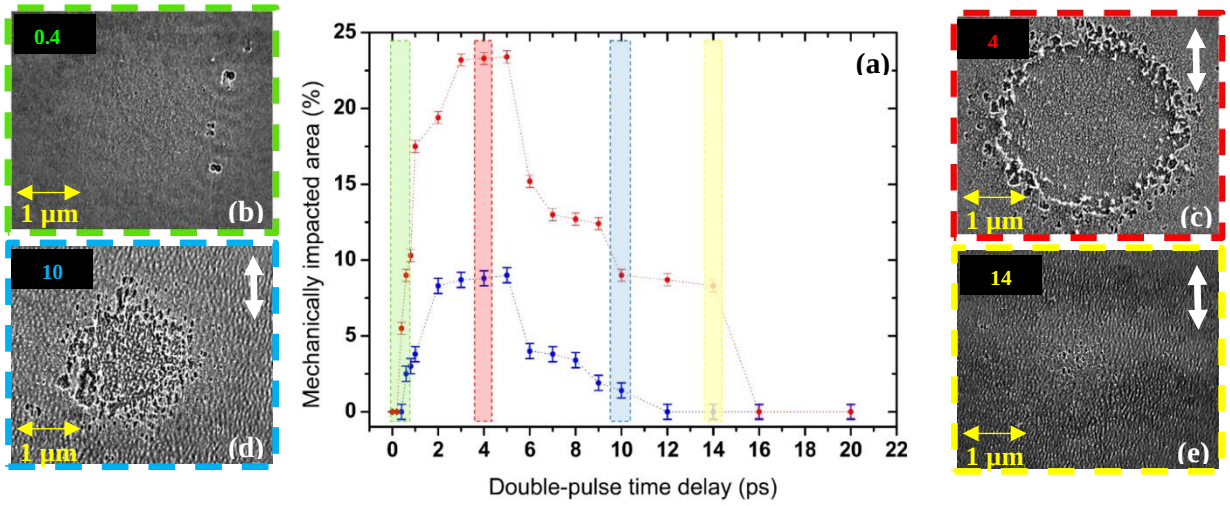

Fig. 6.4 Laser induced surface modification dependence on double-pulse time delay Δ*t* upon irradiation of a Ni(100) surface with N_{DPS} = 2 for a fixed peak fluence of 0.38 J/cm² under F_{th}. (a) Spallation surface area, blue curve, and HSFL covered area, red curve, as a function of Δt, which covers a range between 0 and 20 ps. Dashed colored rectangles on the curves correspond to SEM micrographs for different Δ*t*: Dashed green, red, blue and yellow rectangles are related to 0.4ps, 4ps, 10ps and 14ps respectively. (b-e) SEM micrographs of laser impact for selected Δt. Electric field polarization is indicated by the double white arrow in the top right of each micrograph.

These tensile stresses, increasing in depth, can cause cavitation in the melted part under the surface, thus leading to conditions which favor ejection of the liquid layer. For delays between 2 ps and 6 ps corresponding to the peak values of the two curves in fig. 6.4a, stress wave's magnitude increases due to an increase of the delayed pulse energy absorption. Thus tensile stresses are strong enough to cause spallation of the melted layer. For larger delays > 14 ps, electronic heat conduction initialized by the absorption of the first pulse energy is not interrupted by the delayed second pulse, the greater part of the energy has been already transferred to the crystal lattice. Thus melting of the region initialized by the first pulse starts to shrink due to resolidification before the arrival of the delayed pulse. In this case, energy cannot be cumulated due to resolidification, where the delayed pulse encounter a solid in an equilibrium state. Indeed, the surface region has enough time to expand during the laser heating and the magnitude of laser induced stresses wave decreases down to a level where spallation cannot be achieved, where the transient appearing of voids under spallation threshold can be captured by the resolidification front.

Accordingly to this experiment, a notable observation, however, is the presence of a time delay window between 0.6ps and 12ps corresponding to the liquid lifetime, where spallation and HSFL formation occur. This time delay window coincides with the generation of a liquid region induced by the first pulse, which is likely to alter the target response to irradiation by a second delayed pulse. Therefore, time required for spallation is governed by the presence of second pulse induced voids in the liquid region. Thus spallation threshold can be reduced or increased for the first and final delays in this liquid lifetime window respectively, which explains the shape of the spallation and HSFL curves.

6.6 Simulations of laser-induced melt fracture conditions

The nucleation and cavitation processes in a stretched metastable system have already been described by molecular dynamics and hydrodynamic simulations. In particular for metals, it has been shown that the dynamics of the bubbles could affect the outer surface relief on the spalled layer as the surface tension force can reach the same order of magnitude as the inertia force[238]. The response of a Ni surface to ultrashort laser pulse heating has been investigated by J.P. Colombier using the 2T-hydrodynamics code Esther[43,239], to simulate the appearance of tensile stresses subsequent to the unloading of thermomechanical stress created by the ultrafast laser heating. Following laser excitation in a sub-ablation regime, the one-dimensional in-depth calculation of the successive thermodynamic states defines the energy, density and pressure distributions for both electrons and ionic species inside the material. The investigated fluences have been set at 0.19 J/cm² and 0.38 J/cm², corresponding to previous experimental conditions and also to melting and ablation fluence thresholds, respectively. The spatiotemporal dynamics of the material density and total pressure, including electron and lattice contributions, is reported in fig. 6.5. For the lower fluence, a thin liquid film ≃ 5 nm thickness is formed at the surface between 3 ps and 18 ps (fig. 6.5a). This liquid lifetime is fully consistent with the observation of fig. 6.4, for which the first half of the double-pulse contains the same energy as used in the simulation. It means that the material response can be enhanced by a second pulse as long as the surface remains in a liquid state. For the single-pulse higher fluence shown in fig. 6.5b, the liquid layer is thicker, up to 60 nm, and the resolidification occurs at around 750 ps. This depth agrees well with the surface relief revealed in fig. 6.2. Early thermomechanical excitation of the electrons in the first picosecond is visible in fig. 6.5c, followed by the shock propagation deeper into the solid at a maximal pressure of 12 GPa. The sharp drop in pressure generates two rarefaction waves, propagating in the forward and backward directions, and creating local tensile stress which triggers potentially nucleation and cavitation processes. Based on tensile strengths of liquids, 2T-hydrodynamics simulations reveal cavitation processes under high strain rate if a relevant cavitation criterion is met.

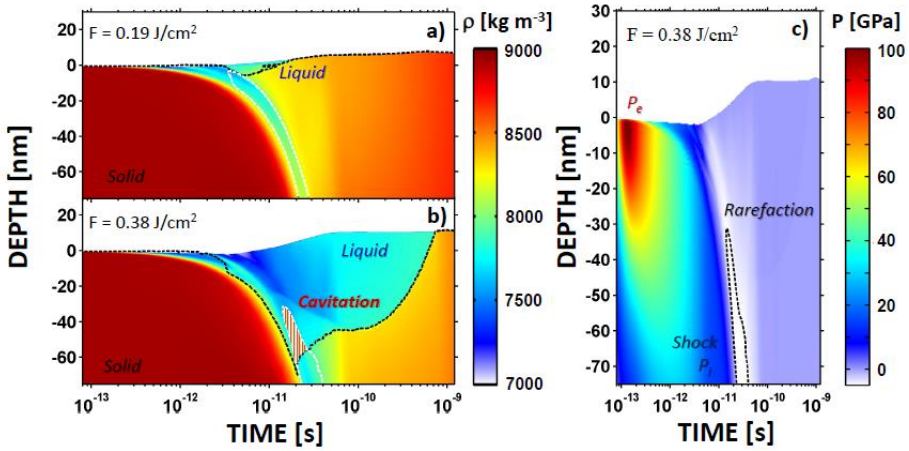

Figure 6.5 Spatiotemporal evolution of material density (a,b) and total pressure (c) calculated by a hydrodynamic simulation of a nickel sample irradiated with a 60 fs laser pulse at an incident fluence of 0.19 J/cm² (a) and 0.38 J/cm² (b-c). The black dashed lines indicate the solid-liquid interface for density evolution and the tensile strength limit for pressure diagram (c). Melt fracture is supposed to occur when the material experiences a high tensile stress in a liquid state as represented by the red hatched area in (b).

Following the Grady's criterion in liquid metals at moderately high strain rates[240], spall formation is predominantly governed by surface tension as viscosity contribution is negligible. The elastic and kinetic energies conditions to exceed the surface energy required to fracture the liquid define the melt strength Ps, which is estimated to be around ≃5 GPa. Ps limit is plotted in black dashed line in fig. 6.5c and reported in the melted zone in fig. 6.5b as a red hatched area. Following these considerations, the cavitation process in the stretched liquid is expected to occur 50 nm below the surface, between 15 and 25 ps after the laser pulse, which is fully consistent with the characteristic time to form liquid fracture t_s ≃ 9 ps derived from the Grady's model. According to this simulation, voids may be formed below the surface and the fast cooling process in about 100 ps (as visible by the swift melting-recrystallization front) can freeze the voids before they collapse under the action of surface tension.

6.7 Scenario for forming nanovoids and nanoreliefs

Taken as a whole, this work illustrates light enhancement of near-field and coherent superposition of light with far-field scattering. The periodic electromagnetic absorptions revealed by FDTD calculations for different roughnesses are visualized by post-mortem microstructural analysis. The formation of periodic nanovoids under the surface was observed and the regularly aligned nanocavitations drive the formation of $nf_{//}$. Special features $nf_{//}$ with Λ≃145 nm periodicity and subsurface nanovoids as small as 5-10 nm, spontaneously triggered by femtosecond laser. TEM observation reveals that $nf_{//}$ consist of nanopeaks of 30 nm amplitude resulting from the frozen nanojets at the edges of exploding nanovoids. Local spallation is expected to occur in tiny volumes in a self-organized and periodic arrangement, where absorbed laser energy is maximal. For microscopically rough metallic surfaces irradiated by ultrashort laser pulse, the surface energy re-distribution is non-trivial and directly related to the complex light scattering on roughness centers. As the roughness size is considerably smaller than λ, the local field enhancement, consisting of evanescent near fields along the electric field direction, follows a Rayleigh-like scattering distribution[111,241].

The superposition of the individual scattered near-fields around nanoroughness centers triggers structures elongated along the laser polarization direction with a periodicity driven by the roughness centers concentration. From the very beginning of multipulse irradiations, they develop as periodic nanocraters surrounded by nanopeaks due to localized phase transition, and spallation process. For the optimized conditions used for 2 pulses irradiations, the process of both nanopeak and void creation at nanoscale as observed in fig. 6.2 highlights the hydrodynamic nature of the high spatial frequency LIPSS formation. Exploiting feedback process for higher number of pulses, this kind of LIPSS does not survive at the center of the irradiation spot as ff⊥ (LSFL) and ff// features prevail, even if they are still present at the external region for high accumulation dose conditions. TEM cross-section discloses uniformly positioned nanovoids frozen below the surface, suggesting that nanospallation process was stopped by rapid cooling and interrogating on the dynamics of the discussed mechanism. Following the laser irradiation, a thin surface layer undergoes melting on a timescale which lasts a few ps, where the size of the liquid region is determined by the electron dependent electronic

thermal diffusion and electron-phonon relaxation time [37]. By splitting energy required to reach local conditions for solid to liquid transition, the proposed double-pulse experiment probes the liquid lifetime. Figure 6.4 shows that a maximal synergy is reached for a delay of 4 ps, corresponding to the characteristic electron-phonon coupling time as reproduced by the simulation shown in fig. 6.5. A thin liquid layer subsists 12 ps, therefore spallation is no longer possible for longer Δt. It is remarkable that local nanovoids are observed on a longer time-delay, indicating that energy required for the material to experience cavitation on the nanoscale is just below the spallation regime. Considering microstructural results on irradiated Ni (111), evidencing that nanoripples are associated with liquid layer[14], this demonstrates the $nf_{//}$ LIPSS are formed for fluence values slightly higher than melting threshold and lower than spallation regime, promoting nanocavitation process due to local field enhancement. The process has been proven to result from the rarefaction wave stretching forcefully the bottom of the liquid layer, as manifested by the hydrodynamics simulation given in fig. 6.5. The liquid layer fracturing is expected to start ~ 20 ps after the laser pulse, around 50 nm below the surface, as the kinetic energy associated with tensile stress exceeds the tensile strength. At high fluence around F_{th}, voids expansion is faster than the cooling time, and their simultaneous and coherent explosion deforms the surface, producing periodic nanoreliefs (fig. 6.2). For lower fluence, nanovoids growth is frozen below the crest of the $ff_{\perp}$ by the cooling time at the solid-liquid melt front, exhibiting an original and extraordinary embedded periodic ordering. The phenomenon is expected to be universal, thus periodic nanocavitation process may be applicable to other laser-irradiated metals experiencing a high energy confinement below the surface.

6.8 Conclusion

This chapter sheds light on the intricate role of electromagnetic and hydrodynamic mechanisms driving periodic surface modifications on ultrafast irradiated surface. The periodic nature of the mechanical response is attributed to the light self-arrangement including near-field enhancement, coherent superposition of scattered waves with incident light and roughness mediated feedback effects. The following conclusions can be drawn by combining electromagnetic modeling, TEM microstructural analysis, pump-probe-like double-pulse irradiations and hydrodynamic simulations. LIPSS formation and growth are driven by the joint effects of structured electromagnetic field distributions at the corrugated surface and the thermomechanical dynamics of the irradiated surface. In particular, highly periodic energy deposition due to local electric field enhancement on roughness centers fosters such thermomechanical conditions that drive local nanocavitation process in a periodic manner. High spatial frequency LIPSS are originated from the periodically organized explosion of nanovoids. Moreover, the embedded nanovoids have been shown to form in specific conditions, rendering the crest of classic ripples a nanoporous state. This work paves the way for evaluating optimal laser conditions to create periodic structures on the nanoscale, realized when an ultrafast laser pulse irradiates a corrugated surface to force it into a stretched liquid state. The ideal fluence should be sought between the liquid formation threshold and the photomechanical ablation regime leading to the spallation process. Mastering both surface roughness and excitation regime could help find the route to create the smallest periodic nanostructures ever produced by light.

Chapter 7

Random Coupled Nanoholes Triggering Self-Organized Nanostructures Probed by Photoemission Electron Microscopy

Feedback mechanism in the course of LIPSS formation is often evoked as the main process driving the final ripples topography. In this chapter, we employ PEEM to experimentally investigate the pulse-to-pulse evolution of the local near-field distribution on a set of light induced periodic surface arrangements of matter that consists of different periodicities induced earlier by ultrashort laser pulses with different laser shots on titanium. The experimental data are interpreted by comparison with electromagnetic simulations and calculations. While the local-field enhancement distribution is investigated on a single and collective nanoholes performed by electromagnetic calculations, we unveil the periodic character of electrons photoemitted from nanoholes in the LIPSS region, where a periodic behavior of the laser energy deposition is verified, following the same modulation of LIPSS periodicity. By correlating LIPSS periodicity with that of the photoelectron signal, we demonstrate that the concentration of the collective local-field enhancing centers play a prominent role in reducing LIPSS periodicity, combining experimental results to hydrodynamic and electromagnetic calculations. Mapping the evolution of the photoelectron signal paves the way towards a better understanding of the complex mechanisms involved in LIPSS formation.

7.1 Introduction

The combination of nonlinear laser interaction and induced material instabilities triggers the formation of self-assembled structures through optical feedback. The optical feedback concept is often argued in LIPSS formation, as the periodic behavior of the mechanical response is assigned to the light self-assembled involving optical field enhancement, coherent superposition of incident photons with scattered waves and corrugation mediated feedback effects. In the multi-pulse regime, it is generally accepted that LIPSS periodicity exhibits a decrease when the number of laser pulses impinging the target increases even if the reasons are still unclear. In fact, the physical mechanisms occurring pulse after pulse are still uncertain, as the transient location of interpulse light absorption may be dictated by the previous topography or it does drive the topography. In this study, a better comprehension is pursued, by uncloaking the role of the concentration and distribution of the local-field enhancing centers in reducing LIPSS periodicity.

Comprehending the behavior of dynamical surfaces and probing the optical response of the evolving coupling between light and roughness require microscopically resolutions able to resolve the ripples periods. On one hand, in spite of the laser-based microscopies possibility in providing femtosecond or even attosecond time domain laser pulses, acquiring spatial resolution down to a few nanometers remains intractable considering the diffraction limit of light. On the other, an inverted situation occurs when electrons are applied for imaging. In this case, nanometric spatial resolution can be attained limited by a narrow temporal resolution.

7.2 Experimental conditions

Before irradiation, Ti sample was first mechanically polished then finished with colloidal silica, providing an excellent surface mirror-like with roughness of about ~ 2 nm. Ti oxidizes slowly, which enables efficient PEEM measurements, since PEEM is sensible to the extreme surface. If the surface is oxidized, no signal can be detected. For laser-induced surface structuring, we use the same experimental setup described in chapter 2. Laser-induced surface structuring was analyzed using SEM. The sample consisted of a set of laser impacts where ripples are formed with different number of laser pulses ranging from 1 to 20 pulses at a fixed peak fluence of 0.24 J/cm² below single-pulse ablation threshold. After LIPSS formation, the sample was then analyzed by PEEM at CEA Saclay by L. Douillard. The schematic representation of the PEEM-LIPSS characterization is provided in fig. 7.1b.

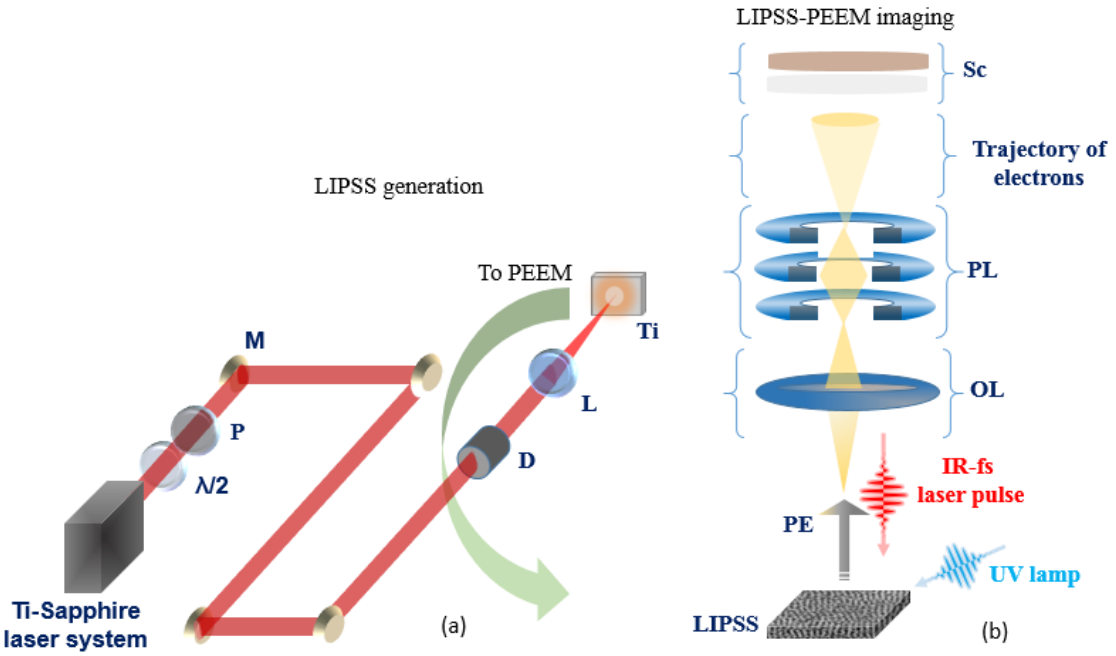

Fig 7.1 (a) LIPSS formation experimental setup and (b) LIPSS-PEEM characterization setup. In (a) P represents polarizer, M mirror, D densities, L lens and Ti Titanium sample. In (b) PE represents photoelectrons emitted from the surface, OL objective lens, PL projective lens and SC screen.

For PEEM measurements, the light source used was a cw mode-locked Ti-Sapphire laser system (Tsunami, Spectra Physics Inc.) providing IR photons with a central wavelength ranging from 720-900 nm, with pulse duration equals to 150fs. The wavelength value was fixed to 800 nm (1.55 eV) for coherency with LIPSS formation conditions. Laser pulses were focused on the sample through a normal incidence with a 500 mm focal length lens. The commercial photoemission electron microscope instrument is of Elmitec GmbH LEEM/PEEM III type, performing in ultrahigh vacuum, where pressure lies in the low range of 10^{-10} mbar, and with no energy filtering (total electron yield). The lateral resolution achieved by PEEM is 20 nm. A charge-coupled device camera (CCD) recorded digitized real-space images for ulterior investigation.

7.3 SEM characterization of LIPSS with different periodicities

In order to enable access to the dynamic of LSFL formation, LIPSS with different periodicities are formed with consecutively number of laser pulses. Fig 7.2 illustrates SEM images of 3 different sites corresponding to low (1 pulse), medium (10 pulses) and high (20 pulses) dose of laser irradiation.

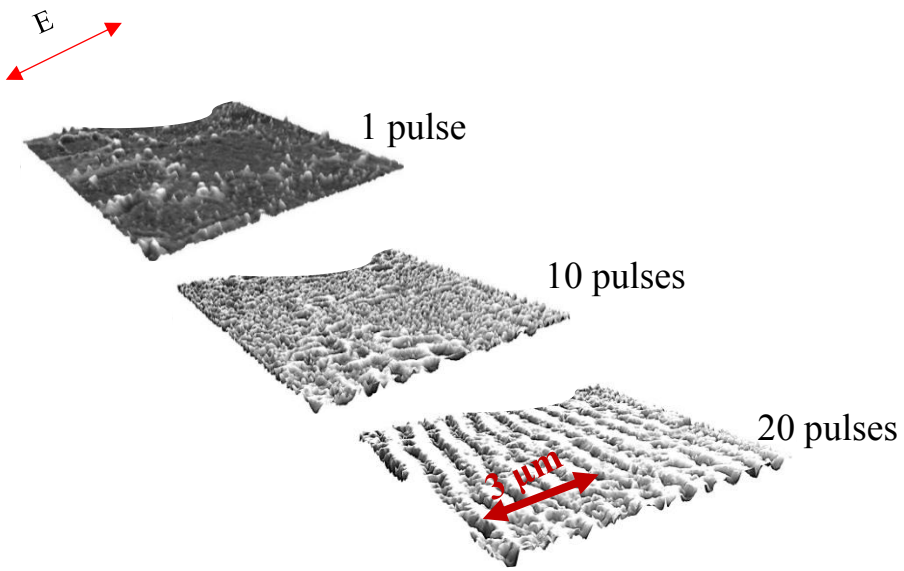

Fig 7.2 SEM images of LIPSS pre-structured with consecutively number of laser pulses starting with 1 pulse to 20 pulses at a normal angle of incidence, in the aim of dynamical PEEM study. The electric field polarization is given by the double red arrow.

The development of surface structures produced on Ti close to laser-ablation threshold laser fluence of 0.24 J/cm² is shown in fig 7.2. It shows laser-induced surface nanoroughness distributed sparsely and randomly after 1 laser shot. At 10 pulses, a microscale periodic pattern is marked over the initially induced random nanoroughness. At this phase, we observe only small patches of periodic ripples in diverse regions within the irradiated spot. Increasing the number of laser pulses bring LIPSS to grow and coalesce, leading to a clear extended ripples pattern with a period of about 640 nm for 20 laser shots.

LIPSS periodicity decreases when increasing number of laser pulses. In order to highlight this behavior, a 2D-FFT amplitude is performed for each laser impact with different number of laser pulse, allowing thus to plot LIPSS periodicity as a function of the number of laser pulses, as seen in figure 7.3.

Multiple laser pulses are necessary for the development of stable LIPSS patterns at the same spot. From fig 7.3, LIPSS final morphology saturates for applied number of laser pulses larger than 20. LSFL periodicity dependence on incident applied number of laser pulses has been studied for diverse materials in the literature and the common trend suggests that LSFL periodicity decreases as the applied number of laser pulses impinging the surface increases, until reaching the saturation regime for a high number of laser shots, developing thus a stable ripple pattern.

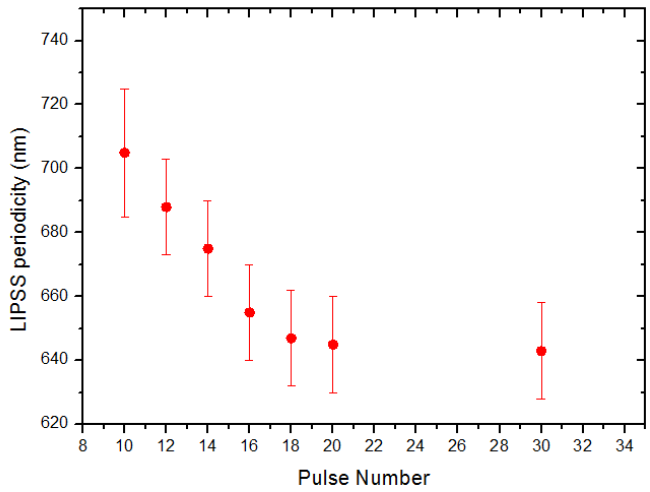

Fig 7.3 Plot of LIPSS periodicity evolution as a function of the number of laser pulses. The periodicity dispersion is indicated by the red bar.

The error bars revealing the variability of a certain periodicity are calculated by measuring the FWHM of the Lorentzian function fitting the 2D-FFT graph [Gwyddion software].

7.4 Experimental results and discussion

7.4.1 1PPE-PEEM and 3PPE-PEEM imaging

In a PEEM image, the brightness of one imaged zone is directly proportional to the number of the electrons photoemitted from that zone. Thus knowing the physical mechanisms behind electron photoemission is of high importance regarding data interpretation. Upon illumination of the Ti target with a UV lamp, electrons are linearly photoemitted since one photon (1P) absorption events produce electrons of kinetic energy exceeding the work function of Ti (4.33 eV[242]). Under IR laser illumination at a central wavelength of 800 nm (1.55 eV) and polarization perpendicular to LIPSS orientation, overcoming of the Ti work function requires a multiphoton absorption. In our case, a three photon (3P) absorption process as lowest order is expected to dominate. It should be noted that PEEM only probes the first few nm beneath the surface in relation to the inelastic mean free path of the photoemitted electrons, which gives an evidence of the presence of the electric field in this region. So, in a 3PPE-PEEM experiment, the intensity of the photoemitted electron signal is proportional to the sixth power E^6 of the local electric field, whereas linear photoelectric events scale as E^2. Areas of enhanced electromagnetic near field intensities generate high photoelectron yields manifested as hot spots on the 3PPE-PEEM images, with a spatial distribution given by the following formula:

$$Y(r)\alpha \int |E|^{2n} dt \qquad (7.1)$$

Where Y(r) represents the photoelectron yield. The net electric field *E* enhances the *n*-photon photoemission (nPPE) yield by a factor of 2n with n representing the number of photons needed to surmount the materials work function, which

is equals to 3 in the case of Ti. It is worth noting that the PEEM peculiar resolution is sample topography dependent, along with the light source and the field of view.

To guide the eye, a 1PPE-PEEM image is superimposed with a 3PPE-PEEM image of the same region, as displayed in fig.7.4a, where ripples are pre-formed with 20 laser pulses at a fluence of 0.24 J/cm². We use the cross-correlation method, described in chapter 3, in order to reveal all the photoelectrons emission centers. Extreme local-field enhancement is manifested by hot spots originated from 3PPE-PEEM, while the topography denotes the fingerprint of the 1PPE-PEEM. Here, nanoholes are represented by the white ridges. The photoemission yield can be observed enhanced in the vicinity of nanoholes. This visual observation needs further investigation on 3PPE-PEEM images, where only hot spots can be extracted. The combination of 3PPE-PEEM image with its corresponding SEM image can thus indicate the exact location of the enhancing centers.

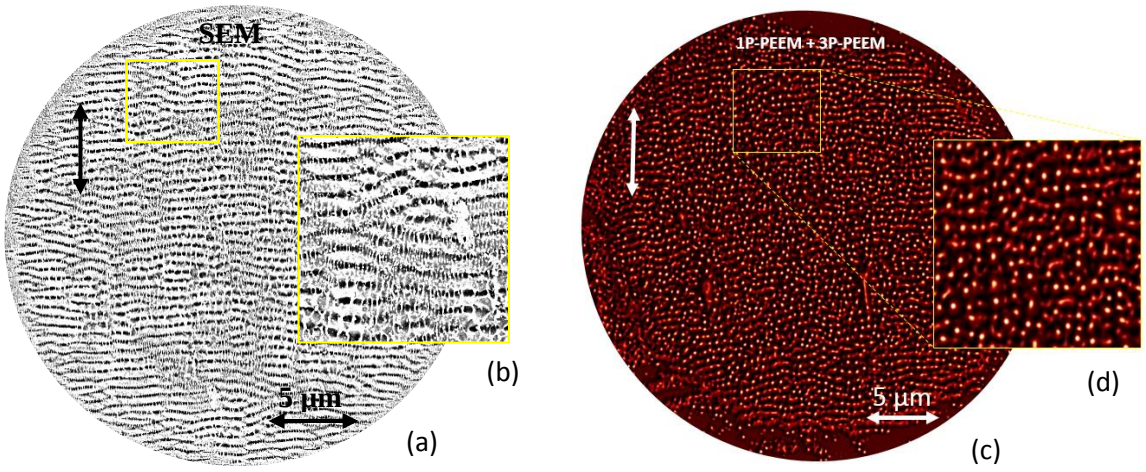

Fig.7.4 Mapping of the near-field and the topography of a site where LIPSS are formed with 20 laser pulses at 0.24 J/cm². (a) SEM image of LIPSS (b) a magnification of the yellow area where holes between structures are visible in black. (c) Combination of a 1-photon PEEM image and a 3-photons PEEM image, where the local field enhancement localization arising from 3PPE-PEEM is manifested by hot spots colored white. Here LIPSS represents regions with black color. The field of view FOV is 40 µm. (d) a magnification of the yellow square, where the hot spots are seen located in the holes region.

7.4.2 3PPE-PEEM hot spot localization and features

In order to localize the emission centers of photoelectrons, i.e. hot spots, a laser impact where LSFL are pre-formed with 20 laser pulses at 0.24 J/cm² is probed. We investigate this impact as our starting point since it provides topography with different roughness centers, where LSFL are well formed. Fig 7.5a shows a 3PPE-PEEM image probing LSFL pre-structured with 20 laser shots, where the local field enhancement is manifested by hot spots. This image is acquired simultaneously when probing the laser impact. One can consider that the hot spots, due to a greater corrugation of the nanostructures which could confine the electric field to the power sixth, would mask the signature of the coupling with lower roughness centers. Indeed, a cross-correlation between a hot spot and 3PPE-PEEM image is necessary, which

exalts all the emission centers, as shown in fig 7.5b. An FFT-amplitude is performed on the CC 3PPE-PEEM image, in order to reveal a periodicity of the photoelectrons. It is obvious from the two symmetric zones in the FFT that a periodic character of photoelectrons exists, with a high dispersion.

For better visualization of the photoelectrons periodic character as well as their emission sites, the SEM image in fig 7.5c of the corresponding area along with the PEEM cross-correlation image in fig 7.5b are superimposed, as shown in fig 7.5d. Here, the hot spots are seen to follow the structures, emitted from holes. A small yellow circle area is chosen and magnified in order to highlight this effect.

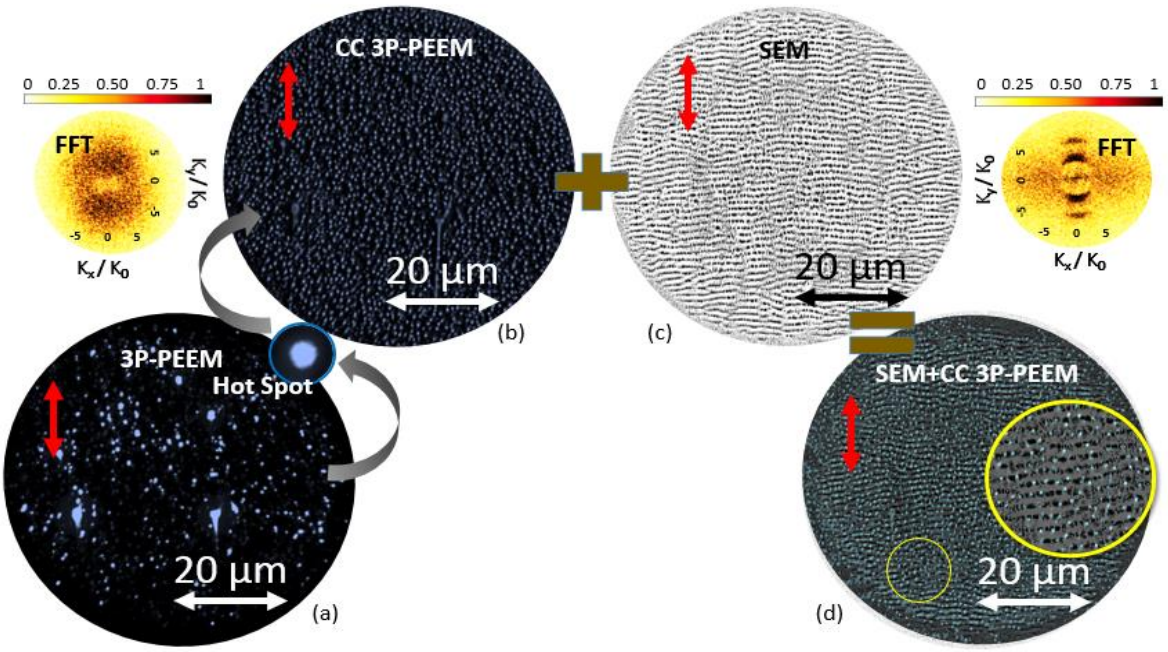

Fig.7.5 High-resolution near-field mapping of LIPSS (a) 3PPE-PEEM of a site irradiated with 20 laser pulses at an incident peak fluence of 0.24 J/cm². The red arrow shows the laser polarization. Near-field enhancement sites excited under LIPSS formation experimental conditions are imaged as hot spots colored in blue. (b) 3PPE-PEEM autocorrelation map revealing all the emitting sites, dazzled in (a). Map is obtained by correlation of the raw PEEM image with a generic hot spot profile. A 2D fast Fourier Transform FFT amplitude is performed for (b), which shows two identical symmetrical zones indicating a periodical behavior of the hot spot distribution, with a moderate dispersion of about 50 nm. (c) A SEM micrograph of the zone of interest, including a FFT of the same zone displaying a periodicity of about 640 nm with a lower dispersion. (d) Combination of (b) and (c). A magnification of the yellow circle clearly shows the location of the high near field hot spots in respect to the LIPSS topography.

It should be noted here that outside the laser impact, no signal is detected. The emitted photoelectrons results only from the nanostructures. In addition, no IR-laser induced-damage of LSFL is observed during PEEM experiment. Imaging the field enhancement at LSFL pre-formed with 20 laser shots triggers optical feedback concept investigation, owing to a modulated photoelectrons emission.

7.4.3 Dynamics of LIPSS formation

Mapping of the near field distribution for different topographies corresponding to LSFL formed with different number of laser shots constitutes a unique perspective to investigate the dynamics of LIPSS formation.

Fig 7.6 displays SEM images being superimposed with PEEM cross-correlated images for 4 different sites corresponding to LIPSS formation with 1, 5, 10 and 20 pulses. The hot spots designating the position of the electrons photoemitted are colored in blue. The images reveal a marked difference regarding the evolution of the concentration of the hot spots as well as their periodic character. In fact, photoelectrons emitted from the 1 pulse site are randomly distributed whereas they begin to evolve with increasing number of laser pulses. For LIPSS formed with 10 and 20 pulses, hot spots can be seen following the sub-wavelength structures, emitted from nanoholes. This result indicates that interpulse light absorption is located in nanoholes, which may drive the topography following subsequent pulse irradiation.

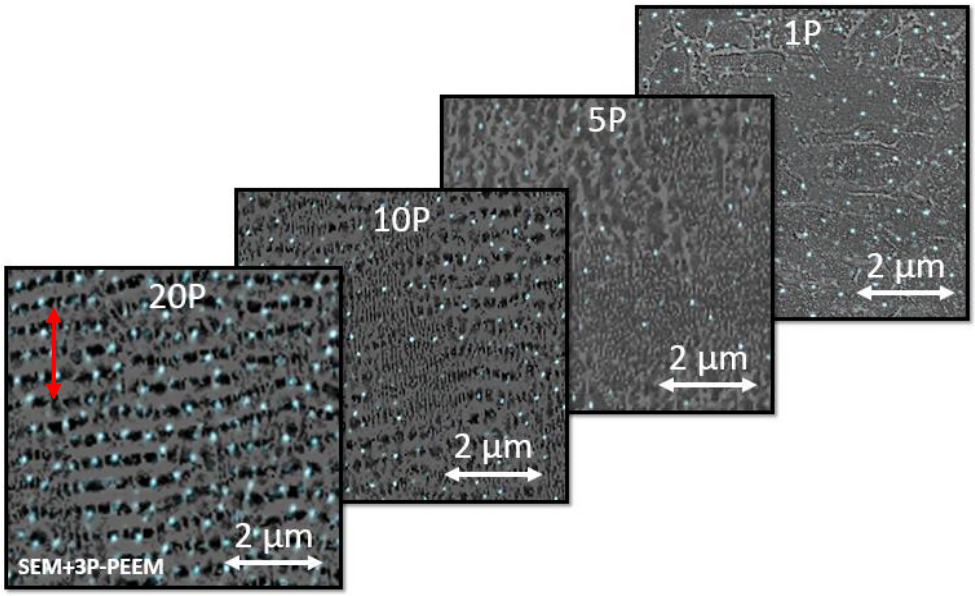

Fig.7.6 Combination of SEM and high-resolution PEEM near-field mapping of LIPSS formed with different number of laser pulses. The red arrow shows the laser polarization. Hot spots (blue points) are randomly localized in the case of 1 pulse topography and start to follow LIPSS structures when increasing the number of laser pulses. Hot spots correspond to topographical nanoholes of the metallic surface.

In order to gain access to the evolution of the hot spots concentration with respect to the number of laser pulses, we use an image processing software, Imago, developed by L. Douillard, allowing, by a system of masks, to count the hot spots on an image.

7.4.4 Link between hot spots and LIPSS periodicity

Probing the local field distribution for LSFL pre-formed with consecutively number of laser pulses has revealed that the energy is deposited in peculiar locations, i.e. nanoholes, where the emission yield of the photoelectrons is high, imprinting a hot spot. The emitted photoelectrons were shown to be randomly distributed for low number of laser pulse irradiation, and follow the periodic nanostructures when increasing the number of laser shots. Since photoelectrons are seen to follow LSFL, an attention should be addressed to their periodic character.

Fig 7.7a shows a plot of LIPSS and photoelectrons periodicity as a function of the number of laser pulses. LIPSS periodicity is extracted from the SEM-FFT amplitude analysis shown in fig 7.7c. In order to obtain a complementary visualization of the field distribution on the LSFL topography, we plot the radially average autocorrelation, i.e. RAA, for each image with consecutively number of laser pulses corresponding to the CC 3PPE-PEEM. RAA function enables to highlight possible periodicities of a given image, which is sometimes difficult to apprehend from the original image, as in the case of circular hot spots. The autocorrelation function is calculated here as the inverse Fourier transform of the product of the Fourier transform of the image with its conjugate. Fig 7.7b shows the normalized autocorrelation of the emitted photoelectrons from three different sites, which includes LIPSS formed with 5, 10 and 20 laser shots.

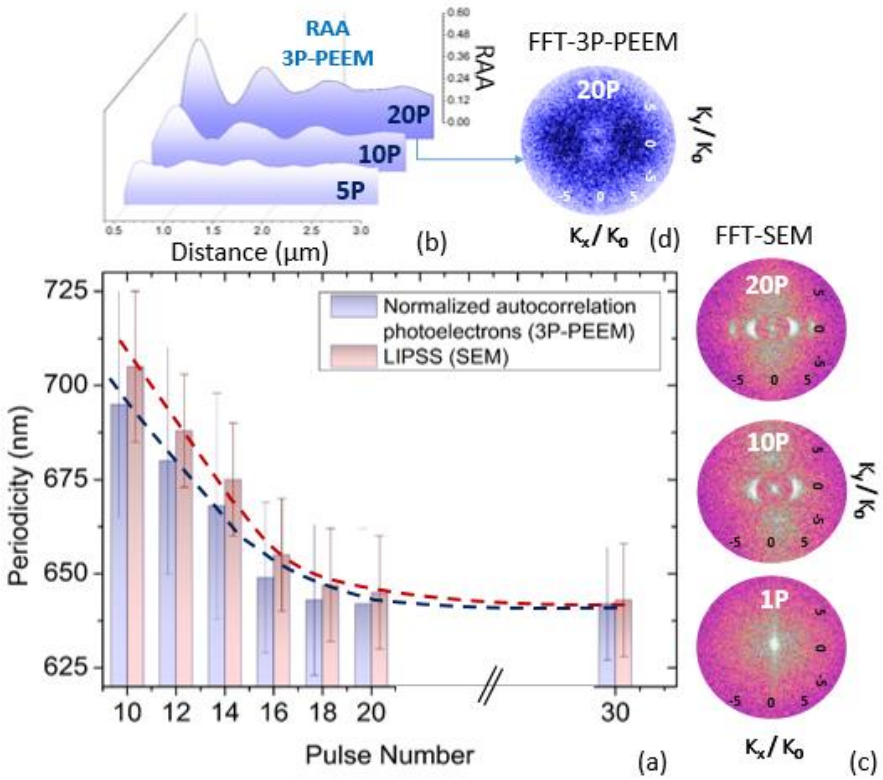

Fig.7.7 Evolution of LIPSS and photoelectron site periodicity as a function of the number of laser pulses. (a) a diagram plot of LIPSS periodicity obtained by the FFT performed on the corresponding SEM images for sites irradiated between 10 and 30 pulses, and photoelectron site periodicity obtained by the radially average autocorrelation RAA performed on the corresponding cross correlated 3PPE-PEEM images for the same sites. Red and blue diagrams represent LIPSS and photoelectron site periodicity, respectively. (b) FFT of LIPSS (c) RAA of photoelectrons as a function of the distance and (d) FFT of a 3P-PEEM image for a 20 pulses LIPSS site.

The RAA plot confirms a periodicity character associated to photoelectrons. It is obvious that a periodic character of photoelectrons starts at 10 pulses where the first peak of the curve is located at 668 nm. This periodic character is amplified for LIPSS formed with 20 pulses, where the first peak of the corresponding curve is shifted down by 23 nm to a periodicity of about 645 nm.

The dashed blue and red curves in fig 7.7a represent the evolution of the photoelectrons and LIPSS periodicity as a function of the pulse number, respectively. For LIPSS pre-structured with moderate number of laser pulses, i.e. 10 pulses, a shift between the two curves is present, which decreases when increasing the number of laser pulses, reaching saturation for high number of laser pulses.

Examining carefully the emission centers of photoelectrons, i.e. holes, by superimposing the CC 3PPE-PEEM of each image with its corresponding SEM image, suggests that the energy is deposited in the valleys, where the optical intensity is always larger than that of the ridges, which deepens thus the valleys through local-field enhancement. As a consequence, the ripples pattern is enhanced via positive feedback. Surface topography dynamic as well as LIPSS periodicity evolution with the applied number of laser pulses is a question congenitally linked to the feedback nature. This involves a strong connection between interpulse laser-induced surface roughness and the field, where several scenarios were proposed including plasma gradients, plasmonic contribution and effective optical indices of corrugates surfaces[99,243]. An untimely ripple pattern develops on the surface after the first laser pulses, where valleys and ridges are formed on the surface morphology. Subsequent laser pulses interact with an amended surface, where the local field is enhanced by peculiar regions.

Our results show that this decrease in LSFL periodicity is directly linked to the periodicity of photoelectrons, evidencing that the energy is deposited with a periodicity lower than that of the LSFL.

7.5 3D electromagnetic calculations

7.5.1 Solving Maxwell equations

Electromagnetic simulations are performed with the help of Anton Rudenko at Hubert-Curien laboratory by using 3D Finite-Difference Time-Domain method with $\Delta(x,y,z) = 20$ nm resolution and 1000 x 1000 x 150 calculation cells. The intensity I is calculated by averaging the sum of squared electric fields over 30 optical periods, corresponding to θ = 40 fs (FWHM) pulse duration of temporally Gaussian pulse at λ = 800 nm irradiation. The optical properties of Ti with n=3.14 and k=4.0 for the laser wavelength λ = 800 are used in simulations, whereas holes are half-spheres with n=1 and k=0. Convolutional perfect matched layers (CPML) of 15 cells thickness are applied on the borders of the grid to avoid non-physical reflections. The spatially focused Gaussian beam is chosen as the source with w_0 = 20 µm beam waist, linear polarization along Y axis and propagation along Z axis.

7.5.2 Analysis

SEM image in Fig. 7.5c gives us complete information about the three-dimensional surface topography. The energy deposition on the surface irradiated by 20 pulses is then calculated by Finite-Difference Time-Domain method, solving full-vector Maxwell equations. The intensity in cube below the surface is traced in Fig. 7.8a and correlates well with 3PPE-PEEM image in Fig. 7.5b. The hot spots correspond here to the positions of the deepest holes, whereas the periodic patterns are less intense. The calculations reveal the inhomogeneous nature of the topography below LIPSS.

To elucidate the role of the nanoholes in the establishment of final interference patterns and possible LIPSS pulse-by-pulse evolution, we perform electromagnetic simulations with different concentrations of randomly distributed nanoholes of R = 20 nm below surface.

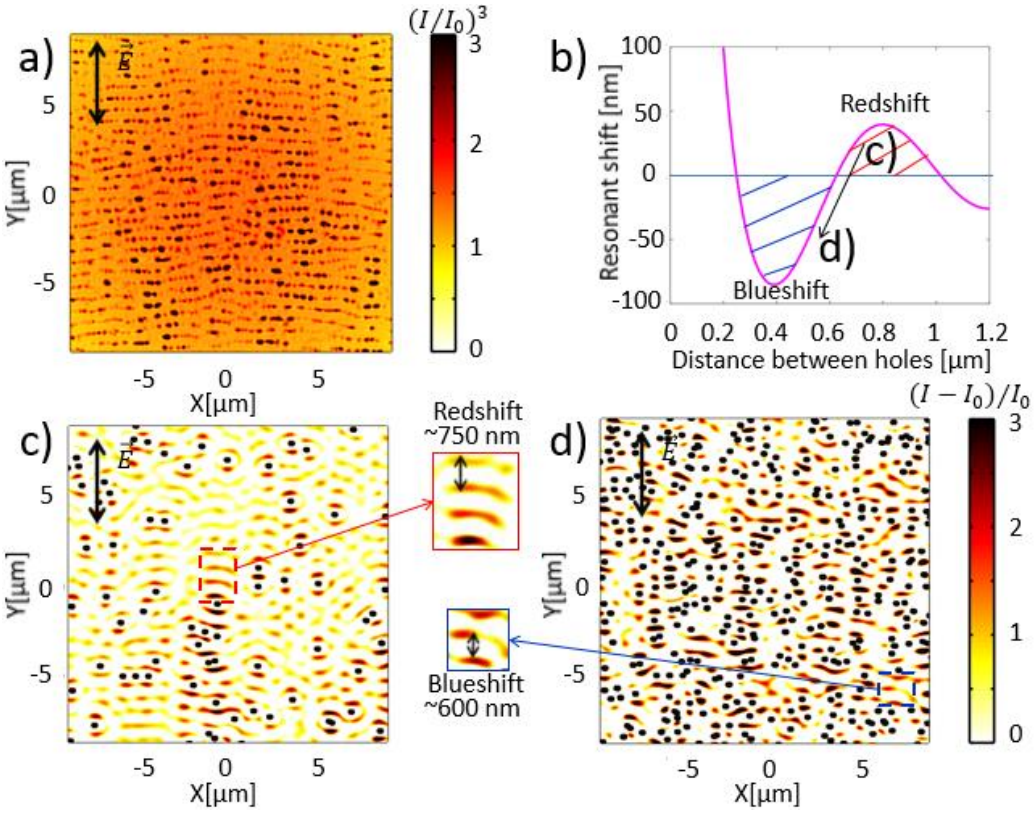

Fig. 7.8 (a) cubic intensity distribution I^3 calculated by 3D-FDTD simulations 20 nm below Ti rough surface with experimentally defined topology shown in Fig. 7.3c in the transverse plane perpendicular to laser propagation. (b) Predictions of resonant wavelength shift as a function of the average distance between the nanoholes by coupled-dipole approach. (c,d) Intensity distributions below the surface with randomly distributed nanoholes of R = 20 nm and average spacings (c) d = 1 nm and (d) d = 500 nm.

The absorbed energies corresponding to the nanoholes with average spacing of d = 1 nm and d = 500 nm are shown in Figs. 7.8c,d. The collective effects of coupled nanoholes influence the periodicity of the resulting interference patterns. For larger nanohole spacing, the period is found to be close to laser wavelength 750 nm, whereas for subwavelength

nanohole spacing the period is significantly smaller 600 nm due to the surface wave retardation by the presence of the nanoholes. The simplest model which takes account for the phase retardation is the coupled-dipole model, based on discrete dipole approximation[244–246] . Such an approximation is valid if the holes are significantly smaller than the laser wavelength R << and the distances between them are few times larger than their sizes d >> R.

Following this approach, the collective response of the system as well as the resonant frequency shift are defined as a function of the positions of dipoles. For instance, the dependency between the resonant shift and the average distance between the nanoholes is plotted in Fig. 7.8b. While decreasing the distance between the nanoholes, the resonant wavelength shifts to smaller values, which is obtained by FDTD simulations. The characteristic blue shift was previously evidenced by optical spectroscopy of randomly distributed nanoholes on thin gold films[247] . According to our simulations, the situation with average distance between the dipoles of 625 nm corresponds to a local equilibrium, which coincides with final saturated LIPSS periodicity. We can conclude that the periodicity of LIPSS follows the average spacing between the nanoholes pulse-by-pulse, approaching the saturated value, where no further resonant wavelength shift is expected.

7.6 Conclusion

In this chapter, the interpulse feedback mechanism driving the final topography of LIPSS is outlined by employing the photoemission electron microscopy. The results indicate that light absorption is localized and enhanced in the vicinity of nanoholes, evidencing a modulated energy deposition. The periodicity of the emitted photoelectrons, which can be manifested by hot spots, is lower than that of LIPSS for a low number of applied laser pulses, and then saturates when increasing the number of laser pulses. To elucidate the role of nanoholes in the constitution of final interference patterns and possible LIPSS interpulse evolution, the experimental results were coupled to electromagnetic calculations with different concentrations of randomly distributed nanoholes. It was found that LIPSS periodicity follows the average spacing between the nanoholes pulse-by-pulse, approaching the saturated value, where no further resonant wavelength shift is expected.

Chapter 8

Surface-roughness control generating nanoholes with extreme periodicities by double-pulse experiment

In this last chapter, we address the control of surface-roughness by investigating the dynamics and physical mechanisms leading to unconventional nanostructures formation, i.e. nanowells with extreme small periodicities. For that purpose, one-color double fs-pulse experiment involving a Mach-Zehnder interferometer is employed to irradiate Ni and Cr monocrystalline samples. The results show that one can obtain an array of nanoholes with 20 diameters spaced as small as 60 nm. The onset of nanoholes array structures formation requires a time-delay window between the pulses, dependent on the incident fluence and the state of polarization between the two delayed pulses. Structuring surfaces with nanoholes of 20 nm in diameter and 60 nm in spacing by direct femtosecond irradiation paves the way towards potential applications. This work is the object of the patent number 1856499.

8.1 Introduction

From light-induced random surface disordered conformations to anisotropically periodic self-arrangement of matter, driven optical local field enhancement and resonant excitations enable electromagnetic field design. The combination of nonlinear interaction with light aspects and matter instability on surface topographies triggers self-assembled structures formation through optical feedback. We have seen in the previous chapters that ultrafast laser energy can be confined on nanometric spatial scales by nonlinear interaction, where matter can be structured beyond the diffraction limit by the mean of an inhomogeneous localized absorption event. The onset of LIPSS formation was shown to be influenced by the surface topography, where the size and shape of the roughness centers play a significant role in HSFL formation as seen in chapter 4, and by defects generation as shown in chapter 5. Thus the control of the surface topography can influence HSFL features, and can generate unconventional structures, i.e. holes. The formation of holes structures was reported to be highly dependent on the surface inhomogeneities and roughness features[248] .

Nanometer scale dimensions nanoholes array structures have gained an increasing attention for their potential applications, which will be discussed at the end of this chapter. Nanohole structures on semiconductors have been successfully produced by direct electrochemical etching[249], self-assembly nanosphere mask[250] and laser assisted nanosphere imprinting[251] on Silicon. Furthermore, nanoholes were also produced by electron beam lithography and focused ion beam in a point by point process, where structuring a large surface of nanoholes can be time exhausting. However, it remains difficult to fabricate nanoholes on metal surfaces despite their high melting and boiling temperature[252]. Nevertheless, few groups have successfully fabricated holes on metals by the mean of pulses lasers. Pronko and his coworkers (1995) produced a 300 nm hole by a 3 µm spot size beam on Ag using a 200 fs pulsed Ti:sapphire laser[253]. Perrie et al. ablated Al (2004) in a He environment with a beam diameter of 300 µm employing a raster scan pattern, and fabricated microholes throughout the scanned area. The pattern of microholes was irregular in size and arrangements, with diameters close to 15 µm[254]. Nayak and Gupta (2010) irradiated a Ti foil at a peak fluence of 1.2 J/cm² with 1000 laser shots in order to generate random holes[255]. The size of the holes varied from a few micrometers to a few hundred nanometers. The production of large scale and low-cost of nanoholes is remaining a challenge[256]. A fast nanoholes fabrication with extreme periodicities and dimensions on metal surfaces employing direct laser irradiation has not been reported before.

This chapter offers a new experimental setup for the generation of ‘nanowells’ with ultimate periodicities by controlling the transient surface roughness. Owing to non-altered surface, scattering process is reduced conserving the isotropy of the surface. With extreme irradiation conditions, some period agencement of nanoholes are reported on fcc (Nickel), with periodicities as small as 60 nm.

8.2 Experimental conditions

In this work, a Ni monocrystalline sample with (100) orientation was irradiated by one-color double-fs pulse sequence using a Mach-Zehnder interferometer, described in chapter 2. The sample was polished using the same procedure explained in chapter 2. Temporal delay Δt between both pulses of a sequence was scanned between -50ps and +50ps (resolution better than ~0.15ps). The beam wait diameter was 50 µm. Concerning the polarization state of both pulses, a half-wave plate inserted in one interferometer path optionally rotated the polarization direction. In this work, we use mainly crossed polarization, *s* and *p* polarization states. Negative delays implies the arrival of s-polarized pulse prior to *p*/*s*-polarized pulse. The number of single pulses is designated by N_{SP}, and N_{DPS} denotes the number of double-pulse sequences. Each pulse of the double-pulse sequence is kept below the LIPSS formation threshold of the corresponding material. Thus the joint action of the double pulses lead to LIPSS formation. In other terms, 'sub-damage threshold conditions' were realized in all cases. Laser-induced nanostructures, namely nanoholes and HSFL, are characterized using SEM.

8.3 Nanoholes formation features

The surface morphology of the achieved nanoholes arrays is characterized by SEM in secondary electron imaging mode. Fig 8.1a illustrates a SEM micrograph of a site irradiated with double-pulse sequences on a Ni (100), where N_{DPS} equals 25, at a peak fluence of 0.24 J/cm² and a time-delay of 24 ps. The polarization between two delayed pulses of a sequence is crossed. For a better visualization of nanoholes, a magnification of a small area from fig 8.1a is performed.

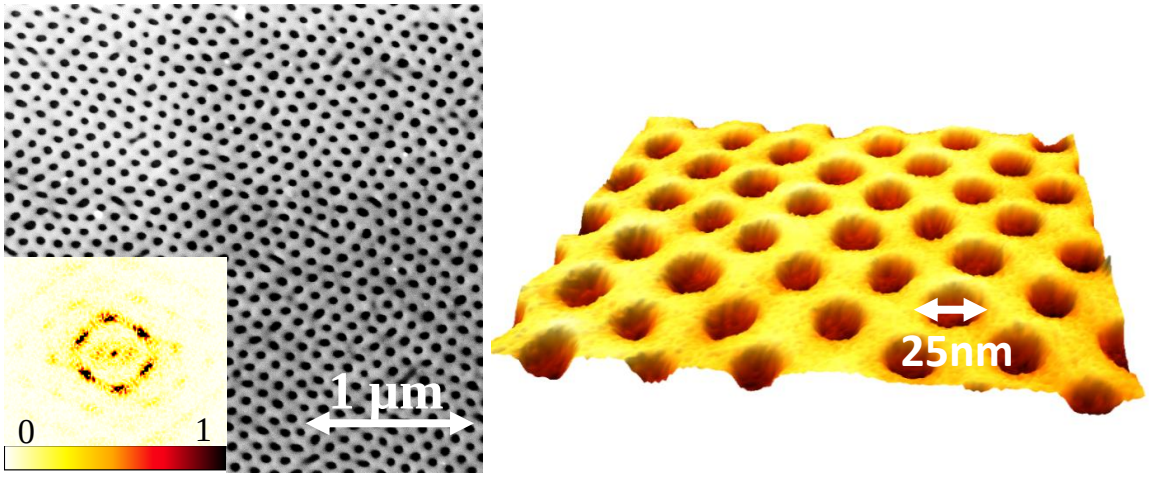

Fig 8.1 (a) SEM micrograph of laser-induced nanoholes generated on Ni (100) surface orientation by double-pulse sequence at 0.24 J/cm², where the number of double pulse sequences was set to 25. The FFT performed on (a) is given as inset in the left side of the image. (b) A treated SEM micrograph of (a), as a 3D perspective to observe the scale of the nanoholes.

The unconventional structures generated in this experiment consist of nanoholes which form an hexagonal array, with periodicities close to 60 nm. From the SEM image, the average diameters of nanoholes is determined to be 25±5 nm. The achieved area equals approximately 15x15 µm². Larger areas can be structured using point by point irradiation method or by line scan method. The 2D-FFT performed on fig. 8.1a highlights the hexagonal arrangement of nanoholes.

In order to address the physical mechanisms behind nanoholes growth and their morphology features, experimental parameters variation is required. In this section, we investigate the impact of the polarization of the two pulses, the time delay between the two pulses of a sequence, the pulse fluence and the number of laser pulses. A window of experimental parameters accounting for a well-defined nanoholes formation is revealed.

8.3.1 Incident pulse fluence dependence

In this section, we irradiate Ni (100) with 25 laser pulses at an incident fluence ranging from 0.18 J/cm² to 0.4 J/cm², by scanning the time-delay between the two pulses of a double-pulse sequence starting from 0ps till 50ps. The polarization of the double pulses of a sequence is crossed. Fig. 8.2 shows laser induced pattern formation as a function of the peak fluence and time-delay. Above a fluence value of 0.34 J/cm², and for all time-delays, only LSFL formation was observed exhibiting an orientation perpendicular to the polarization of the second pulse and periodicity close to the laser wavelength (632 nm). For delays between 0ps and 12ps, a turbulent surface topography is induced, where no familiar pattern can be observed for fluences lower than 0.34 J/cm². Chaotic and rugged structures are favored by low-fluence for short time-delay irradiation. For time-delays between 12ps and 30ps, different patterns can be induced in the same irradiated spot, in the fluence range of 0.18-0.36 J/cm². Only for a narrow values of time-delay and fluence highlighted by the dashed blue lines in fig 8.2, nanoholes can be formed in the total area of the irradiated spot. The nanoholes were formed at a fluence between 0.2-0.26 J/cm² for a time-delay between 20-30ps. In this time-delay window, increasing fluence to 0.28 J/cm² leads to the formation of HSFL and to LSFL formation aside HSFL and nanoholes for fluences between 0.28 and 0.36 J/cm².

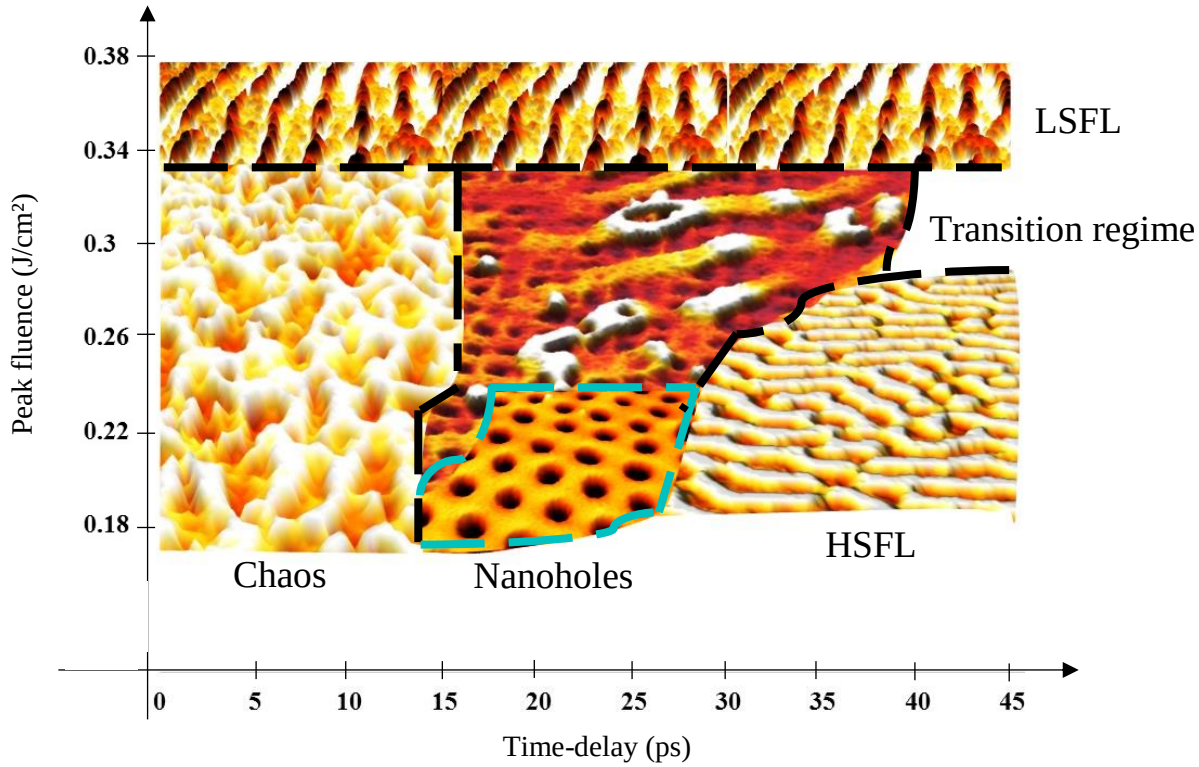

Fig 8.2 Laser-induced pattern formation as a function of the peak fluence and time-delay imposed between the pulses of a double pulse sequence. Different zones are limited by the dashed lines. The zone of interest is delimited by the blue dashed lines. The applied number of double-pulse sequences was set to 25.

It is obvious that for high fluences (above 0.38 J/cm²), LSFL formation is not influenced by the time-delay imposed between the two pulses of a sequence. In fact, the first pulse of the double pulse sequence has sufficient energy to cause LSFL formation. The second pulse then promotes the spatial pattern already marked by the first pulse. Repetitive irradiation (N_{DPS}= 25 in our case) carries on incubation effects until the damage threshold of the sample is locally surpassed and the surface gets rippled.

A coexistence of LSFL, HSFL, and nanoholes is observed in the same irradiated spot, highlighted by the blue zone in figure 8.3. The three different regions, observed in fig 8.3, can be explained by a Gaussian beam profile, as implemented by the blue curve on the laser spot. In this case, these 3 regions appear due to different fluence threshold F_{LSFL}, F_{HSFL} and F_{NH}. In the center of the processed area, due to the highest fluence value, LSFL with period close to laser wavelength and orientation perpendicular to the polarization state of the second pulse appear. Taking into account the laser parameters in our experiment, the peak fluence equals 0.33 J/cm^2 and the single pulse ablation threshold of Ni equals 0.4 J/cm^2. It can be therefore concluded that LSFL appear for fluences between 0.17 and 0.33 J/cm^2, HSFL between 0.20 and 0.12 J/cm^2 and nanoholes between 0.12 and 0.04 J/cm^2.

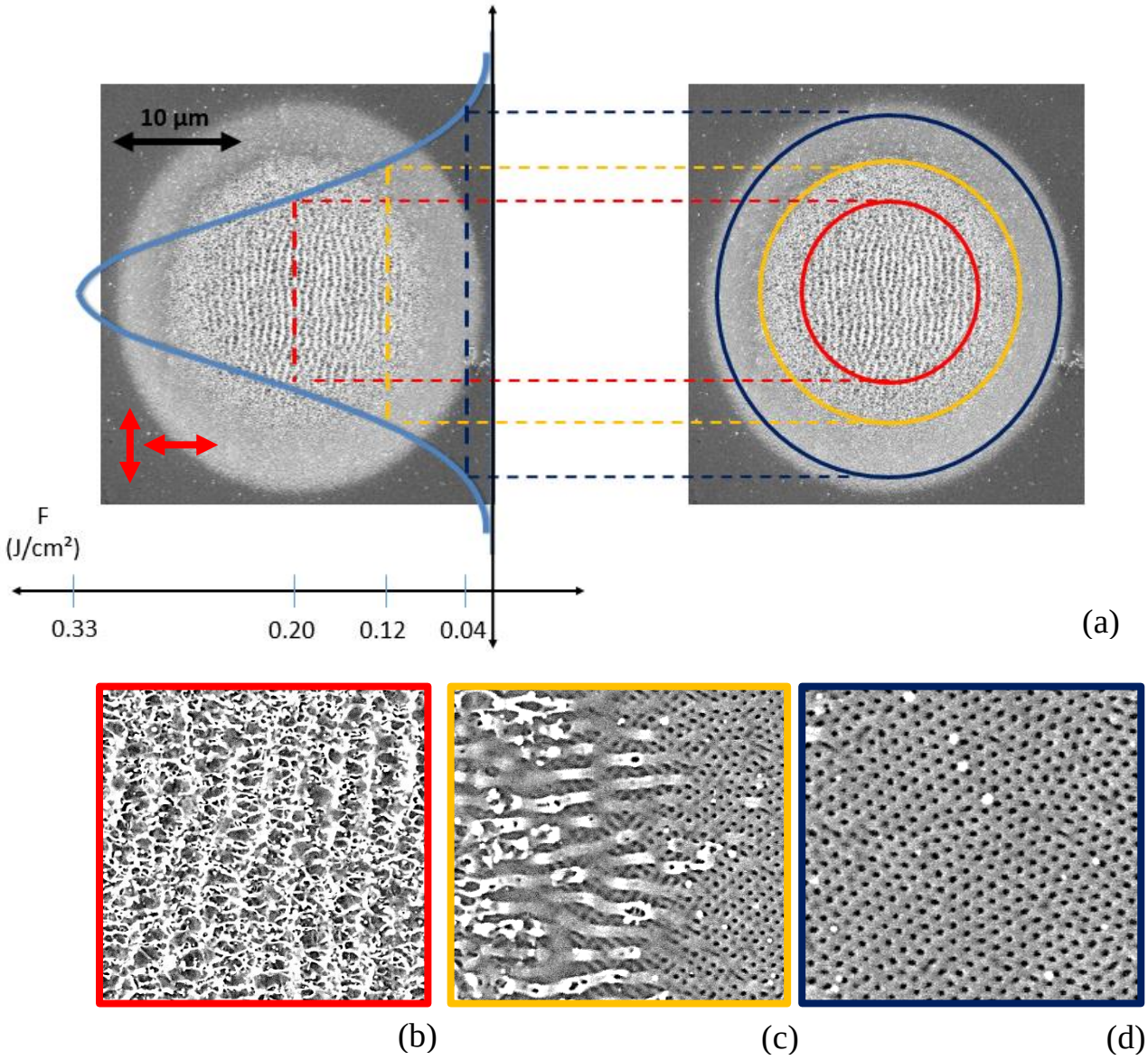

Fig 8.3 (a) SEM micrograph of a site irradiated with a train of double-pulse sequences at a peak fluence of 0.35 J/cm² and N_{DPS}=25. The polarization between the two delayed pulses of a sequence is crossed and presented by the red arrows. The Gaussian beam profile is inserted onto the SEM image in order to investigate the laser-induced periodic nanostructures as a function of the local fluence, where the different regions of LIPSS are marked by colored circles. The red circle corresponds to the local fluence where LSFL are formed and shown in (b), whereas the orange circle corresponds to the coexistence of HSFL parallel to the second pulse polarization, and nanoholes, displayed in (c). The dark blue circle indicates the presence of nanoholes, as shown in (d).

8.3.2 Polarization dependence and time delay-dependence

An intriguing characteristic of the nanoholes arrangement is its strong dependence on the state of polarization of the incident pulses in the double-pulse sequence. Fig 8.4 shows SEM images of different sites performed by fs-double pulse sequences by varying the laser polarization. The delay between the two pulses was set to 24 ps, for a number of

laser pulses equals to 25 at a peak fluence of 0.24 J/cm². These images show the evolution of the nanoholes on Ni (100) surface as a function of the laser polarization. When the two pulses impinging the surface are of the same polarization (parallel), nanoripples of periodicity close to 60 nm are generated parallel to the incident polarization. When rotating the polarization of the second pulse by a half-wave plate, the nanoripples pattern follow accordingly to the second pulse polarization, without any interrelation to the target orientation. When switching to crossed polarization, the arrangement of nanoripples is influenced. Rather than elongated, ordered chains of linear nanostructures, nanoholes are formed. By comparing the results obtained with different polarization states, most apparent difference can be seen with the suppression of nanoripples formation when the polarization of the two-delayed pulses is crossed.

Fig 8.4 SEM images of three different zones irradiated with N_{DPS} = 25 at 0.24 J/cm² with a time-delay of 24ps. The polarization between the pulses of a sequence is varied. Nanoholes are formed only for crossed polarization.

The investigation of the dynamics of the material surface requires insertion of a time-delay between pulses impinging a surface. When the first laser pulse of the double-pulse sequence train arrives at the surface, a part of its energy (about ~ 30%) is absorbed and relaxed via electron thermal diffusion as well as electron-phonon coupling, thus launching a fast and localized isochoric heating, undergone by surface melting. Whereas the first pulse can perturb electronic band structures and drive the system into a non-equilibrium thermal state, time-delay at which the second pulse in the double-pulse train arrives at the surface determines the complex interplay between excitation and relaxation processes.

Fig 8.5 shows a series of SEM images of different laser processed areas performed by varying the time-delay Δt between two pulses of a sequence from 0ps to 50ps. The irradiation was carried out with a peak fluence of 0.24 J/cm² and N_{DPS} of 25 pulses. These images show thus the evolution of surface topography, where nanoholes are formed for a time-delay window between 18ps and 30ps. For shorter Δt, lower than 10ps, a chaotic surface topography is induced. This can be interpreted on the fact that hot electrons at the surface of the material generated by the first pulse are further excited by the second pulse before the energy transfer from the electrons to the lattice. Then the double-pulse together works somewhat similar to a single pulse at a fluence of $2F_{DP} < F_{th}$. As a result, no spallation nor material organized nanostructures are formed, as the energy is not sufficient to cause cavitation in the melted subsurface region. This time window corresponds thus to the cumulating regime as the second pulse arrives before thermal/mechanical relaxation.

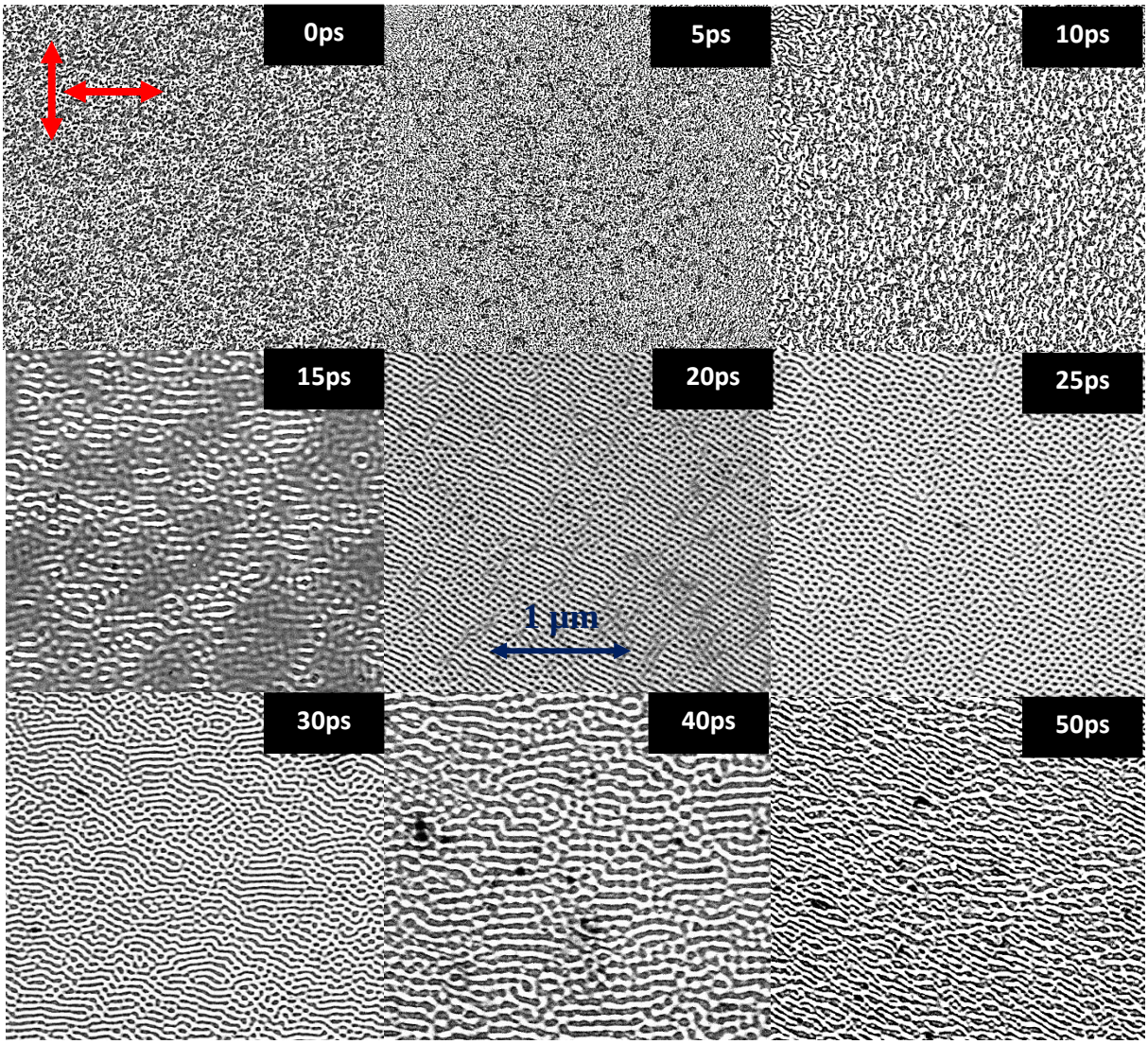

Fig 8.5 A series of SEM images of different sites irradiated with varied time-delay double-pulses sequences, where N_{DPS} = 25 at a fluence of 0.24 J/cm². Here, the polarization between the two delayed pulses of a sequence is crossed and represented by the red arrows. The dark blue scale is true for all the images.

For delays between 12ps and 30ps, a strong modification of thermodynamic and optical properties of the material can occur. Therefore, absorption of the second delayed pulse laser energy increases due to a decrease in Ni reflectivity, which favors conditions leading to voids formation in the liquid region. In this case, energy exceeds spallation threshold, where it is sufficient to cause cavitation, followed by spallation of the melted layer. In fact, first pulse energy has sufficient time to be delivered from the excited electrons to the atomic vibrations, which leads to a rapid heating and forms a liquid region of depth depending on the first pulse fluence. A second delayed pulse will encounter a melted zone which can influence laser induced processes in the surface region of the irradiated target. Interaction between second delayed pulse and the liquid region induced by the first pulse provides the driving force for a buildup of high compressive stresses in the surface region of the irradiated target. An unloading tensile component of the stress wave is generated following the relaxation of the compressive stress in the presence of free surface. These tensile stresses, increasing in

depth, can cause cavitation in the melted part under the surface. The effect of crossed polarization will affect cavitation. Whereas the first pulse of the double sequence will cause cavitation and stretch the induced voids in its polarization direction, the second delayed pulse will stretch the voids in the other direction, which can potentially suggest the role of crossed polarization to explain nanoholes formation in this time-delay window.

For larger delays > 30 ps, electronic heat conduction initialized by the absorption of the first pulse energy is not interrupted by the delayed second pulse, the greater part of the energy has been already transferred to the crystal lattice. Thus melting of the region initialized by the first pulse starts to shrink due to resolidification before the arrival of the delayed pulse. In this case, energy cannot be cumulated due to resolidification, where the delayed pulse encounter a solid in an equilibrium state. Indeed, the surface region has enough time to expand during the laser heating, imprinting thus a transient surface roughness. The second delayed pulse induces local-field enhancement parallel to the polarization on the roughness created/re-excited by the first one, triggering HSFL formation parallel to the electric field polarization. In chapter 6, a notable observation, however, was the presence of a time delay window between 0.6ps and 12ps corresponding to the liquid lifetime, where spallation and HSFL formation occur, for a fluence of 0.38 J/cm². In our case, this time-delay window starts at 12 ps till 30 ps for a fluence of 0.24 J/cm².

8.4 Dynamics of nanoholes formation

Resolving the pulse-to-pulse development of self-arranged periodic nanostructures requires irradiating a material with consecutively number of laser pulses, which can reveal the optical feedback on surface topographies and allows to clearly elucidate the role of inter-pulse laser-induced topography in establishing and developing nanoholes pattern. Fig 8.6 displays SEM images of the nanostructures evolution as a function of number of laser pulses, irradiating Ni(100) at a peak fluence of 0.24 J/cm^2 and a time-delay of 24ps. The onset of the pattern formation is observable following irradiation with a sequence of double-fs pulse. The pattern acquires good visibility after 10 pulses sequences of double pulses. It should be noted here that nanoholes are randomly non-organized for the first N_{DPS}, then begin to evolve in order to form an hexagonal array for a larger N_{DPS}.

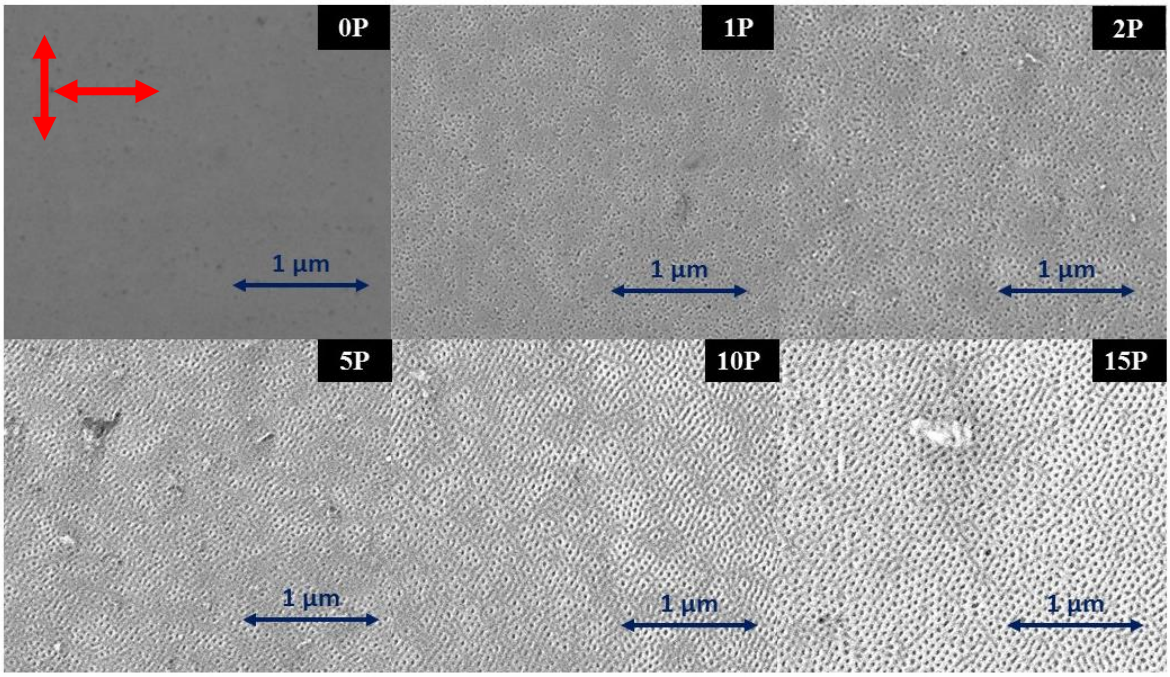

Fig 8.6 SEM images of different sites irradiated with consecutive N_{DPS} with a time-delay of 24ps, a fluence of 0.24 J/cm². The polarization of the delayed pulses of a sequence is crossed and marked by the red arrows.

SEM images of the complete consecutive number of laser pulses series were subjected to two-dimensional fast-fourier transform 2D-FFT. The peaks in the 2D-FFT allows the determination of a lower and upper limit of nanoholes period, which is displayed by error bars in the graph in fig 8.7a. The striking result here is that the periodicity of nanoholes increases when increasing the number of laser pulses, until reaching saturation at 20 pulses. An increase of laser-induced nanostructures periodicity had never been reported before in the literature. One can imagine that the nanoholes coalesce when increasing the number of laser pulses. For a more accurate analysis of nanoholes periodicities and concentration, radially average autocorrelation RAA was performed on the SEM images with different consecutive number of double laser pulses irradiation using ImageJ analysis software[257]. The results are shown in fig 8.7b where we plot the RAA as a function of the distance and the number of laser pulses. RAA calculates the autocorrelation (referred to as pair correlation or two-point correlation) of an image pixels as a function of distance. In spite of the fact that it employs the Fourier transform, it does not experience artifacts caused by the 'periodic' nature of the FFT. The autocorrelation provides information about the typical feature size in an image. The initial slope, first zero and first minimum cover information about the nanoholes dimensions, while the first maximum of the autocorrelation provides the typical distance between two nanoholes. From fig 8.7b, we show that nanoholes formation starts after irradiation with $N_{DPS}= 1$, where the first peak of the RAA is located at a distance of ≃ 63 nm. Increasing further the number of the double-pulse sequences to 6 lead to an increase in the nanoholes concentration, which can be explained by the appearance of multiple peaks in the yellow RAA curve. More pronounced peaks can be observed when increasing $N_{DPS.}$ It can be deducted that nanoholes are distributed randomly first, then begin to evolve periodically until reaching saturation at ≃ 77 nm.

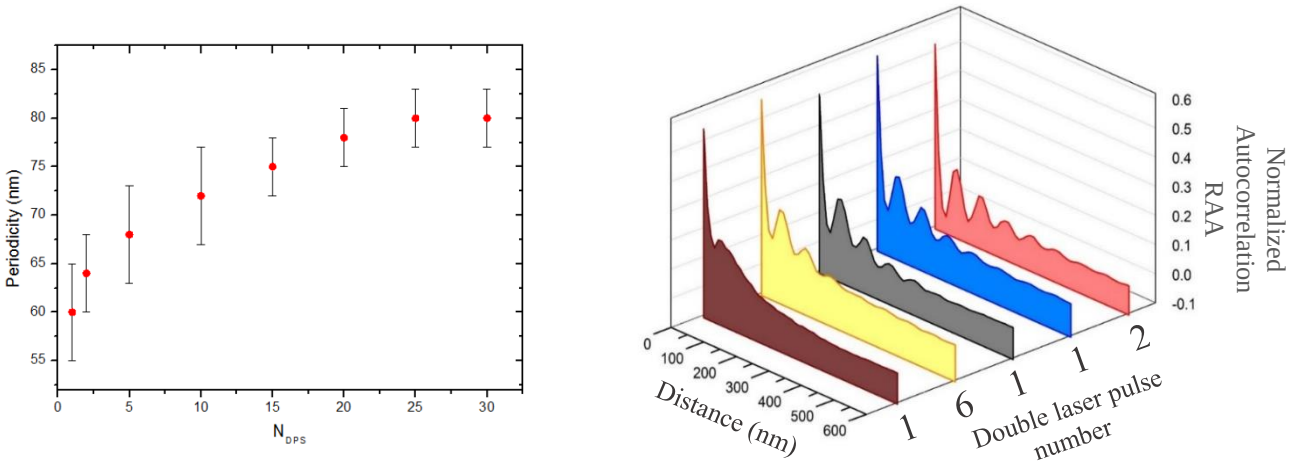

Fig 8.7 (a) Nanoholes periodicities obtained by FFT on SEM images as a function of the number of double pulse sequences and (b) Radially average autocorrelation RAA as a function of distance performed on SEM images where nanoholes with different consecutive number of double laser pulses are used, starting from N_{DPS} = 1 to N_{DPS}= 20.

8.5 Scenarios for nanoholes formation

Laser-induced nanoholes formation has never been reported and suffers from a lack of comprehensible scenario. However, we can try to provide some different hypothesis which can explain the physical mechanisms triggering nanoholes generation.

The first assumption which describes nanoholes formation considers that the target does not reach the melting regime after the first pulse. For simplification, let's consider nanoholes formed at a peak fluence of 0.24 J/cm² with N_{DPS} equals 25.

From a pure electromagnetic scenario, since the peak fluence of each single pulse of a sequence is very low, 0.12 J/cm², the first pulse impinging the surface can generate a high concentration of roughness centers randomly distributed. A second delayed pulse thus will encounter a forest of disconnected nanoroughness centers, making it difficult to enhance the local field, as seen in the previous chapter, where a high concentration of roughness centers can annihilate the formation of LIPSS. We recall that LSFL result from the coherent superposition between the incident field and the scattered far-field by distant roughness centers, while HSFL are triggered by the coherent interference between the incident field and the scatted-near field by much closer roughness centers[5]. Furthermore, when ripples are generated with linearly polarized laser radiation, their orientation could be either parallel or perpendicular. In the case of double pulse irradiation, the orientation of ripples is dominated by the state of polarization of the second pulse[124,158]. In the frame of nanoholes formation, the orientation is at 45° with respect to the crossed polarization, and is not directly defined by the polarization of the double-pulse sequence.

The second assumption considers that the target has reached its melting regime upon irradiation with the first pulse. A second delayed pulse will thus encounter a liquid region. In fact, the first pulse energy has sufficient time to be delivered

from the excited electrons to atomic vibrations, which leads to a rapid heating and forms a liquid region with its depth depending on the fluence of 0.24 J/cm². Therefore, the laser energy absorption of the second pulse increases effectively due to a decrease of Ni reflectivity, which favors conditions leading to nanovoids formation in the liquid region. In chapter 6, we have seen that nanovoids trapped under the surface as well as nanocavities emerged at the surface were behind HSFL formation on fcc material, for a fluence at 0.39 J/cm² with 2 single pulses irradiation. In the multi-double-pulse regime, since the polarization between the two delayed pulses of a sequence is crossed, one can imagine that the first pulse enables stretching of the nanovoids in one direction, while the second delayed pulse permits nanoholes stretching in the other direction. Thus nanoholes formation can result from nanovoids growth.

The third assumption is that laser-induced nanoholes are reaction-diffusion-like chemical patterns, or dubbed 'Turing patterns'[258–262] . Reaction-diffusion systems represent mathematical models underlying several physical phenomena: the most common is space-time modification of chemical substances concentration transformed into each other by the mean of local chemical reactions, and diffusion which enables the spread of the substances in space. Turing revealed that a uniform state may evolve in some circumstances via a diffusive instability toward a new state in which the concentrations are stationary and periodically organized. Turing patterns include self-organized patterns like stripes and hexagons. It can also explain the formation of turbulent structures. Turing patterns compared to fs-double-pulse patterns is displayed in fig 8.8. This model can be useful when current patterns are too simple to generate rich behavior. However, it can be viewed as artificial to have relevance to actual physical problem.

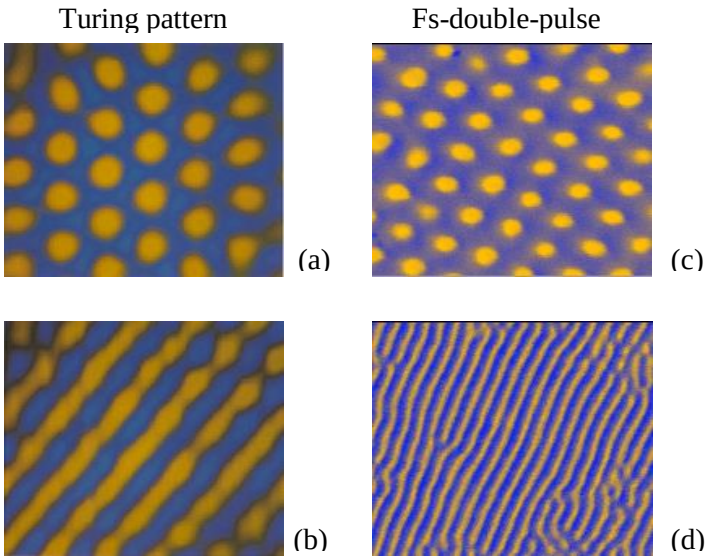

Fig 8.8 A correlation between (a,b) Turing patterns[259] and (c,d) fs-double pulse laser patterns. (a) Nearly time independent hexagonal pattern of spots observed in a chlorite-iodide-malonic-acid (CIMA) system of chemicals that are reacting in a thin cylindrical polyacrylamide gel of diameter 25.4 mm and thickness 2.00 mm. (b) Nearly-time independent stripe pattern observed instead of hexagonal patter for slightly different external conditions. (c) Hexagonal nanoholes formed by fs-double pulse sequences at 0.24 J/cm² and a time-delay of 24 ps between the two pulses. The polarization of the two delayed pulses is crossed. (d) Nanoripples formed by fs-double pulse sequences at 0.24 J/cm² and a time-delay of 24 ps between the two pulses. The polarization of the two delayed pulses is parallel.

8.6 Applications

The presence of nanostructures on a surface can find many applications, where nano-patterns covered surfaces go in hand with a modification in surface features. For example, wetting may be modified, which may be of interest in biomedical applications. In particular, one can then create very hydrophobic surfaces, or even hydrophilic surfaces, which can then be used in micro-channels to separate fluids. It is also possible to create surfaces with improved friction properties, for example for gliding pads such as skis, or even to limit wear between parts in contact. The interaction of light with the surface can be modified, which can change the color of the material as perceived by an observer, or change the absorption capacity of light, which can find application in the field of energies renewable energy, and in particular photovoltaic energy. In fact, a nano-structured surface can be very selective in wavelength, which allows for example to absorb only certain wavelengths. Other applications may benefit from a nano-structured surface, for example in the field of plasmonics, photonic crystals or near-field optics.

8.7 Conclusion

In this chapter, the control of surface-roughness by investigating the dynamics and physical mechanisms leading to unconventional nanostructures formation, i.e. nanoholes, has been addressed. The pattern consists of nanoholes of 20 nm in diameter, and the distance between two nanoholes is approximately 60 nm. The results show that the onset of nanoholes array structures formation requires a time-delay window of 18-30ps between the delayed pulses, slightly dependent on the incident fluence. It was also shown that nanoholes are polarization dependent. If the polarization between the two delayed pulses is parallel, nanoripples are formed. In the case of crossed polarization, nanoholes are generated. Different scenarios were also proposed to investigate nanoholes formation, ranging from electromagnetic approach to hydrodynamic scenario. A correlation to Turing pattern was also suggested. Structuring a large nanoholes area paves the way towards potential applications in a large range of fields such as photonic crystals, plasmonics and near-field optics.

Chapter 9

General conclusions and outlook

The general conclusions of this thesis are presented in this chapter, and a perspective for future work is also reported.

General conclusion and future work

Irradiation of materials by ultrashort laser pulses triggers anisotropically structured arrangement of matter on the nanoscale, the laser-induced periodic surface structures (LIPSS), or 'ripples'. Ultrashort laser energy deposited and distributed inhomogeneously in the material launches local thermal stresses and transient phase changes which paves the way towards microstructural modifications.

This thesis investigated ultrashort laser-metal interaction mechanisms in the aim of establishing a correlation between the creation and resorption of microstructural defects in metals and the periodic self-organization effects occurring after ultrashort laser irradiation, since LIPSS are generated at the threshold of phase transition with relevant competition with defects. HSFL generation was put on the forefront of ripples formation investigation since the physical mechanisms leading to their formation is still debated. Irradiated surface alteration as well as in-depth microstructural modifications contribution on HSFL formation, taking into account crystalline orientation, has been elucidated and constituted the core of this thesis. Furthermore, since optical feedback in LIPSS is often evoked, LIPSS features evolution is probed.

This thesis offered a collaborative work with different laboratories: it let access to different characterization microscopies and analysis tools: Atomic force microscopy aiming for topographical investigation of laser induced-roughness and LIPSS morphology was performed by S. Reynaud at the Hubert-Curien laboratory. For surface analysis, electron back-scattered diffraction characterization of LIPSS and defects was performed at Ecole nationale supérieure des mines de Saint-Etienne EMSE, by C. Maurice. Regarding in-depth analysis, thin lamellas extraction using the lift-out technique as well as in-depth characterization of defects was carried out at Mateis INSA Lyon by T. Douillard employing focused ion beam and the transmission electron microscopy. In order to probe LIPSS features evolution, a collaboration was established with the radiation-matter institute of CEA-Saclay, using the photoemission electron microscopy technique by L. Douillard.
For theoretical analysis, a collaboration was made with the University of Virginia, where L.V. Zhigilei and his coworkers performed molecular dynamic simulations on laser-induced defects. Finally, electromagnetic calculations and hydrodynamic simulations were performed at the Hubert-Curien laboratory by A. Rudenko and J.P. Colombier.
As a result of these experimental studies coupled to molecular dynamic and hydrodynamic simulations, the following results have been obtained:

i. The appearance of the periodic surface structures, i.e. HSFL, therefore, can be traced back to the initial surface roughness generated by the first laser pulse when irradiating a bcc material with two laser shots in the sub-phase explosion regime, where laser-induced surface topography is strongly dependent on crystalline orientation. The characteristics of nanoscale surface morphology are defined by the competition between the evolution of transient liquid structures generated in the spallation process and the rapid resolidification of the surface region of the target. The strong dependence of the surface topography produced in single pulse irradiation experiments on the crystallographic orientation of target surface may be related to the anisotropy of the crystallization front propagation, which provides more time for the relaxation of molten surfaces when the solidification process is

slower. The connection between the initial nanoscale roughness generated by the first laser pulse and the subsequent formation of periodic surface structures, established in the present study, contributes to the progress towards the general goal of untangling the complex multiscale phenomenon of the LIPSS formation.

ii. The singular response of different crystalline orientation regarding laser-induced roughness is explained by an extended study carried on microstrucutal modifications on the surface and in-depth. The discrepancy between dislocations emission in the (110) and (111) Cr samples and their absence in (001) Cr sample in the melting regime, underlines an explicit understanding on the onset conditions of dislocations emission in the irradiated targets, which are crystallographic orientation dependent. Therefore, resolved shear stresses calculation in the 48 slip systems is performed for the three large-scale simulations discussed in the previous section. It is found that laser-induced defects can alter the surface topography and the region beneath-it, which can impact in turn the roughness centers features promoting HSFL formation, where (100) in bcc materials is more favorable to LIPSS formation, while (110) orientation showed a weak tendency to form ripples.

iii. In order to infer the phase transition undergone in the LIPSS formation conditions, a high resolution microstructural analysis approach is employed, including epitaxial regrowth and nanocavitation investigation. HSFL formation is found to be the result of periodic nanovoids trapped beneath the surface as well as nanocavities emerged at the surface on fcc materials.

iv. The dynamics of LIPSS formation recalling feedback mechanism driving the final morphology of LIPSS is investigated by employing the photoemission electron microscopy. Probing the local field on LIPSS pre-structured with consecutive number of laser pulses indicates that light absorption is localized and enhanced in the vicinity of nanoholes, which outlines a modulated energy deposition. Furthermore, the shift in periodicity between the emitted photoelectrons, which can be manifested by hot spots, and that of LIPSS for a low number of applied laser pulses, elucidate the role of nanoholes in the constitution of final interference patterns and possible LIPSS interpulse evolution. The experimental results combined with electromagnetic calculations with different concentrations of randomly distributed nanoholes reveal that LIPSS periodicity follows the average spacing between the nanoholes pulse-by-pulse, approaching the saturated value, where no further resonant wavelength shift is expected.

v. Finally, the control of transient surface-roughness by studying the dynamics and physical mechanisms paving the way towards unconventional nanostructures formation, i.e. nanoholes on extreme size features, has been brought in the forefront at the end of this thesis. The results reveal that periodically arranged arrays of nanoholes of 20 nm in diameter and 60 nm in spacing can be obtained by direct laser illumination. The onset of nanoholes array structures formation requires a threshold time-delay window between the delayed pulses, slightly dependent on the incident fluence. Nanoholes show a strong dependency on the incident polarization. If the polarization between the two delayed pulses is parallel, nanoripples are formed with periodicity down to 60 nm.

In the case of crossed polarization, nanoholes are generated. Different scenarios were also proposed to investigate nanoholes formation, ranging from electromagnetic approach to hydrodynamic scenario. A correlation to Turing pattern was also suggested. Structuring a large nanoholes area paves the way towards potential applications in different fields such as photonic crystals, plasmonics and near-field optics.

The obtained results identify interesting directions for ulterior research:

a. The intricate physical mechanisms involved in nanoholes formation can be investigated in an in-depth study by extracting a thin lamella from the nanoholes processed area, and to analyze it using transmission electron microscopy. One can understand whether stretching of nanovoids can be involved in nanoholes formation or dominated by pure electromagnetic effect. Additionally, molecular dynamic simulations as well as hydrodynamic calculations can be coupled to the experimental work, where investigation of the behavior of an hexagonal array of nanoholes can be carried out as a function of the incident laser polarization. The use of more complex vector beam polarization can be also useful. It is also worth shaping the pulse by SLM for nanoholes formation. Furthermore, regarding the broad range of applications which can be implemented by these unconventional structures, structuring a large surface, i.e. (2x2) mm^2, can be essential for wetting tests, magnetic investigation, where the Kerr coefficient can be measured for example, surface design, wavelength selective and other applications in the fields such as plasmonics, photonic crystals and near-field optics. Other type of materials can be also aimed for: thin films, bcc/hcp materials and polycrystalline samples.
b. Elucidating the role of incident irradiation angle, fluence variation of the delayed-pulse and medium refractive index on nanoholes features. One can expect to control nanoholes dimensions. Irradiating samples in water can be useful for redeposit material removal, which improves the quality of the processed nanostructures area.
c. In-situ time-resolved investigation of nanoholes formation dynamics. One can expect to irradiate a fcc target in a PEEM chamber with fs-double pulse sequences, and probe simultaneously the transient formation of nanoholes. The probe pulse can be applied after the first pulse of the double-pulse sequence, which reveals the state of the surface induced by the first pulse before arrival of the delayed pulse. This experimental setup can be applied also to LIPSS formation, especially high-spatial frequency nanostructures oriented parallel to the laser polarization with periodicities much lower than the laser wavelength. This study permits to probe the transient interpulse roughness, and to unveil the location of local-field enhancement responsible for the reduction of high-spatial frequency nanostructures periodicities when increasing the number of laser pulses.

References

(1) Bonse, J.; Krüger, J.; Höhm, S.; Rosenfeld, A. Femtosecond Laser-Induced Periodic Surface Structures. *J. Laser Appl.* **2012**, *24* (4), 042006.

(2) Borowiec, A.; Haugen, H. K. Subwavelength Ripple Formation on the Surfaces of Compound Semiconductors Irradiated with Femtosecond Laser Pulses. *Appl. Phys. Lett.* **2003**, *82* (25), 4462–4464.

(3) Nemanich, R. J.; Biegelsen, D. K.; Hawkins, W. G. Aligned, Coexisting Liquid and Solid Regions in Laser-Annealed Si. *Phys. Rev. B* **1983**, *27* (12), 7817–7819.

(4) Bonse, J.; Baudach, S.; Krüger, J.; Kautek, W.; Lenzner, M. Femtosecond Laser Ablation of Silicon-Modification Thresholds and Morphology. *Appl. Phys. A Mater. Sci. Process.* **2002**, *74* (1), 19–25.

(5) Zhang, H.; Colombier, J. P.; Li, C.; Faure, N.; Cheng, G.; Stoian, R. Coherence in Ultrafast Laser-Induced Periodic Surface Structures. *Phys. Rev. B.* **2015**, *92* (17), 174109.

(6) Abou-Saleh, A.; Karim, E. T.; Maurice, C.; Reynaud, S.; Pigeon, F.; Garrelie, F.; Zhigilei, L. V.; Colombier, J. P. Spallation-Induced Roughness Promoting High Spatial Frequency Nanostructure Formation on Cr. *Appl. Phys. A* **2018**, *124* (4), 308.

(7) Reif, J.; Varlamova, O.; Varlamov, S.; Bestehorn, M. The Role of Asymmetric Excitation in Self-Organized Nanostructure Formation upon Femtosecond Laser Ablation. *AIP Conference Proceedings* **2012**; *1464* (1), 428–441.

(8) Sedao, X.; Abou Saleh, A.; Rudenko, A.; Douillard, T.; Esnouf, C.; Reynaud, S.; Maurice, C.; Pigeon, F.; Garrelie, F.; Colombier, J.-P. Self-Arranged Periodic Nanovoids by Ultrafast Laser-Induced Near-Field Enhancement. *ACS Photonics* **2018,** *5* (4), 1418-1426.

(9) Bonse, J.; Sturm, H.; Schmidt, D.; Kautek, W. Chemical, Morphological and Accumulation Phenomena in Ultrashort-Pulse Laser Ablation of TiN in Air. *Appl. Phys. A* **2000**, *71* (6), 657–665.

(10) Skolski, J. Z. P.; Römer, G. R. B. E.; Obona, J. V.; Ocelik, V.; Huis In 't Veld, A. J.; De Hosson, J. T. M. Laser-Induced Periodic Surface Structures: Fingerprints of Light Localization. *Phys. Rev. B* **2012**, *85* (7), 075320.

(11) Le Harzic, R.; Dörr, D.; Sauer, D.; Stracke, F.; Zimmermann, H. Generation of High Spatial Frequency Ripples on Silicon under Ultrashort Laser Pulses Irradiation. *Appl. Phys. Lett.* **2011**, *98* (21), 211905.

(12) Li, X.-F.; Zhang, C.-Y.; Li, H.; Dai, Q.-F.; Lan, S.; Tie, S.-L. Formation of 100-Nm Periodic Structures on a Titanium Surface by Exploiting the Oxidation and Third Harmonic Generation Induced by Femtosecond Laser Pulses. *Opt. Express* **2014**, *22* (23), 28086–28099.

(13) Reif, J.; Varlamova, O.; Costache, F. Femtosecond Laser Induced Nanostructure Formation: Self-Organization Control Parameters. *Appl. Phys. A* **2008**, *92* (4), 1019-1024.

(14) Sedao, X.; Shugaev, M. V; Wu, C.; Douillard, T.; Esnouf, C.; Maurice, C.; Reynaud, S.; Pigeon, F.; Garrelie, F.; Zhigilei, L. V; et al. Growth Twinning and Generation of High-Frequency Surface Nanostructures in Ultrafast Laser-Induced Transient Melting and Resolidification. *ACS Nano* **2016**, *10* (7), 6995–7007.

(15) Dufft, D.; Rosenfeld, A.; Das, S. K.; Grunwald, R.; Bonse, J. Femtosecond Laser-Induced Periodic Surface Structures Revisited: A Comparative Study on ZnO. *J. Appl. Phys.* **2009**, *105* (3), 034908.

(16) Volkov, S. N.; Kaplan, A. E.; Miyazaki, K. Evanescent Field at Nanocorrugated Dielectric Surface. *Appl. Phys. Lett.* **2009**, *94* (4), 041104.

(17) Buividas, R.; Rosa, L.; Šliupas, R.; Kudrius, T.; Šlekys, G.; Datsyuk, V.; Juodkazis, S. Mechanism of Fine Ripple Formation on Surfaces of (Semi)Transparent Materials via a Half-Wavelength Cavity Feedback.

Nanotechnology **2011**, *22* (5), 055304.

(18) Martsinovskiĭ, G. A.; Shandybina, G. D.; Smirnov, D. S.; Zabotnov, S. V.; Golovan', L. A.; Timoshenko, V. Y.; Kashkarov, P. K. Ultrashort Excitations of Surface Polaritons and Waveguide Modes in Semiconductors. *Opt. Spectrosc.* **2008**, *105* (1), 67–72.

(19) Straub, M.; Afshar, M.; Feili, D.; Seidel, H.; König, K. Surface Plasmon Polariton Model of High-Spatial Frequency Laser-Induced Periodic Surface Structure Generation in Silicon. *J. Appl. Phys.* **2012**, *111* (12), 124315.

(20) Sedao, X.; Maurice, C.; Garrelie, F.; Colombier, J. P.; Reynaud, S.; Quey, R.; Blanc, G.; Pigeon, F. Electron Backscatter Diffraction Characterization of Laser-Induced Periodic Surface Structures on Nickel Surface. *Appl. Surf. Sci.* **2014**, *302*, 114–117.

(21) Mittendorfer, F.; Eichler, A.; Hafner, J. Structural, Electronic and Magnetic Properties of Nickel Surfaces. *Surf. Sci.* **1999**, *423* (1), 1–11.

(22) Demaske, B.; Zhakhovsky, V.; Inogamov, N.; Oleynik, I. Ultrashort Shock Waves in Nickel Induced by Femtosecond Laser Pulses. *Phys. Rev. B* **2013**, *87* (5), 054109.

(23) Helms, A. L.; Draper, C. W.; Jacobson, D. C.; Poate, J. M.; Bernasek, S. L. Epitaxy and Defects in Laser-Irradiated, Single-Crystal Bismuth. *J. Mater. Res.* **1988**, *3* (6), 1097–1103.

(24) Aicheler, M.; Sgobba, S.; Arnau-Izquierdo, G.; Taborelli, M.; Calatroni, S.; Neupert, H.; Wuensch, W. Evolution of Surface Topography in Dependence on the Grain Orientation during Surface Thermal Fatigue of Polycrystalline Copper. *Int. J. Fatigue* **2011**, *33* (3), 396–402.

(25) Tsu, R.; Hodgson, R. T.; Tan, T. Y.; Baglin, J. E. Order-Disorder Transition in Single-Crystal Silicon Induced by Pulsed Uv Laser Irradiation. *Phys. Rev. Lett.* **1979**, *42* (20), 1356–1358.

(26) Sedao, X.; Maurice, C.; Garrelie, F.; Colombier, J.-P.; Reynaud, S.; Quey, R.; Pigeon, F. Influence of Crystal Orientation on the Formation of Femtosecond Laser-Induced Periodic Surface Structures and Lattice Defects Accumulation. *Appl. Phys. Lett.* **2014**, *104* (17), 171605.

(27) Balling, P.; Schou, J. Femtosecond-Laser Ablation Dynamics of Dielectrics: Basics and Applications for Thin Films. *Reports Prog. Phys.* **2013**, *76* (3), 036502.

(28) Colombier, J. P.; Combis, P.; Audouard, E.; Stoian, R. Transient Optical Response of Ultrafast Nonequilibrium Excited Metals: Effects of Electron-Electron Contribution to Collisional Absorption. *Phys. Rev. E* **2008**, *77* (3), 036409.

(29) Anisimov, S. I.; Kapeliovich, B. L.; Perel-man, T. L. Electron Emission from Metal Surfaces Exposed to Ultrashort Laser Pulses. *J. Exp. Theor. Phys.* **1974**, *66* (2), 375–377.

(30) Hohlfeld, J.; Wellershoff, S.-S.; Güdde, J.; Conrad, U.; Jähnke, V.; Matthias, E. Electron and Lattice Dynamics Following Optical Excitation of Metals. *Chem. Phys.* **2000**, *251* (1–3), 237–258.

(31) Farm, W. S.; Storz, R.; Tom, H. W. K.; Bokor, J. Direct Measurement of Nonequilibrium Electron-Energy Distributions in Sub-Picosecond Laser-Heated Gold Films. *Surf. Sci.* **1993**, *283* (1–3), 221–225.

(32) Surez, C.; Bron, W. E.; Juhasz, T. Dynamics and Transport of Electronic Carriers in Thin Gold Films. *Phys. Rev. Lett.* **1995**, *75* (24), 4536–4539.

(33) Colombier, J. P.; Bevillon, E.; Silaeva, E.; Stoian, R. Nonequilibrium Optical Response of Metals Irradiated by Ultrafast Laser Pulses **2018**, *10519*, 1051905.

(34) Aeschlimann, M.; Bauer, M.; Pawlik, S.; Weber, W.; Burgermeister, R.; Oberli, D.; Siegmann, H. C. Ultrafast Spin-Dependent Electron Dynamics in Fcc Co. *Phys. Rev. Lett.* **1997**, *79* (25), 5158–5161.

(35) Lin, Z.; Zhigilei, L. V.; Celli, V. Electron-Phonon Coupling and Electron Heat Capacity of Metals under Conditions of Strong Electron-Phonon Nonequilibrium. *Phys. Rev. B* **2008**, *77* (7), 075133.

(36) Hostetler, J. L.; Smith, A. N.; Czajkowsky, D. M.; Norris, P. M. Measurement of the Electron-Phonon Coupling Factor Dependence on Film Thickness and Grain Size in Au, Cr, and Al. *Appl. Opt.* **1999**, *38* (16), 3614-3620.

(37) Colombier, J. P.; Garrelie, F.; Faure, N.; Reynaud, S.; Bounhalli, M.; Audouard, E.; Stoian, R.; Pigeon, F. Effects of Electron-Phonon Coupling and Electron Diffusion on Ripples Growth on Ultrafast-Laser-Irradiated Metals. *J. Appl. Phys.* **2012**, *111* (2), 024902.

(38) Chichkov, B. N.; Momma, C.; Nolte, S.; von Alvensleben, F.; Tünnermann, A. Femtosecond, Picosecond and Nanosecond Laser Ablation of Solids. *Appl. Phys. A* **1996**, *63* (2), 109–115.

(39) Fujimoto, J. G.; Liu, J. M.; Ippen, E. P.; Bloembergen, N. Femtosecond Laser Interaction with Metallic Tungsten and Nonequilibrium Electron and Lattice Temperatures. *Phys. Rev. Lett.* **1984**, *53* (19), 1837–1840.

(40) Agranat, M. B.; Anisimov, S. I.; Makshantsev, B. I. The Anomalous Thermal Radiation of Metals Produced by Ultrashort Laser Pulses. *Appl. Phys. B* **1992**, *55* (5), 451–461.

(41) Girardeau-Montaut, J. P.; Girardeau-Montaut, C. Theory of Ultrashort Nonlinear Multiphoton Photoelectric Emission from Metals. *Phys. Rev. B* **1995**, *51* (19), 13560–13567.

(42) Schäfer, C.; Urbassek, H. M.; Zhigilei, L. V. Metal Ablation by Picosecond Laser Pulses: A Hybrid Simulation. *Phys. Rev. B.* **2002**, *66* (11), 1154041–1154048.

(43) Colombier, J. P.; Combis, P.; Bonneau, F.; Le Harzic, R.; Audouard, E. Hydrodynamic Simulations of Metal Ablation by Femtosecond Laser Irradiation. *Phys. Rev. B* **2005**, *71* (16), 165406.

(44) Colombier, J. P.; Guillermin, M.; Garrelie, F.; Audouard, E.; Stoian, R. Simulations of Controlled Spectral Emission of Al Plasmas Generated by Temporally Tailored Laser Irradiation. *AIP Conf. Proc.*, **2010**, *1278* (1), 312–323.

(45) Mannion, P. T.; Magee, J.; Coyne, E.; O'Connor, G. M.; Glynn, T. J. The Effect of Damage Accumulation Behaviour on Ablation Thresholds and Damage Morphology in Ultrafast Laser Micro-Machining of Common Metals in Air. *Appl. Surf. Sci.* **2004**, *233* (1–4), 275–287.

(46) Anisimov, S. I.; Luk'yanchuk, B. S. Selected Problems of Laser Ablation Theory. *Physics-Uspekhi* **2002**, *45* (3), 293–324.

(47) Bäuerle, D. Laser Processing and Chemistry: Recent Developments. *Appl. Surf. Sci.* **2002**, *186* (1–4), 1–6.

(48) Vogel, A.; Noack, J.; Hüttman, G.; Paltauf, G. Mechanisms of Femtosecond Laser Nanosurgery of Cells and Tissues. *Appl. Phys. B* **2005**, *81* (8), 1015–1047.

(49) Zhigilei, L. V.; Lin, Z.; Ivanov, D. S. Atomistic Modeling of Short Pulse Laser Ablation of Metals: Connections between Melting, Spallation, and Phase Explosion. *J. Phys. Chem. C* **2009**, *113* (27), 11892–11906.

(50) Karim, E. T.; Lin, Z.; Zhigilei, L. V. Molecular Dynamics Study of Femtosecond Laser Interactions with Cr Targets. *AIP Conf. Proc.*, **2012**, *1464* (1), 280–293.

(51) Lin, Z.; Zhigilei, L. V. Time-Resolved Diffraction Profiles and Atomic Dynamics in Short-Pulse Laser-Induced Structural Transformations: Molecular Dynamics Study. *Phys. Rev. B* **2006**, *73* (18), 184113.

(52) Ivanov, D. S.; Zhigilei, L. V. Effect of Pressure Relaxation on the Mechanisms of Short-Pulse Laser Melting. *Phys. Rev. Lett.* **2003**, *91* (10), 105701.

(53) Lin, Z.; Leveugle, E.; Bringa, E. M.; Zhigilei, L. V. Molecular Dynamics Simulation of Laser Melting of Nanocrystalline Au. *J. Phys. Chem. C* **2010**, *114* (12), 5686–5699.

(54) Mannion, P.; O'Connor, G. M.; Coyne, E.; Howard, H.; Glynn, T. J. The Onset of Phase Explosion and the Role of Damage Accumulation in Ultrafast Laser Processing of Common Metals in Air. *Proc. of SPIE* **2004**, *5448*, 961–973.

(55) Glenzer, S. H.; Landen, O. L.; Neumayer, P.; Lee, R. W.; Widmann, K.; Pollaine, S. W.; Wallace, R. J.; Gregori, G.; Höll, A.; Bornath, T. Observations of Plasmons in Warm Dense Matter. *Phys. Rev. Lett.* **2007**, *98* (6), 065002.

(56) Su, J. T.; Goddard, W. A. Excited Electron Dynamics Modeling of Warm Dense Matter. *Phys. Rev. Lett.* **2007**, *99* (18), 185003.

(57) Ernstorfer, R.; Harb, M.; Hebeisen, C. T.; Sciaini, G.; Dartigalongue, T.; Miller, R. J. D. The Formation of Warm Dense Matter: Experimental Evidence for Electronic Bond Hardening in Gold. *Science.* **2009**, *323* (5917), 1033–1037.

(58) Hoekstra, J. G.; Qadri, S. B.; Scully, J. R.; Fitz-Gerald, J. M. Laser Surface Modification of a Crystalline Al-Co-Ce Alloy for Enhanced Corrosion Resistance. *Adv. Eng. Mater.* **2005**, *7* (9), 805–809.

(59) Kaspar, J.; Luft, A. Microstructure Formed in Body Centred Cubic Metals by Laser Shock Processing. *Surf. Eng.* **2001**, *17* (5), 379–383.

(60) Allmen, M. V.; Blatter, A. Laser Beam Interactions with Materials: Physical Principles and Applications **2013**, *2*.

(61) Bäuerle, D. Laser Processing and Chemistry, *App. Surf. Sci.* **2002**, *186* (1–4), 1–6.

(62) Koumvakalis, N.; Lee, C. S.; Bass, M. Single And Multiple Pulse Catastrophic Damage In Diamond-Turned Cu And Ag Mirrors at 10.6, 1.06, and 0.532 μm. *Opt. Eng.* **1983**, *22*, 224415–224419.

(63) Thomas, S. J.; Harrison, R. F.; Figueira, J. F. Observations of the Morphology of Laser-Induced Damage in Copper Mirrors. *Appl. Phys. Lett.* **1982**, *40* (3), 200–202.

(64) Marrs, C. D.; Faith, W. N.; Dancy, J. H.; Porteus, J. O. Pulsed Laser-Induced Damage of Metals at 492 nm. *Appl. Opt.* **1982**, *21* (22), 4063.

(65) Sparks, M.; Loh, E. Temperature Dependence of Absorptance in Laser Damage of Metallic Mirrors: I Melting. *J. Opt. Soc. Am.* **1979**, *69* (6), 847.

(66) Cullis, A. G.; Chew, N. G.; Webber, H. C.; Smith, D. J. Orientation Dependence of High Speed Silicon Crystal Growth from the Melt. *J. Cryst. Growth* **1984**, *68* (2), 624–638.

(67) Jee, Y.; Becker, M. F.; Walser, R. M. Laser-Induced Damage on Single-Crystal Metal Surfaces. *J. Opt. Soc. Am. B* **1988**, *5* (3), 648.

(68) Yater, J. A.; Thompson, M. O. Orientation Dependence of Laser Amorphization of Crystal Si. *Phys. Rev. Lett.* **1989**, *63* (19), 2088–2091.

(69) Karim, E. T.; Wu, C.; Zhigilei, L. V. Molecular Dynamics Simulations of Laser-Materials Interactions: General and Material-Specific Mechanisms of Material Removal and Generation of Crystal Defects. *Springer Ser. Mater. Sci.* **2014**, *195*, 27–49.

(70) Wu, C.; Karim, E. T.; Volkov, A. N.; Zhigilei, L. V. Atomic Movies of Laser-Induced Structural and Phase Transformations from Molecular Dynamics Simulations. *Springer Ser. Mater. Sci.* **2014**, *191*, 67–100.

(71) Lin, Z.; Johnson, R. A.; Zhigilei, L. V. Computational Study of the Generation of Crystal Defects in a Bcc Metal Target Irradiated by Short Laser Pulses. *Phys. Rev. B* **2008**, *77* (21), 214108.

(72) Wu, C.; Zhigilei, L. V. Nanocrystalline and Polyicosahedral Structure of a Nanospike Generated on Metal Surface Irradiated by a Single Femtosecond Laser Pulse. *J. Phys. Chem. C* **2016**, *120* (8), 4438–4447.

(73) Wu, C.; Christensen, M. S.; Savolainen, J. M.; Balling, P.; Zhigilei, L. V. Generation of Subsurface Voids and a Nanocrystalline Surface Layer in Femtosecond Laser Irradiation of a Single-Crystal Ag Target. *Phys. Rev. B* **2015**, *91* (3), 035413.

(74) McNally, P. J. Techniques: 3D Imaging of Crystal Defects. *Nature* **2013**, *496* (7443), 37.

(75) Azushima, A.; Kopp, R.; Korhonen, A.; Yang, D. Y.; Micari, F.; Lahoti, G. D.; Groche, P.; Yanagimoto, J.; Tsuji, N.; Rosochowski, A. Severe Plastic Deformation (SPD) Processes for Metals. *CIRP Ann.* **2008**, *57* (2), 716–735.

(76) Raj, R.; Ashby, M. F. On Grain Boundary Sliding and Diffusional Creep. *Metall. Trans.* **1971**, *2* (4), 1113–1127.

(77) Arzt, E.; Ashby, M. F.; Verrall, R. A. Interface Controlled Diffusional Creep. *Acta Metall.* **1983**, *31* (12), 1977–1989.

(78) Chen, M.; Ma, E.; Hemker, K. J.; Sheng, H.; Wang, Y.; Cheng, X. Deformation Twinning in Nanocrystalline Aluminum. *Science* **2003**, *300* (5623), 1275–1277.

(79) Zhu, Y. T.; Liao, X. Z.; Wu, X. L. Deformation Twinning in Nanocrystalline Materials. *Prog. Mater. Sci.* **2012**, *57* (1), 1–62.

(80) Yoo, M. H. Slip, Twinning, and Fracture in Hexagonal Close-Packed Metals. *Metall. Trans. A* **1981**, *12* (3), 409–418.

(81) Weinberger, C. R.; Boyce, B. L.; Battaile, C. C. Slip Planes in bcc Transition Metals. *Int. Mater. Rev.* **2013**, *58* (5), 296–314.

(82) Marichal, C.; Van Swygenhoven, H.; Van Petegem, S.; Borca, C. {110} Slip with {112} Slip Traces in bcc Tungsten. *Sci. Rep.* **2013**, *3*, 2547.

(83) Asaro, R. J.; Rice, J. R. Strain Localization in Ductile Single Crystals. *J. Mech. Phys. Solids* **1977**, *25* (5), 309–338.

(84) Qin, Q.; Bassani, J. L. Non-Schmid Yield Behavior in Single Crystals. *J. Mech. Phys. Solids* **1992**, *40* (4), 813–833.

(85) Lim, H.; Weinberger, C. R.; Battaile, C. C.; Buchheit, T. E. Application of Generalized Non-Schmid Yield Law to Low-Temperature Plasticity in Bcc Transition Metals. *Model. Simul. Mater. Sci. Eng.* **2013**, *21* (4), 045015.

(86) Winther, G. Slip Systems Extracted from Lattice Rotations and Dislocation Structures. *Acta Mater.* **2008**, *56* (9), 1919–1932.

(87) Birnbaum, M. Semiconductor Surface Damage Produced by Ruby Lasers. *J. Appl. Phys.* **1965**, *36* (11), 3688–3689.

(88) Bonse, J.; Hohm, S.; Kirner, S. V.; Rosenfeld, A.; Kruger, J. Laser-Induced Periodic Surface Structures-A Scientific Evergreen. *J. Sel. Top.* **2017**, *23* (3), 109-123.

(89) Emmony, D. C.; Howson, R. P.; Willis, L. J. Laser Mirror Damage in Germanium at 10.6 Mm. *Appl. Phys. Lett.* **1973**, *23* (11), 598–600.

(90) Keilmann, F.; Bai, Y. H. Periodic Surface Structures Frozen into CO2 Laser-Melted Quartz. *Appl. Phys. A* **1982**, *29* (1), 9–18.

(91) Sipe, J. E.; Young, J. F.; Preston, J. S.; Van Driel, H. M. Laser-Induced Periodic Surface Structure. I. Theory. *Phys. Rev. B* **1983**, *27* (2), 1141–1154.

(92) Guosheng, Z.; Fauchet, P. M.; Siegman, A. E. Growth of Spontaneous Periodic Surface Structures on Solids during Laser Illumination. *Phys. Rev. B* **1982**, *26* (10), 5366–5381.

(93) Van Driel, H. M.; Sipe, J. E.; Young, J. F. Laser-Induced Periodic Surface Structure on Solids: A Universal Phenomenon. *Phys. Rev. Lett.* **1982**, *49* (26), 1955–1958.

(94) Young, J. F.; Preston, J. S.; Van Driel, H. M.; Sipe, J. E. Laser-Induced Periodic Surface Structure. II. Experiments on Ge, Si, Al, and Brass. *Phys. Rev. B* **1983**, *27* (2), 1155–1172.

(95) Young, J. F.; Sipe, J. E.; Van Driel, H. M. Laser-Induced Periodic Surface Structure. III. Fluence Regimes, the Role of Feedback, and Details of the Induced Topography in Germanium. *Phys. Rev. B* **1984**, *30* (4), 2001–2015.

(96) Bonse, J.; Munz, M.; Sturm, H. Structure Formation on the Surface of Indium Phosphide Irradiated by Femtosecond Laser Pulses. *J. Appl. Phys.* **2005**, *97* (1), 013538.

(97) Bonse, J.; Höhm, S.; Rosenfeld, A.; Krüger, J. Sub-100-Nm Laser-Induced Periodic Surface Structures upon Irradiation of Titanium by Ti:Sapphire Femtosecond Laser Pulses in Air. *Appl. Phys. A* **2013**, *110* (3), 547–551.

(98) Dorronsoro, C.; Bonse, J.; Siegel, J. Self-Assembly of a New Type of Periodic Surface Structure in a Copolymer by Excimer Laser Irradiation above the Ablation Threshold. *J. Appl. Phys.* **2013**, *114* (15), 153105.

(99) Vorobyev, A. Y.; Makin, V. S.; Guo, C. Periodic Ordering of Random Surface Nanostructures Induced by Femtosecond Laser Pulses on Metals. *J. Appl. Phys.* **2007**, *101* (3), 034903.

(100) Wagner, R.; Gottmann, J. Sub-Wavelength Ripple Formation on Various Materials Induced by Tightly Focused Femtosecond Laser Radiation. *J. Phys. Conf. Ser.* **2007**, *59* (1), 333–337.

(101) Guillermin, M.; Garrelie, F.; Sanner, N.; Audouard, E.; Soder, H. Single- and Multi-Pulse Formation of Surface Structures under Static Femtosecond Irradiation. *Appl. Surf. Sci.* **2007**, *253* (19), 8075–8079.

(102) Daminelli, G.; Krüger, J.; Kautek, W. Femtosecond Laser Interaction with Silicon under Water Confinement. *Thin Solid Films* **2004**, *467* (1–2), 334–341.

(103) Crawford, T. H. R.; Haugen, H. K. Sub-Wavelength Surface Structures on Silicon Irradiated by Femtosecond Laser Pulses at 1300 and 2100 Nm Wavelengths. *Appl. Surf. Sci.* **2007**, *253* (11), 4970–4977.

(104) Costache, F.; Kouteva-Arguirova, S.; Reif, J. Sub–damage–threshold Femtosecond Laser Ablation from Crystalline Si: Surface Nanostructures and Phase Transformation. *Appl. Phys. A* **2004**, *79* (4–6), 1429–1432.

(105) Sokolowski-Tinten, K.; von der Linde, D. Generation of Dense Electron-Hole Plasmas in Silicon. *Phys. Rev. B* **2000**, *61* (4), 2643–2650.

(106) Jeschke, H. O.; Garcia, M. E.; Lenzner, M.; Bonse, J.; Krüger, J.; Kautek, W. Laser Ablation Thresholds of Silicon for Different Pulse Durations: Theory and Experiment. *Appl. Surf. Sci.* **2002**; *197*, 839–844.

(107) Lindenberg, A. M.; Engemann, S.; Gaffney, K. J.; Sokolowski-Tinten, K.; Larsson, J.; Hillyard, P. B.; Reis, D. A.; Fritz, D. M.; Arthur, J.; Akre, R. A. X-Ray Diffuse Scattering Measurements of Nucleation Dynamics at Femtosecond Resolution. *Phys. Rev. Lett.* **2008**, *100* (13), 135502.

(108) Skolski, J. Z. P.; Römer, G. R. B. E.; Vincenc Obona, J.; Huis In 'T Veld, A. J. Modeling Laser-Induced Periodic Surface Structures: Finite-Difference Time-Domain Feedback Simulations. *J. Appl. Phys.* **2014**, *115* (10), 103102.

(109) Römer, G. R. B. E.; Skolski, J. Z. P.; Oboňa, J. V.; Huis In 't Veld, A. J. Finite-Difference Time-Domain Modeling of Laser-Induced Periodic Surface Structures. *Phys. Procedia* **2014**, 56, 1325–1333.

(110) Bévillon, E.; Stoian, R.; Colombier, J. P. Nonequilibrium Optical Properties of Transition Metals upon Ultrafast Electron Heating. *J. Phys. Condens. Mat.* **2018**, *30* (38), 385401.

(111) Rudenko, A.; Colombier, J. P.; Höhm, S.; Rosenfeld, A.; Krüger, J.; Bonse, J.; Itina, T. E. Spontaneous Periodic Ordering on the Surface and in the Bulk of Dielectrics Irradiated by Ultrafast Laser: A Shared Electromagnetic Origin. *Sci. Rep.* **2017**, *7* (1), 12306.

(112) Miyazaki, H. T.; Kurokawa, Y. Squeezing Visible Light Waves into a 3-Nm-Thick and 55-Nm-Long Plasmon Cavity. *Phys. Rev. Lett.* **2006**, *96* (9), 097401.

(113) Barnes, W. L.; Dereux, A.; Ebbesen, T. W. Surface Plasmon Subwavelength Optics. *Nature* **2003**, *424* (6950), 824–830.

(114) Otto, A. Excitation of Nonradiative Surface Plasma Waves in Silver by the Method of Frustrated Total Reflection. *Zeitschrift für Phys.* **1968**, *216* (4), 398–410.

(115) Kretschmann, E.; Raether, H. Radiative Decay of Non Radiative Surface Plasmons Excited by Light. *J. Phys. Sci.* **1968**, *23* (12), 2135–2136.

(116) Bonse, J.; Rosenfeld, A.; Krüger, J. On the Role of Surface Plasmon Polaritons in the Formation of Laser-Induced Periodic Surface Structures upon Irradiation of Silicon by Femtosecond-Laser Pulses. *J. Appl. Phys.* **2009**, *106* (10), 104910.

(117) Sokolowski-Tinten, K.; Barty, A.; Boutet, S.; Shymanovich, U.; Chapman, H.; Bogan, M.; Marchesini, S.; Hau-

Riege, S.; Stojanovic, N.; Bonse, J. Short-Pulse Laser Induced Transient Structure Formation and Ablation Studied with Time-Resolved Coherent XUV-Scattering. *AIP Conf. Proc.* **2010**, *1278* (1), 373–379.

(118) Huang, M.; Zhao, F.; Cheng, Y.; Xu, N.; Xu, Z. Origin of Laser-Induced near-Subwavelength Ripples: Interference between Surface Plasmons and Incident Laser. *ACS Nano* **2009**, *3* (12), 4062–4070.

(119) Miyaji, G.; Miyazaki, K. Origin of Periodicity in Nanostructuring on Thin Film Surfaces Ablated with Femtosecond Laser Pulses. *Opt. Express* **2008**, *16* (20), 16265.

(120) Garrelie, F.; Colombier, J.-P.; Pigeon, F.; Tonchev, S.; Faure, N.; Bounhalli, M.; Reynaud, S.; Parriaux, O. Evidence of Surface Plasmon Resonance in Ultrafast Laser-Induced Ripples. *Opt. Express* **2011**, *19* (10), 9035.

(121) Derrien, T. J. Y.; Krüger, J.; Itina, T. E.; Höhm, S.; Rosenfeld, A.; Bonse, J. Rippled Area Formed by Surface Plasmon Polaritons upon Femtosecond Laser Double-Pulse Irradiation of Silicon: The Role of Carrier Generation and Relaxation Processes. *Appl. Phys. A* **2014**, *117* (1), 77–81.

(122) Derrien, T. J. Y.; Itina, T. E.; Torres, R.; Sarnet, T.; Sentis, M. Possible Surface Plasmon Polariton Excitation under Femtosecond Laser Irradiation of Silicon. *J. Appl. Phys.* **2013**, *114* (8), 083104.

(123) Raether, H., Surface Plasmons on Gratings, *Surface Plasmons on Smooth and Rough Surfaces and on Gratings* **1988**, *111, 91–116.*

(124) Höhm, S.; Rosenfeld, A.; Krüger, J.; Bonse, J. Laser-Induced Periodic Surface Structures on Titanium upon Single- and Two-Color Femtosecond Double-Pulse Irradiation. *Opt. Express* **2015**, *23* (20), 25959.

(125) Colombier, J. P.; Garrelie, F.; Brunet, P.; Bruyère, A.; Pigeon, F.; Stoian, R.; Parriaux, O. Plasmonic and Hydrodynamic Effects in Ultrafast Laser-Induced Periodic Surface Structures on Metals. *J. Laser Micro Nanoeng.* **2012**, *7* (3), 362–368.

(126) Colombier, J.-P.; Brunet, P.; Bévillion, E.; Garrelie, F.; Stoian, R.; Albu, C.; Simion, S.; Zamfirescu, M.; Pigeon, F. Génération de Rides Sub-Microniques à La Surface d'un Métal Irradié Par Des Impulsions Lasers Femtosecondes : Effets Plasmoniques et Hydrodynamiques. *21ème Congrès Français de Mécanique* **2013**.

(127) Cherne, F. J.; Baskes, M. I.; Deymier, P. A. Properties of Liquid Nickel: A Critical Comparison of EAM and MEAM Calculations. *Phys. Rev. B* **2002**, *65* (2), 024209.

(128) Egry, I.; Lohoefer, G.; Jacobs, G. Surface Tension of Liquid Metals: Results from Measurements on Ground and in Space. *Phys. Rev. Lett.* **1995**, *75* (22), 4043.

(129) Terakawa, M.; Takeda, S.; Tanaka, Y.; Obara, G.; Miyanishi, T.; Sakai, T.; Sumiyoshi, T.; Sekita, H.; Hasegawa, M.; Viktorovitch, P. Enhanced Localized near Field and Scattered Far Field for Surface Nanophotonics Applications. *Prog. Quant. Electron.*. **2012**, *36* (1), 194–271.

(130) Golosov, E. V.; Ionin, A. A.; Kolobov, Y. R.; Kudryashov, S. I.; Ligachev, A. E.; Makarov, S. V.; Novoselov, Y. N.; Seleznev, L. V.; Sinitsyn, D. V.; Sharipov, A. R. Near-Threshold Femtosecond Laser Fabrication of One-Dimensional Subwavelength Nanogratings on a Graphite Surface. *Phys. Rev. B* **2011**, *83* (11), 115426.

(131) Bonse, J.; Rosenfeld, A.; Kruger, J. Implications of Transient Changes of Optical and Surface Properties of Solids during Femtosecond Laser Pulse Irradiation to the Formation of Laser-Induced Periodic Surface Structures. *Appl. Surf. Sci.* **2011**, *257* (12), 5420–5423.

(132) Bonchbruevich, A. M.; Libenson, M. N.; Makin, V. S.; Trubaev, V. V. Surface Electromagnetic-Waves in Optics. *Opt. Eng.* **1992**, *31* (4), 718–730.

(133) Akhmanov, S. A.; Emel'yanov, V. I.; Koroteev, N. I.; Seminogov, V. N. Interaction of Powerful Laser Radiation with the Surfaces of Semiconductors and Metals: Nonlinear Optical Effects and Nonlinear Optical Diagnostics. *Uspekhi Fiz. Nauk* **1985**, *147* (12), 675.

(134) Höhm, S.; Rosenfeld, A.; Krüger, J.; Bonse, J. Femtosecond Diffraction Dynamics of Laser-Induced Periodic Surface Structures on Fused Silica. *Appl. Phys. Lett.* **2013**, *102* (5), 054102.

(135) Preston, J. S.; Sipe, J. E.; Van Driel, H. M.; Luscombe, J. Optical Absorption in Metallic-Dielectric

Microstructures. *Phys. Rev. B* **1989**, *40* (6), 3931–3941.

(136) Zhang, C.-Y.; Yao, J.-W.; Liu, H.-Y.; Dai, Q.-F.; Wu, L.-J.; Lan, S.; Trofimov, V. a.; Lysak, T. M. Colorizing Silicon Surface with Regular Nanohole Arrays Induced by Femtosecond Laser Pulses. *Opt. Lett.* **2012**, *37* (6), 1106.

(137) Fauchet, P. M.; Siegman, A. E. Surface Ripples on Silicon and Gallium Arsenide under Picosecond Laser Illumination. *Appl. Phys. Lett.* **1982**, *40* (9), 824–826.

(138) Ruiz de la Cruz, A.; Lahoz, R.; Siegel, J.; de la Fuente, G. F.; Solis, J. High Speed Inscription of Uniform, Large-Area Laser-Induced Periodic Surface Structures in Cr Films Using a High Repetition Rate Fs Laser. *Opt. Lett.* **2014**, *39* (8), 2491.

(139) Gurevich, E. L. Mechanisms of Femtosecond LIPSS Formation Induced by Periodic Surface Temperature Modulation. *Appl. Surf. Sci.* **2016**, *374*, 56–60.

(140) Tsibidis, G. D.; Barberoglou, M.; Loukakos, P. A.; Stratakis, E.; Fotakis, C. Dynamics of Ripple Formation on Silicon Surfaces by Ultrashort Laser Pulses in Subablation Conditions. *Phys. Rev. B* **2012**, *86* (11), 115316.

(141) Bonse, J.; Munz, M.; Sturm, H. Scanning Force Microscopic Investigations of the Femtosecond Laser Pulse Irradiation of Indium Phosphide in Air. *Trans. Nanotechnol.* **2004**, *3* (3), 358–367.

(142) Huang, M.; Zhao, F.; Cheng, Y.; Xu, Z. Effects of the Amorphous Layer on Laser-Induced Subwavelength Structures on Carbon Allotropes. *Opt. Lett.* **2012**, *37* (4), 677–679.

(143) Emel'yanov, V. I. Self-Organization of Ordered Nano- and Microstructures on the Semiconductor Surface under the Action of Laser Radiation. *Laser Phys.* **2008**, *18* (6), 682–718.

(144) Öktem, B.; Pavlov, I.; Ilday, S.; Kalaycioğlu, H.; Rybak, A.; Yavaş, S.; Erdoğan, M.; Ilday, F. Ö. Nonlinear Laser Lithography for Indefinitely Large-Area Nanostructuring with Femtosecond Pulses. *Nat. Photonics* **2013**, *7* (11), 897–901.

(145) Derrien, T. J. Y.; Koter, R.; Krüger, J.; Höhm, S.; Rosenfeld, A.; Bonse, J. Plasmonic Formation Mechanism of Periodic 100 nm-Structures upon Femtosecond Laser Irradiation of Silicon in Water. *J. Appl. Phys.* **2014**, *116* (7), 074902.

(146) Jia, T. Q.; Zhao, F. L.; Huang, M.; Chen, H. X.; Qiu, J. R.; Li, R. X.; Xu, Z. Z.; Kuroda, H. Alignment of Nanoparticles Formed on the Surface of 6H-SiC Crystals Irradiated by Two Collinear Femtosecond Laser Beams. *Appl. Phys. Lett.* **2006**, *88* (11), 111117.

(147) Nürnberger, P.; Reinhardt, H.; Kim, H. C.; Yang, F.; Peppler, K.; Janek, J.; Hampp, N. Influence of Substrate Microcrystallinity on the Orientation of Laser-Induced Periodic Surface Structures. *J. Appl. Phys.* **2015**, *118* (13), 134306.

(148) Siegman, A. E.; Fauchet, P. M. Stimulated Wood's Anomalies on Laser-Illuminated Surfaces. *J. Quantum Electron.* **1986**, *22* (8), 1384–1403.

(149) Okamuro, K.; Hashida, M.; Miyasaka, Y.; Ikuta, Y.; Tokita, S.; Sakabe, S. Laser Fluence Dependence of Periodic Grating Structures Formed on Metal Surfaces under Femtosecond Laser Pulse Irradiation. *Phys. Rev. B* **2010**, *82* (16), 165417.

(150) Höhm, S.; Rosenfeld, A.; Krüger, J.; Bonse, J. Femtosecond Laser-Induced Periodic Surface Structures on Silica. *J. Appl. Phys.* **2012**, *112* (1), 014901.

(151) Bonse, J.; Krüger, J. Pulse Number Dependence of Laser-Induced Periodic Surface Structures for Femtosecond Laser Irradiation of Silicon. *J. Appl. Phys.* **2010**, *108* (3), 034903.

(152) Miyaji, G.; Miyazaki, K.; Zhang, K.; Yoshifuji, T.; Fujita, J. Mechanism of Femtosecond-Laser-Induced Periodic Nanostructure Formation on Crystalline Silicon Surface Immersed in Water. *Opt. Express* **2012**, *20* (14), 14848.

(153) Wang, C.; Huo, H.; Johnson, M.; Shen, M.; Mazur, E. The Thresholds of Surface Nano-/Micro-Morphology Modifications with Femtosecond Laser Pulse Irradiations. *Nanotechnology* **2010**, *21* (7), 075304.

(154) Albu, C.; Dinescu, A.; Filipescu, M.; Ulmeanu, M.; Zamfirescu, M. Periodical Structures Induced by Femtosecond Laser on Metals in Air and Liquid Environments. *Appl. Surf. Sci.* **2013**, *278*, 347–351.

(155) Höhm, S.; Rosenfeld, A.; Krüger, J.; Bonse, J. Area Dependence of Femtosecond Laser-Induced Periodic Surface Structures for Varying Band Gap Materials after Double Pulse Excitation. *Appl. Surf. Sci.* **2013**, *278*, 7–12.

(156) Kim, J.; Na, S.; Cho, S.; Chang, W.; Whang, K. Surface Ripple Changes during Cr Film Ablation with a Double Ultrashort Laser Pulse. *Opt. Lasers Eng.* **2008**, *46* (4), 306–310.

(157) Gedvilas, M.; Miksys, J.; Raciukaitis, G. Flexible Periodical Micro- and Nano-Structuring of a Stainless Steel Surface Using Dual-Wavelength Double-Pulse Picosecond Laser Irradiation. *RSC Adv.* **2015**, *5* (92), 75075-75080.

(158) Hashida, M.; Nishii, T.; Miyasaka, Y.; Sakagami, H.; Shimizu, M.; Inoue, S.; Sakabe, S. Orientation of Periodic Grating Structures Controlled by Double-Pulse Irradiation. *Appl. Phys. A* **2016**, *122* (4), 484.

(159) Höhm, S.; Herzlieb, M.; Rosenfeld, A.; Krüger, J.; Bonse, J. Dynamics of the Formation of Laser-Induced Periodic Surface Structures (LIPSS) upon Femtosecond Two-Color Double-Pulse Irradiation of Metals, Semiconductors, and Dielectrics. *Appl. Surf. Sci.* **2016**, *374*, 331–338.

(160) Strickland, D.; Mourou, G. Compression of Amplified Chirped Optical Pulses. *Opt. Commun.* **1985**, *55* (6), 447–449.

(161) Liu, J. M. Simple Technique for Measurements of Pulsed Gaussian-Beam Spot Sizes. *Opt. Lett.* **1982**, *7* (5), 196.

(162) de Harven, E. Electron Microscopy: Remarks on 40 Years Of Ultrastructural Explorations. *CA. Cancer J. Clin.* **1977**, *27* (5), 281–288.

(163) Freundlich, M. M. Origin of the Electron Microscope. *Science* **1963**, *142* (3589), 185–188.

(164) Humphreys, F. J. Grain and Subgrain Characterisation by Electron Backscatter Diffraction. *J. Mater. Sci.* **2001**, *36* (16), 3833–3854.

(165) Maitland, T.; Sitzman, S. EBSD Technique and Materials Characterization. *Scanning Microscopy for Nanotechnology. Techniques and Applications*; **2007**, *14*.

(166) Prior, D. J.; Boyle, A. P.; Brenker, F.; Cheadle, M. C.; Austin, D.; Lopez, G.; Peruzzo, L.; Potts, G. J.; Reddy, S.; Spiess, R.. The Application of Electron Backscatter Diffraction and Orientation Contrast Imaging in the SEM to Textural Problems in Rocks. *Am. Mineral.* **1999**, *84* (11–12), 1741–1759 .

(167) Wright, S. I.; Nowell, M. M. EBSD Image Quality Mapping. *Microsc. Microanal.* **2006**, *12* (1), 72–84.

(168) Maitland, T.; Sitzman, S. Electron Backscatterd Diffraction (EBSD) Technique and Materials Characterization Examples. *Scanning Microsc. Nanotechnol. Tech. Appl.* **2007**, *14*.

(169) Stojakovic, D. Electron Backscatter Diffraction in Materials Characterization. *Process. Appl. Ceram.* **2012**, *6* (1), 1–13.

(170) Hao, E.; Schatz, G. C. Electromagnetic Fields around Silver Nanoparticles and Dimers. *J. Chem. Phys.* **2004**, *120* (1), 357–366.

(171) Stewart, M. E.; Mack, N. H.; Malyarchuk, V.; Soares, J. A. N. T.; Lee, T.-W.; Gray, S. K.; Nuzzo, R. G.; Rogers, J. A. Quantitative Multispectral Biosensing and 1D Imaging Using Quasi-3D Plasmonic Crystals. *Proc. Natl. Acad. Sci.* **2006**, 103 (46), 17143–17148.

(172) Hell, S. W.; Wichmann, J. Breaking the Diffraction Resolution Limit by Stimulated Emission: Stimulated-Emission-Depletion Fluorescence Microscopy. *Opt. Lett.* **1994**, *19* (11), 780–782.

(173) Rust, M. J.; Bates, M.; Zhuang, X. Sub-Diffraction-Limit Imaging by Stochastic Optical Reconstruction Microscopy (STORM). *Nat. Methods* **2006**, *3* (10), 793.

(174) Betzig, E.; Patterson, G. H.; Sougrat, R.; Lindwasser, O. W.; Olenych, S.; Bonifacino, J. S.; Davidson, M. W.; Lippincott-Schwartz, J.; Hess, H. F. Imaging Intracellular Fluorescent Proteins at Nanometer Resolution. *Science*

2006, *313* (5793), 1642–1645.

(175) Hess, S. T.; Girirajan, T. P. K.; Mason, M. D. Ultra-High Resolution Imaging by Fluorescence Photoactivation Localization Microscopy. *Biophys. J.* **2006**, *91* (11), 4258–4272.

(176) Kusko, C.; Dinescu, A.; Rebigan, R.; Kusko, M.; Cristea, D. SNOM Measurements on Metalic Nanostructures. *Proc. Inter. Semicond. Conf.* **2009**, *1*, 197–200.

(177) Bauer, E.; Mundschau, M.; Swiech, W.; Telieps, W. Surface Studies by Low-Energy Electron Microscopy (LEEM) and Conventional UV Photoemission Electron Microscopy (PEEM). *Ultramicroscopy* **1989**, *31* (1), 49–57.

(178) Swiech, W.; Fecher, G. .; Ziethen, C.; Schmidt, O.; Schönhense, G.; Grzelakowski, K.; M. Schneider, C.; Frömter, R.; Oepen, H. .; Kirschner, J. Recent Progress in Photoemission Microscopy with Emphasis on Chemical and Magnetic Sensitivity. *J. Electron Spectros. Relat. Phenomena* **1997**, *84* (1–3), 171–188.

(179) Günther, S.; Kaulich, B.; Gregoratti, L.; Kiskinova, M. Photoelectron Microscopy and Applications in Surface and Materials Science. *Prog. Surf. Sci.* **2002**, 70 (4–8), 187–260.

(180) Locatelli, A.; Bauer, E. Recent Advances in Chemical and Magnetic Imaging of Surfaces and Interfaces by XPEEM. *J. Phys. Condens. Matter* **2008**, *20* (9), 093002.

(181) Nettesheim, S.; Von Oertzen, A.; Rotermund, H. H.; Ertl, G. Reaction Diffusion Patterns in the Catalytic CO-Oxidation on Pt(110): Front Propagation and Spiral Waves. *J. Chem. Phys.* **1993**, *98* (12), 9977–9985.

(182) Meyer zu Heringdorf, F. J.; Reuter, M. C.; Tromp, R. M. Growth Dynamics of Pentacene Thin Films. *Nature* **2001**, *412* (6846), 517.

(183) Gerlach, R.; Maroutian, T.; Douillard, L.; Martinotti, D.; Ernst, H. J. A Novel Method to Determine the Ehrlich-Schwoebel Barrier. *Surf. Sci.* **2001**, *480* (3), 97–102.

(184) Rotermund, H. H.; Nettesheim, S.; Vonoertzen, A.; Ertl, G. Observation of Surface-Diffusion of Adsorbates on Metal-Surfaces by Photoemission Electron-Microscopy (Peem). *Surf. Sci.* **1992**, *275* (1–2), L645–L649.

(185) Scholl, A. Applications of Photoemission Electron Microscopy (PEEM) in Magnetism Research. *Curr. Opin. Solid State Mater. Sci.* **2003**, *17* (1), 59–66.

(186) Schonhense, G. Magnetic Domain Imaging of Thin Metallic Layers Using PEEM. *Phys. Low Dimens. Syst.* **2001**, 309–333.

(187) van Veghel, M. G. A.; Zeijlmans van Emmichoven, P. A. Anti-Ferromagnetic Contrast in NiO (001) Studied with Threshold Photoemission Electron Microscopy. *J. Magn. Magn. Mater.* **2007**, *311* (2), 565–577.

(188) Lemke, C.; Leißner, T.; Jauernik, S.; Klick, A.; Fiutowski, J.; Kjelstrup-Hansen, J.; Rubahn, H.-G.; Bauer, M. Mapping Surface Plasmon Polariton Propagation via Counter-Propagating Light Pulses. *Opt. Express* **2012**, *20* (12), 12877–12884.

(189) Zhang, L.; Kubo, A.; Wang, L.; Petek, H.; Seideman, T. Imaging of Surface Plasmon Polariton Fields Excited at a Nanometer-Scale Slit. *Phys. Rev. B* **2011**, *84* (24), 245442.

(190) Douillard, L.; Charra, F. High-Resolution Mapping of Plasmonic Modes: Photoemission and Scanning Tunnelling Luminescence Microscopies. *J. Phys. D.* **2011**, *44* (46), 464002.

(191) Douillard, L.; Charra, F. High-Resolution Microscopy of Plasmon Field Distributions by Scanning Tunneling Luminescence and Photoemission Electron Microscopies. *Comptes Rendus Physique* **2012**, *13*, 815–829.

(192) Douillard, L.; Charra, F.; Korczak, Z.; Bachelot, R.; Kostcheev, S.; Lerondel, G.; Adam, P. M.; Royer, P. Short Range Plasmon Resonators Probed by Photoemission Electron Microscopy. *Nano Lett.* **2008**, *8* (3), 935–940.

(193) Schmidt, O.; Fecher, G. H.; Hwu, Y.; Schönhense, G. The Spatial Distribution of Non-Linear Effects in Multi-Photon Photoemission from Metallic Adsorbates on Si(1 1 1). *Surf. Sci.* **2001**, *482*, 687–692.

(194) Cinchetti, M.; Gloskovskii, A.; Nepjiko, S. A.; Schönhense, G.; Rochholz, H.; Kreiter, M. Photoemission

Electron Microscopy as a Tool for the Investigation of Optical near Fields. *Phys. Rev. Lett.* **2005**, *95* (4), 047601.

(195) Kubo, A.; Jung, Y. S.; Kim, H. K.; Petek, H. Femtosecond Microscopy of Localized and Propagating Surface Plasmons in Silver Gratings. *J. Phys. B At. Mol. Opt. Phys.* **2007**, *40* (11), S259.

(196) Sun, Q.; Ueno, K.; Yu, H.; Kubo, A.; Matsuo, Y.; Misawa, H. Direct Imaging of the near Field and Dynamics of Surface Plasmon Resonance on Gold Nanostructures Using Photoemission Electron Microscopy. *Light Sci. Appl.* **2013**, *2* (12), e118.

(197) Munzinger, M.; Wiemann, C.; Rohmer, M.; Guo, L.; Aeschlimann, M.; Bauer, M. The Lateral Photoemission Distribution from a Defined Cluster/Substrate System as Probed by Photoemission Electron Microscopy. *New J. Phys.* **2005**, *7* (1), 68.

(198) Wiemann, C.; Bayer, D.; Rohmer, M.; Aeschlimann, M.; Bauer, M. Local 2PPE-Yield Enhancement in a Defined Periodic Silver Nanodisk Array. *Surf. Sci.* **2007**, *601* (20), 4714–4721.

(199) Chelaru, L. I.; Horn-Von Hoegen, M.; Thien, D.; Meyer Zu Heringdorf, F. J. Fringe Fields in Nonlinear Photoemission Microscopy. *Phys. Rev. B* **2006**, *73* (11), 115416.

(200) Hrelescu, C.; Sau, T. K.; Rogach, A. L.; Jäckel, F.; Laurent, G.; Douillard, L.; Charra, F. Selective Excitation of Individual Plasmonic Hotspots at the Tips of Single Gold Nanostars. *Nano Lett.* **2011**, 11 (2), 402–407.

(201) Douillard, L.; Charra, F.; Fiorini, C.; Adam, P. M.; Bachelot, R.; Kostcheev, S.; Lerondel, G.; De La Chapelle, M. L.; Royer, P. Optical Properties of Metal Nanoparticles as Probed by Photoemission Electron Microscopy. *J. Appl. Phys.* **2007**, *101* (8), 083518.

(202) Stockman, M. I.; Kling, M. F.; Kleineberg, U.; Krausz, F. Attosecond Nanoplasmonic-Field Microscope. *Nat. Photonics* **2007**, *1* (9), 539.

(203) Peppernick, S. J.; Joly, A. G.; Beck, K. M.; Hess, W. P. Plasmonic Field Enhancement of Individual Nanoparticles by Correlated Scanning and Photoemission Electron Microscopy. *J. Chem. Phys.* **2011**, *134* (3), 034507.

(204) Peppernick, S. J.; Joly, A. G.; Beck, K. M.; Hess, W. P. Plasmon-Induced Optical Field Enhancement Studied by Correlated Scanning and Photoemission Electron Microscopy. *J. Chem. Phys.* **2013**, *138* (15), 154701.

(205) Word, R. C.; Dornan, T.; Könenkamp, R. Photoemission from Localized Surface Plasmons in Fractal Metal Nanostructures. *Appl. Phys. Lett.* **2010**, *96* (25), 251110.

(206) Fitzgerald, J. P. S.; Word, R. C.; Könenkamp, R. Subwavelength Visualization of Light in Thin Film Waveguides with Photoelectrons. *Phys. Rev. B* **2014**, *89* (19), 195129.

(207) Fitzgerald, J. P. S.; Word, R. C.; Saliba, S. D.; Könenkamp, R. Photonic Near-Field Imaging in Multiphoton Photoemission Electron Microscopy. *Phys. Rev. B* **2013**, *87* (20), 205419.

(208) Tsibidis, G. D.; Fotakis, C.; Stratakis, E. From Ripples to Spikes: A Hydrodynamical Mechanism to Interpret Femtosecond Laser-Induced Self-Assembled Structures. *Phys. Rev. B* **2015**, *92* (4), 041405.

(209) Costache, F.; Henyk, M.; Reif, J. Surface Patterning on Insulators upon Femtosecond Laser Ablation. *Appl. Surf. Sci.* **2003**, 208, 486–491.

(210) Bevillon. E.; Stoian R.; Colombier J. P. Nonequilibrium optical properties of transition metals upon ultrafast electron heating. *J. Phys. Cond. Matter* **2018**, *30* (38), 385410.

(211) Palik, E.D. *Handbook of optical constants of solids* **1997**.

(212) Ivanov, D.; Zhigilei, L. Combined Atomistic-Continuum Modeling of Short-Pulse Laser Melting and Disintegration of Metal Films. *Phys. Rev. B* **003**, *68* (6), 064114.

(213) Zhigilei, L. V; Garrison, B. J. Pressure Waves in Microscopic Simulations of Laser Ablation. *Materials Research Society Symposium - Proceedings*; **1999**; *538*, 491–496.

(214) Zhigilei, L. V.; Garrison, B. J. Microscopic Mechanisms of Laser Ablation of Organic Solids in the Thermal and

Stress Confinement Irradiation Regimes. *J. Appl. Phys.* **2000**, *88* (3), 1281–1298.

(215) Wu, C.; Zhigilei, L. V. Microscopic Mechanisms of Laser Spallation and Ablation of Metal Targets from Large-Scale Molecular Dynamics Simulations. *Appl. Phys. A* **2014**, *114* (1), 11–32.

(216) Leveugle, E.; Ivanov, D. S.; Zhigilei, L. V. Photomechanical Spallation of Molecular and Metal Targets: Molecular Dynamics Study. *Appl. Phys. A* **2004**, *79* (7), 1643–1655.

(217) Demaske, B. J.; Zhakhovsky, V. V.; Inogamov, N. A.; Oleynik, I. I. Ablation and Spallation of Gold Films Irradiated by Ultrashort Laser Pulses. *Phys. Rev. B* **2010**, *82* (6), 064113.

(218) Lorazo, P.; Lewis, L. J.; Meunier, M. Thermodynamic Pathways to Melting, Ablation, and Solidification in Absorbing Solids under Pulsed Laser Irradiation. *Phys. Rev. B* **2006**, *73* (13), 134108.

(219) Lai, H. Y.; Huang, P. H. Laser-Irradiated Thermodynamic Behaviors of Spallation and Recombination at Solid-State Interface. *Appl. Surf. Sci.* **2008**, *254* (10), 3067–3073.

(220) Anisimov, S. I.; Zhakhovskii, V. V; Inogamov, N. A.; Nishihara, K.; Oparin, A. M.; Petrov, Y. V. Destruction of a Solid Film under the Action of Ultrashort Laser Pulse. *J. Exp. Theor. Phys. Lett.* **2003**, *77* (11), 606–610.

(221) Luo, S. N.; Ahrens, T. J.; Çağın, T.; Strachan, A.; Goddard, W. A.; Swift, D. C. Maximum Superheating and Undercooling: Systematics, Molecular Dynamics Simulations, and Dynamic Experiments. *Phys. Rev. B* **2003**, *68* (13), 134206.

(222) Paltauf, G.; Dyer, P. E. Photomechanical Processes and Effects in Ablation. *Chem.Rev.* **2003**, *103* (2), 487–518.

(223) Shugaev, M. V.; Wu, C.; Armbruster, O.; Naghilou, A.; Brouwer, N.; Ivanov, D. S.; Derrien, T. J. Y.; Bulgakova, N. M.; Kautek, W.; Rethfeld, B.; et al. Fundamentals of Ultrafast Laser-Material Interaction. *MRS Bull.* **2016**, *41* (12), 960–968.

(224) Vorobyev, A. Y.; Guo, C. Femtosecond Laser Nanostructuring of Metals. *Opt. Express* **2006**, *14* (6), 2164–2169.

(225) Vincenc Oboňa, J.; Ocelík, V.; Rao, J. C.; Skolski, J. Z. P.; Römer, G. R. B. E.; Huis In 't Veld, A. J.; Hosson, J. T. M. D. Modification of Cu Surface with Picosecond Laser Pulses. *Appl. Surf. Sci.* **2014**, *303*, 118–124.

(226) Vorobyev, A. Y.; Guo, C. Enhanced Absorptance of Gold Following Multipulse Femtosecond Laser Ablation. *Phys. Rev. B* **2005**, *72* (19), 195422.

(227) Dai, Y.; He, M.; Bian, H.; Lu, B.; Yan, X.; Ma, G. Femtosecond Laser Nanostructuring of Silver Film. *Appl. Phys. A* **2012**, *106* (3), 567–574.

(228) Zhao, Q.-Z.; Malzer, S.; Wang, L.-J. Self-Organized Tungsten Nanospikes Grown on Subwavelength Ripples Induced by Femtosecond Laser Pulses. *Opt. Express* **2007**, *15* (24), 15741–15746.

(229) Ashkenazy, Y.; Averback, R. S. Kinetic Stages in the Crystallization of Deeply Undercooled Body-Centered-Cubic and Face-Centered-Cubic Metals. *Acta Mater.* **2010**, *58* (2), 524–530.

(230) Wilkinson, A. J.; Dingley, D. J. Quantitative Deformation Studies Using Electron Back Scatter Patterns. *Acta Metall. Mater.* **1991**, *39* (12), 3047–3055.

(231) Keller, R. R.; Roshko, A.; Geiss, R. H.; Bertness, K. A.; Quinn, T. P. EBSD Measurement of Strains in GaAs Due to Oxidation of Buried AlGaAs Layers. *Microelectron. Eng.* **2004**, *75* (1), 96–102.

(232) Petrov, R.; Kestens, L.; Wasilkowska, A.; Houbaert, Y. Microstructure and Texture of a Lightly Deformed TRIP-Assisted Steel Characterized by Means of the EBSD Technique. *Mater. Sci. Eng. A* **2007**, *447* (1–2), 285–297.

(233) Walther, T.; Humphreys, C. J. A Quantitative Study of Compositional Profiles of Chemical Vapour-Deposited Strained Silicon-Germanium/Silicon Layers by Transmission Electron Microscopy. *J. Cryst. Growth* **1999**, *197* (1–2), 113–128.

(234) Pennycook, S. J. Z-Contrast Stem for Materials Science. *Ultramicroscopy* **1989**, *30* (1–2), 58–69.

(235) Ishizuka, K. A Practical Approach for STEM Image Simulation Based on the FFT Multislice Method.

Ultramicroscopy **2002**, *90* (2–3), 71–83.

(236) Mie, G. Beitr??Ge Zur Optik Tr??Ber Medien, Speziell Kolloidaler Metall??Sungen. *Ann. Phys.* **1908**.

(237) Liu, H.; Lalanne, P. Microscopic Theory of the Extraordinary Optical Transmission. *Nature* **2008**, *452* (7188), 728.

(238) Zhakhovskii, V. V; Inogamov, N. A.; Nishihara, K. New Mechanism of the Formation of the Nanorelief on a Surface Irradiated by a Femtosecond Laser Pulse. *JETP Lett.* **2008**, *87* (8), 423–427.

(239) Colombier, J. P.; Combis, P.; Audouard, E.; Stoian, R. Guiding Heat in Laser Ablation of Metals on Ultrafast Timescales: An Adaptive Modeling Approach on Aluminum. *New J. Phys.* **2012**, *14* (1), 013039.

(240) Grady, D. E. The Spall Strength of Condensed Matter. *J. Mech. Phys. Solids* **1988**, 36 (3), 353–384.

(241) Rudenko, A.; Colombier, J. P.; Itina, T. E. From Random Inhomogeneities to Periodic Nanostructures Induced in Bulk Silica by Ultrashort Laser. *Phys. Rev. B* **2016**, *93* (7), 075427.

(242) Derry, G. N.; Kern, M. E.; Worth, E. H. Recommended Values of Clean Metal Surface Work Functions. *J. Vac. Sci. Technol. A* **2015**, *33* (6), 060801.

(243) Sakabe, S.; Hashida, M.; Tokita, S.; Namba, S.; Okamuro, K. Mechanism for Self-Formation of Periodic Grating Structures on a Metal Surface by a Femtosecond Laser Pulse. *Phys. Rev. B* **2009**, *79* (3), 033409.

(244) Yurkin, M. A.; Hoekstra, A. G. The Discrete Dipole Approximation: An Overview and Recent Developments. *J. Quant. Spectrosc. Radiat. Transf.* **2007**, *106* (1–3), 558–589.

(245) Markel, V. A. Coupled-Dipole Approach to Scattering of Light from a Onedimensional Periodic Dipole Structure. *J. Mod. Opt.* **1993**, *40* (11), 2281–2291.

(246) Yang, W. H.; Schatz, G. C.; Van Duyne, R. P. Discrete Dipole Approximation for Calculating Extinction and Raman Intensities for Small Particles with Arbitrary Shapes. *J. Chem. Phys.* **1995**, *103* (3), 869–875.

(247) McMahon, J. M.; Henzie, J.; Odom, T. W.; Schatz, G. C.; Gray, S. K. Tailoring the Sensing Capabilities of Nanohole Arrays in Gold Films with Rayleigh Anomaly-Surface Plasmon Polaritons. *Opt. Express* **2007**, *15* (26), 16119–18129.

(248) Kuršelis, K.; Kiyan, R.; Chichkov, B. N. Formation of Corrugated and Porous Steel Surfaces by Femtosecond Laser Irradiation. *Appl. Surf. Sci.* **2012**, *258* (22), 8845–8852.

(249) Zhang, X. G. Morphology and Formation Mechanisms of Porous Silicon. *J. Electrochem. Soc.* **2004**, *151* (1), C69–C80.

(250) Huang, M. J.; Yang, C. R.; Chiou, Y. C.; Lee, R. T. Fabrication of Nanoporous Antireflection Surfaces on Silicon. *Sol. Energy Mater. Sol. Cells* **2008**, *92* (11), 1352–1357.

(251) Wu, W.; Dey, D.; Memis, O. G.; Katsnelson, A.; Mohseni, H. Fabrication of Large Area Periodic Nanostructures Using Nanosphere Photolithography. *Nanoscale Res. Lett.* **2008**, *13* (10), 351.

(252) Lugomer, S.; Mihaljević, B.; Peto, G.; Toth, A. L.; Horvath, E. Spongelike Metal Surface Generated by Laser in the Semiconfined Configuration. *J. Appl. Phys.* **2005**, *97* (7), 073305.

(253) Pronko, P. P.; Dutta, S. K.; Squier, J.; Rudd, J. V.; Du, D.; Mourou, G. Machining of Sub-Micron Holes Using a Femtosecond Laser at 800 nm. *Opt. Commun.* **1995**, *114* (1–2), 106–110.

(254) Perrie, W.; Gill, M.; Robinson, G.; Fox, P.; O'Neill, W. Femtosecond Laser Micro-Structuring of Aluminium under Helium. *Appl. Surf. Sci.* **2004**, *230* (1–4), 50–59.

(255) Nayak, B. K.; Gupta, M. C. Self-Organized Micro/Nano Structures in Metal Surfaces by Ultrafast Laser Irradiation. *Optics and Lasers in Engineering* **2010**, *48* (10), 940–949

(256) Wang, F.; Yu, H. Y.; Wang, X.; Li, J.; Sun, X.; Yang, M.; Wong, S. M.; Zheng, H. Maskless Fabrication of Large Scale Si Nanohole Array via Laser Annealed Metal Nanoparticles Catalytic Etching for Photovoltaic

Application. *J. Appl. Phys.* **2010**, *108* (2), 024301.

(257) Schneider, C. A.; Rasband, W. S.; Eliceiri, K. W. NIH Image to ImageJ: 25 Years of Image Analysis. *Nature Methods* **2012**, *9* (7), 671.

(258) Reinitz, J. Turing Centenary: Pattern Formation. *Nature* **2012**, *482* (7386), 464.

(259) Ouyang, Q.; Swinney, H. L. Transition from a Uniform State to Hexagonal and Striped Turing Patterns. *Nature* **1991**, *352* (6336), 610.

(260) Kondo, S.; Miura, T. Reaction-Diffusion Model as a Framework for Understanding Biological Pattern Formation. *Science* **2010**, *329* (5999), 1616–1620.

(261) Yang, L.; Dolnik, M.; Zhabotinsky, A. M.; Epstein, I. R. Pattern Formation Arising from Interactions between Turing and Wave Instabilities. *J. Chem. Phys.* **2002**, *117* (15), 7259–7265.

(262) Turing, A. M. The Chemical Basis of Morphogenesis, *Phil. Trans. R. Soc. Lon. B* **1953**, *237* (641), 37–72.

(263) Karim, E.T. Atomistic Simulation Study of Short Pulse Laser-Induced Generation of Crystal Defects In Metal Targets. **2015,** doi.org/10.18130/V34K3J.